

Superconducting Integrated Circuits at Sub-millimeter Wavelengths

Hähnle, S.A.

DOI

[10.4233/uuid:91047108-e77e-4d3b-956e-1e97ee8f8c47](https://doi.org/10.4233/uuid:91047108-e77e-4d3b-956e-1e97ee8f8c47)

Publication date

2021

Document Version

Final published version

Citation (APA)

Hähnle, S. A. (2021). *Superconducting Integrated Circuits at Sub-millimeter Wavelengths*. [Dissertation (TU Delft), Delft University of Technology]. <https://doi.org/10.4233/uuid:91047108-e77e-4d3b-956e-1e97ee8f8c47>

Important note

To cite this publication, please use the final published version (if applicable).
Please check the document version above.

Copyright

Other than for strictly personal use, it is not permitted to download, forward or distribute the text or part of it, without the consent of the author(s) and/or copyright holder(s), unless the work is under an open content license such as Creative Commons.

Takedown policy

Please contact us and provide details if you believe this document breaches copyrights.
We will remove access to the work immediately and investigate your claim.

Superconducting Integrated Circuits at Sub-millimeter Wavelengths

Superconducting Integrated Circuits at Sub-millimeter Wavelengths

DISSERTATION

for the purpose of obtaining the degree of doctor
at Delft University of Technology
by the authority of the Rector Magnificus, Prof.dr.ir. T.H.J.J. van der Hagen,
chair of the board for Doctorates,
to be defended publicly on
Monday 15 November at 10:00 o'clock

by

Sebastian Andrej HÄHNLE

Master of Science in Physics,
Heidelberg University, Germany,
born in Munich, Germany.

This dissertation has been approved by the:

promotor: Prof. dr. ir. J. J. A. Baselmans

copromotor: Dr. A. Endo

Composition of the doctoral committee:

Rector Magnificus

Chairman

Prof.dr. J.J.A. Baselmans

Delft University of Technology, promotor

Dr. A. Endo

Delft University of Technology, copromotor

Independent members:

Prof.dr. N. Llombart Juan,

Delft University of Technology

Prof.dr. P.M. Sarro

Delft University of Technology

Prof.dr. E. Driessen,

Institut de Radioastronomie Millimétrique

Dr.ir. P. de Visser,

Netherlands Institute for Space Research

Dr. S. Doyle,

Cardiff University



The work presented in this thesis has been performed at TU Delft and SRON (Netherlands Institute for Space Research).

Keywords: Transmission Lines, Dielectric Loss, Radiation Loss, Sub-millimeter Loss, Fabry-Pérot Resonator, Low-temperature Detectors, Sub-millimeter systems.

Cover design by: Sebastian Andrej Hähnle.

Printed by: Ipskamp Drukkers B.V., Enschede, Netherlands.

Copyright © 2021 by S. A. Hähnle. All rights reserved.

An electronic version of this dissertation is available at: <http://repository.tudelft.nl/>

ISBN 978-94-6421-528-1

Contents

1	Introduction	1
1.1	The Terahertz Gap	1
1.1.1	Low Temperature Detectors	2
1.2	Superconducting Integrated Circuits	4
1.2.1	DESHIMA Filterbank	5
1.3	Outline of the Thesis	6
2	Theory	9
2.1	Superconductivity	9
2.1.1	General Introduction	9
2.1.2	Complex Conductivity	12
2.2	Superconducting Transmission Lines	17
2.2.1	Transmission Line Basics	17
2.2.2	Superconducting Lines	20
2.2.3	Microstrips	21
2.2.4	Co-Planar Waveguides	26
2.3	Superconducting Transmission line Fabry-Pérot Resonators	29
2.3.1	Resonance Frequency	29
2.3.2	Transmission spectrum	29
2.3.3	Quality Factor	31
2.4	Simulating a Transmission Line Fabry-Pérot Resonator	35
2.4.1	Coupler Simulation	35
2.4.2	Radiation Loss Simulation	37
2.5	Microwave Kinetic Inductance Detector	41
2.5.1	Response	42
2.5.2	Noise	44
2.5.3	Hybrid Design	46
2.6	Optical Efficiency	48
3	Experimental Background	51
3.1	Fabrication	51
3.1.1	Leaky-Lens Antenna	51
3.1.2	Co-Planar Waveguide Fabry-Pérot	54

3.1.3	Microstrip Fabry-Pérot	56
3.2	Terahertz Spectrum Measurement	58
3.3	Antenna Characterization	59
3.3.1	Beam Pattern Measurement	59
3.3.2	Optical Efficiency Measurement	61
3.4	Readout Electronics	62
4	Large Angle Optical Access in a sub-Kelvin Cryostat	67
4.1	Introduction	67
4.2	System Overview	68
4.3	Detailed System Design	69
4.3.1	Spectral Filtering	69
4.3.2	Geometric Throughput	72
4.4	Conclusion	73
5	An Ultra Wideband Leaky Lens Antenna for Broadband Spectroscopic Imaging Applications	75
5.1	Introduction	75
5.2	Device and Antenna Design	76
5.3	Fabrication	78
5.3.1	Assembly	79
5.4	Measurements and Results	79
5.4.1	Beam Patterns	79
5.4.2	Optical Efficiency	82
5.5	Conclusion	84
6	Suppression of radiation loss in high kinetic inductance superconducting co-planar waveguides	87
6.1	Introduction	87
6.2	Radiation Loss Theory	88
6.3	Device	90
6.3.1	Fabry-Pérot Concept	90
6.3.2	Chip Design	91
6.4	Experimental Setup	92
6.5	Measurements and Results	93
6.5.1	Fabry-Pérot Spectra	93
6.5.2	Internal Loss	94
6.6	Conclusion	96
7	Losses in superconducting microstrips at sub-mm wavelengths	97
7.1	Introduction	97
7.2	Device Design	98
7.3	Fabrication	100

7.4	Experimental Setup	100
7.4.1	Microwave Measurement	100
7.4.2	Submillimeter Measurement	101
7.5	Measurements and Results	101
7.6	Microwave Measurement	101
7.6.1	Submillimeter Measurements	103
7.7	Conclusions	105
8	Conclusion	107
8.1	Wideband Leaky-Lens Antenna	107
8.2	On-chip Fabry-Pérot Resonator	108
8.3	Transmission Line Losses	109
8.4	Future Outlook	110
8.4.1	Advanced Astronomical Instrumentation	110
8.4.2	Physics at Sub-millimeter Wavelengths	111
8.5	Impact of the Research	112
A	Process Flow Details	115
A.1	LT122: Leaky-Lens Antenna	115
A.2	LT121: Co-Planar Waveguide Fabry-Perot	119
A.3	LT189: Microstrip Fabry-Perot	122
	Summary	145
	Summary	149
	List of Publications	153
	Curriculum Vitae	155
	Acknowledgements	157

Chapter 1

Introduction

1.1 The Terahertz Gap

There is a strong interest from the astronomical community in the terahertz frequency regime ($0.1 - 10$ THz), as it contains a large fraction of the universe's integrated spectral brightness, as shown in Fig. 1.1a), yet is poorly explored. This is largely due to low atmospheric transmission caused by water absorption lines, which makes observations from ground based telescopes difficult for frequencies of $0.1 - 1$ THz and practically impossible for $1 - 10$ THz, requiring balloon- or satellite-based experiments. Additionally, detector technology for this frequency range has only become available in recent decades. Astronomical sources in this frequency range include protostars and protoplanetary disks [1], dust in the interstellar medium [2], sub-millimeter galaxies [3] and the cosmic microwave background (CMB) [4], with the latter two of particular interest in the context of this thesis.

Precise measurements of the E- and B-modes of the CMB polarization around > 0.1 THz are a probe of the earliest universe, as detection of primordial B-modes in the CMB would be direct evidence for inflation theory [5]. However, these measurements must be carefully corrected for the foreground signal of polarized dust. Proper isolation of the foreground requires observations at different frequencies, which are ideally carried out with the same instrument [6, 7].

The Sunyaev-Zeldovich (SZ)-effect is a modification of the CMB spectrum caused by inverse Compton scattering of CMB photons with high-energy electrons in hot gases [8]. Observations of the SZ-effect are of particular interest in the study of galactic clusters where they offer insights into the intracluster medium, complementary to X-ray observations (see Fig. 1.1d)). These observations require measurements of the (medium resolution) spectral- and spatial dependence of CMB fluctuations in the range of $0.05 - 1$ THz [9].

Sub-millimeter galaxies (SMGs), also sometimes referred to as luminous infrared galaxies or dusty star-forming galaxies, are very dusty galaxies in the early universe with high star formation rates [3, 10]. Optical signals from sources inside these galaxies are absorbed by dust, which is heated and re-emits light at lower temperatures. Consequently, these

galaxies are almost exclusively visible in the far-infrared regime and make up a large part of the cosmic infrared background (CIB). While a vast number of SMGs have been detected with continuum imaging surveys [11] (see Fig. 1.1b)), spectroscopic surveys are required to determine their redshift and physical properties.

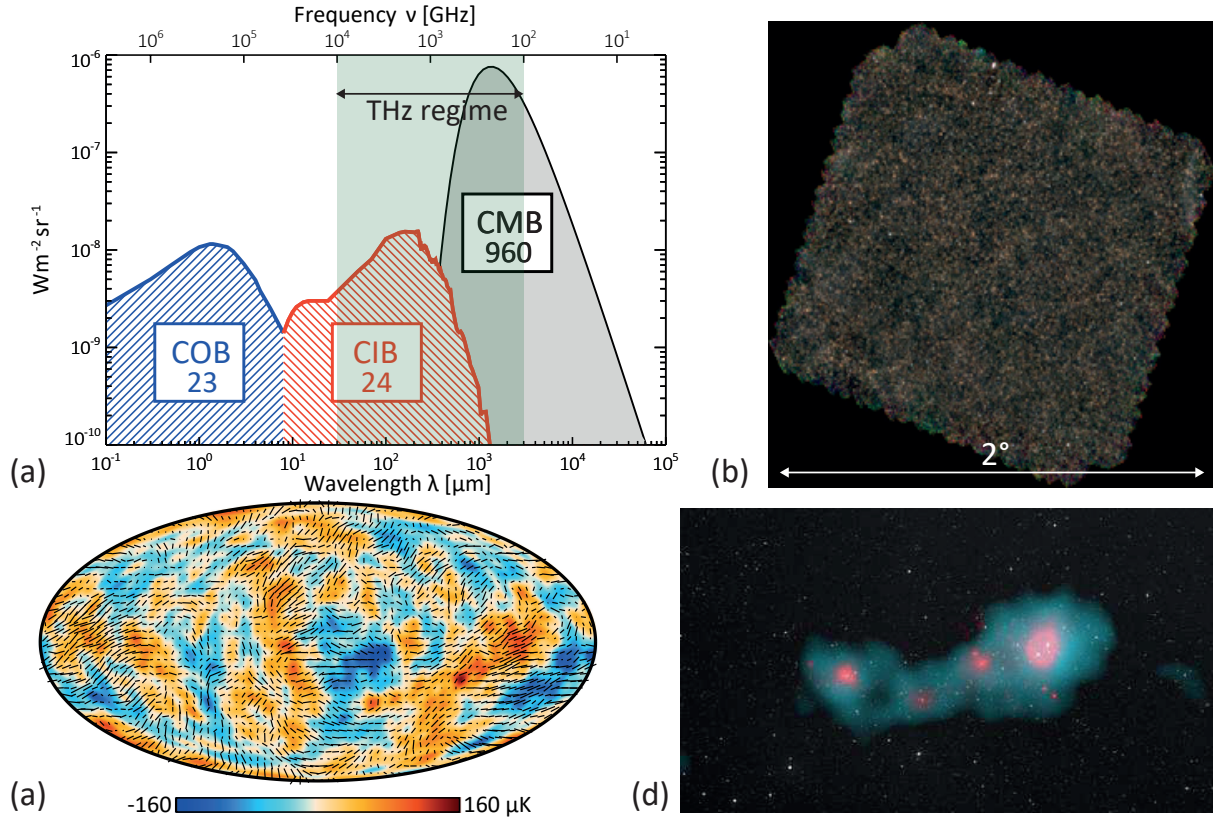


Figure 1.1: (a) Spectral energy distributions of the highest intensity backgrounds in the universe and their approximate brightness in $\text{nWm}^{-2}\text{sr}^{-1}$ written in the boxes. From left to right: the Cosmic Optical Background (COB), the Cosmic Infrared Background (CIB) and the Cosmic Microwave Background (CMB) (From [11]) (b) The Herschel-SPIRE 2 degree COSMOS field [11] at 250 μm (blue), 350 μm (green) and 350 μm (red). Each point represent a sub-millimeter galaxy with thousands visible in this field of view. (c) Polarization map of the CMB, overlaid on the temperature fluctuation (both smoothed to 5deg), measured by *Planck* (from [4]) (d) Composite image of the Shapley super-cluster, overlaying optical from DSS (*white*), x-ray from ROSAT (*pink*) and the thermal Sunyaev-Zeldovich effect seen by *Planck* (*blue*) (From [12])

1.1.1 Low Temperature Detectors

Astronomy, aside from the recent successes in detecting neutrinos and gravitational waves, is intrinsically limited to detecting the amplitude and phase of light as a function of direction and frequency. This can be separated in imaging or spectroscopic observations. In the terahertz regime, different types of low-temperature detectors are currently used to fill these roles separately.

High-resolution spectroscopy is carried out with heterodyne detectors, using either superconductor-insulator-superconductor (SIS)-mixers or hot-electron bolometers (HEB)-mixers. The frequency range of SIS-mixers is limited to the superconducting bandgap, with a current upper limit of 1.2 THz using NbTiN [13]. HEB-mixers are generally used at higher frequencies, where SIS-mixers are not available. Heterodyne receivers preserve both amplitude- and phase-information of the incoming signal over a bandwidth of several GHz. This makes them intrinsically suitable for high-resolution spectroscopy ($R > 1,000,000$), but also notoriously hard to multiplex as each receiver requires its own broad-band cabling, cryogenic amplifier and room temperature electronics. Current instruments are consequently limited to array sizes of the order of ~ 10 pixels [14], where the largest array is implemented in the SuperCam with 64 pixels [15].

Dedicated imaging observations are therefore carried out with direct power detectors, primarily transition edge sensors (TES)-arrays [16] or microwave kinetic inductance detectors (MKID)-arrays [17]. TES arrays currently employ time-domain multiplexing or frequency-domain multiplexing in the MHz range, limited to ~ 100 pixels per readout line. For MKIDs, frequency-domain multiplexing in the microwave regime enables ~ 1000 pixels per readout line. Current imaging arrays contain in the order of $\sim 10^3$ pixels [18], with the largest arrays implemented in NIKA2 [19] with $\sim 3,000$ MKID pixels and SCUBA-2 [20] with 10,000 TES pixels.

While spectroscopy and imaging are possible independently, there does not yet exist a combined imaging spectrometer in the terahertz regime comparable to the integral field units (IFU) used in the optical regime [21], where a spectrometer is attached to each spatial pixel, thereby offering observations with instantaneous spatial and spectral resolution. On one side, Heterodyne detectors offer intrinsic frequency resolution, but they can not be scaled to large arrays due to system complexity. On the other side, TES and MKID arrays can be combined with dispersive elements, such as gratings, analogous to optical instruments. This has been realized in instruments with < 10 spatial pixels [22, 23], but the required grating size at terahertz frequencies turns this approach unfeasible for larger arrays. Another method for TES or MKID based spectroscopy is to place a Fourier Transform Spectrometer (FTS) in front of an imaging array, as implemented in the KISS [24], CONCERTO [25] and SPIRE [26] instruments, essentially exchanging the spatial scanning of a dispersive instrument for spectral scanning. This approach has the advantage, that existing imaging arrays can be easily repurposed for spectroscopic measurements, however it suffers from additional photon noise compared to a dispersive instrument, as each detector receives the full frequency band, thereby increasing integration time compared to the narrow-band detectors of a dispersive instrument. Consequently, an FTS based instrument requires a large pixel count n compared to the resolution R to achieve mapping speeds comparable to a single pixel dispersive instrument with equal resolution. Both grating and FTS based instruments can obtain spectroscopic images, but require either spectral or significant spatial scanning for this purpose. This significantly limits the mapping speed of these instruments compared to the instantaneous spatial and spectral resolution offered by an IFU.

A way around the limitations of both FTS and grating spectrometers in order to realize

an imaging spectrometer at terahertz frequencies, would be the integration of spectroscopic elements with an MKID or TES array on a single chip using low-loss superconducting transmission line technology. Such a superconducting integrated circuit (SIC) could circumvent the size constraints of a grating spectrometer, by miniaturization via two paths: First, transmission lines exhibit a more compact lateral field distribution than that of a quasi-optical beam propagating in vacuum, which allows for smaller and more tightly spaced elements. Small element sizes are further supported by a reduced wavelength due to the larger dielectric constant of a transmission line. Second, transmission line circuits can be used for more intricate spectrometer designs, which could not be implemented using optical elements. Compared to an FTS instrument, it would offer the lower photon noise of narrow-band detectors. While the large number of detectors ($n \times R$) required to cover both spatial (n) and spectral resolution (R) of a true imaging spectrometer can be challenging to achieve, it represents a limitation by the readout system and not by the fundamental properties of the optical system. However, creating an efficient imaging spectrometer with SICs requires highly complex, yet near lossless circuitry, and is therefore a significant technological challenge.

1.2 Superconducting Integrated Circuits

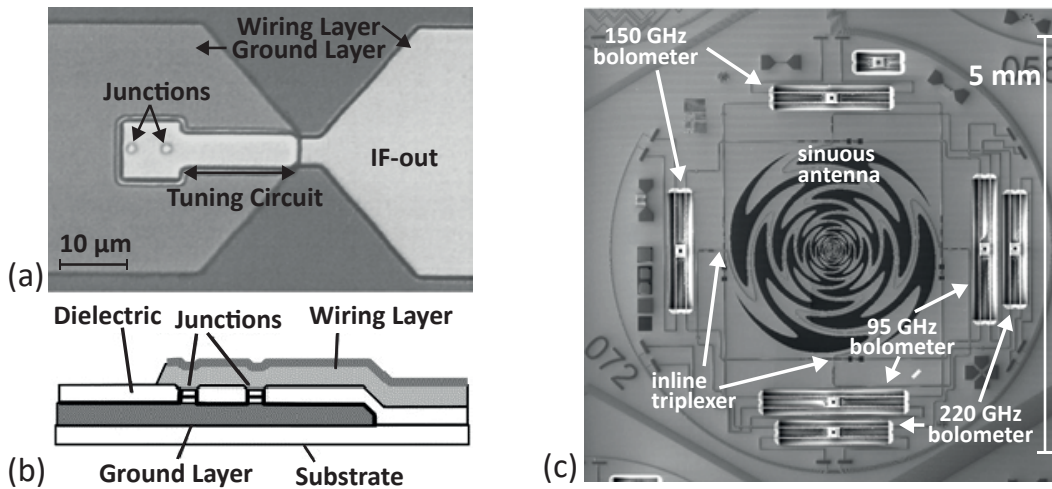


Figure 1.2: (a) Twin-junction SIS-mixer for ~ 1 THz with a NbTiN/SiO₂/Al microstrip tuning circuit (adapted from Ref. [13]). (b) Cross section of the circuit shown in panel a) (adapted from Ref. [13]). (c) Single pixel of SPT-3G, showing the broadband sinuous antenna, inline triplexers that define the three observing bands, and six TES bolometers measuring three bands in two polarizations (From [27]).

While SICs are relatively well established at microwave frequencies, due to their use in qubits [28] and microwave readout of TES/MKID arrays, scaling them to terahertz frequencies is not a trivial matter and often requires completely new approaches.

The first SIC at terahertz frequencies can be considered in the context of SIS-mixers,

where a small tuning circuit is necessary for impedance matching (see Fig. 1.2a)) [29, 30]. Later additions to the terahertz circuit include the use of planar double-slot antennas instead of horn antennas [13], and on-chip local oscillator signal generation using flux flow oscillators [31]. It should be noted, that while the combination of flux flow oscillator and SIS mixer represented the first integrated receivers based on superconducting circuits, they suffered in noise temperature compared to the non-integrated devices as they could not be optimized as easily. This critically put the technology out of contention for state-of-the-art instruments.

Similar developments occurred for imaging instruments in order to integrate spectral resolution and independent detection of orthogonal linear polarizations. This led to the creation of multichroic and multipolarization cameras by moving optical elements, such as polarizers and low-pass/high-pass filters, onto the chip, thereby separating the signal from a single wideband antenna into different components which are then fed to separate detectors [27] (see Figure 1.2c)). One pixel on such a camera then corresponds to a single antenna with multiple detectors, with multiple pixels placed on a single chip. These devices are primarily used for CMB experiments, using TES as detectors [27, 32]. While such a camera could already be argued to be a very-low resolution imaging spectrometer ($R \sim 5$), the real target for an imaging spectrometer should be considered to have at least medium spectral resolution ($R > 300$) over an instantaneous bandwidth of at least one octave ($> 1 : 2$).

1.2.1 DESHIMA Filterbank

The DESHIMA instrument represents the first step towards such an imaging spectrometer, realizing a medium resolution on-chip filterbank. A first prototype of DESHIMA has recently demonstrated this technology with first light at the ASTE telescope [33], with other similar instruments, such as SuperSpec [34] and Micro-Spec [35] currently in development. The DESHIMA prototype chip, shown schematically in Fig. 1.3a), has 49 spectral channels at 330 – 370 GHz with resolution $R \approx 300$ behind a single narrow-band antenna ($\approx 10\%$ bandwidth). Each spectral channel consists of a terahertz-resonator which is coupled on one side to the transmission line connected to the antenna and on the other side to a MKID. The resonators act as filters, selecting the frequency of the signal detected by the attached MKID with the spectral resolution given by the resonators quality factor $Q = R$. All elements of the filterbank are realized with co-planar waveguide (CPW) transmission lines made of a single superconducting NbTiN layer, which is lossless up to its bandgap frequency of $2\Delta_{NbTiN} \approx 1.1$ THz (for $T_c = 15$ K). Incoming terahertz radiation is absorbed in a small Al section of the hybrid Al/NbTiN MKID [36], due to the lower bandgap of $2\Delta_{Al} \approx 90$ GHz.

DESHIMA successfully measured the spectrum of a luminous infrared galaxy, resolving a slightly redshifted CO emission line as shown in Fig. 1.3b). However, several issues need to be addressed on the way to a fully operational and competitive instrument.

- Efficiency: The prototype has a coupling efficiency of only 2% from in front of the

cryostat window to being absorbed in the MKID, which is primarily due to radiation loss in the CPW terahertz resonators. This can be solved with an improved filter design [37] and moving to microstrip transmission lines, thereby eliminating radiation losses. However, while microstrips do not radiate significantly, they suffer from material dependent dielectric losses which can limit efficiency due to losses in both the resonator and the transmission line from the antenna.

- Resonator quality factor: A spectral resolution of $R \gtrsim 500$ is desired, up from the prototype of $R \approx 300$. Spectral resolution is given by the resonators quality factor $R = Q$. Therefore, achieving this without suffering from losses inside the resonator requires a dielectric material with $Q_i \gtrsim 10,000$ when microstrips are used.
- Wideband filterbank: Finally, the narrowband prototype needs to be scaled to a wideband instrument, requiring a wideband antenna with a bandwidth up to 1 : 3 and high optical efficiency. Additionally, the number of channels increases proportional to the filterbank bandwidth, increasing the complexity of the circuit [37].

An imaging spectrometer in the range of 0.1 – 1 THz can be envisioned with on-chip filterbanks based on the large bandgap of NbTiN by drastically scaling the number of spatial pixels. As each pixel is connected to an on-chip filterbank, massive miniaturization of the superconducting integrated circuits is required. The key to this miniaturization are low-loss microstrip transmission lines, as they provide slower phase velocities, reduced cross-talk range, and simpler circuit elements than comparable CPW lines. However, dielectric losses at sub-kelvin temperatures - the main loss mechanism in superconducting microstrips - are extremely challenging to measure in the millimeter/sub-millimeter regime, and therefore not well studied.

1.3 Outline of the Thesis

In this thesis, I present my work on building blocks required for a future imaging spectrometer, with a focus on dedicated experimental techniques facilitating their development. This includes the design of a cryogenic platform for fast and flexible measurements, measurements of a wideband antenna prototype operating at 300–900 GHz and the development of on-chip Fabry-Perot resonators which allow precise measurements of CPW and microstrip transmission line losses at sub-millimeter wavelengths.

Chapter 2 provides the relevant theoretical background for this thesis, starting with an overview of superconductivity and the complex conductivity of a superconductor based on Mattis-Bardeen theory. We then treat superconducting transmission lines, focusing on the propagation- and loss-properties of co-planar waveguides and microstrips. Building on this, we introduce transmission line Fabry-Perot resonators (FPR) and how to obtain the internal quality factor and consequently transmission line losses from the FPRs transmission spectrum. EM-simulations of different FPR components carried out in Sonnet are also given here. Finally, we show the response and noise properties of microwave kinetic

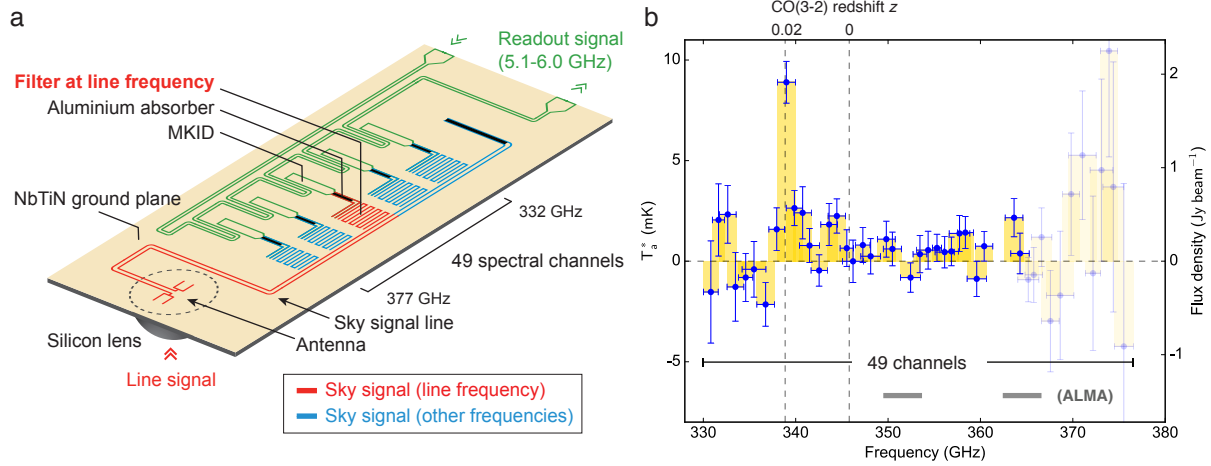


Figure 1.3: (a) Schematic of the filterbank design in the DESHIMA prototype. The path of a terahertz signal at 339 GHz from the twin-slot antenna through the corresponding bandpass filter to the MKID is shown in red. (b) Spectrum of VV 114 measured with the DESHIMA prototype, with the response of each spectral channel plotted as a function of the channels peak frequency. See Endo et al. [33] for details on the analysis. (From [33])

inductance detectors (MKIDs), specifically the hybrid Al-NbTiN design which we use for all terahertz measurements in this thesis.

In *Chapter 3* we collect the cleanroom fabrication route and experimental setups used during the course of this thesis. This comprises three different chip types — a leaky-lens antenna, a co-planar waveguide Fabry-Perot and a microstrip Fabry-Perot — as well as three separate laboratory setups to measure terahertz spectra, antenna beam patterns and optical efficiency. In the end, we discuss the multiplexing readout electronics common to all of these setups.

In *Chapter 4* we present the optical access design of the cryostat we used for most experiments in this thesis. The optical access contains no reflective or refractive elements, providing a direct line-of-sight between room temperature and the chip at sub-kelvin temperatures. A first-order numerical approximation of the geometric throughput combined with careful spectral filtering, including the use of RT-MLI (Radio-Transparent Multi Layer Insulation), to achieve a large opening angle and wide spectral band despite the limited cooling power of a ^4He - ^3He sorption cooler.

In *Chapter 5*, we show the design and characterization of an ultra wide-band, superconducting leaky-lens antenna, based on previous leaky-lens antenna designs at different frequency bands. Beam pattern and optical efficiency measurements at three frequency bands (350 GHz, 650 GHz and 850 GHz) are in good agreement with simulations, with a diffraction limited beam and an aperture efficiency of $\eta_{ap} \approx 0.4$ over the full 1 : 3 bandwidth.

Chapter 6 presents the first on-chip FPR experiment at 350 GHz. Here, we measure losses of CPW transmission lines with varying width made of a 100 nm, high kinetic inductance NbTiN film. We extract the internal quality factor Q_i from the measured loaded

quality factor Q_L using simulations of the coupler properties Q_c . The measurements show a suppression of radiation loss compared to a perfect electric conductor CPW, due to a reduced phase velocity caused by the high kinetic inductance NbTiN. This result is in excellent agreement with simulations, but the suppression is lower than expected from analytic solutions.

In *Chapter 7* we improve on the on-chip FPR design of *Chapter 6* by including multiple FPRs with differing lengths but identical line and coupler properties on a single chip. This makes it possible to extract Q_c and Q_i independently from a single chip measurement by exploiting the mode number dependence of Q_c . A chip with four NbTiN/a-Si/NbTiN microstrip FPRs is measured and the loss tangent of a-Si at 350 GHz is given. Microwave microstrip resonators on the same chip are measured to obtain power dependent losses at 5.5 GHz. The losses at microwave frequencies are in agreement with two-level system theory, but an unexpected increase is found at 350 GHz. We close by providing possible hypotheses for this behaviour.

Chapter 2

Theory

2.1 Superconductivity

2.1.1 General Introduction

Electric Conductors

A single atom is made up of a single central nucleus surrounded by electrons which occupy orbitals with discrete energy states. In a crystalline solid state material, nuclei are arranged in a periodic lattice, surrounded by the more mobile electrons. The available energy states are broadened into quasi-continuous energy bands separated by band gaps without available states, which are determined by the lattice geometry and the ion-electron interactions. Electrons occupy the lowest energy levels available in order to minimize the total energy of the system. As electrons are fermions with spin $1/2$, the Pauli exclusion principle applies and a single energy state can only be occupied by two electrons of opposite spin, requiring higher energy states to be filled. When all electrons are distributed the electrons occupy states up to a certain energy, which is defined as the Fermi energy E_F .

Depending on the configuration of the bands, band gaps and the Fermi energy, three categories of electric conductors can be defined as shown in Fig. 2.1: Metal, Semiconductor and Insulator. In a metal, the Fermi energy lies within a partially filled band and vacant energy states are easily accessible to electrons. This allows the redistribution of electron energies under an applied electric field, leading to a preferred direction in the average electron momentum and thus generating a net current. In semiconductors and insulators, the Fermi energy lies in the energy gap between two gaps. The lower band, called valence band, is therefore fully occupied, and electrons must be excited to the upper band (conduction band) for current to flow. A semiconductor has a relatively small energy gap allowing thermal excitations into the conduction band. An insulator has a large energy gap compared to the thermal energy and therefore does not conduct except in the case of high energy excitation (e.g. photons).

In a normal metal, electron transport can be described with a free electron model where the interactions between electrons are negligible. An intuitive model to understand

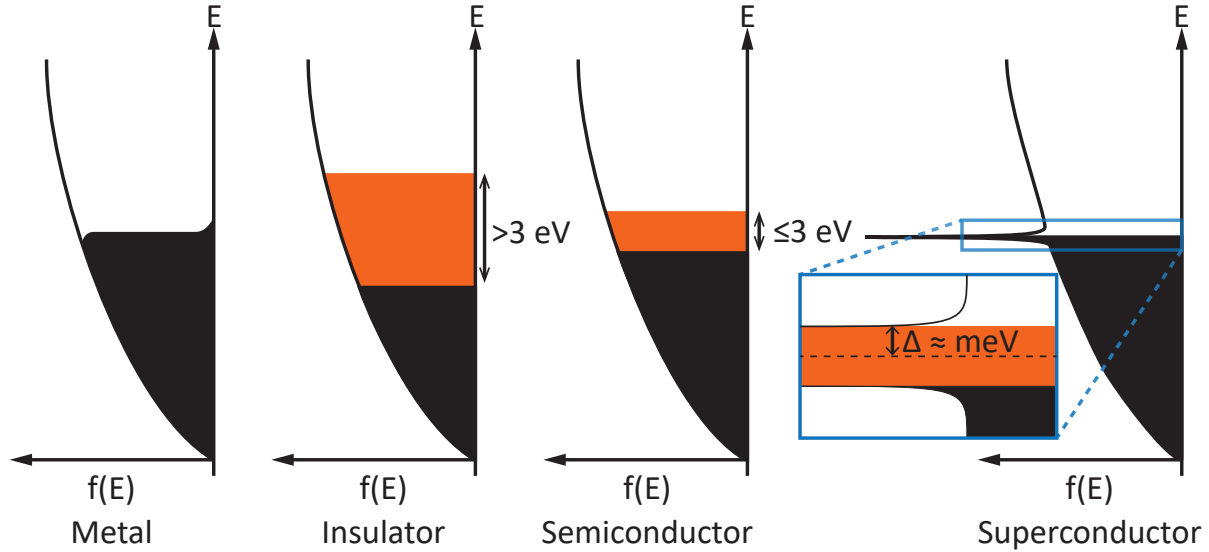


Figure 2.1: The density of electronic states in a metal, insulator, semiconductor and superconductor. Occupied states at low temperature are indicated by the black region with the Fermi energy given by the upper edge of the region. The band gaps of the respective materials are shown in red. In the superconductor, the Fermi energy of the normal conducting state is in the middle of the indicated band gap.

the conduction of metals and semiconductors is the classical Drude model [38]. This model describes the motion of conducting particles in a lattice as competition between the acceleration by the electric field \vec{E} and relaxation by scattering events. For an alternating electric field of frequency ω the complex conductivity of a normal metal is given by:

$$\sigma(\omega) = \sigma_1 - \sigma_2 = \frac{\sigma_0}{1 + (\omega\tau)^2} - i\omega\tau \frac{\sigma_0}{1 + (\omega\tau)^2} \quad (2.1)$$

where τ is the relaxation time or mean time between two scattering events and $\sigma_0 = n_c e^2 \tau / m$ is the conductivity for DC current given by the density of conduction electrons n_c and the electron mass m and charge e . The real and imaginary parts of the conductivity represent the resistive and inductive properties of the metal respectively. The latter is due to the electron inertia and referred to as a kinetic term. As τ for a metal is small even at low temperatures, the kinetic term is generally negligible, though it can be significant for large ω .

Cooper pairs

In a superconductor, electrons near the Fermi energy are in a bound state due to the existence of an attractive force between electrons. Cooper [39] showed that any attractive potential will bind two electrons in a pair, with the strongest effect occurring for pairs of opposite momentum and spin. In a conventional superconductor, the attractive force

emerges due to interaction with lattice vibrations (phonons) and is dependent on the strength of electron-phonon interactions. This can be understood using a simple picture: A negatively charged electron attracts the positively charged ions in the lattice deforming it when moving through it. This deformation in turn attracts a second electron, pairing its behaviour to the first. The importance of the lattice property has been realized due to the dependence of the superconductors critical temperature T_c on the isotope mass of the material [40] [41].

The pairing process is not limited to a single Cooper pair, but all electrons near the Fermi energy will form pairs as long as it is energetically favourable. As Cooper pairs are bosonic particles to which the Pauli exclusion principle does not apply, they condense into a collective ground state. This ground state was postulated by Bardeen, Cooper and Schrieffer (BCS) [42] and can be described by a macroscopic wavefunction

$$\Psi = \|\Delta\| \exp(i\phi) \quad (2.2)$$

given by the energy gap Δ and a single phase ϕ .

Quasiparticles

In a superconductor at $T = 0$ K all charge carriers around the Fermi energy are condensed into Cooper pairs. At finite temperatures, excitations arise in the form of quasiparticles which have a minimum energy $E \geq \Delta$ and are due to the breaking of Cooper pairs via absorption of a phonon or photon. Each broken Cooper pair creates two quasiparticles, which can be both electron-like and hole-like or a mixture of the two, but can be treated as single fermionic particles like in normal metals. As two quasiparticles are created, a minimum phonon or photon energy of

$$\hbar\omega \geq 2\Delta \quad (2.3)$$

is required for the process. Due to collective nature of the groundstate, its binding energy is affected by these excitations. The resulting temperature dependent energy gap is given by

$$\frac{1}{N_0 V_{sc}} = \int_{\Delta(T)}^{k_B T_D} \frac{1 - 2f(E)}{\sqrt{E^2 - \Delta^2(T)}} dE \quad (2.4)$$

where N_0 is the single-spin density of states at the Fermi surface, V_{sc} the potential energy describing electron-phonon exchange, T_D the Debye temperature, T the temperature, E the energy relative to the Fermi level, and k_B the Boltzmann constant. For fermions in thermal equilibrium, $f(E)$ is the Fermi-Dirac distribution given by

$$f(E) = \frac{1}{1 + \exp(E/k_B T)}. \quad (2.5)$$

Eq. 2.4 gives an implicit relation for $\Delta(T)$ and has to be solved iteratively. Only for $T = 0$ and $T \rightarrow T_c$ can an exact expression be derived [43]. For $T = 0$, the energy gap in the BCS

theory is related to the critical temperature as

$$2\Delta_0 = 3.52k_B T_c. \quad (2.6)$$

The density of quasiparticles inside the superconductor is given by

$$n_{qp} = 4N_0 \int_0^\infty N_s(E, T) f(E) dE \quad (2.7)$$

where N_s is the normalized BCS quasiparticle density of states given by

$$N_s(E, T) = \frac{E}{\sqrt{E^2 - \Delta(T)^2}}. \quad (2.8)$$

In thermal equilibrium, $f(E)$ is given by the Fermi-Dirac distribution of Eq. 2.5. If at low temperatures $T \ll T_c$, the density of thermally excited quasiparticles can be approximated as

$$n_{qp} = 2N_0 \sqrt{2\pi k_B T \Delta_0} \exp\left(\frac{-\Delta_0}{k_B T}\right). \quad (2.9)$$

As the superconducting state is energetically favorable, any generated quasiparticles will naturally recombine to a Cooper pair, emitting a phonon in the process. The timescale associated with the recombination is given by the quasiparticle lifetime, which can be approximated for a thermal equilibrium as [44]

$$\tau_{qp} = \frac{\tau_0}{\sqrt{\pi}} \left(\frac{k_B T_c}{2\Delta}\right)^{5/2} \sqrt{\frac{T_c}{T}} \exp(\Delta/k_B T) = \frac{\tau_0}{n_{qp}} \frac{N_0 (k_B T_c)^3}{2\Delta^2} \quad (2.10)$$

where τ_0 is the characteristic electron-phonon interaction time.

2.1.2 Complex Conductivity

Two fluid model

In a superconductor at finite temperatures, both Cooper pairs and quasiparticles contribute as charge carriers. This system can be described using a two fluid model where the real and imaginary components of the complex conductivity

$$\sigma = \sigma_1 - i\sigma_2 \quad (2.11)$$

are determined by the quasiparticles and Cooper pairs respectively. This can be expressed in the Drude model of Eq. 2.1 as

$$\sigma(\omega) = \frac{n_{qp} e^2 \tau}{m} - i \frac{n_s e^2}{\omega m} \quad (2.12)$$

where n_{qp} is the density of quasiparticles and n_s is the density of electrons bound in Cooper pairs. The first term is resistive due to scattering of quasiparticles. The second term is

inductive and due to the inertia of the superconducting Cooper pairs. In contrast to Eq. 2.1, where an inductive term can also be found, the kinetic inductance of the Cooper pairs is generally not negligible. It should be highlighted, that while this term behaves analogous to an inductor, it describes kinetic energy stored in the Cooper pairs and not energy in a generated magnetic field.

Length scales

The behaviour of a superconductor depends on the relation of several length scales: The magnetic penetration depth λ_m , the electron mean free path l , the coherence length ξ_0 and in the case of thin films the film thickness t .

The magnetic penetration depth describes the length scale over which an applied magnetic field decays inside a superconductor and was first derived by London and London [45] as

$$\lambda_L = \sqrt{\frac{m}{\mu_0 n_s e^2}} \quad (2.13)$$

The magnetic field decays due to the generation of a screening current on the superconductor surface which creates an equal and opposite field, resulting in no magnetic field inside the superconductor. This is known as the Meissner Effect.

However, first measurements of λ_m found values larger than predicted by Eq. 2.13 [46]. This is due to the non-local response of the superconductor. In a normal metal, the current at a given location depends on the mean free path $l = v_f \tau$, given by the mean scattering time and the Fermi velocity. The sphere of influence or the size of a single Cooper pair is called coherence length

$$\xi_0 = \hbar v_F / \pi \Delta_0 \quad (2.14)$$

with the Fermi velocity v_F , the reduced Planck constant \hbar and the energy gap Δ_0 at $T = 0$.

In a normal metal, the current at a given location depends on the electric field in a volume around it, where the volume is given by l . The corresponding volume in a superconductor is given by the effective coherence length [47]

$$\frac{1}{\xi} = \frac{1}{\xi_0} + \frac{1}{l} \quad (2.15)$$

where the electron mean free path limits the range of ξ_0 given by Eq. 2.14.

Different limiting cases for the electrodynamic response of the superconductor can be defined based on the relations of these length scales, with the two axes of clean vs dirty and local vs non-local:

- The clean limit, $l \gg \xi_0$, where $\xi = \xi_0$
- The dirty limit, $l \ll \xi_0$, where the mean free path limits the coherence length $\xi = l$
- The non-local limit, $\lambda_m \ll \xi$, where the Cooper pair is larger than the magnetic penetration depth. This can be understood as a spatial variation of the field over

the extent of a Cooper pair leading to a non-local response. In this regime, $\lambda_m = 0.65(\lambda_L \xi_0)^{1/3}$.

- The local limit, $\lambda_m \gg \xi$, where the coherence length is shorter than the penetration depth of the magnetic field. In this regime, $\lambda_m = \lambda_L \sqrt{1 + \xi_0/l}$, which results in $\lambda_m \approx \lambda_L$ in the clean limit
- The extreme anomalous limit is the combination of the clean and non-local limits. $l \gg \xi_0$, $\lambda_m \ll \xi$.

For thin film superconductors, the thickness of the film can also affect its electrodynamic response. For superconductors in a magnetic field with $t < l$, the thickness is the limiting scattering lengthscale. When the applied magnetic field is perpendicular to the film, the magnetic penetration depth is given by the Pearl length, $\lambda_\perp \approx \lambda_m^2/t$, due to the interaction of magnetic vortices created by the field [48]. In this thesis, the focus lies on NbTiN transmission lines and aluminum based Microwave Kinetic Inductance Detectors (MKIDs). NbTiN has typical values of $\lambda_m = 260$ nm, $\xi_0 = 170$ nm and $l \ll \xi_0$ (using $v_F = 1.9 \times 10^6$ m/s and $\tau = 3.0 \times 10^{-16}$ s) [49], placing it firmly in the local ($\lambda_m \gg \xi$) and dirty ($l \ll \xi_0$) limit. For bulk aluminum, typical values are $\lambda_m = 16$ nm, $\xi_0 = 1.6 \times 10^3$ nm and $l = 525$ nm (using $v_F = 2.03 \times 10^6$ m/s and $\tau = 2.6 \times 10^{-13}$ s), placing it in the non-local $\lambda_m \ll \xi$ and dirty ($l \ll \xi_0$) limit. However, for the thin films used in this thesis ($t \approx 50$ nm), the mean free path is reduced to around $l \approx 16$ nm, therefore placing the film in the local and dirty limit.

A convenient approximation for the penetration depth in the dirty and local limit is given by [50] [51]

$$\lambda_m = \sqrt{\frac{\hbar \rho_n}{\pi \Delta \mu_0}} \approx 105 \text{ [nm]} \times \sqrt{\frac{\rho [\mu\Omega \text{ cm}]}{T_c [\text{K}]}} \quad (2.16)$$

where ρ_n is the normal state resistivity near the superconductor transition.

Mattis-Bardeen Theory

A solution for the complex conductivity, based on the BCS theory and valid in both the dirty and the extreme anomalous limits, was derived by Mattis and Bardeen [52]. The resulting real and imaginary parts of the conductivity are given by

$$\begin{aligned} \frac{\sigma_1}{\sigma_N} &= \frac{2}{\hbar\omega} \int_{\Delta}^{\infty} |f(E) - f(E + \hbar\omega)| g_1(E) dE \\ &+ \frac{1}{\hbar\omega} \int_{\min(\Delta - \hbar\omega, -\Delta)}^{-\Delta} |1 - 2f(E + \hbar\omega)| g_1(E) dE \end{aligned} \quad (2.17)$$

$$\frac{\sigma_2}{\sigma_N} = \frac{1}{\hbar\omega} \int_{\max(\Delta - \hbar\omega, -\Delta)}^{\Delta} |1 - 2f(E + \hbar\omega)| g_2(E) dE \quad (2.18)$$

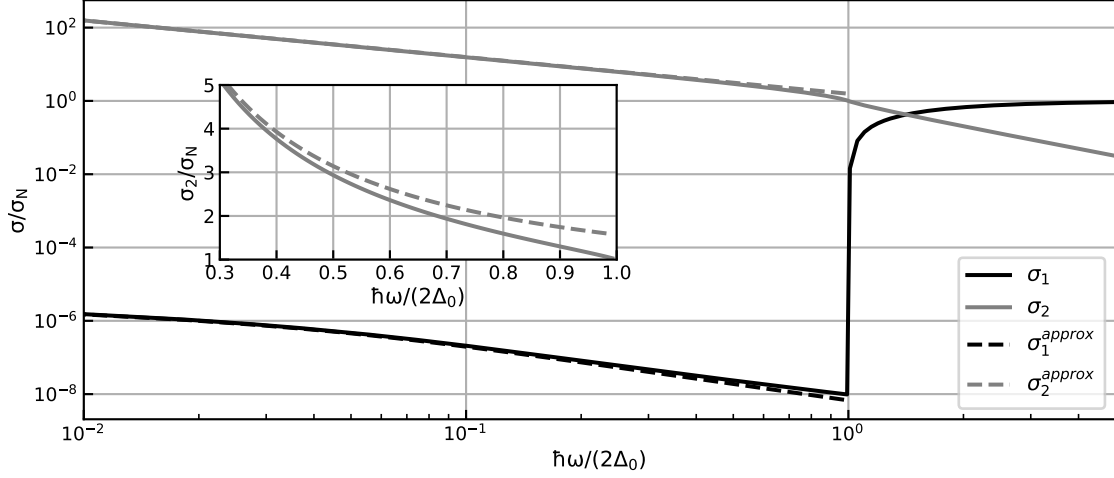


Figure 2.2: Frequency dependence of σ_1 and σ_2 calculated at $T = T_c/10$ and using $\Delta = \Delta_0$. The solid lines are the full Mattis-Bardeen equations 2.17 and 2.18. The dashed lines show the approximation given by Eqs. 2.21–2.22. The inset highlights the deviation between the full solution and approximation for σ_2 .

where $\omega = 2\pi f$, $\sigma_N = 1/\rho_N$ is the normal state conductivity, $\Delta \approx 1.76k_B T_c$ is the superconductors gap energy, $f(E)$ is the density of states generally given by the Fermi-Dirac distribution, and $g_1(E)$ and $g_2(E)$ are defined as

$$g_1(E) = \frac{E^2 + \Delta^2 + \hbar\omega E}{(E^2 - \Delta^2)^{1/2} [(E + \hbar\omega)^2 - \Delta^2]^{1/2}} \quad (2.19)$$

$$g_2(E) = \frac{E^2 + \Delta^2 + \hbar\omega E}{(\Delta^2 - E^2)^{1/2} [(E + \hbar\omega)^2 - \Delta^2]^{1/2}}. \quad (2.20)$$

The first integral in Eq. 2.17 describes the resistance due to the thermal quasiparticle population, while the second integral is due to power absorption via the breaking of Cooper pairs and therefore only relevant when $\hbar\omega \geq 2\Delta$. σ_1 therefore shows a sharp absorption edge at the gap frequency as seen in Fig. 2.2. The temperature dependence of σ_1 and σ_2 is shown in Fig. 2.3. The integral boundaries assume a hard gap with no available states at $|E| < \Delta$, which will lead to deviations in the limits of $T \rightarrow T_c$ and $\hbar\omega \rightarrow 2\Delta$ in the presence of sub-gap states or a broadened density of states.

For a thermal quasiparticle distribution and $kT, \hbar\omega < 2\Delta$, Eqns. 2.17 and 2.18 can be simplified to [53]

$$\frac{\sigma_1}{\sigma_N} = \frac{4\Delta}{\hbar\omega} \exp(-\Delta/k_B T) \sinh\left(\frac{\hbar\omega}{2k_B T}\right) K_0\left(\frac{\hbar\omega}{2k_B T}\right), \quad (2.21)$$

$$\frac{\sigma_2}{\sigma_N} = \frac{\pi\Delta}{\hbar\omega} \left[1 - 2 \exp(-\Delta/k_B T) \exp\left(\frac{-\hbar\omega}{2k_B T}\right) I_0\left(\frac{\hbar\omega}{2k_B T}\right) \right], \quad (2.22)$$

where I_0 and K_0 are the modified Bessel functions of the first and second kind respectively.

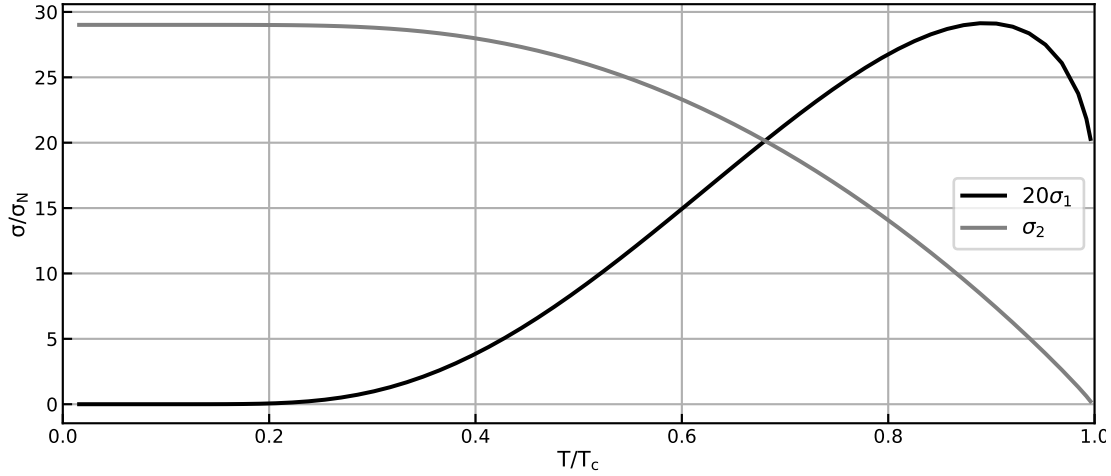


Figure 2.3: Temperature dependence of σ_1 and σ_2 calculated at $\hbar\omega = \Delta/20$.

Surface Impedance

From the complex conductivity, the surface impedance then follows from [54] as

$$Z_s = \sqrt{\frac{i\mu_0\omega}{\sigma_1 - i\sigma_2}} \coth\left(t\sqrt{i\omega\mu_0(\sigma_1 - i\sigma_2)}\right) = R_s + i\omega L_s \quad (2.23)$$

given in $[Z_s] = \Omega/\square$ with the surface resistance R_s and the surface inductance

$$L_s = \frac{\text{Im}(Z_s)}{\omega}. \quad (2.24)$$

This surface inductance is due to the acceleration of Cooper pairs in an AC field while the surface resistance is dependent on the number of unpaired electrons (quasiparticles) in the superconductor. The term $\coth(t\sqrt{i\omega\mu_0(\sigma_1 - i\sigma_2)})$ is only relevant for thin films ($t \lesssim \lambda_m$) and is equal to unity otherwise.

Low frequency limit

For thick films, low frequencies and low temperatures ($\sigma_1 \ll \sigma_2$) simplified expressions can be retrieved for the surface resistance and inductance as $R_s = \sqrt{\frac{\mu_0\omega}{\sigma_2}}$ and $L_s = \sqrt{\frac{\mu_0}{\omega\sigma_2}} = \mu_0\lambda_m$. The latter relation follows from the London equations (Eqns. 2.12,2.13) assuming $\sigma \approx -i\sigma_2$. Additionally, it is useful in this regime to use the simplified expressions for σ_1 and σ_2 of Eqns. 2.21 and 2.22.

These approximations start to break down at frequencies $\nu > 2\Delta/3$, as shown in Fig. 2.4, where the full solution for L_s shows a significant increase, while a constant value is found in the approximations.

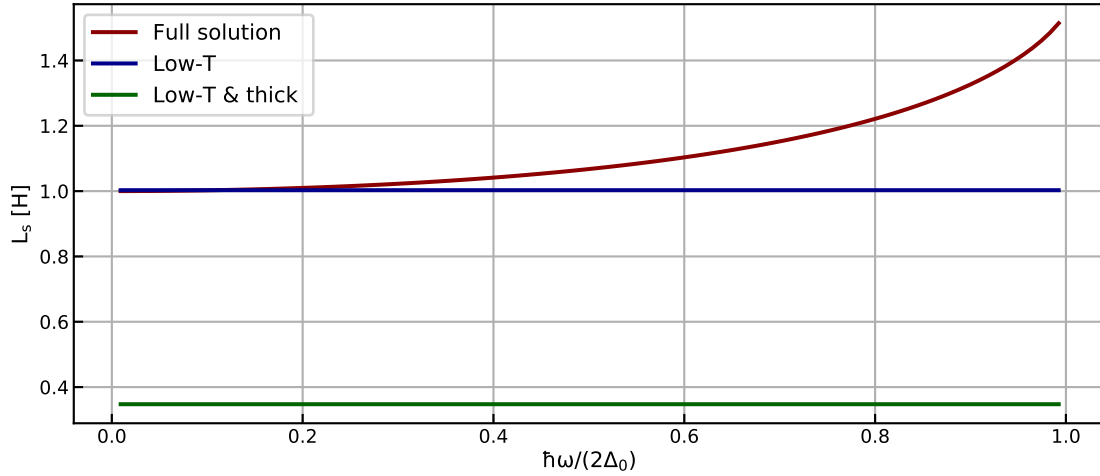


Figure 2.4: Frequency dependent surface inductance for a thin film of NbTiN using $T_c = 14.7\text{ K}$, $\rho_N = 102\text{ }\mu\Omega\text{ cm}$, $t = 100\text{ nm}$ and $T = T_c/10$. The *red* line shows the full solution using Eqs. 2.17 and 2.18 in Eq.2.23, the *blue* line is an approximation using the simplified expressions for σ_1 and σ_2 (Eqs. 2.21 and 2.22 in Eq.2.23) and the *green* line uses the thick film approximation $L_s = \mu_0\lambda_m$ combined with Eq. 2.16.

2.2 Superconducting Transmission Lines

2.2.1 Transmission Line Basics

Concept

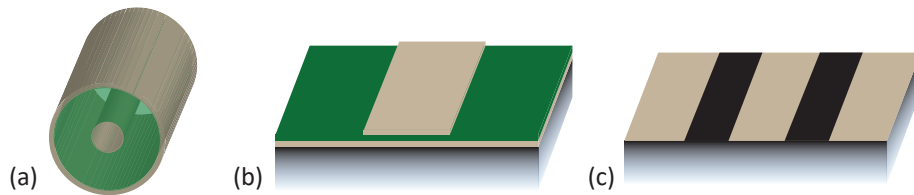


Figure 2.5: a) A co-axial cable. b) A Microstrip transmission line. c) A co-planar waveguide.

A transmission line is a structure consisting of at least two metal lines, separated by an insulating dielectric material, which allows the controlled propagation of a traveling EM (electromagnetic)-wave along it. Fig. 2.2.1 shows three commonly used geometries: Co-axial line, microstrip and co-planar waveguide (CPW). The co-axial line consists of an inner conductor surrounded by a concentric cylindrical outer conductor. It is most commonly used for connecting cables in microwave applications. The microstrip and CPW are planar transmission lines made of one or more layers, which makes them ideal for lithographic processing.

Lumped Element Circuit Model

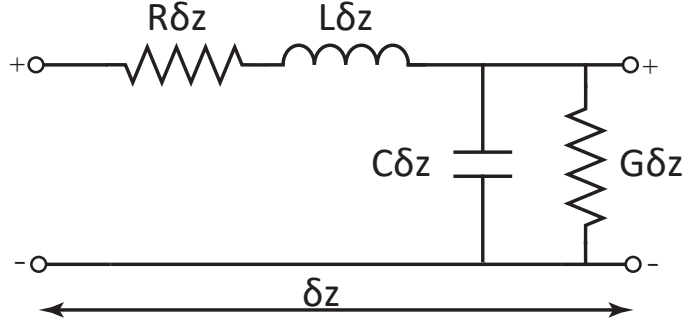


Figure 2.6: Transmission line circuit model. Figure after [55].

In circuit theory, individual elements are small compared to the electric wavelength λ . A circuit can therefore be described by discrete lumped elements, where the current and voltage does not change significantly over the physical extent of one element. A Transmission line however is generally comparable in length to λ or even many wavelengths long. Consequently, the current and voltage on the line change significantly along its length and it is therefore a distributed-parameter network.

In the lumped-element circuit model, the transmission line is split into infinitesimally short sections across which current and voltage do not change significantly. Each section of length δz can therefore be modeled by a lumped-element circuit as shown in Figure 2.6, where the two wires represent the conductor and ground of the transmission line, while R , L_g , C and G are given per unit-length and defined as [55]:

- R = series resistance per unit length, in Ω/m , due to the finite conductance in both conductors.
- L = series inductance per unit length, in H/m , due to the geometric inductance of the conductors.
- G = shunt conductance per unit length, in S/m , due to leakage current through the separating dielectric. For all applications relevant to this thesis, the shunt conductance is negligible due to the use of high resistivity dielectrics where $G = 0$.
- C = shunt capacitance per unit length, in F/m , due to the proximity of the two conductors.

Characteristic impedance and Propagation Constant

The propagation of a wave along the transmission line can be described by two parameters, the propagation constant and the characteristic impedance. Both can be found by applying Kirchhoff's law to the circuit model in Figure 2.6 and solving the resulting wave equations

for voltage and current. The characteristic impedance is the ratio of voltage and current of the propagating wave and given by

$$Z_0 = \sqrt{\frac{R + i\omega L}{G + i\omega C}} \quad (2.25)$$

which is generally a complex value. The propagation constant describes the evolution of the waves complex amplitude

$$A(z) = A(0)e^{\gamma z} \quad (2.26)$$

and is given by

$$\gamma = \alpha + i\beta = \sqrt{(R + i\omega L_g)(G + i\omega C)} \quad (2.27)$$

with the loss in magnitude and phase velocity determined by the attenuation constant α and the phase constant β respectively.

Attenuation Constant, Loss Tangent and Quality Factor

Ohmic losses for a superconducting transmission line at $T \ll T_c$ and $\hbar\omega < \Delta$ are in theory, and also in most practical cases, vanishingly small. However, depending on its geometry, other loss sources need to be considered, primarily radiation loss and dielectric loss. In order to quantify these losses three different parameters, attenuation constant, loss tangent and internal quality factor, are being used commonly depending on the loss source and the application. It is therefore convenient to be aware of the various definitions and relationships.

- The attenuation constant α is defined via the propagation constant in Eq. 2.27. It is the direct measure of the loss in amplitude of an EM wave traveling along a lossy transmission line. When using the exponential Eq. 2.26 it has units of [Np/m], but a decibel scale is also commonly used with units of [dB/m]. Conversion between Np and dB is given by a simple factor: $\alpha[\text{dB/m}] \approx 8.686 \times \alpha[\text{Np/m}]$.
- The internal quality factor is defined as the energy stored in the EM-wave to the energy lost per cycle

$$Q_i = \frac{\omega E_{\text{stored}}}{P_{\text{loss}}}, \quad (2.28)$$

where P_{loss} is the power lost by internal dissipation. For a transmission line, this relation is given by

$$Q_i = \frac{\beta}{2\alpha}. \quad (2.29)$$

As it is also a fundamental property of resonators and comparatively easy to measure, it is commonly used in this context. This is expanded on in section 2.3.

- The loss tangent $\tan \delta$ is defined for the interaction of an electric field with a dielectric material and as such only applicable directly to dielectric loss. It is a unitless parameter and inversely proportional to the internal quality factor

$$\tan \delta = \frac{1}{Q_i}. \quad (2.30)$$

Effective Dielectric Constant

An EM-wave propagating in free space has a phase velocity of $v_{ph} = 1/\sqrt{\mu_0\epsilon_0}$, which is the speed of light with $\mu_0 = 4\pi \times 10^{-7} \text{H/m}$ and $\epsilon_0 = 8.854 \times 10^{-12} \text{F/m}$ the vacuum permeability and vacuum permittivity respectively. When the wave propagates through a dielectric material its electric field interacts with the said material, leading to a retardation of the wave. The resulting phase velocity can be expressed as

$$v_{ph} = \frac{1}{\sqrt{\mu_0\epsilon_0\epsilon_r}} = \frac{c}{\sqrt{\epsilon_r}} \quad (2.31)$$

with the dielectric constant or relative permittivity ϵ_r . In many transmission line geometries, only a fraction of the field is contained in the dielectric material, while the remainder is in free space. This effect can be expressed using an effective dielectric constant ϵ_{eff} , which is determined by the field distribution of the wave resulting in

$$\epsilon_{eff} = c^2 LC \quad (2.32)$$

and has a value $1 \leq \epsilon_{eff} \leq \epsilon_r$. Consequently, the phase velocity of a transmission line is given as

$$v_{ph} = \frac{c}{\sqrt{\epsilon_{eff}}}. \quad (2.33)$$

2.2.2 Superconducting Lines

In a superconducting transmission line, the metallic conductors are replaced by superconductors with a sheet resistance R_s and sheet inductance L_s which can be calculated using Mattis-Bardeen theory (Eq. 2.23). R_s and L_s are material parameters and therefore valid for any transmission line geometry. However, the total resistance R and kinetic inductance L_k seen by the propagating EM-wave are a function of the transmission line geometry. Solutions for the resulting impedance and propagation constant of microstrips and CPWs are given in sections 2.2.3 and 2.2.4 respectively.

While ohmic losses are small, they should still be considered in the case of very low loss transmission lines. The quality factor of the line can be calculated using Eq. 2.28 to be [56]

$$Q_i = \frac{\omega L}{R} = \frac{1}{\alpha_k} \frac{\omega L_s}{R_s} \quad (2.34)$$

where

$$\alpha_k = \frac{L_k}{(L_k + L_g)} \quad (2.35)$$

is the kinetic inductance fraction of the line.

It is often also convenient to include the effect of the kinetic inductance on the phase velocity in the effective dielectric constant using

$$\epsilon_{eff}^{sc} = c^2(L_g + L_k)C. \quad (2.36)$$

This relation allows $\epsilon_{eff} > \epsilon_r$, which shows clearly that it should be considered a naive approach to describe transmission line behaviour and does not represent an effect due to the dielectric material. While it is commonly used in engineering, it can lead to quantitatively wrong results if used improperly.

Dispersion near the superconducting gap frequency

For most cases, ϵ_{eff} can be assumed constant with frequency, in turn leading to a constant phase velocity and a dispersionless transmission line. However, for a superconductor at frequencies $\hbar\omega > 2\Delta/3$, the kinetic inductance has a significant frequency dependence, as shown in Fig. 2.4. Consequently, ϵ_{eff}^{sc} is highly dispersive at frequencies approaching the superconducting gap, as shown in Fig. 2.7.

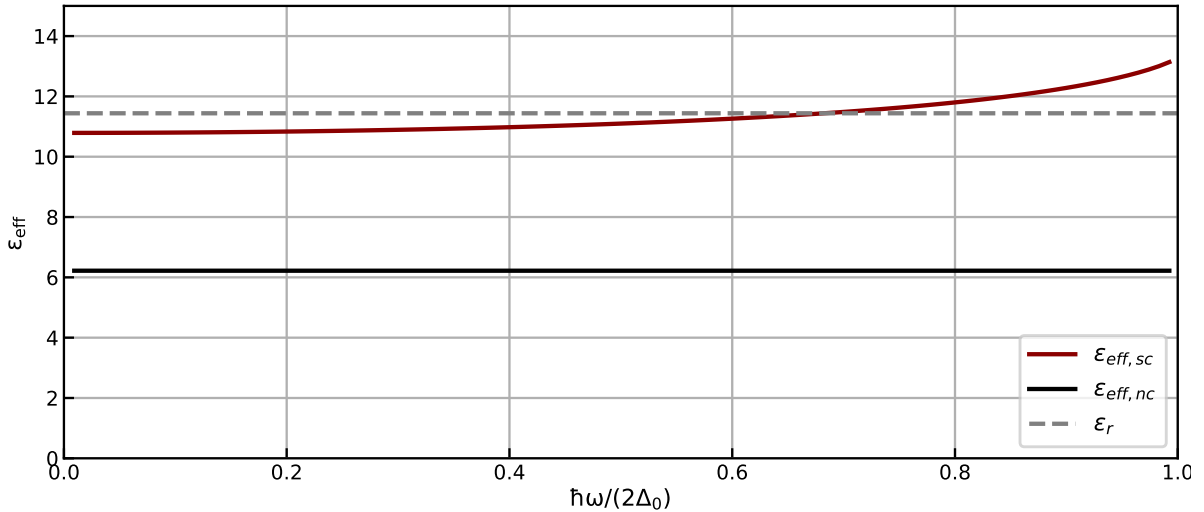


Figure 2.7: Effective dielectric constant of a CPW as function of frequency in the case of a superconducting CPW (*red* line) and a normal conductor (*black*). The dielectric constant of the substrate is shown as a dashed line. The CPW has a line and gap width of $w = s = 3.5 \mu\text{m}$, while the superconductor is the same as that used for Fig. 2.4.

2.2.3 Microstrips

Geometry

A microstrip is a multi-layer structure as shown in Fig. 2.8a), consisting of a conducting line of thickness t and width w separated from the ground plane by dielectric layer of height

h . The whole structure is usually on top of a thick substrate, but as it is fully covered by the ground plane it does not affect the electromagnetic properties of the transmission line. The field distribution of the propagating mode is shown in Fig. 2.8a).

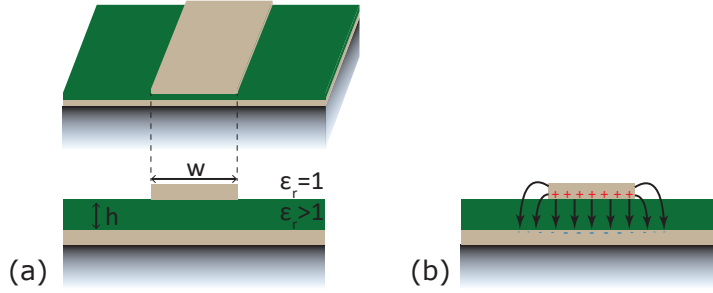


Figure 2.8: (a) Microstrip geometry (b) Electric field and current distribution in a microstrip.

Characteristic impedance and propagation constant

The propagating waves' field is primarily confined in the dielectric medium below the conducting line, however fringing fields due to the finite width of the line can generally not be neglected. The effective dielectric constant due to the field distribution is given by [55]

$$\epsilon_{eff} = \frac{\epsilon_r + 1}{2} + \frac{\epsilon_r - 1}{2} \frac{1}{\sqrt{1 + 12h/w}}. \quad (2.37)$$

The propagation constant is then given by

$$\beta_m = \frac{2\pi\sqrt{\epsilon_{eff}}}{\lambda_0} \quad (2.38)$$

where λ_0 is the wavelength in free space. The characteristic impedance of the line is given by

$$Z_m = \begin{cases} \frac{60}{\sqrt{\epsilon_{eff}}} \ln \left(\frac{8h}{w} + \frac{w}{4h} \right) & \text{for } w/h \leq 1 \\ \frac{1}{\sqrt{\epsilon_{eff}}} \frac{120\pi}{w/h + 1.393 + 0.667 \ln(w/h + 1.444)} & \text{for } w/h \geq 1. \end{cases} \quad (2.39)$$

However, this is insufficient to describe superconducting microstrips, as Eqns. 2.38 and 2.39 do not consider the kinetic inductance. The best model currently available to describe the superconducting case was derived by Yassin and Withington [57] as

$$\left(\frac{\beta}{Z_0} \right) = \left(\frac{\beta_m}{Z_m} \right) \left(1 + 2\chi \frac{\lambda}{h} \right)^{1/2} \quad (2.40)$$

where β_m and Z_m are the model values given by Eqns. 2.38 and 2.39 respectively and λ is the magnetic penetration depth of the superconductor and χ is the penetration factor.

An analytic expression for χ based on conformal mapping techniques is given by [57] as

$$\chi = \begin{cases} \frac{Is1+Is2+Ig1+Ig2+\pi}{2\ln(rb/(ra))} & \text{for } w/h < 2 \\ \frac{Is1+Is2+Ig1+Ig2+\pi}{2\ln(2rb/(ra))} & \text{otherwise} \end{cases} \quad (2.41)$$

which includes contributions from the bottom surface of the conducting line

$$Is1 = \ln \left(\frac{2p - (p+1)ra + 2\sqrt{pRa}}{ra(p-1)} \right) \quad (2.42)$$

$$Ra = (1-ra)(p-ra) \quad (2.43)$$

the top surface of the line

$$Is2 = \ln \left(\frac{(p+1)rb - p - 2\sqrt{pRb}}{rb(p-1)} \right) \quad (2.44)$$

$$Rb = (rb-1)(rb-p) \quad (2.45)$$

and the ground plane

$$Ig1 = \ln \left(\frac{(p+1)rb + 2p + 2\sqrt{pRb'}}{rb(p-1)} \right) \quad (2.46)$$

$$Rb' = (rb+1)(rb+p) \quad (2.47)$$

$$Ig2 = \ln \left(\frac{(p+1)ra + 2p + 2\sqrt{pRa'}}{ra(p-1)} \right) \quad (2.48)$$

$$Ra' = (ra+1)(ra+p). \quad (2.49)$$

ra is given by

$$\ln(ra) = -1 - \frac{\pi w}{2h} - \frac{p+1}{\sqrt{p}} \tanh^{-1}(p^{-1/2}) - \ln \left(\frac{p-1}{4p} \right) \quad (2.50)$$

and rb is given as

$$rb = \begin{cases} rbo & \text{for } w/h \geq 5 \\ rbo - \sqrt{(rbo-1)(rbo-p)} + (p+1) \tanh^{-1} \left(\sqrt{\frac{rbo-p}{rbo-1}} \right) & \\ -2\sqrt{p} \tanh^{-1} \left(\sqrt{\frac{rbo-p}{p(rbo-1)}} \right) + \frac{\pi w}{2h} \sqrt{p} & \text{otherwise} \end{cases} \quad (2.51)$$

where rbo is given as

$$rbo = \eta + \frac{p+1}{2} \ln v \quad (2.52)$$

with

$$\eta = \sqrt{p} \left(\frac{\pi w}{2h} + \frac{p+1}{2\sqrt{p}} \left(1 + \ln \left(\frac{4}{p-1} \right) \right) \right) - 2 \tanh^{-1} p^{-1/2} \quad (2.53)$$

$$v = \max(\eta, p) \quad (2.54)$$

$$p = 2b^2 - 1 + 2b\sqrt{b^2 - 1} \quad (2.55)$$

$$b = 1 + t/h \quad (2.56)$$

Two-level system loss

Superconducting microstrips exhibit strong losses due to the presence of the dielectric layer between conductor and ground plane. This dielectric loss, $Q_{i,die}$, is generally attributed to a population of two-level tunneling systems (TLSs) in the amorphous dielectric medium which is interacting with the electric field of the propagating wave and [58, 59]. The

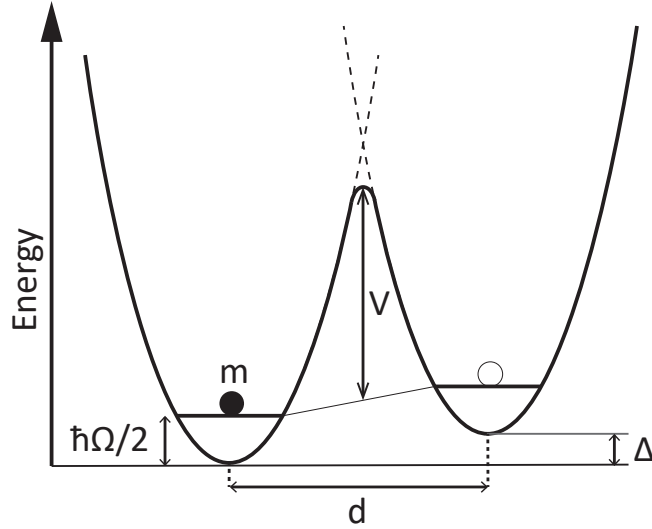


Figure 2.9: Schematic of a particle of mass m in the double well potential of a two-level system with the asymmetry energy Δ , the well distance d , the ground state energy $\hbar\Omega/2$ of the particle in an isolated well and the potential barrier V . Figure after [60].

existence of TLSs is attributed to the disordered structure of amorphous materials which allows an atom or group of atoms to switch between two local minima of the potential energy landscape. At low temperatures switching between the two minima can only occur via quantum tunneling through a barrier. While the exact microscopic origin of TLSs is not certain [61], their macroscopic effects can be well described with the standard tunneling model (STM), where a single TLS is given by a particle of mass m in a double-well potential characterized by an asymmetry Δ_{TLS} and a potential barrier V as shown in Fig. 2.9a). The

energy difference between the two available energy levels in the TLS can then be derived as [60]

$$E_{TLS} = \sqrt{\Delta_{TLS}^2 + \Delta_0^2}. \quad (2.57)$$

where Δ_0 is the tunnel splitting given by

$$\Delta_0 \approx \hbar \Omega e^{-\kappa} \quad (2.58)$$

with the tunneling parameter κ . For the potential geometry given in Fig. 2.9, κ is given by [60]

$$\kappa \approx \frac{d}{2\hbar} \sqrt{2mV} \quad (2.59)$$

where d is the well distance. The dielectric material contains a population of TLSs with a density of states $N(E)$. In the STM, both Δ_{TLS} and Δ_0 are assumed to be randomly distributed, due to the random nature of the amorphous material, whereby the density of states is energy independent and given as a sample specific constant N .

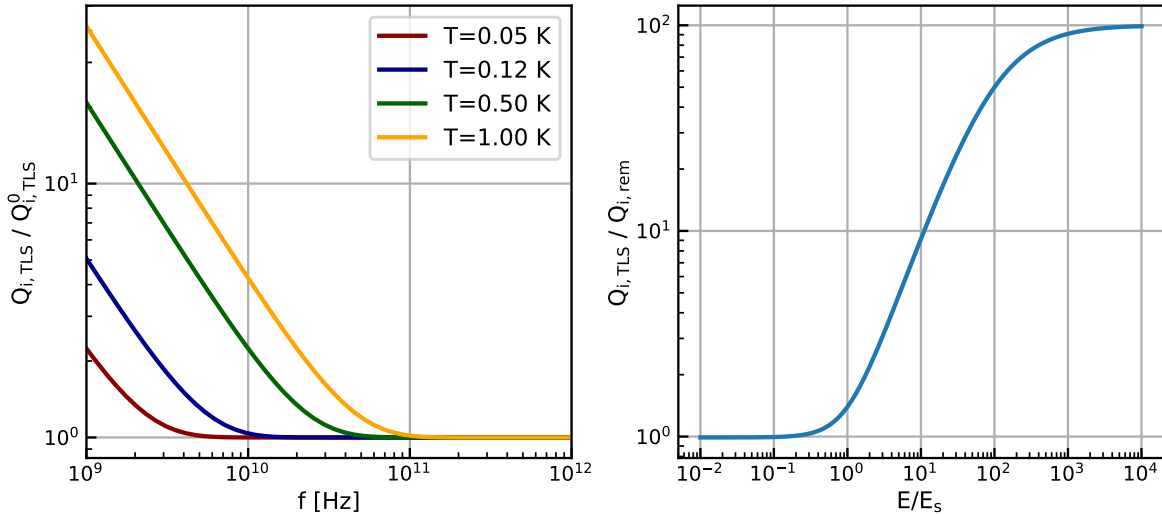


Figure 2.10: a) Frequency dependence of the dielectric loss $Q_{i,dielectric}$ in the weak field limit at different temperatures. b) Electric field dependence of Q_i as function of E_s , given by Eq. 2.62 for $Q_{i,dielectric}/Q_{i,rem} = 0.1$.

TLSs carry a dipole moment p , which allows coupling to an EM-wave propagating along the microstrip. Interaction with the electric field alters the real and imaginary parts of the dielectric constant, leading to dissipation and changes in the phase velocity. For weak fields, the dissipation is given by the loss tangent as

$$\delta_{TLS} = \frac{1}{Q_{i,dielectric}} = F \delta_{TLS}^0 \tanh\left(\frac{\hbar\omega}{2k_B T}\right) \quad (2.60)$$

where $\tan \delta_{TLS}^0 = \pi N p^2 / 3 \epsilon_r$ is the loss tangent at low temperatures ($T \ll \hbar \omega / 2 k_B$) and in a weak electric field. The filling factor

$$F = W_r^e / W^e \quad (2.61)$$

represents the fraction of electric energy inside the TLS hosting dielectric W_r^e over the total electric energy stored in the EM-wave. Figure 2.10a) shows the frequency dependence of Eq. 2.60 at various temperatures. Dielectric loss due to TLSs at $f > 100$ GHz is independent of temperature for $T \leq 1$ K. At $T = 120$ mK, where devices relevant for this thesis are usually operated, $\tan \delta_{TLS}$ only changes by a factor of 5 from $f > 100$ GHz to microwaves. This relatively constant behaviour with frequency is due to the assumption of an energy independent density of states $N(E) = N$.

For strong electric fields, the number of excited TLSs starts to become saturated, leading to a reduction in dielectric loss. The total loss in the transmission line can then be expressed by its quality factor as [60] [62] [63]

$$\frac{1}{Q_i} = \frac{1}{Q_{i,diel}} \sqrt{1 + (E/E_s)^2} + \frac{1}{Q_{i,rem}} \quad (2.62)$$

where $Q_{i,diel}$ is the quality factor in the weak field limit given by Eq. 2.60, E_s is a saturation field strength and $Q_{i,rem}$ contains all other loss sources of the transmission line. For weak fields, the loss is dominated by TLSs, while stronger fields reduce the contribution of $Q_{i,diel}$ until it is negligible compared to $Q_{i,rem}$ (see Fig. 2.10b)).

2.2.4 Co-Planar Waveguides

Geometry

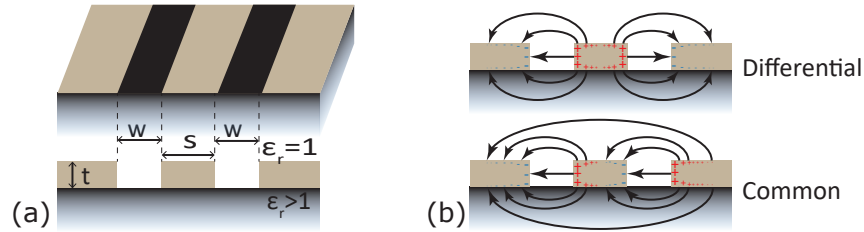


Figure 2.11: (a) CPW geometry. (b) Differential mode (also CPW mode) and common mode. Shown are electric field lines and charge distribution due to current flow.

A co-planar waveguide (CPW), as shown in Fig. 2.11a), is a planar transmission line with a central conductor of width s separated from two ground planes by a gap of width w . The structure is deposited on a thick substrate with a dielectric constant $\epsilon_r > 1$. While the CPW can be covered by another dielectric, it is usually directly exposed to free space with $\epsilon_r = 1$. Unlike the microstrip, a CPW can support two fundamental modes as shown

in Fig. 2.11b): The differential mode and the common mode. In the differential mode the two ground planes are on the same potential and considered balanced. This is the intended mode of propagation and also usually referred to as the CPW-mode. Any imbalance of the two ground plane potentials, e.g. due to a bend in the line, is represented by an excitation of the common mode. This mode represents a leaky mode excitation across both slots of the CPW, and as such is strongly radiating [64]. Great care in circuit design is therefore required to avoid common mode excitations where possible. In this thesis, only the propagation of the differential mode is considered unless explicitly stated otherwise.

Characteristic impedance and Propagation Constant

The line capacitance and geometric inductance of a CPW are given by its geometry as

$$L_g = \frac{\mu_0 K(k')}{4K(k)} \quad (2.63)$$

$$C = 4\epsilon_0 \epsilon_{eff,geo} \frac{K(k)}{K(k')} \quad (2.64)$$

where $k = s/(s + 2w)$, $k'^2 = 1 - k^2$, K is the complete elliptic integral of the first kind and

$$\epsilon_{eff,geo} \approx (1 + \epsilon_r)/2 \quad (2.65)$$

is the effective dielectric constant visible to the line capacitance due to the substrate below the CPW line.

The kinetic inductance L_k of the CPW can be calculated analytically as

$$L_k = g_c L_{s,c} + g_g L_{s,g} \quad (2.66)$$

where $L_{s,c}$ and $L_{s,g}$ are the surface inductances of the central line and groundplane as given by eqs.2.23 and 2.24, and g_c and g_g are their respective geometry factors [65]

$$g_c = \frac{1}{4s(1 - k^2)K^2(k)} \left[\pi + \ln \left(\frac{4\pi s}{t} \right) - k \ln \left(\frac{1 + k}{1 - k} \right) \right] \quad (2.67)$$

$$g_g = \frac{1}{4s(1 - k^2)K^2(k)} \left[\pi + \ln \left(\frac{4\pi(s + 2w)}{t} \right) - \frac{1}{k} \ln \left(\frac{1 + k}{1 - k} \right) \right]. \quad (2.68)$$

The geometry factors were originally described in *Foundations for Microwave Engineering* by R.E.Collin [66] for the losses in the central line and groundplane of a CPW, and have been intuitively adapted to apply for the kinetic inductance contribution. This adaptation has been verified by comparison with simulations, e.g. Sonnet, and has been found to be in excellent agreement with experimental results over the last years.

In the case of a single film CPW with surface inductance $L_s = L_{s,c} = L_{s,g}$, Eq. 2.36 can then be rewritten as

$$\epsilon_{eff} = c^2(L_g + gL_s)C \quad (2.69)$$

with $g = g_c + g_g$.

The characteristic impedance and propagation constant are obtained analogous to ϵ_{eff} using Eqns. 2.25 and 2.27 as

$$Z_0 = \sqrt{(L_g + gL_s)/C} \quad (2.70)$$

$$\beta = \sqrt{(L_g + gL_s)C} \quad (2.71)$$

Radiation Loss

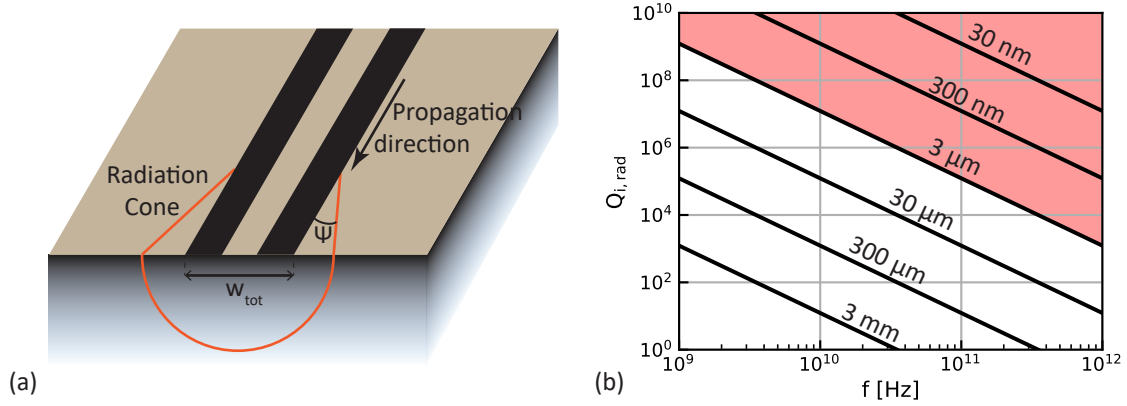


Figure 2.12: a) Radiation cone of the propagating CPW mode with radiation angle Ψ and CPW width $w_{tot} = s + 2w$. b) Radiation loss α_{rad} of a perfect electric conductor according to Eq. 2.72 as function of frequency for various CPW widths w_{tot} . The red shaded area indicates line dimensions which are difficult to realize in fabrication.

For a perfect electric conductor (PEC), the effective dielectric constant is given by Eq. 2.65, which is smaller than ϵ_r of the substrate. Consequently, the phase velocity $v_{ph} = c/\sqrt{\epsilon_{eff}}$ of the guided CPW mode is faster than that in the substrate. This creates a shockwave in the substrate, leading to a radiation cone characterized by the radiation angle Ψ as shown in Fig. 2.12a). The frequency dependent loss factor α at high frequencies due to this shockwave has been derived by Frankel et al. [67] from the electric and magnetic field distributions in the dielectric materials due to the current distribution in a PEC as

$$\alpha_{rad} = \left(\frac{\pi}{2}\right)^5 2 \left(\frac{(1 - \cos^2(\Psi))^2}{\cos(\Psi)} \right) \frac{(s + 2w)^2 \epsilon_r^{3/2}}{c^3 K(\sqrt{1 - k^2}) K(k)} f^3 \quad (2.72)$$

where K is the complete elliptical integral of the first kind and $k = s/(s + 2w)$. The frequency dependence of $Q_{i,rad} = \beta/2\alpha_{rad}$ is shown in Fig. 2.12b) for different CPW widths $w_{tot} = s + 2w$. At microwave frequencies, small w_{tot} can be used to reduce radiation loss to negligible levels. However, the strong increase at higher frequencies due to $\alpha_{rad} \propto f^3$ can usually not be compensated this way, as the required dimensions $w = s < 1 \mu m$ are difficult to fabricate.

It can be seen in Eq. 2.72, that the magnitude of radiation loss is strongly dependent on Ψ which is given by the discrepancy of the dielectric constants

$$\cos(\Psi) = \frac{\sqrt{\epsilon_{eff}}}{\sqrt{\epsilon_r}}. \quad (2.73)$$

For a PEC CPW, this ratio is only dependent on the substrate and independent of the conductor properties. However, for a superconducting CPW, the kinetic inductance modifies the lines phase velocity, which can be expressed as a change in ϵ_{eff} using Eq. 2.36. Conceptually, using a CPW with high L_k therefore leads to a suppression of the radiation loss, as the radiative angle Ψ is reduced. If L_k is sufficiently large to obtain $\epsilon_{eff} \geq \epsilon_r$, the radiative shockwave does not form as the phase velocity of the CPW line is slower than in the substrate, resulting in theoretically zero radiation loss.

It should be noted, that Eq. 2.72 is derived from the field distribution of the propagating CPW mode in the dielectric medium of a PEC CPW. As the reduction in v_{ph} due to the kinetic inductance of a superconductor is not based on the field interaction with the dielectric medium, substituting ϵ_{eff}^{sc} of Eq. 2.36 in Eq. 2.72 can lead to quantitatively wrong results in the regime of $\epsilon_{eff} < \epsilon_{eff}^{sc} < \epsilon_r$. This does however not affect the qualitative statement that the radiative shockwave does not form at all for $\epsilon_{eff}^{sc} > \epsilon_r$, as that is a consequence of the phase velocity change and is not dependent on the exact field distribution.

2.3 Superconducting Transmission line Fabry-Pérot Resonators

2.3.1 Resonance Frequency

The transmission line Fabry-Pérot resonator (FPR), schematically shown in Fig. 2.13, is an in-line resonator made of a transmission line section of length l_{FP} which is connected to the feed network by a coupler on each end. Generally, two identical couplers are used, either open-ended or shorted, resulting in a half-wave resonator with resonance peaks at frequencies

$$F_n = n \frac{c}{2l_{FP}\sqrt{\epsilon_{eff}}} = nF_0 \quad (2.74)$$

where ϵ_{eff} is the effective dielectric constant of the transmission line, n is the mode number. F_0 is the resonance frequency of the fundamental mode $n = 1$ and also determines the frequency spacing between adjacent peaks of higher order modes.

2.3.2 Transmission spectrum

The transmission spectrum of the FPR can be described by its scattering parameters, where transmission through the resonator is given by $|S_{21}|$, with ports 1 and 2 defined

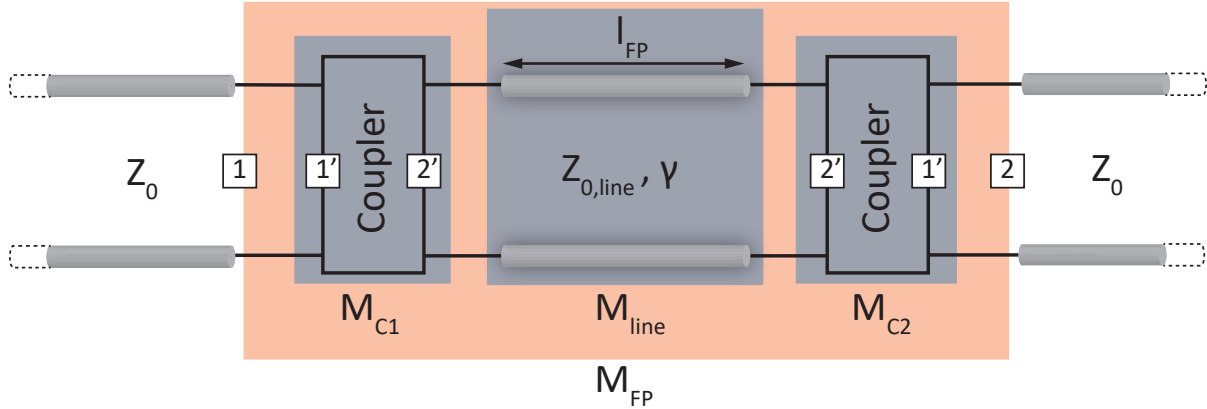


Figure 2.13: Schematic of a Transmission line Fabry-Pérot resonator (FPR). The elements corresponding to the ABCD matrices M_{C1} , M_{line} , M_{C2} are shaded in blue and the FPR described by M_{FP} is shaded in red. Ports 1 and 2 of the FPR, as well as ports 1' and 2' of the individual couplers, are indicated at the edges of their respective elements.

directly outside the coupling structures as shown in Fig. 2.13. The full transmission curve including higher order resonances can be calculated by cascading the ABCD matrices of the individual elements:

$$M_{FP} = M_{C1} M_{line} M_{C2} = \begin{bmatrix} A & B \\ C & D \end{bmatrix} \quad (2.75)$$

where M_{FP} is the ABCD matrix of the full resonator and M_{C1} , M_{line} , M_{C2} correspond to the couplers and resonator line as shown in Fig. 2.13. This approach requires the use of ABCD matrices, as scattering matrices can not be cascaded this way.

The ABCD matrices of the individual elements are readily available in literature [55]. For the couplers, they can be obtained from the scattering matrix as

$$M_{C1} = M_{C2} = \begin{bmatrix} \frac{(1+S_{1'1'})(1-S_{2'2'})+S_{1'2'}S_{2'1'}}{2S_{2'1'}} & Z_p \frac{(1+S_{1'1'})(1+S_{2'2'})-S_{1'2'}S_{2'1'}}{2S_{2'1'}} \\ \frac{1}{Z_p} \frac{(1-S_{1'1'})(1-S_{2'2'})-S_{1'2'}S_{2'1'}}{2S_{2'1'}} & \frac{(1-S_{1'1'})(1+S_{2'2'})+S_{1'2'}S_{2'1'}}{2S_{2'1'}} \end{bmatrix} \quad (2.76)$$

where $S_{i'j'}$ and Z_p are the scattering parameters and port impedances of the couplers as shown in Fig. 2.13. Note, that the couplers are usually symmetrical and reciprocal networks, setting $S_{1'1'} = S_{2'2'}$ and $S_{1'2'} = S_{2'1'}$. If the coupler is given by a simple in-line capacitance, the matrix can be expressed as

$$M_{C1} = \begin{bmatrix} 1 & \frac{1}{i\omega C_c} \\ 0 & 1 \end{bmatrix} \quad (2.77)$$

with the coupling capacitance C_c .

The resonator line matrix M_{line} is given by

$$M_{line} = \begin{bmatrix} \cosh(\gamma l_{FP}) & Z_{0,line} \sinh(\gamma l_{FP}) \\ \frac{1}{Z_{0,line}} \sinh(\gamma l_{FP}) & \cosh(\gamma l_{FP}) \end{bmatrix}. \quad (2.78)$$

where $Z_{0,line}$ and $\gamma = \alpha + i\beta$ are the characteristic impedance and propagation constant of the resonator line as defined by Eqns. 2.25 and 2.27 respectively.

The transmission through the FPR can then be retrieved using

$$S_{21} = \frac{2(AD - BC)}{A + B/Z_0 + CZ_0 + D} \quad (2.79)$$

where Z_0 is the characteristic impedance of the transmission line outside the resonator. An example spectrum is shown in Fig. 2.14 using $l_{fp} = 10$ mm, $\epsilon_{eff} = 12$.

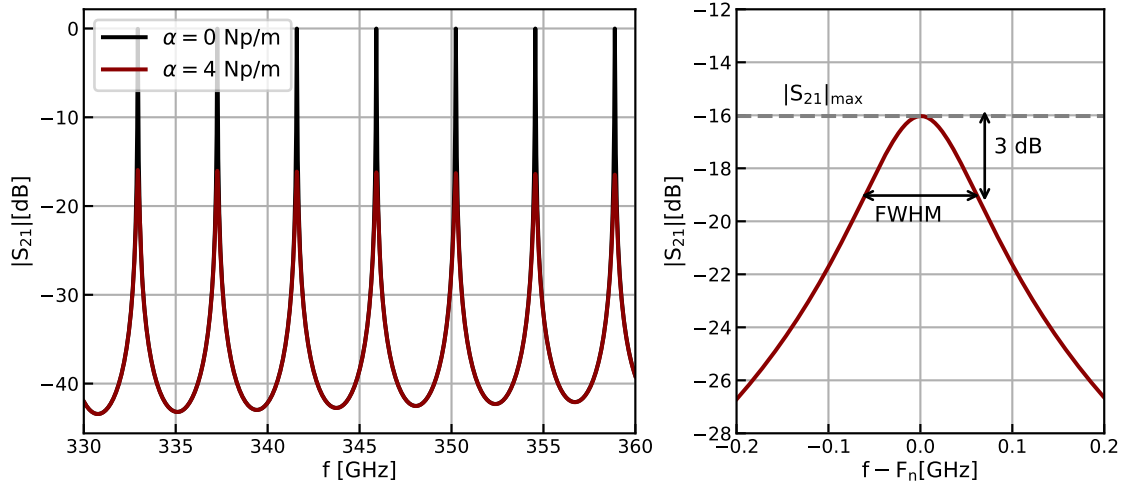


Figure 2.14: (a) Transmission of a Fabry-Pérot resonator for no losses ($\alpha = 0$ Np/m) and medium losses ($\alpha = 4$ Np/m). (b) Single Lorentzian peak at mode number n , with losses ($\alpha = 4$ Np/m).

2.3.3 Quality Factor

Another approach to describe the FPR transmission spectrum is to treat it as a series of independent Lorentzian peaks as shown in Fig. 2.14a). A single peak in the spectrum is then given by

$$\left(|S_{21}|^2\right)_n = I_n \frac{Q_{L,n}^2}{Q_{L,n}^2 + 4 \left(\frac{f - F_n}{F_n}\right)^2} \quad (2.80)$$

where $I_n = |S_{21}|_{max}$ is the peak transmission and $Q_{L,n}$ is the loaded quality factor given by

$$Q_{L,n} = \frac{F_n}{FWHM_n} \quad (2.81)$$

where FWHM is the peaks full width at half maximum as indicated in Fig. 2.14b). The loaded Q-factor Q_L is a measure of the resonators power loss, defined by Eq. 2.28, which can be separated in a internal component Q_i and a coupling component Q_c

$$\frac{1}{Q_L} = \frac{1}{Q_i} + \frac{1}{Q_c}. \quad (2.82)$$

Coupling strength

The coupling Q-factor Q_c is a measure of the coupling strength between the resonator and the external circuit. As coupling relates to energy leakage from the coupler, a high Q_c corresponds to a weak coupling.

The power loss per cycle through a *single coupler* of the FPR is given by

$$P_{loss} = NfE_{stored}|S_{2'1'}|^2 \quad (2.83)$$

where $S_{2'1'}$ is the transmission through the coupler and N is the number of times the coupler is encountered per cycle. For an FPR, N is given by the mode number as $N = 1/n$. Combining Eq. 2.28 and 2.83 then results in

$$Q_{c1} = \frac{n2\pi}{|S_{2'1'}|^2} \quad (2.84)$$

The second coupler can then be included to obtain the total coupling Q-factor as

$$\frac{1}{Q_c} = \frac{1}{Q_{c1}} + \frac{1}{Q_{c2}} = \frac{n\pi}{|S_{2'1'}|^2} = nQ_{c0} \quad (2.85)$$

where $Q_{c1} = Q_{c2}$ is assumed for the latter relations and Q_{c0} is the coupling factor for the fundamental mode $n = 1$.

Internal losses

Any energy lost from the FPR which can not be retrieved in the external circuit is combined in the internal Q-factor Q_i . Depending on the transmission line geometry, the following loss mechanisms need to be taken into account:

- Resistive loss $Q_{i,ohm}$. The resistive losses in a superconductor are the result of quasi-particle excitations. For $T \ll T_c$ and $\hbar\omega \ll 2\Delta_0$ this loss is usually negligible (see section 2.2.2), but should be considered in the case of very low-loss transmission lines.
- Radiation loss $Q_{i,rad}$. This is the dominant loss mechanism for CPW lines, due to the shockwave formation in the substrate when $\epsilon_{eff} < \epsilon_r$ (see section 2.2.4). This loss can theoretically be completely eliminated if the phase velocity in the CPW can be reduced such that $\epsilon_{eff} > \epsilon_r$. Furthermore, the common mode of the CPW due to potential imbalances in the ground planes is strongly radiating and can contribute to radiation loss, if it is excited.

In the case of microstrips, radiation loss is generally negligible as the fields of the propagating wave are well confined between line and ground plane.

- Dielectric loss $Q_{i,diel}$. Dissipation in dielectric materials is due to interaction with two-level systems (TLSs) which occur in amorphous structures (see 2.2.3). This is

the dominant loss mechanism for microstrip lines, due to amorphous dielectric layer between the conducting line and the ground plane.

For CPW lines, $Q_{i,diel}$ is usually small as they are fabricated on a crystalline substrate. However, TLSs at the surface and interface between metal and dielectric can occur and contribute to the loss.

- Radiation loss at the coupler $Q_{i,c}$. In contrast to all other loss sources, this is not an intrinsic property of the transmission line, but happens due to the coupling structure which represents a discontinuity in the line and will therefore inevitably radiate power. It can be difficult to accurately determine the absolute power radiated this way. However, as this power loss only occurs at the coupler, the resulting $Q_{i,c}$ has the same linear dependence on the mode number n as the coupling Q-factor Q_c .

When considering the behaviour of the FPR as a function of mode number, it is therefore advantageous to consider $Q_{i,c}$ as an unknown modification to Q_c as

$$Q'_c = n \frac{Q_{c0} Q_{i,c0}}{Q_{c0} + Q_{i,c0}} \quad (2.86)$$

where $Q_{i,c0}$ is the Q-factor for the fundamental mode $n = 1$.

However, this is not a valid approach when the total loss Q_i of the resonator is in consideration, e.g. when considering the peak heights of the transmission spectrum.

Lorentzian Peak Height

The maximum of the Lorentzian resonance peak can be expressed as

$$|S_{21}|_{max} = \frac{Q_L}{Q_c} = \frac{Q_i}{Q_c + Q_i}. \quad (2.87)$$

Fig. 2.14a) shows the FPR transmission for two cases. In the coupler dominated case ($Q_c \ll Q_i$ for $\alpha = 0$ Np/m) the transmission at the resonance frequency is unity, $|S_{21}|_{max} = 0$ dB. If Q_L is dominated by losses ($Q_c \gg Q_i$ for $\alpha = 0$ Np/m), the peak transmission is reduced and a strong function of Q_i .

Internal Power and Photon Number

The dielectric loss in a microstrip resonator depends strongly on the electric field (see section 2.2.3). However, the field strength is often not uniform across the TLS hosting dielectric. It is therefore often convenient to express equation 2.62 as a function of the resonators internal power P_{int} as

$$\frac{1}{Q_i} = \frac{1}{Q_{i,diel}} (1 + (P_{int}/P_s))^{1/2} + \frac{1}{Q_{i,rem}} \quad (2.88)$$

where $P_s \propto E_s^2$ is the saturation power corresponding to the saturation field strength E_s . P_{int} is defined here as the power of the forward- or backward traveling wave inside the resonator,

$$P_{int} = \frac{V_+^2}{2Z_0}, \quad (2.89)$$

with the voltage $V_+ = V_-$ and characteristic line impedance Z_0 .

The internal power is related to the total energy stored in a resonator of length $L = k\lambda$ as

$$E_{res} = \frac{2kP_{int}}{f} \quad (2.90)$$

where the factor of two in Eq. 2.90 is due to the inclusion of both the forward- and backward traveling wave, while k is related to the mode number n of a half-wave resonator as $k = n/2$ ($k = n/4$ for a quarter-wave resonator).

The internal power can be retrieved from the applied readout power P_{read} and the resonators quality factor as [65]

$$P_{int} = \frac{1}{2k\pi} \frac{Q^2}{Q_c} P_{read}. \quad (2.91)$$

Note, that for the fundamental mode of the half-wave resonator ($k = 1/2$), the internal power is seemingly directly given by the energy stored in the resonator $P_{int} = E_{res} \cdot f$. However, it is important to carefully distinguish between $E_{res} \cdot f$ and P_{int} for FPRs at higher mode numbers ($k \geq 1$), as only P_{int} provides a direct measure of the local field strength at a given point in the resonator, while $E_{res} \cdot f$ is an integration of the field across the whole resonator length. When considering two resonators with identical Q-values and the same readout power P_{read} but different k parameter, P_{int} will be smaller for the resonator with larger k value while $E_{res} \cdot f$ is independent of k . However, as $Q_c \propto n \propto k$, the internal power P_{int} of a single resonator in the Q_c -limited regime ($Q_c \approx Q$) behaves as $P_{int} \propto Q_c/k = \text{const}$ and is therefore independent of k , while $E_{res} \cdot f$ increases linearly according to Eq. 2.90.

Another commonly used approach, is to use photon number instead of internal power, rewriting 2.88 as

$$\frac{1}{Q_i} = \frac{1}{Q_{i,diel}} (1 + (\langle n_{ph} \rangle / n_s))^{1/2} + \frac{1}{Q_{i,rem}}, \quad (2.92)$$

where n_s is the saturation number and $\langle n_{ph} \rangle$ is the average photon number in the forward traveling wave per $\lambda/2$

$$\langle n_{ph} \rangle = \frac{P_{int}}{hf^2} \quad (2.93)$$

with the frequency f . Note, that this definition is identical to that of the total photon number in a half-wave resonator.

2.4 Simulating a Transmission Line Fabry-Pérot Resonator

A Fabry-Pérot resonator (FPR) is very long compared to the relevant wavelengths ($L_{FP} \gtrsim 40\lambda$) with feature sizes much smaller than a wavelength, due to the narrow transmission lines. This makes a simulation of the full structure impractical, as the fine mesh and large box size lead to prohibitively long simulation times. It is therefore preferable to split the resonator into its separate components, i.e. the coupling structures and the transmission line, and cascade them using ABCD matrices as discussed in section 2.3.2. The following subsections will introduce the simulations relevant to the chapters of this thesis:

- CPW-CPW coupler in section 2.4.1 as used for Chapter6.
- CPW-MS coupler in section 2.4.1 as used for Chapter7.
- Radiation loss of a CPW line in section 2.4.2 as used for Chapter6.
- Radiation loss of a short CPW Fabry-Pérot Resonator 2.4.2 as used for Chapter6

All simulations are performed in Sonnet [68], which is a commercial 3D planar EM software capable of simulating superconducting structures at high frequencies.

2.4.1 Coupler Simulation

CPW-CPW Coupler

The CPW-CPW coupler is simulated in a small box of $32 \times 32 \mu\text{m}^2$ with a cell size of $0.5 \mu\text{m}$ as shown in Fig. 2.15a), resulting in the scattering matrix S , with S_{21} shown in Fig. 2.15b) as function of frequency. The box size is chosen as small as possible without impacting the simulation result. Both top and bottom of the box are defined as lossless metal, with a layer of vacuum above and a layer of lossless Sapphire below the metalization with $h_{diel} = 100 \mu\text{m}$ for both layers. Superconducting NbTiN is implemented using the "general model" with zero resistance and a finite sheet inductance L_s . A lookup table with the frequency dependence for L_s , generated using 2.24, is used as input for the model. The coupling structure is implemented as an overlapping coupler with a short to ground, where the coupling strength can be tuned by changing the overlap parameter p (see Fig. 2.15a)).

This coupler design is used in Chapter6, where port 1 on the left side is connecting to either an antenna or detector, while port 2 is part of the FPR. The position of the overlapping slots is adjusted for different CPW line widths on the resonator side to keep $s_0 = 2 \mu\text{m}$ constant, which is the smallest possible feature size (due to fabrication constraints) and maximizes the coupling strength. Due to the frequency dependence of L_s , and thus the line impedance Z_0 , the line will be slightly mismatched with the constant port impedance Z_p . To account for this, a reference plane close to the coupler is used and the port impedances are set to 50Ω . The scattering matrix for the correct port impedance is then retrieved in post processing. This also makes optimization in the design phase easier,

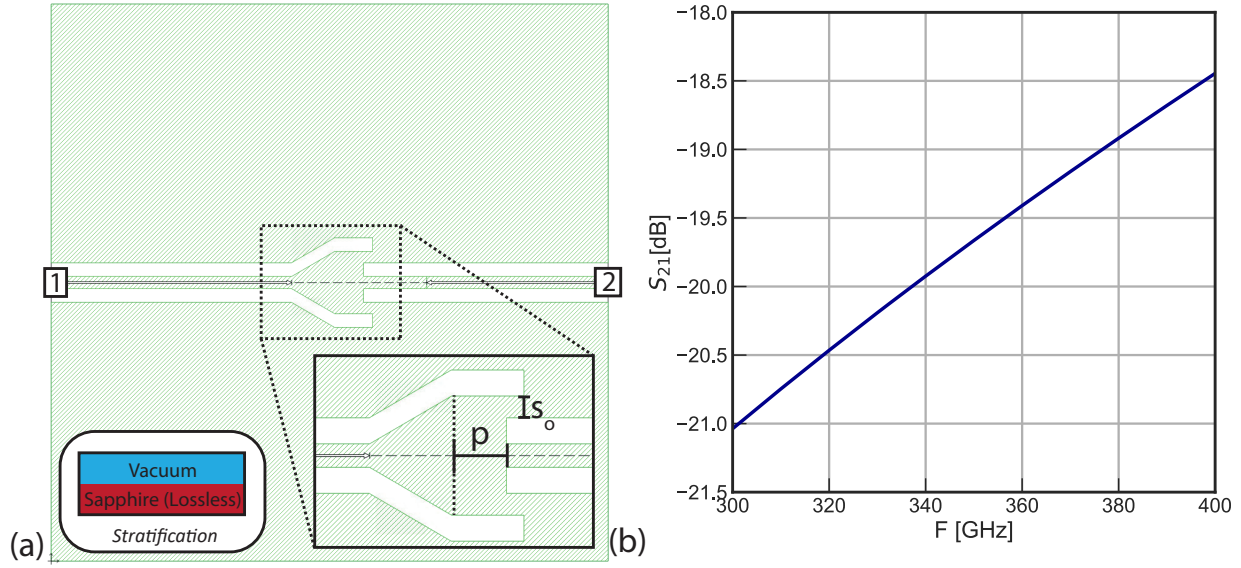


Figure 2.15: (a) Sonnet box of the coupler simulation with inset showing the stratification and a zoom-in on the the coupling structure. NbTiN is shown in green; substrate in white. (b) Simulated S_{21} of the measured chip in Chapter 6, where $s = 1.95 \mu\text{m}$ and $w = 2.15 \mu\text{m}$ and L_s given by the NbTiN $T_c = 14.7 \text{ K}$ and $\rho_n = 102 \mu\Omega\text{cm}$. Output from Sonnet, with 50Ω port impedance.

as the port impedance does not need to be adjusted in the simulation setup if the line impedance changes.

In order to obtain the coupler geometry for a desired Q_c of the FPR, a sweep of p is performed from 300 to 400 GHz. Note, that the dimensions of the fabricated chip will differ slightly from the design. Therefore, simulations for the fabricated chips are carried out with the measured dimensions and a cell size of $0.05 \mu\text{m}$ to properly sample the geometry.

CPW-Microstrip Coupler

The simulation of the CPW-microstrip coupler uses a similar set up to that of section 2.4.1, with a slightly larger box of $128 \times 128 \mu\text{m}^2$, as shown in Fig. 2.16a), to account for the larger coupler size. The addition of the microstrip requires another dielectric layer (here using amorphous silicon (a-Si) with $\epsilon_r = 10$), as well as another superconducting NbTiN layer.

The coupling structure has the microstrip line continue over the shortened end of the CPW in a paddle-like geometry, where the coupling strength can be tuned via the overlap length $L_{overlap}$ as shown in Fig. 2.16a) and b). In order to minimize the effect of fabrication uncertainties, such as misalignment and overetching, the overlapping microstrip line is widened such that its width is given by

$$w_{paddle} = w_{cpw} + s_{cpw} \quad (2.94)$$

where w_{cpw} and s_{cpw} are the CPW gap and line width respectively.

Box size [μm^2]	128×128
Cell size [μm^2]	0.5×0.5
F [GHz]	300..400
s_{cpw} [μm]	1.95
w_{cpw} [μm]	2.15
s_0 [μm]	2
p [μm]	4.55
T_c [K]	14.7
ρ_n [$\mu\Omega\text{ cm}$]	102
t [μm]	0.1

Table 2.1: Parameters used for the simulation of the CPW-CPW coupler shown in 2.15b) based on fabricated chip dimensions. The surface inductance of the top (L_s^{top}) and bottom layer (L_s^{bot}) of NbTiN are obtained from the respective critical temperature T_c , normal resistance ρ_n and thickness t as given in Chapter 7.

Simulations to obtain Q_c of the FPR as a function of p are then carried out analogous to section 2.4.1.

2.4.2 Radiation Loss Simulation

CPW line loss

Retrieving radiation loss of any structure in Sonnet requires a careful setup of the simulation. Any loss in the structure corresponds to power that does not reach the ports of the simulation and can therefore be obtained from the scattering matrix as

$$P_{rad} = 1 - P_{out} = 1 - (|S_{11}|^2 + |S_{21}|^2). \quad (2.95)$$

The Sonnet box used to simulate the radiation loss in a CPW, shown in Fig. 2.17, fulfills the following requirements for an accurate result:

- The structure is able to radiate freely.
- Radiated power is not absorbed in the ports.
- The structure is otherwise lossless (e.g. ohmic losses, dielectric losses).

An in-depth analysis of this simulation box can be found in [69]. In this section, the resulting best practices are explained and summarized.

The CPW can radiate when the propagating field can couple to modes in the surrounding media, i.e. the vacuum above and the Sapphire substrate below. However, the lossless metal walls of the Sonnet box act as a waveguide with a cut-off frequency given by the box size, below which no modes can be excited. Therefore, the box is made sufficiently large compared to the freespace wavelength λ_0 ($Y_{box} = X_{box} \gtrsim 2\lambda_0 = 2048 \mu\text{m}$) to allow

Box size [μm^2]	128×128
Cell size [μm^2]	0.5×0.5
F [GHz]	350
a-Si thickness [μm]	0.25
w_{ms} [μm]	2
s_{cpw} [μm]	2
w_{cpw} [μm]	2
w_{paddle} [μm]	4
T_c^{top} [K]	15.1
ρ_n^{top} [$\mu\Omega\text{ cm}$]	138
t^{top} [μm]	0.3
T_c^{bot} [K]	15.0
ρ_n^{bot} [$\mu\Omega\text{ cm}$]	104
t^{bot} [μm]	0.22

Table 2.2: Parameters used for the simulation of the CPW-microstrip coupler shown in 2.16b). The surface inductances of the top (L_s^{top}) and bottom layer (L_s^{bot}) of NbTiN are obtained from the respective critical temperature T_c , normal resistance ρ_n and thickness t as given in Chapter 7.

Box size [μm^2]	2048×2048
Cell size [μm^2]	0.5×0.5
Groundplane width [μm]	400
CPW length [μm]	800..1800
Vacuum layer thickness	$\lambda_0/4$
Lossless substrate thickness [μm]	100
Lossy substrate thickness [μm]	100,000
Loss tangent	1
F [GHz]	350

Table 2.3: Parameters used for the radiation loss simulation.

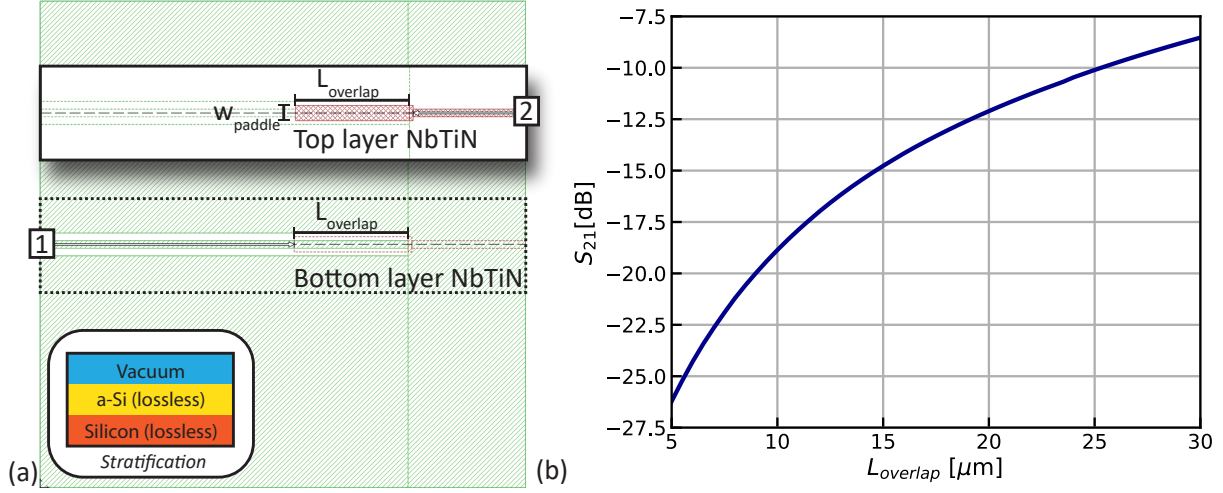


Figure 2.16: (a) Sonnet box of the coupler simulation with inset showing the stratification. The lower NbTiN layer, containing the CPW and the microstrip groundplane, is shown in green with the substrate in white. The top NbTiN layer, containing the microstrip line, is shown in red in a separate inset which is shown offset to its true location indicated by the dotted outline. (b) Simulated S_{21} as a function of p at 350 GHz for the coupler used in Chapter 7 with the parameters given in Table 2.4.1. Output from Sonnet, with 50Ω port impedance.

all relevant modes to be excited. All relevant dimensions used in the simulation are also summarized in Table 2.4.2.

The simulation is set up as shown in Fig. 2.17a) with superconducting NbTiN and a $100 \mu\text{m}$ thick lossless Sapphire substrate equivalent to section 2.4.1, resulting in no ohmic or dielectric losses. However, for a fully enclosed lossless metal box with no lossy components, any radiated power will be reflected back and eventually absorbed in one of the ports and result in $P_{\text{rad}} = 0$. To avoid this in the Sonnet simulation, the top and bottom walls are set to free space, where radiation at the boundary is absorbed. However, surface waves in the Sapphire substrate are still confined by reflections at the sidewall. A thick lossy layer of Sapphire is placed below the lossless layer in order to attenuate these surface waves, before they can be absorbed in the ports. Ports are set up as co-calibrated internal ports in a push-pull configuration with a floating ground connection (see Fig. 2.17a)) and without de-embedding. Note, that de-embedding is possible and can be preferable [69], but was not functioning reliably during the work in Chapter 6 and therefore not used.

To avoid reflections, the port impedance is set to the line impedance, which is retrieved from a separate simulation. The metalization is confined to a patch in the middle of the box such that the sidewalls do not affect the radiating structure. This approach also allows for excitation of all relevant radiative modes, while minimizing the simulation time, by keeping the ground plane size small.

In summary, the following design rules need to be followed:

- A large box size compared to the wavelength $Y_{\text{box}} = X_{\text{box}} \gtrsim 2\lambda_0$.
- The top and bottom wall of the box are set to the "free space" boundary condition.

- Two layers of substrate, one lossless layer ($\tan \delta = 0$) of medium thickness directly below the metalization and one lossy, very thick layer ($\tan \delta = 1$) below that.
- Co-calibrated internal ports with a floating ground connection.
- The superconductor is a metal using the general model with L_s set as the surface inductance in pH/\square .

To make certain that the simulated P_{rad} is not affected by any other systematic errors in the simulation, a sweep of the CPW length L_{cpw} is performed and a linear fit through the resulting $P_{rad}(L_{cpw})$ is used to determine the loss factor α , as shown in Fig. 2.17b). The groundplane can be kept at a constant width for this purpose. The corresponding internal quality factor is then given by $Q_i = \beta/(2\alpha)$, with $Q_i = 15100$ for the narrowest line with $s = w = 2 \mu\text{m}$.

This simulation method was verified by comparing a PEC simulation ($L_s = 0 \text{ pH}/\square$) with analytical models, which found good agreement as shown in Fig. 2.17c). Additionally, good agreement was found with simulations of superconducting CPW carried out in the 3D EM software CST [70].

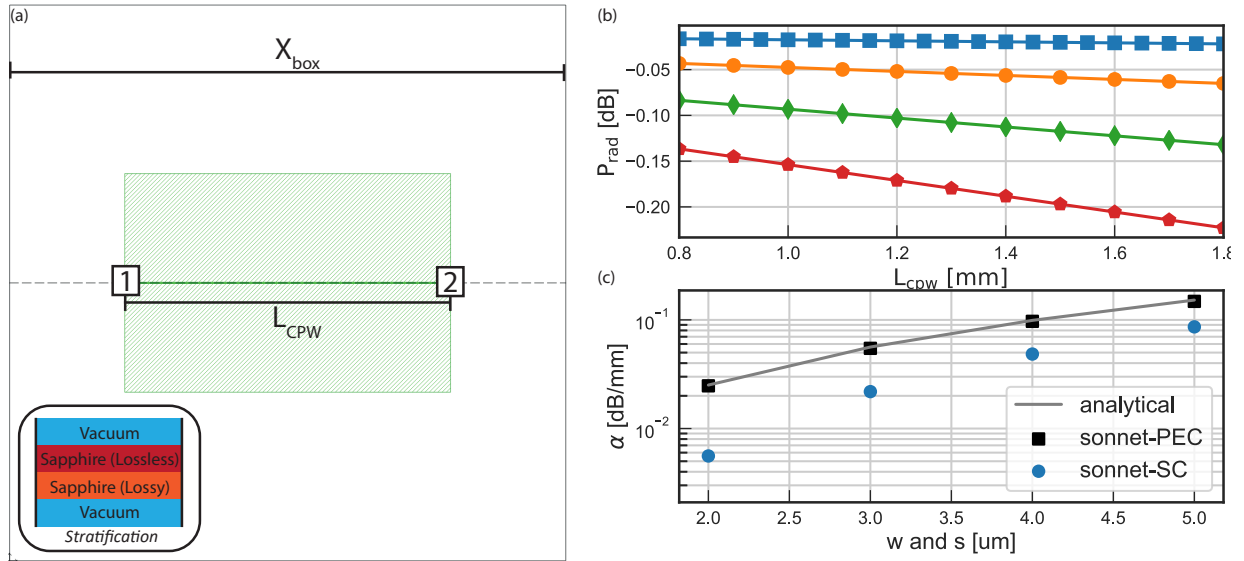


Figure 2.17: (a) Sonnet box to simulate the radiation loss of a straight CPW line with inset showing the stratification of the dielectric layers. (b) Simulated loss as function of line length for different NbTiN CPWs where $s=w$ (2 μm : blue; 3 μm : orange; 4 μm : green; 5 μm : red). The Straight lines are linear fits. (c) Loss factor alpha as function of CPW line width. Sonnet-SC corresponds to the fitted values of plot (b). Sonnet-PEC is compared to the analytical solution for a PEC CPW, showing good agreement.

Resonator loss

While a full length FPR is too large to implement in Sonnet, shorter resonators can be simulated as shown in Fig 2.18a) to obtain the loss at a given frequency as function of mode

number. For this purpose, the same box as in section 2.4.2 is used, but the simple straight line is exchanged for a 2-port FPR with the couplers as given in 2.4.1 and a resonator length such that

$$L_{res} = n \frac{c}{2F\sqrt{\epsilon_{eff}}} \quad (2.96)$$

with the resonance frequency $F = 350$ GHz, the dielectric constant of the line ϵ_{eff} and the mode number n , which is varied from 1 to 14. The simulation for each mode number is carried out in a small range around the resonance frequency, resulting in a S_{21} peak which is dependent on mode number as shown in Fig. 2.18b) for a CPW with $s = w = 2 \mu\text{m}$. The downshift in resonance frequency at small mode numbers, shown in Fig. 2.18b), is due to the coupling inductance, which represents a larger fraction of the total resonator inductance for shorter resonators. The loaded quality factor Q_L of the peak is given by

$$\frac{1}{Q_L} = \frac{1}{Q_i} + \frac{1}{Q_c} = \frac{1}{Q_{i,l}} + \frac{1}{Q_{i,c}} + \frac{1}{Q_c} \quad (2.97)$$

with the coupling strength Q_c , the internal loss of the line $Q_{i,l}$ and the loss at the coupler $Q_{i,c}$.

Both $Q_{i,c}$ and Q_c are linear in mode number and can be expressed as $Q_{i,c} = nQ_{i,c1}$ and $Q_c = nQ_{c1}$, where the index 1 corresponds to the value at $n = 1$. This can be intuitively understood as a reduced impact of the coupler on the resonator behaviour when the resonator becomes longer than the wavelength. The peak height of the resonator is given by

$$|S_{21}^{max}| = \frac{Q_L}{Q_c}, \quad (2.98)$$

and can therefore be used to distinguish between internal losses and the coupling strength. Fitting Q_c and Q_i results in $Q_{c1} = 212$, $Q_{i,c1} = 1307$ and $Q_{i,l} = 16980$. As $Q_{i,l}$ is independent of mode number, the resonator is in a Q_c limited regime for low n and transitions to a $Q_{i,l}$ dominated regime at high n , while $Q_{i,c}$ is negligible in both regimes. The obtained value for $Q_{i,l}$ shows good agreement with the pure line simulation of $Q_i = 15100$ in section 2.4.2. Slight deviations between these two values are expected, as the current distributions differ between a resonating structure and a simple straight line, thus affecting the radiating fields.

2.5 Microwave Kinetic Inductance Detector

Microwave kinetic inductance detectors (MKIDs) were first proposed by Day et al. in 2003 [17]. An MKID is a superconducting resonator capable of efficiently absorbing photons in part of its structure. Photon absorption changes the surface impedance of the superconductor (see section 2.1.2), causing a change in resonator parameters, as will be shown later in this section. The superconducting resonator is coupled to a readout line as shown in Fig. 2.19a), through which a microwave signal can be sent. When the signal frequency differs from the resonance frequency, the signal is not affected by the resonator,

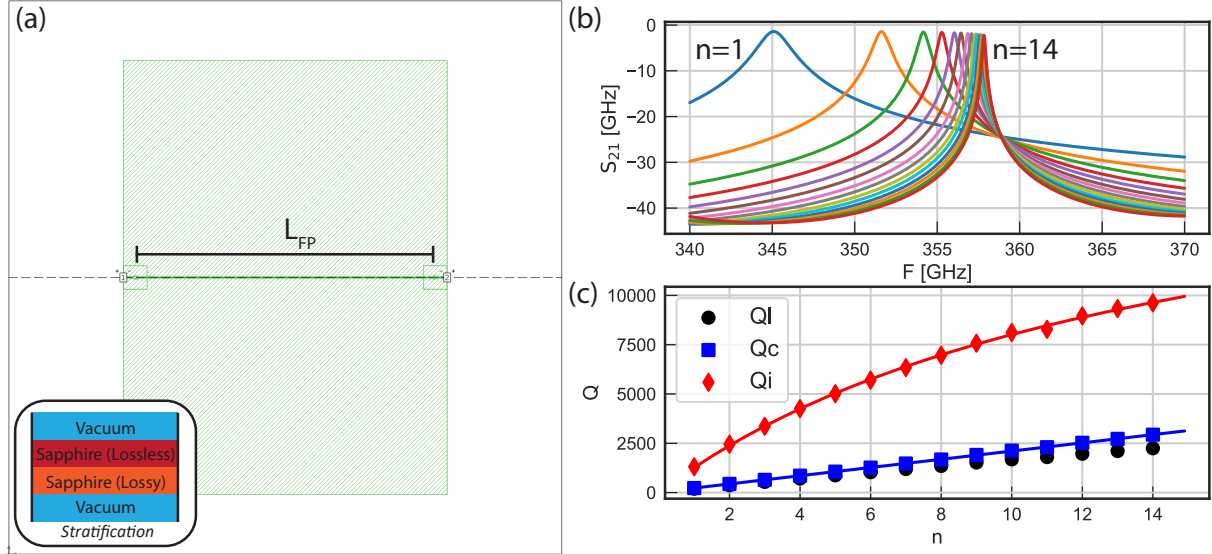


Figure 2.18: (a) Sonnet box to simulate the radiation loss of a short Fabry-Pérot resonator, with inset showing the stratification of the dielectric layers. (b) Simulated S_{21} for different resonator lengths, corresponding to different mode numbers n . (c) Quality factors extracted from the peaks in figure b shown as points with fits for Q_i and Q_c shown as lines.

resulting in unity transmission $|S_{21}| = 0$ dB. For frequencies close to the resonance frequency, power is reflected back to the input port, resulting in a lorentzian transmission dip in $|S_{21}|$. MKIDs can be easily multiplexed in frequency domain by ensuring a resonance frequency spacing of the different MKID resonators as shown in Fig. 2.19. In this case each MKID can be probed by a signal or tone corresponding to its resonance frequency since this tone is not affected by the other MKIDs.

2.5.1 Response

In a dark environment, where no photon absorption occurs, the superconducting resonator has a certain resonance frequency f_0 and loaded quality factor Q_L . For a quarter-wave resonator,

$$f_0 = \frac{c}{4l\sqrt{\epsilon_{eff}^{sc}}} = \frac{1}{4l\sqrt{L_l C_l}} \quad (2.99)$$

where l is the resonator length and ϵ_{eff}^{sc} is the effective dielectric constant given by Eq. 2.36, while L_l and C_l are the inductance and capacitance per unit length. If a photon with energy higher than the bonding energy of a Cooper pair, 2Δ , is absorbed in the superconductor, it can break a Cooper pair, creating a number of quasiparticles proportional to the photon energy. Since the complex conductivity depends on the Cooper pair and quasiparticle densities, the absorbed photon will cause a change in complex conductivity which can be derived in the limit of $kT, \hbar\omega < 2\Delta$ by combining Eqns. 2.21 and 2.22 with Eq. 2.9 to

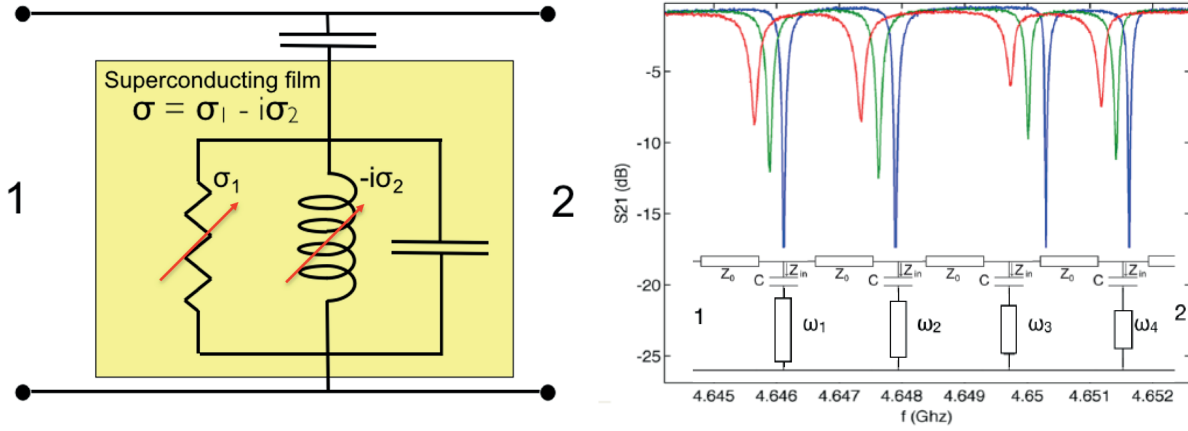


Figure 2.19: (a) Circuit schematic of a superconducting quarterwave resonator in parallel to the microwave transmission line. The resistance and inductance change when a photon is absorbed. (b) Microwave transmission between ports 1 and 2 for the shown circuit containing four MKIDs in a frequency multiplexing scheme.

give [53]

$$\frac{d\sigma_1}{dn_{qp}} \simeq \sigma_N \frac{1}{N_0 \hbar \omega} \sqrt{\frac{2\Delta_0}{\pi k_B T}} \sinh\left(\frac{\hbar \omega}{2k_B T}\right) K_0\left(\frac{\hbar \omega}{2k_B T}\right), \quad (2.100)$$

$$\frac{d\sigma_2}{dn_{qp}} \simeq \sigma_N \frac{-\pi}{2N_0 \hbar \omega} \left[1 + 2 \sqrt{\frac{2\Delta_0}{\pi k_B T}} \exp\left(\frac{-\hbar \omega}{2k_B T}\right) I_0\left(\frac{\hbar \omega}{2k_B T}\right) \right] \quad (2.101)$$

with σ_N is the normal state conductivity, Δ_0 the superconducting energy gap at $T = 0$ and I_0 and K_0 the modified Bessel functions of the first and second kind. $\omega = 2\pi f$, where f is the resonance frequency of the MKID. Note that the change in quasiparticle density n_{qp} is expressed as a change in temperature, where the relation between temperature and n_{qp} is given by Eq. 2.9. The change in σ_1 and σ_2 causes a shift in resonance frequency δf_0 which is given by

$$\frac{df_0}{dN_{qp}} = \frac{\alpha_k \beta f_0}{4|\sigma|V} \frac{d\sigma_2}{dn_{qp}} \quad (2.102)$$

and a decrease in the intrinsic quality factor Q_i , given by

$$\frac{d(1/Q_i)}{dN_{qp}} = \frac{\alpha_k \beta}{2|\sigma|V} \frac{d\sigma_1}{dn_{qp}} \quad (2.103)$$

where V is the volume in which n_{qp} is changed, $N_{qp} = n_{qp}V$ is total number of quasiparticles in said volume, α_k is the kinetic inductance fraction of Eq. 2.35 and $\beta = 1 + \frac{2d/\lambda}{\sinh(2d/\lambda)}$ with the penetration depth λ and film thickness d ($\beta = 2$ for thin films where $2d < \lambda$). σ_1 and σ_2 are given by Eq. 2.17 and Eq. 2.18 respectively. Fig. 2.20a) demonstrates the changing resonator behaviour due to an increase in quasi-particle density. With increasing n_{qp} the resonance frequency shifts to lower frequencies and the transmission dip depth decreases.

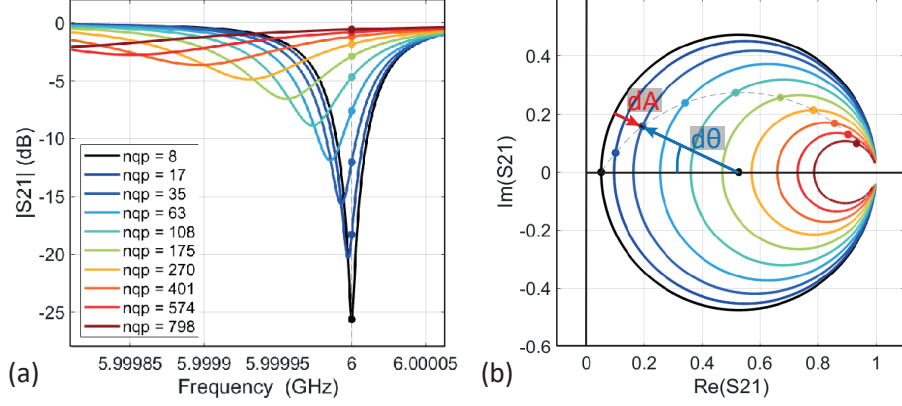


Figure 2.20: (a) Resonance dip of an MKID as function of quasiparticle density n_{qp} . The dotted line shows the change in transmission for a readout tone located at the resonance frequency at $n_{qp} = 8$. (b) Resonance circles in the complex plane corresponding to the resonance dips in the left figure. The amplitude and phase response of Eqns. 2.104 and 2.105 as function of n_{qp} are shown by the dotted line using the center of the resonance circle for $n_{qp} = 8$ as reference point.

Although the magnitude of transmission $|S_{21}|$ gives a good indication of the resonators response, it is more convenient to use the resonance circle in the complex plane for readout as shown in Fig. 2.20b). In this case, the response due to a changing quasiparticle density is given by [71] as a change in amplitude

$$\frac{dA}{dN_{qp}} = -\frac{\alpha_k \beta Q_l}{|\sigma|V} \frac{d\sigma_1}{dn_{qp}} \quad (2.104)$$

and phase

$$\frac{d\theta}{dN_{qp}} = -\frac{\alpha_k \beta Q_l}{|\sigma|V} \frac{d\sigma_2}{dn_{qp}}. \quad (2.105)$$

Here, Q_l is assumed to be constant. Phase response is usually the preferred read-out method as it is larger than the response in amplitude (see Fig. 2.21) and, in contrast to amplitude response, monotonic with power as can be understood from Fig. 2.20.

2.5.2 Noise

Various noise sources must be considered to understand the noise spectrum of an MKID. The individual contributions will be introduced in the following section and can be broadly separated into three different categories:

- Fundamental to pair-breaking detection - *generation-recombination (GR) noise*.
- Fundamental to detecting thermal radiation - *photon noise*.
- Non-fundamental sources, either of the detector or the microwave readout - *two-level system (TLS) noise* and *amplifier noise*.

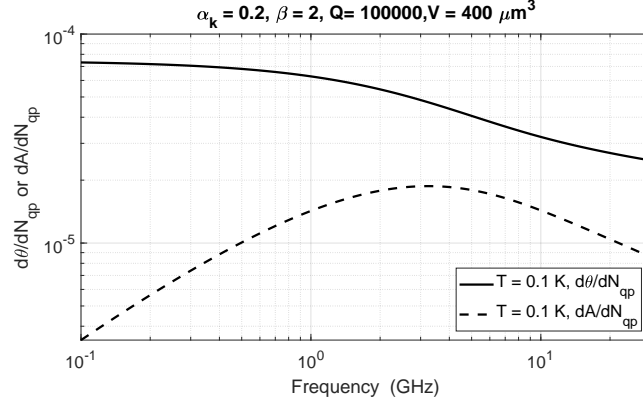


Figure 2.21: Amplitude and phase responsivity for an example MKID at operating temperature $T \approx T_c/10$.

Non-fundamental sources deteriorate detector performance and should therefore be reduced to negligible levels.

Generation-Recombination Noise

Generation-recombination (GR) noise is the result of the dynamic equilibrium between Cooper pairs and quasiparticles inside a superconductor [72] [65]. Both generation by phonons and recombination are Poissonian processes in which the variance is determined by the number of quasiparticles in the superconductor. The power spectral density in amplitude ($x = a$) or phase ($x = \theta$) is given by [65]

$$S_{x,GR} = \frac{4N_{qp}\tau_{qp}}{1 + \omega^2\tau_{qp}^2} \frac{(dx/dN_{qp})^2}{1 + \omega^2\tau_{res}^2} \quad (2.106)$$

where τ_{res} is the ring time of the MKID resonator and dx/dN_{qp} is the response in amplitude or phase given by Eqns. 2.104 and 2.105 respectively. The GR noise level is effectively constant due to $N_{qp} \propto 1/\tau_{qp}$. For aluminium based resonators operating at ~ 5 GHz, the roll off is given by the quasiparticle lifetime as $\tau_{qp} \ll \tau_{res}$.

Photon Noise

Photon noise is only present under optical load and is due to the random arrival rate of photons at the detector, which is a fundamental property of thermal radiation sources. It is therefore the fundamental noise source for any power integrating detector. The PSD is given by [65]

$$S_P = 2P_{rad}\hbar\omega(1 + \eta_{opt}O) \quad (2.107)$$

where P_{rad} is the average radiation power and $(1 + \eta_{opt}O)$ is the correction to Poissonian statistics due to photon bunching for a single mode, with O the mode occupation. η_{opt} is

the optical efficiency, which is the fraction of P_{rad} that is absorbed in the MKID.

System Noise

Although not a inherent noise source of the MKID, the system noise can limit the performance of the detector. System noise has a white PSD, which is related to the system noise temperature T_{noise} as [65]

$$S_{system} = \frac{4k_B T_{noise}}{P_{read}} \left(1 + \frac{Q_c}{Q_i}\right)^2. \quad (2.108)$$

where P_{read} is the microwave readout power in the feedline near the MKID. For a well designed readout system the system noise temperature is limited by the low-noise cryogenic amplifier and is therefore commonly referred to as amplifier noise. The second term in Eq. 2.108 corrects for the MKID dip depth. To reduce the effect of the system noise, a low Q_c/Q_i ratio is favorable. However, reducing Q_c in order to reduce S_{21}^{min} also reduces the responsivity of the resonator. Hence, the typical ideal case is $Q_c = Q_i$, which corresponds to $S_{21}^{min} = -6$ dB.

Two-level Sytem Noise

Two-level sytem (TLS) noise is the result of random fluctuations of TLSs in a dielectric material (see section 2.2.3), which can be understood as a fluctuation of the effective dielectric constant ϵ_{eff} . As a result, it is only present in the frequency or phase response of an MKID, and not in amplitude. The noise spectrum has a characteristic slope of $S_{TLS,\theta} \propto \omega^{-0.5}$ and is reduced for larger readout signals $S_{TLS,\theta} \propto P_{read}^{-0.5}$ [73]. In a CPW resonator, TLS noise can be reduced by using wider lines, with a dependency of $S_{TLS,\theta} \propto w_{tot}^{-1.6}$ [74].

The absolute level of the PSD does depend strongly on the MKID geometry, readout power and the properties of the dielectric materials and surface layers. However, using empirical reference values, the universal behaviour can be used to express the PSD as:

$$S_{TLS} = S_{ref,metal} \left(\frac{W}{W_{ref}}\right)^{-1.6} \left(\frac{P}{P_{ref}}\right)^{-0.5} \left(\frac{F}{F_{ref}}\right)^{-0.5} \int_0^{L_{Res}} \cos^3\left(\frac{l}{L_{res}}\pi/2\right) \delta l \quad (2.109)$$

where $S_{ref,mat}$ is the reference value for a given material combination given at the power $P_{ref} = -40$ dB m, noise frequency $F_{ref} = 1$ kHz and CPW width $W_{ref} = 7$ μ m (with $w = 2$ μ m and $s = 3$ μ m). The integral takes into account the dependence on the varying electric field strength along the resonator length L_{res} .

2.5.3 Hybrid Design

The hybrid MKID consists of two sections, a narrow hybrid section with an Al center line and NbTiN ground planes and a wide NbTiN section as shown in Fig. 2.22 [36]. Making

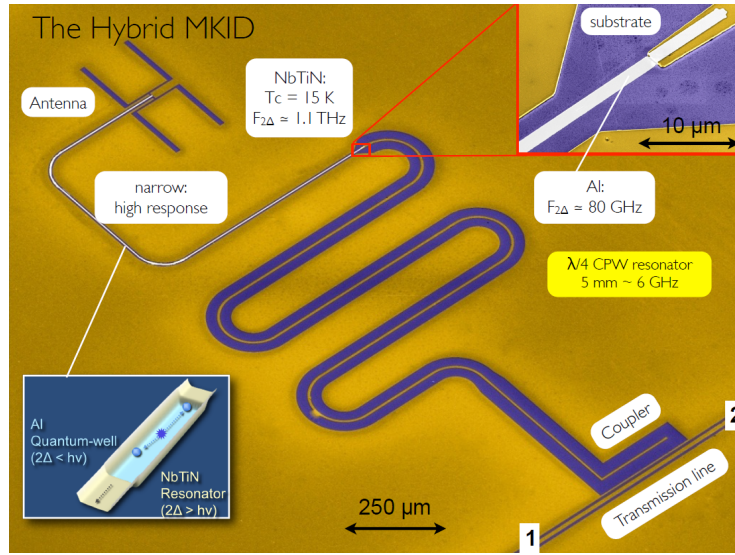


Figure 2.22: Hybrid MKID picture.

the hybrid section narrow decreases the active volume V , which increases the detector sensitivity (see Eq. 2.105). Al is chosen because of the following properties:

- Favourable energy gap frequency of roughly 90 GHz. The gap frequency of the superconductor determines the frequency to which the detector is sensitive. The MKID is designed for the far infrared frequency range, $f > 300$ GHz, which requires a gap frequency lower than 300 GHz.
- Aluminium based MKIDs have been proven experimentally to be the most sensitive MKIDs [36].

The narrow Al section is placed at the shorted end of the resonator, where the current and consequently the MKIDs sensitivity to changes in n_{qp} is maximum. The section length is such that $> 90\%$ of incoming power is absorbed.

Unfortunately a narrow Al section suffers from TLS noise. This becomes evident in a pure Al MKID as shown in Fig. 2.23, where the phase noise is dominated by TLS. To decrease the the TLS noise of the MKID, the second section is made wider and from NbTiN, which has a lower level of TLS noise (see 2.5.2). This section is placed at the coupled open end of the resonator, where the electric field is strongest and the TLS noise would thus be maximum. As a result, the total TLS contribution to the phase noise is reduced to a point where the fundamental generation-recombination noise is dominant, as shown in Fig. 2.23b).

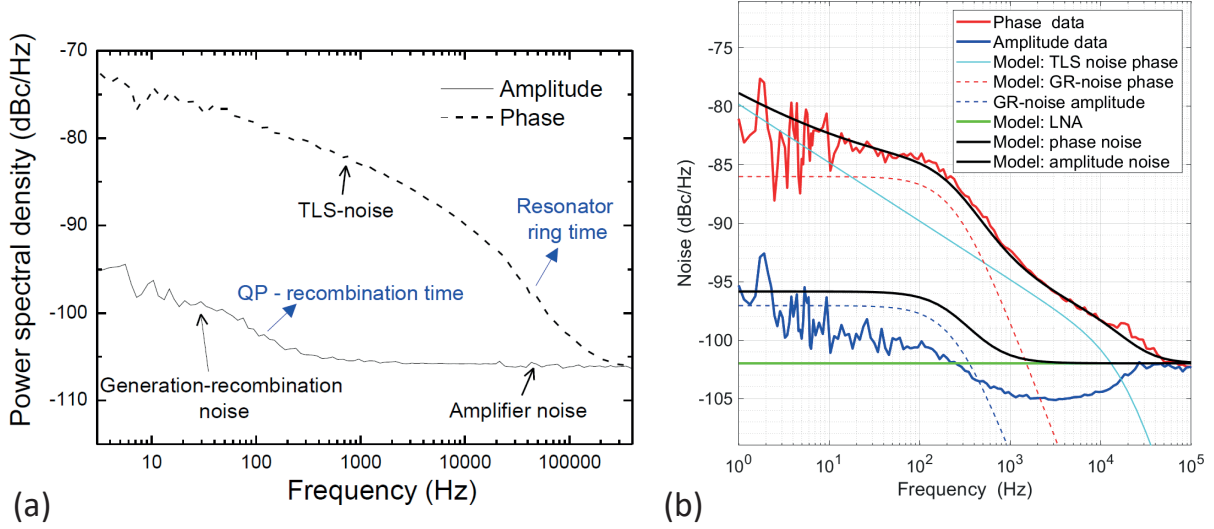


Figure 2.23: (a) Noise spectrum in amplitude and phase of a CPW MKID made of only aluminum. Figure from de Visser [65]. (b) Noise spectrum in amplitude and phase of a hybrid MKID. The model values are retrieved from a-priori calculations based on the hybrid MKID geometry and response data.

2.6 Optical Efficiency

The response and noise of the MKID discussed in section 2.5, is a measure of the power P_{abs} absorbed in the MKID. However, the usual quantity of interest is the power P_{source} emitted by a given source. As such, any losses on the quasi-optical path between source and MKID need to be quantified and calibrated to relate P_{abs} to P_{source} . This is generally done by defining efficiencies for various aspects of the quasi-optical path, which can then be multiplied together to obtain a total system efficiency

$$\eta_{tot} = \eta_1 \cdot \eta_2 \cdot \dots \cdot \eta_n. \quad (2.110)$$

Of particular interest here is the optical efficiency η_{opt} , which characterizes the performance of the horn or lens-antenna coupling radiation to the MKID. In the following section, the definition for η_{opt} as used in this thesis is given, and a calibration method is shown.

Measuring η_{opt} requires a well defined power source. Figure 2.24 shows a simplified setup, where an incoherent blackbody emitter is coupled to a lens-antenna through a limiting aperture defining the opening angle Ω , and a filter stack with a frequency dependent transmission $F(\nu)$.

In the case of a single polarized system, achieved by adding a polarizer to the setup or using a single polarized antenna, P_{abs} can be related to P_{source} by using [75]:

$$P_{abs} = \eta_{opt}(\nu) P_{Source} \quad (2.111)$$

$$= \frac{1}{2} \int_{\Delta\nu} \eta_{opt}(\nu) B_\nu \lambda^2 F(\nu) d\nu \quad (2.112)$$

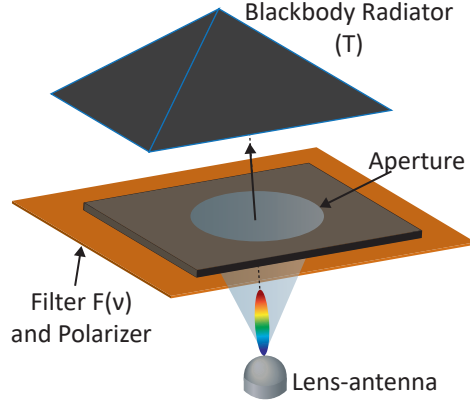


Figure 2.24: Simplified schematic to calibrate the optical efficiency of a lens-antenna. The blackbody with temperature T is coupled to the lens-antenna via a polarizer and filters with total transmission $F(\nu)$. An aperture is located between blackbody and lens-antenna without significantly restricting the beam from the antenna. Not shown is the detector coupled to the lens-antenna. The schematic of a complete experimental setup is shown in Fig. 3.9.

where

$$B_T(\nu) = \frac{\nu^2}{c^2} \frac{2h\nu}{\exp(\frac{h\nu}{k_B T}) - 1} \quad (2.113)$$

is the spectral brilliance of the thermal radiator given by Planck's law at the known source temperature T , $F(\nu)$ is the transmission through the filter stack and λ^2 is the throughput for a single moded antenna [76]. Note, that P_{source} is defined as the power from the radiator in front of the lens, i.e. filtered in frequency, single polarized and single moded.

The term $\eta_{opt}(\nu)$ is the optical coupling efficiency between the source and the detector and is generally frequency dependent. It contains multiple effects, which can be separated to first order into spillover- and radiation efficiency $\eta_{opt}(\nu) = \eta_{so}(\nu)\eta_{rad}(\nu)$. η_{so} describes the spillover between the lens-antenna beam and the limiting aperture of the source while η_{rad} describes the fraction of power which is absorbed in the MKID. η_{rad} is the product of several terms which can typically all be obtained from simulations using commercial software such as CST microwave studio:

- η_{pol} . The polarization efficiency describing the polarization purity of the lens-antenna.
- $\eta_{reflection}$. The reflection efficiency describing how much power is reflected at the lens surface.
- η_{FtB} . The front-to-back ratio of the antenna.
- η_{match} . The impedance matching efficiency between antenna feed and the MKID line.
- η_{CPW} . The fraction of power which is absorbed in the Al center line of the MKID.

The absorbed power P_{abs} cannot be measured independently from η_{opt} . However, it is possible to obtain the optical efficiency via the detector's experimental noise equivalent

power (NEP_{exp}), taken at a reference frequency f_{ref} if the MKID is known to be photon noise limited. This is the case when [36]:

- The noise spectrum is white with a roll-off frequency given by the inverse of the quasiparticle lifetime. I.e. the roll-off increases in frequency with increasing power.
- The noise spectrum changes significantly when the detector is going from a dark state to an illuminated state.

$$NEP_{exp}(P_{source}, f_{ref}) = \sqrt{S_{\theta}(f_{ref})} \left(\frac{d\theta}{dP_{source}} \right)^{-1} = \eta_{opt} \sqrt{S_{\theta}(f_{ref})} \left(\frac{d\theta}{dP_{abs}} \right)^{-1} \quad (2.114)$$

where the phase noise S_{θ} and phase responsivity $\frac{d\theta}{dP_{abs}}$ are the measurables in the experiment. For a photon-noise limited detector, the NEP at the detector is given by

$$NEP_{theory}^2(P_{source}) = NEP_{Poisson}^2 + NEP_{Bunching}^2 + NEP_R^2 \quad (2.115)$$

$$= \int 2\eta_{opt} P_{source,v} h\nu d\nu + \int 2\eta_{opt}^2 P_{source,v} h\nu F(\nu) O_{\nu} d\nu + \int 4\eta_{opt} P_{source,v} \frac{\Delta}{\eta_{pb}} d\nu \quad (2.116)$$

where $O_{\nu} = \frac{1}{\exp(h\nu/k_B T) - 1}$ is the photon occupation number defined at the blackbody emitter, Δ is the superconducting bandgap energy and $\eta_{pb} \approx 0.47$ the pair-breaking efficiency [77]. Note that the bunching term $NEP_{Bunching}^2$ depends on η_{opt}^2 , due to the reduced photon density at the detector affecting the bunching effect.

In the case of a narrow bandwidth, the optical efficiency can be assumed constant and can be taken out of the integral. One can then solve for $\eta_{opt}(\nu_0)$ at the band's center frequency ν_0 by equating Eqns. 2.114 and Eqns. 2.115

$$\eta_{opt}(\nu_0) = \frac{\int 2P_{source,v} h\nu d\nu + \int 4P_{source,v} \frac{\Delta}{\eta_{pb}} d\nu}{NEP_{exp}^2(P_{source}, f_{ref}) - \int 2P_{source,v} h\nu F(\nu) O_{\nu} d\nu} \quad (2.117)$$

Chapter 3

Experimental Background

In the following chapter, the required experimental methods for the different measurement types carried out during the course of this thesis are discussed.

Section 3.1 provides an overview of the fabrication paths for three chip types: The MKID-coupled leaky-lens antenna used in chapter 5, the co-planar waveguide (CPW) Fabry-Pérot resonator used in chapter 6 and the microstrip Fabry-Pérot resonator used in chapter 7. The process documents for each chip are provided in Appendix A for detailed information.

Section 3.2 discusses the laboratory setup used for the measurement of terahertz spectra.

Section 3.3 discusses the laboratory setups used for the characterization of antennas, specifically beam patterns and optical efficiency.

Section 3.4 provides detailed information on the multiplexed microwave readout electronics used in all measurements.

3.1 Fabrication

3.1.1 Leaky-Lens Antenna

Figures 3.1a)-e) show images of the fabricated chip. The slot of the leaky-lens antenna is located on a SiN membrane and coupled directly to the shorted end of a hybrid MKID made of an Al center line and NbTiN ground plane as shown in Fig. 3.1c). The images are front- and backside illuminated, clearly showing the membrane border in Fig. 3.1d). In Fig. 3.1e), the transition from hybrid to wide NbTiN section in the MKID is shown, as well as the removal of the SiN below the NbTiN section. A microwave readout line with Al bridges is meandering between the antenna coupled MKID and two blind reference MKIDs (see Fig. 3.1a)). The full chip has a size of $20 \times 20 \text{ mm}^2$.

The stratification for various elements of the leaky-lens antenna chip during processing is shown in Fig. 3.2. Processing occurs both on the device side (containing the antenna and MKID) and the backside of the wafer. For the detailed process flow document, see

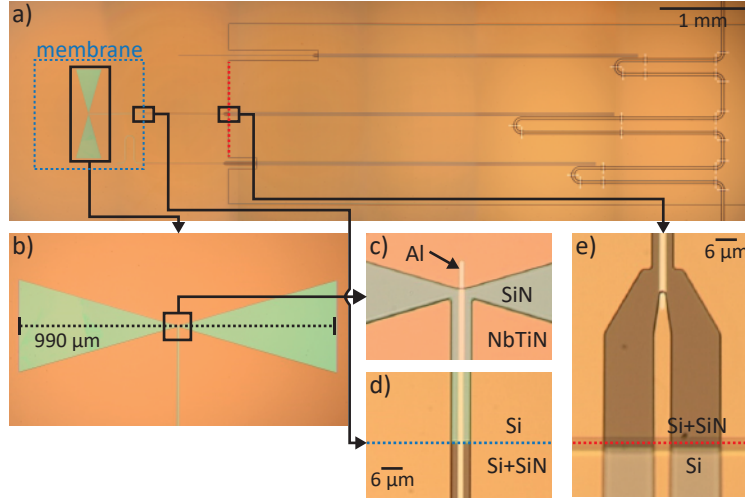


Figure 3.1: (a) Picture of the antenna and MKID area of the chip, taken with front- and backside illumination. The blue dotted line shows the outline of the SiN membrane. Areas marked with black rectangles correspond to Zoom-ins shown in subfigures b), d) and e) as indicated. (b) Zoom-in of the antenna slot. (c) Further zoom-in on the hybrid CPW of the MKID coupling to the antenna slot. The MKID is shorted by the Al center line running on top of the NbTiN ground plane, providing a galvanic connection. (d) Zoom-in of the membrane edge. (e) Zoom-in of the transition between the hybrid and NbTiN sections of the MKID.

Appendix A.1. Unless stated otherwise, all processing was done at the cleanroom of SRON (Netherlands Institute for Space Research) in Utrecht. The major steps shown in Fig. 3.2 are given as follows:

1. The fabrication process starts with a $375\ \mu\text{m}$ thick 4-inch Si wafer (dielectric constant $\epsilon_r = 11.44$) coated on both sides with a $1\ \mu\text{m}$ thick, low tensile stress ($\sim 250\ \text{MPa}$) SiN layer ($\epsilon_r = 7$), deposited using low pressure chemical vapor deposition (LPCVD).
2. The SiN on the front side is etched with reactive ion etching (RIE) using 35 % SF_6 and 65 % O_2 to create a sloped edge.
3. A $350\ \text{nm}$ thick, virtually stress free NbTiN layer is deposited on the front side using reactive sputtering of a NbTi target in a Nitrogen-Argon atmosphere. The process was carried out in a Nordiko 2000 machine in the cleanroom of Kavli Nanolab at the TU Delft [78]. The film has a critical temperature $T_c = 14.9\ \text{K}$ and a resistivity of $\rho_n = 130\ \mu\Omega\text{cm}$.
4. The NbTiN layer is patterned to form the antenna slot, MKID sections and the microwave readout line. It is then etched using the recipe of step 2.
5. A $40\ \text{nm}$ thick layer of β -phase Ta ($T_c \approx 0.6\ \text{K}$) is deposited on the front side.
6. The Ta layer is patterned and etched to form an absorbing mesh.

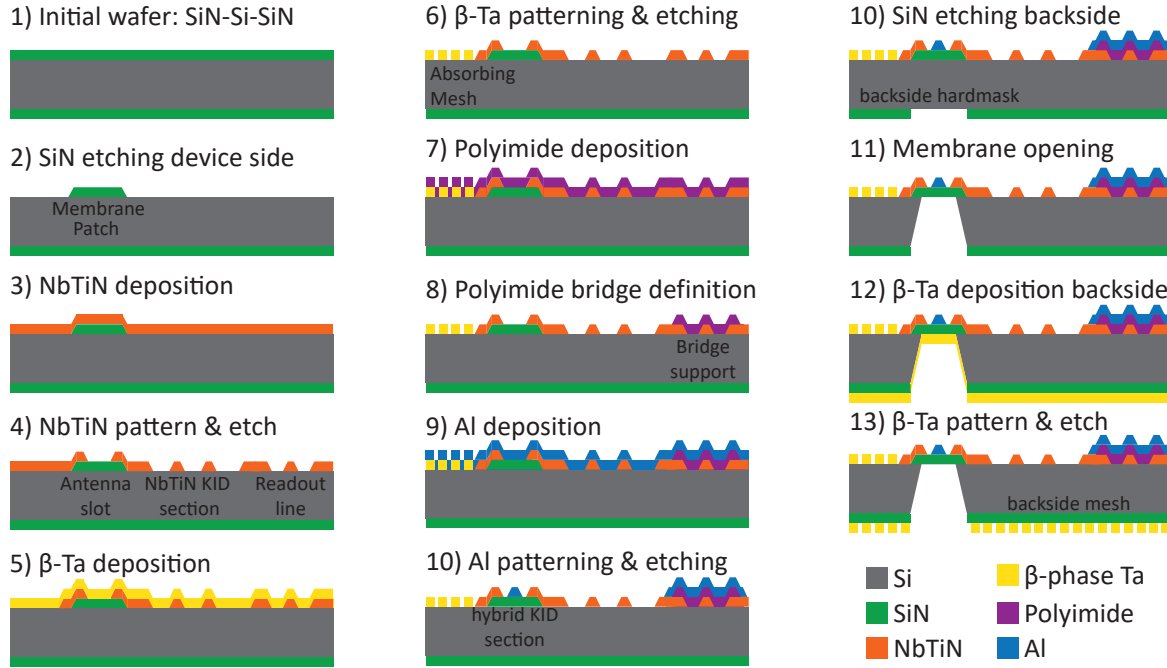


Figure 3.2: Stratification of the leaky-lens antenna chip at each step of the fabrication process. The cross-section shows various important structures, from left to right: The β -Ta absorbing mesh, the SiN membrane with the antenna and the hybrid MKID section, the wide NbTiN MKID section and the microwave readout line with Al-Polyimide bridges.

7. A 1 μm thick layer of polyimide LTC9505 is spin coated on the wafer.
8. The polyimide layer is patterned and cured into dielectric supports for the bridges along the microwave readout line.
9. A 50 nm thick layer of Al ($T_c = 1.25\text{ K}$) is deposited.
10. The Al layer is patterned to form the hybrid MKID center line and bridges along the microwave readout line. The layer is wet etched using TechniEtch Al80 Al etchant (*Microchemicals GmbH*).
11. The backside SiN is patterned and etched to create a hard mask for the Si removal in the next step.
12. The Si wafer is etched in a KOH bath to create the membrane opening from the backside. The front side is protected with a commercial protection tool.
13. A 40 nm thick layer of β -phase Ta is deposited on the backside analogous to step 5.
14. The Ta layer on the backside is patterned and etched analogous to step 6.

The leaky-lens antenna requires a $14\text{ }\mu\text{m}$ small gap between the planar antenna slot and the silicon of the lens on top of the slot. This is realized using a separate, $350\text{ }\mu\text{m}$ thick Si wafer as a spacer. This wafer is coated with $1\text{ }\mu\text{m}$ thick, LPCVD deposited SiN on both sides. The SiN is patterned and etched to create a hard mask, followed by a short, $14\text{ }\mu\text{m}$ deep KOH etch to create the required gap depth at the antenna location.

The device chip, containing the antenna and MKIDs, is placed in a gold-plated copper holder, where it is fixated with small copper clamps pressing on the sides of the chip. Then the spacer wafer and lens are mounted using a procedure described in chapter 5. Finally, Al wire bonds are used to connect the microwave readout line to a PCB circuit board on the holder which ends in an SMA-connector.

3.1.2 Co-Planar Waveguide Fabry-Pérot

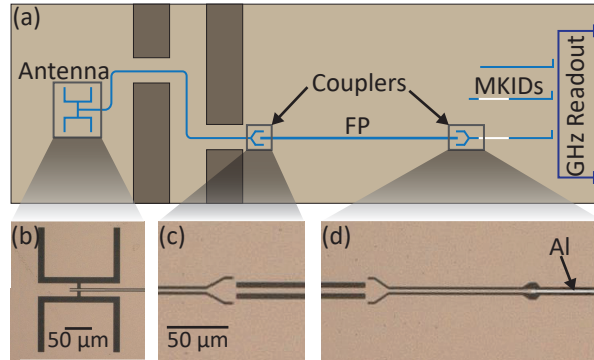


Figure 3.3: (a) Image of the chip center with the tapered antenna slot to the left and the MKID running along the center, coupled to the readout line at the right side. Additional blind MKIDs are located on the top and bottom. (b) The leaky wave slot of the antenna on the SiN membrane. (c) Coupling structure to the narrow section of the MKID. The Al center line is shorted via a galvanic connection to the NbTiN ground plane. (d) Narrow MKID section at the membrane edge, marked by the dashed blue line. The $1\text{ }\mu\text{m}$ thick SiN membrane is transparent and therefore appears slightly blue in the back and front illuminated picture. Below the dashed line, the MKID continues on the SiN layer with Si substrate below. (e) The transition between narrow and wide section of the MKID.

A schematic of the CPW Fabry-Pérot(FP) chip used in chapter 6 is shown in Fig. 3.3a). In this design, a NbTiN CPW FP resonator terminates in two identical coupling structures shown in Figs. 3.3c)-d). One side connects to a double-slot antenna (see Fig. 3.3b), while the other end is connected to the Al-NbTiN section of a quarter-wave hybrid MKID (see section 2.5). The FP-coupled MKID, as well as three other blind resonators, are connected to a CPW microwave readout line with Al/Polyimide bridges to balance the CPW ground planes. The chip section containing the MKIDs is separated from the antenna by a labyrinth to reduce incoming stray light. A Ta-mesh on the chips backside further reduces stray light to the detectors. The full chip has a size of $42 \times 14\text{ mm}^2$. This chip is fabricated on a Sapphire substrate instead of Silicon as it was based on previous chip and MKID designs.

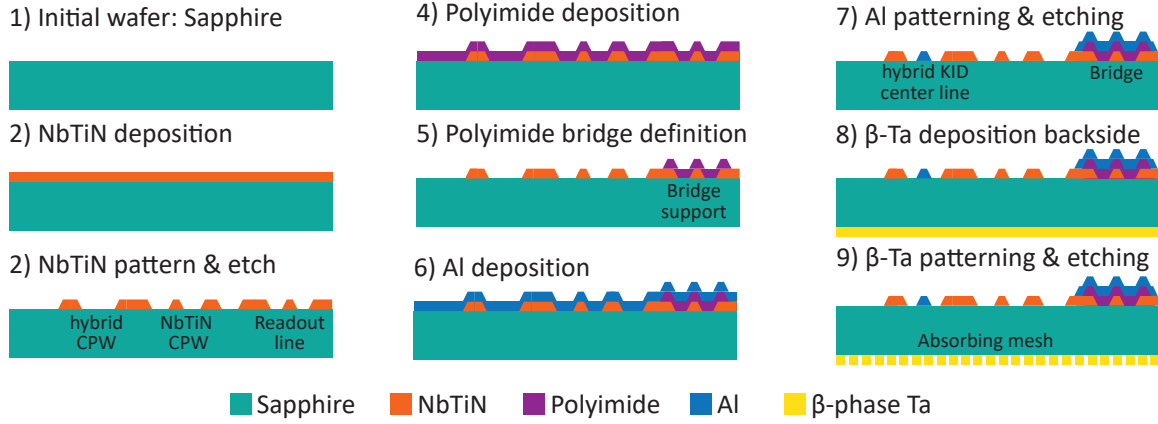


Figure 3.4: Stratification of the co-planar waveguide Fabry-Pérot resonator chip (used in chapter 6) at each step of the fabrication process. The cross-section shows various structures relevant to processing, from left to right: The hybrid MKID section, the wide NbTiN MKID section and the microwave readout line with Al-Polyimide bridges.

The stratification for various elements of this chip during processing is shown in Fig. 3.2 analogous to section 3.1.1. For the detailed process flow document, see Appendix A.2. The major steps, as shown in Fig. 3.4 are given as follows:

1. The fabrication process starts with a 350 μm C-plane Sapphire wafer ($\epsilon_r^C = 11.5$, $\epsilon_r^{AB} = 9.3$).
2. A 100 nm thick NbTiN layer ($T_c = 14.7$ K, $\rho_n = 102 \mu\Omega \text{ cm}$) is deposited on the front side using reactive sputtering of a NbTi target in a Nitrogen-Argon atmosphere. The process was carried out in a Evatec LLS801 machine in the cleanroom cleanroom of SRON in Utrecht using the static deposition method as detailed by Thoen et al. [78].
3. The NbTiN layer is patterned to form the antenna slot, the Fabry-Pérot resonator line, MKID sections and the microwave readout line. It is then etched with reactive ion etching (RIE) using 35 % SF_6 and 65 % O_2 to create a sloped edge.
4. A 1 μm thick layer of polyimide LTC9505 is spin coated on the wafer.
5. The polyimide layer is patterned and cured into dielectric supports for the bridges along the microwave readout line.
6. A 40 nm thick layer of Al ($T_c = 1.28$ K) is deposited.
7. The Al layer is patterned to form the hybrid MKID center line and bridges along the microwave readout line. The layer is wet etched using TechniEtch Al80 Al etchant (*Microchemicals GmbH*).
8. A 40 nm thick layer of β -phase Ta ($T_c \approx 0.6$ K) is deposited on the backside.

9. The Ta layer on the backside is patterned and etched to create an absorbing mesh.

The finished chip is mounted in a gold-plated copper holder, where it is fixated with small copper clamps pressing on the sides of the chip. An 8 mm diameter Si lens is aligned using a microscope based, homemade tool and then glued to the backside of the chip using Loctite 406 cyanoacrylate glue. Markers are located in backside Ta-layer to aid with alignment. Al wire bonds are then used to connect the microwave readout line to a PCB circuit board on the holder which ends in an SMA-connector.

3.1.3 Microstrip Fabry-Pérot

This chips concept is based on that of the CPW-FP chip shown in Fig. 3.3a), exchanging the CPW-FP resonator for a microstrip FP resonator, while keeping everything else as CPW. For a more detailed schematic see Fig. 7.1 in chapter 7. Microstrip structures are made of NbTiN/a-Si/NbTiN, where the lower NbTiN layer contains the CPW elements of the chip.

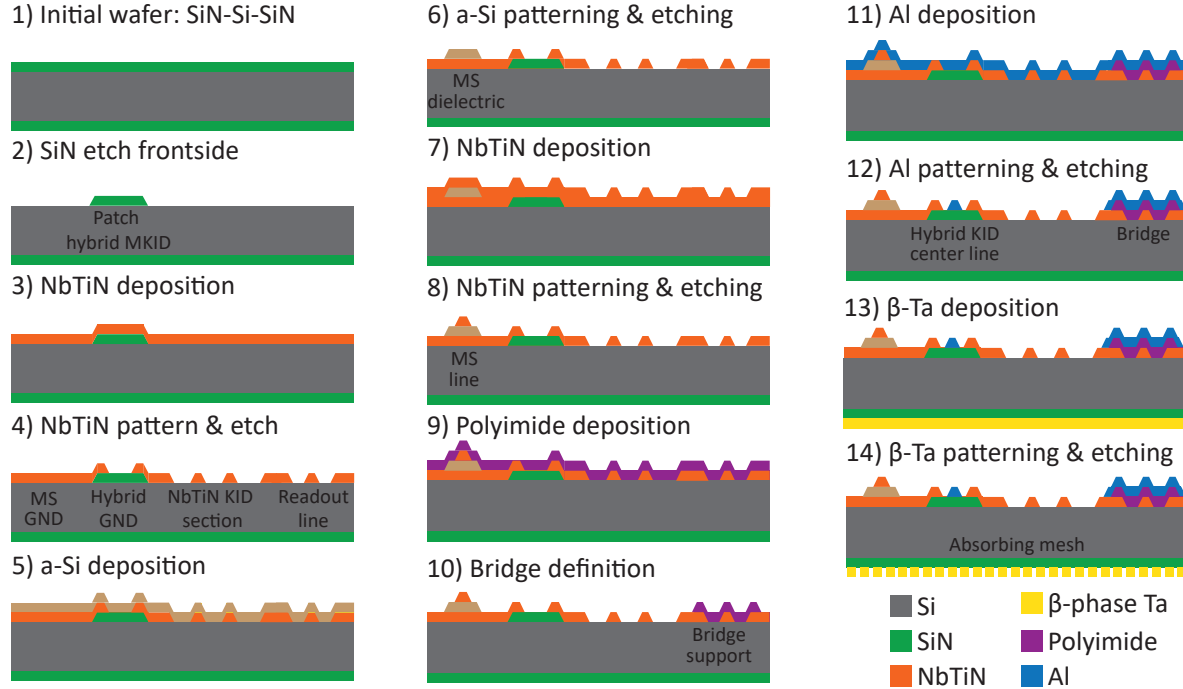


Figure 3.5: Stratification of the microstrip Fabry-Pérot resonator chip (used in chapter 6) at each step of the fabrication process. The cross-section shows various structures relevant to processing, from left to right: The microstrip structures, The hybrid MKID section, the wide NbTiN MKID section and the microwave readout line with Al-Polyimide bridges.

The stratification for various elements of this chip during processing is shown in Fig. 3.2 analogous to section 3.1.1. For the detailed process flow document, see Appendix A.3. The major steps, as shown in Fig. 3.5 are given as follows:

1. The fabrication process starts with a 375 μm thick 4-inch Si wafer (dielectric constant $\epsilon_r = 11.44$) coated on both sides with a 1 μm thick, low tensile stress (~ 250 MPa) SiN layer ($\epsilon_r = 7$), deposited using low pressure chemical vapor deposition (LPCVD).
2. The SiN on the front side is etched with reactive ion etching (RIE) using 35 % SF_6 and 65 % O_2 to create a sloped edge.
3. A 220 nm thick NbTiN layer ($T_c = 14.7$ K, $\rho_n = 102 \mu\Omega \text{ cm}$) is deposited on the front side using reactive sputtering of a NbTi target in a Nitrogen-Argon atmosphere. The process was carried out in a Evatec LLS801 machine in the cleanroom of SRON in Utrecht using the static deposition method as detailed by Thoen et al. [78].
4. The NbTiN layer is patterned to form the antenna slot, the Fabry-Pérot resonator line, MKID sections and the microwave readout line. It is then etched using the same recipe as step 2.
5. A 250 nm thick a-Si layer $\epsilon_r \approx 10$. is deposited using plasma enhanced chemical vapor deposition (PECVD). This process was carried out in the cleanroom of the KAVLI institute at the TU Delft.
6. The a-Si layer is patterned and etched, defining the dielectric layer of the microstrip using the same recipe as step 2. As the process is not selective against NbTiN, the lower NbTiN will experience overetch in places where a-Si is removed. This is accounted for in the chosen NbTiN layer thickness during the design process.
7. A second NbTiN layer of 100 nm is deposited using the same process as step 3.
8. The NbTiN layer is patterned and etched to form the microstrip line using the same process as step 2. Overetch will occur analogous to step 6, which is also accounted for during the design process.
9. A 1 μm thick layer of polyimide LTC9505 is spin coated on the wafer.
10. The polyimide layer is patterned and cured into dielectric supports for the bridges along the microwave readout line.
11. A 50 nm thick layer of Al ($T_c = 1.28$ K) is deposited.
12. The Al layer is patterned to form the hybrid MKID center line and bridges along the microwave readout line. The layer is wet etched using TechniEtch Al80 Al etchant (*Microchemicals GmbH*).
13. A 40 nm thick layer of β -phase Ta ($T_c \approx 0.6$ K) is deposited on the backside.
14. The Ta layer on the backside is patterned and etched to create an absorbing mesh

The final chip is then mounted in the holder using the procedure for the CPW Fabry-Pérot given in section 3.1.2, only exchanging the single lens for a 2x2 Si lens-array with 2 mm lens-diameter

3.2 Terahertz Spectrum Measurement

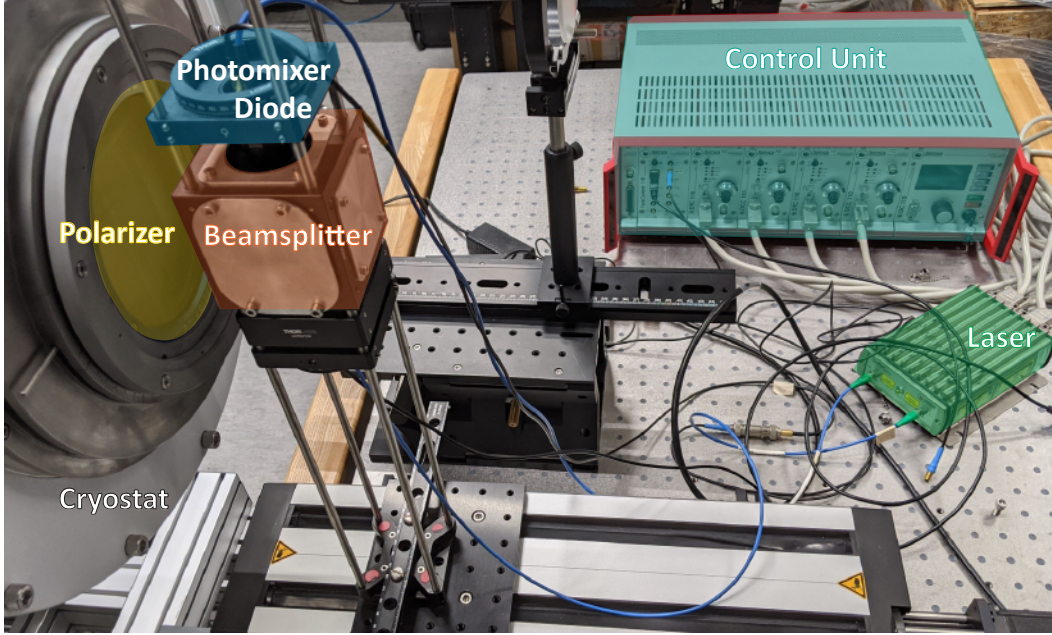


Figure 3.6: Picture of the room temperature setup for terahertz spectrum measurements, showing the arrangement of the photomixer diode (*blue*), beamsplitter (*red*) and the polarizer (*yellow*) mounted on the cryostat window. Also shown are the two lasers (*green*) and the control electronics (*turquoise*) for both the lasers and photomixer diode. The control unit is accessed remotely via a PC.

Transmission spectra of superconducting transmission line Fabry-Pérot resonators (FPR) in this thesis are measured using the setup shown in Fig. 3.6. A chip containing a lens-antenna, FPR and MKID detector(s) is placed on the cold stage of a cryostat, where both FPR and MKIDs are at $T \leq T_c/10$. At room temperature, a frequency-tunable terahertz source is located, which is coupled to the FPR via windows in the cryostat and the lens-antenna on the chip. In the experiment, the frequency of the THz source is changed in discrete steps and the response of the MKID is measured for each individual frequency. Repeating this for a linear frequency sweep gives the spectral response. The separate components of this experiment are given as follows.

Cryostat

Two different cryostats were used during the experiments. A dilution refrigerator operated at a base temperature of $T_b = 120$ mK and a He³/He⁴ sorption cooler with $T_b = 240$ mK. The design of the optical access, which was used in both cryostats, is described in detail in chapter 4. For the measurements in chapters 6 and 7, a frequency band around 350 GHz with > 20 dB out-of-band suppression is defined.

Terahertz Source

For this thesis, a commercial photomixer continuous wave (CW) source was used (TERABEAM 1550 *TOPTICA Photonics AG*). The source provides a linear polarized, single frequency signal that is tunable between $f_{thz} = 0.1 - 1.2$ THz with a minimum step size of ~ 10 MHz and an absolute frequency accuracy of < 2 GHz. A beam splitter is placed in front of the source, attenuating the signal by $\sim 95\%$ to avoid saturation of the MKIDs.

Data Analysis

During measurements, the amplitude of CW source is electrically modulated with a modulation frequency of $f_{mod} = 11.92$ Hz, providing a roughly sinusoidal signal

$$P_{source} = P_{max}(f_{thz}) \sin^2(2\pi f_{mod}t) \quad (3.1)$$

where P_{max} is the maximum output power at the set signal frequency f_{thz} .

At each frequency step, the MKID response is measured for $t = 1$ s at a sampling rate of $f_{sample} \approx 159$ Hz, resulting in time-ordered data (TOD) as shown in Fig. 3.7a). The response X (where X can be phase, amplitude or frequency response) is proportional to the source power as

$$X_{f_{thz}}(t) \propto \eta(f_{thz}) P_{source} \frac{dX}{dP} \quad (3.2)$$

where $\eta(f_{thz})$ is a generalized frequency dependent efficiency describing the path between the source and detector, and $\frac{d\theta}{dP}$ is the responsivity of the detector as given in chapter 2.5.1. The spectrum of the device under investigation (i.e. the Fabry-Pérot resonator) is contained within $\eta(f_{thz})$.

The TOD data of the full frequency sweep is then analysed using a Python script. For each frequency step, a fast fourier transform (FFT) is performed to obtain the response in the frequency domain

$$\hat{X}_{f_{thz}}(f) = \mathcal{F}(X_{f_{thz}}(t)), \quad (3.3)$$

resulting in a spectrum as shown in Fig. 3.7. The response at the frequency bin corresponding to f_{thz} then corresponds to the signal strength at the measured terahertz frequency

$$X(f_{thz}) = \hat{X}(f_{mod}). \quad (3.4)$$

Combining $X(f_{thz})$ of all measured frequency steps then provides the full spectrum as shown in Fig. 3.7.

3.3 Antenna Characterization

3.3.1 Beam Pattern Measurement

Beam pattern measurements were carried out in the Cryolab in the EKL (Else Kooi Lab) at the TU Delft using the setup shown in Fig. 3.8. The cryogenic setup is identical to that of

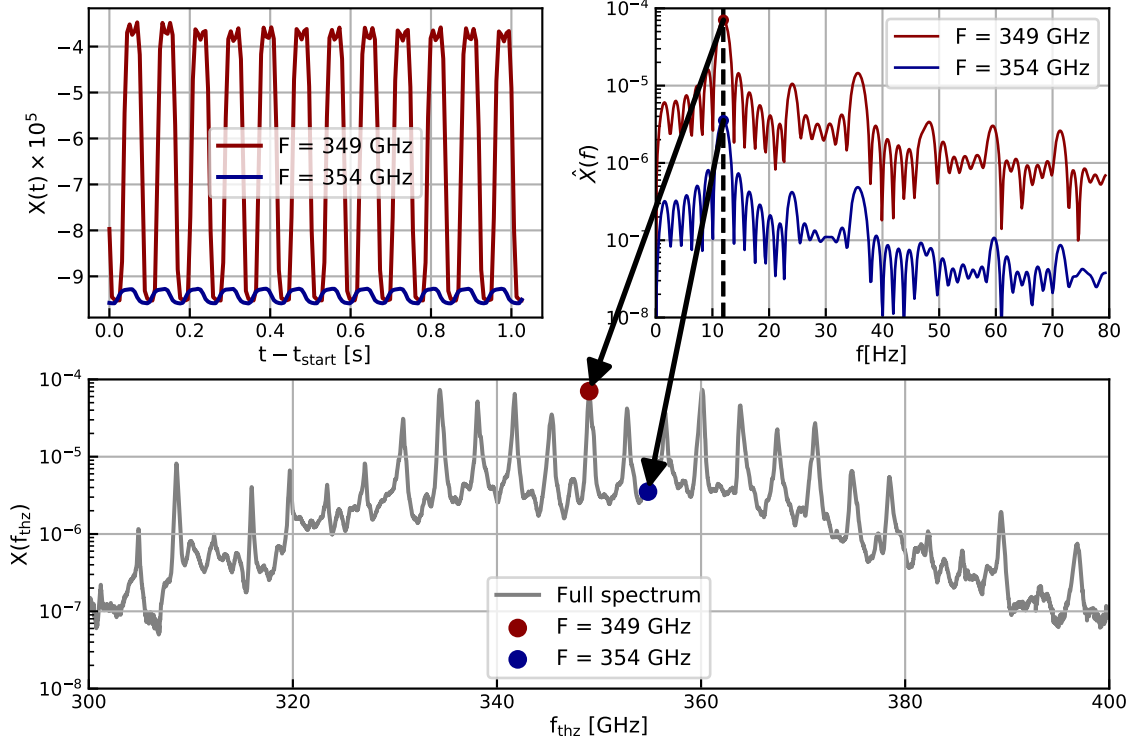


Figure 3.7: (a) Time domain data for a Fabry-Pérot resonator measured at two different terahertz frequencies $f_{\text{thz}} = 349 \text{ GHz}$ (on-peak of the Fabry-Pérot resonator) and $f_{\text{thz}} = 354 \text{ GHz}$ (off-peak of the Fabry-Pérot resonator). (b) Frequency domain data of the data shown in subfigure a) using eq. 3.3. The modulation frequency f_{mod} is shown by the dotted line. (c) Response as function of f_{thz} . The Full spectrum of the measured device is shown by black line. The values at the frequencies shown in subfigures a) and b) are highlighted by the red and blue dot.

the terahertz spectrum measurements (using the He^3/He^4 sorption cooler), while exchanging the photomixer source with a hot source (Scitec Hawkeye IR-19 glowbar operated at $T \approx 1150 \text{ K}$) which is mounted on an XYZ-scanner at room temperature. Blackened plates are used to avoid reflections interfering with the measurement. Three different frequency bands with center frequencies around 350 GHz, 650 GHz and 850 GHz can be measured by changing the filterstack located in the cryostat. The full source assembly is located on a movable optical table, which can be easily exchanged for a separate table containing a different measurement setup.

A beam pattern is obtained by stepping the source through the antennas field of view in a 2D plane, measuring the detector response at each position. Data analysis is then carried out analogous to the terahertz spectrum experiment, but using a mechanical chopper to modulate the signal at $f_{\text{mod}} = 254 \text{ Hz}$, as electronic modulation of the hot source is not feasible.

A complete discussion of the setup during the characterization of the leaky-lens antenna is given in chapter 5. The design of the optical access for the cryostat was carried out as part of this thesis and details on it and the cryostat are given in chapter 4.

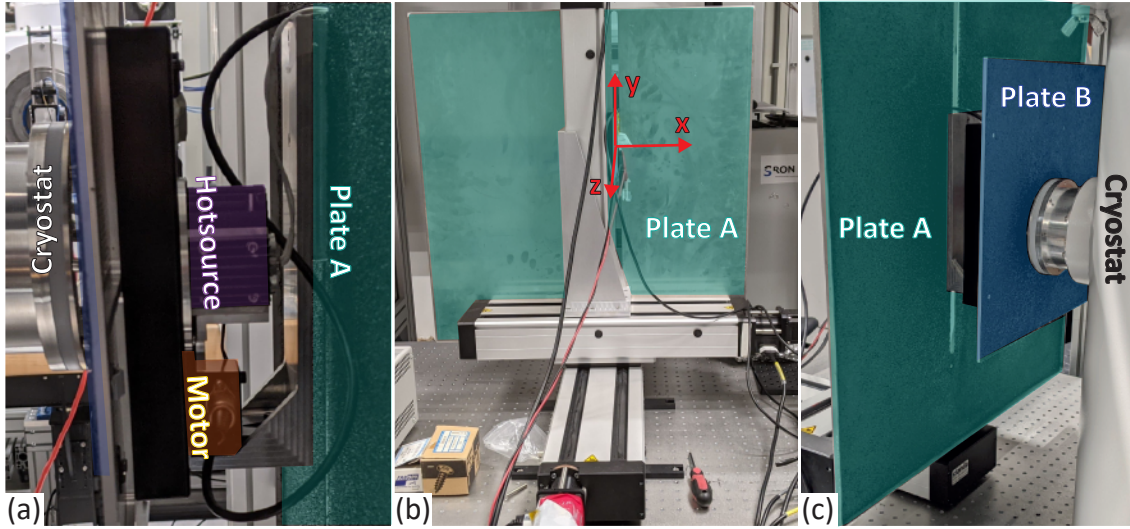


Figure 3.8: (a) Close-up picture of the source assembly, showing the chopper motor (*orange*) and the glowbars casing *purple*. Also indicated is the location of the large blackened plate - Plate A (*turquoise*). (b) Wide-angle picture of the source-scanner assembly backside. The axes of the scanner are indicated with red arrows, and the backside of the large blackened plate - plate A - in *turquoise*. (c) Wide-angle picture of the source-scanner assembly frontside, highlighting the two blackened plates - plate A (*turquoise*) and plate B (*blue*).

3.3.2 Optical Efficiency Measurement

Optical efficiency measurements for the leaky-lens antenna (see chapter 5) were carried out at SRON (Netherlands Institute for Space Research) in Utrecht. The cryogenic setup, shown in Fig. 3.9, was previously used for measurements at frequency bands around 1.54 THz [79], 350 GHz [36] and 850 GHz [75]. For this thesis, the setup was kept identical to these experiments, with the addition of a filterstack centered at 650 GHz, resulting in the three measurement bands shown in Fig. 3.9.

In this experiment, the optical efficiency is obtained via a measurement of the detector's noise equivalent power (NEP) as shown in section 2.6. This method requires a well defined power source with negligible stray light contributions. To this end, the device chip is placed in a box-in-box setup on the cold stage of the adiabatic demagnetisation refrigerator (ADR) at 120 mK as shown in Fig. 3.9, shielding the device from the black-body emission of the cryostats 3K-stage. A small aperture is then opened in the box towards a black-body source which is tunable between 3–40 K using a resistive heater. A well-defined filter stack between the source and the device chip then selects a single frequency band, resulting in a well known source power after filter transmission, given by Eq. 2.112.

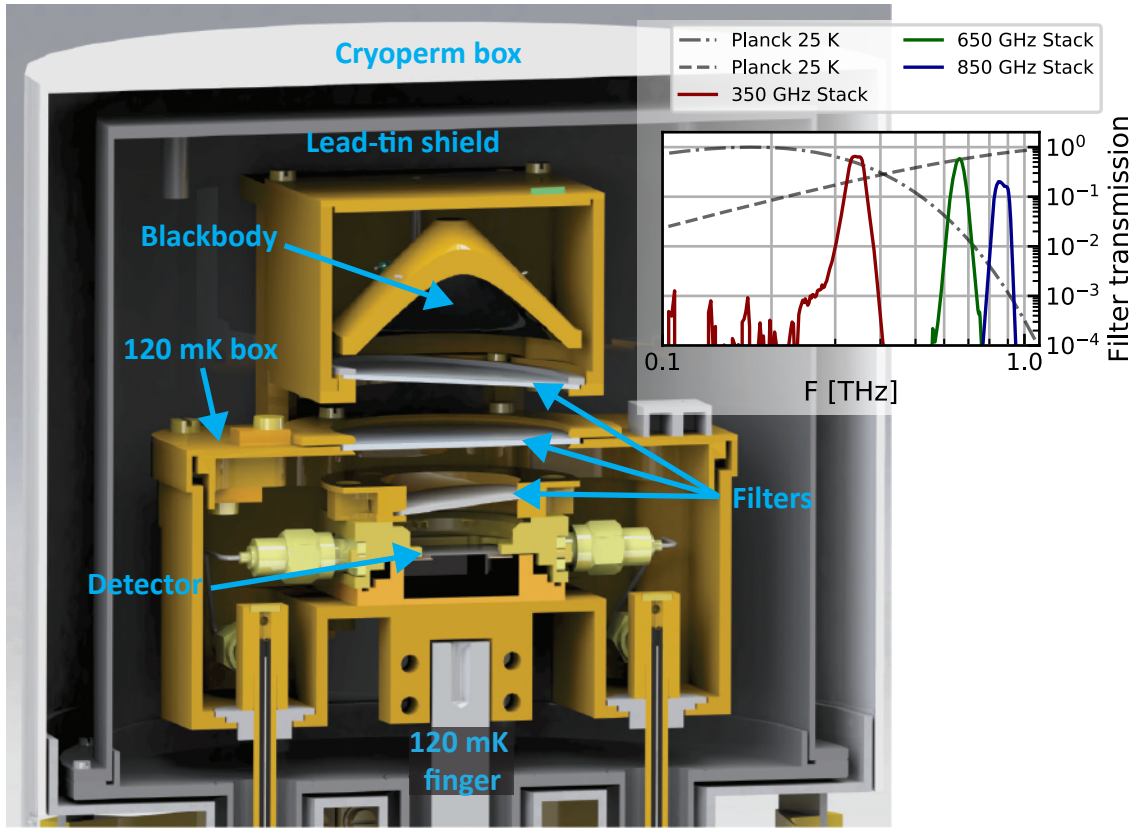


Figure 3.9: Schematic cross-section showing the cold stage of the cryogenic setup used for optical efficiency measurements. The detector is located on the 120 mK finger and surrounded by a 120 mK box, reducing emissions. A blackbody can be heated with a PID-controlled resistive heater, to obtain temperatures between 3 – 40 K. Multiple low- and bandpass filters, located between blackbody and detector, define the desired frequency band. (Inset) The Inset shows the filter transmission for the three used filter stacks with solid lines (350 GHz, 650 GHz, 850 GHz), as well as the normalized spectral brightness of the blackbody source at 3 K and 25 K with dashed lines. (Figure after [65])

3.4 Readout Electronics

The microwave response of the MKIDs is measured using a microwave setup as shown in Fig. 3.10, containing electronics at room temperature and in the cryostat. Frequency domain multiplexing (MUX) is implemented using the SPACEKIDS readout system [80] controlled by a PC running Linux.

In the DAC board, a complex IQ signal is generated using 2 separate DACs, each at 2 Gsample/sec (see 3.1). After passing through a low-pass filter, the IQ components are mixed in an IQ-mixer with a local oscillator (LO) signal as reference, which is also generated in the SPACEKIDS electronics. In this step the 2 DAC outputs are added in I and Q such that they create a -1 to $+1$ GHz signal band around the LO frequency. This signal can contain up to 4000 tones at discrete frequencies at multiples of 3.8 kHz, where the magnitude of each tone can be adjusted separately. The LO is tunable between

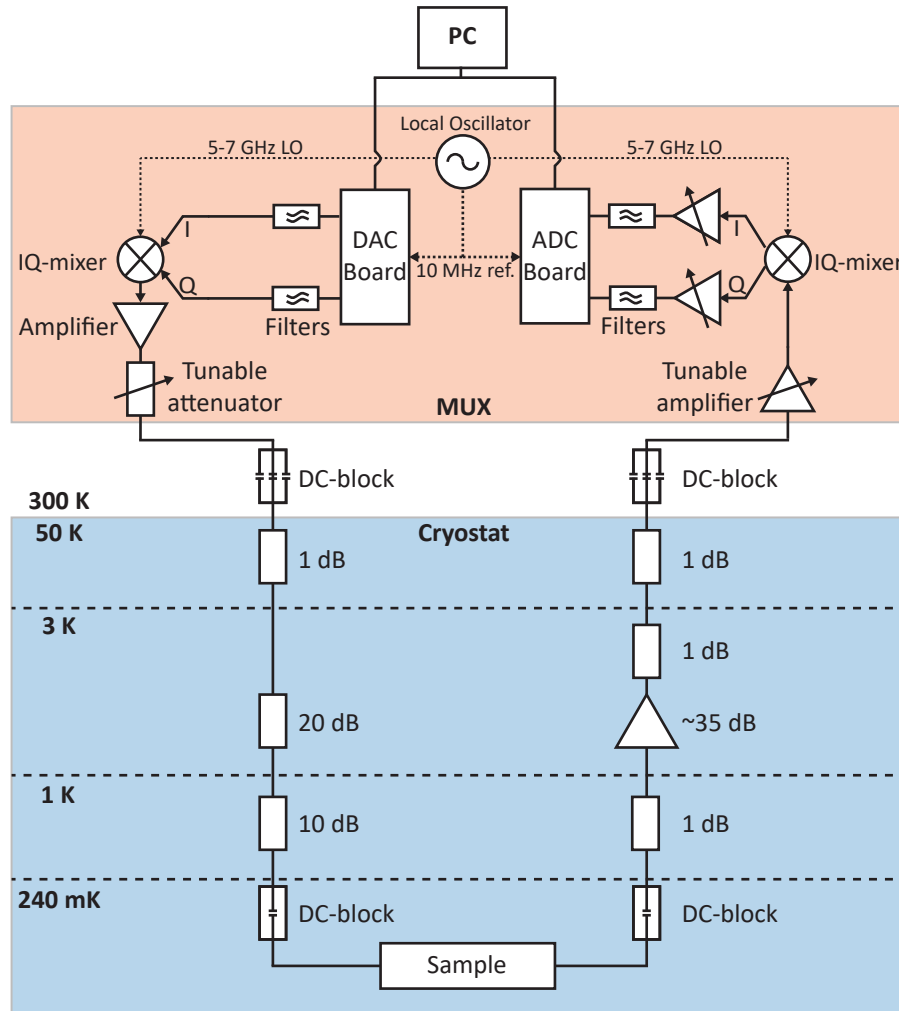


Figure 3.10: Schematic of the microwave readout electronics. The red box highlights the components in the SPACEKIDS system, while the blue box highlights cryogenic components

5 – 7 GHz, resulting in a readout frequency (RF) signal of 2 GHz bandwidth anywhere in the range of 4 – 8 GHz. The signal is then amplified and subsequently attenuated to obtain the desired output power. The microwave signal is then fed to the cryostat through flexible SMA cables and via a DC block, which separates the ground of the cryostat from the room temperature electronics.

In the cryostat, the signal is attenuated by 20 dB at the 3K stage and 10 dB at the 1K stage, to reduce Johnson-Nyquist (thermal) noise from the previous stages. Additional 1 dB attenuators are placed at the other stages to thermalize the cables. From 300 K to the 3K stage CuNi coax cables are used, with superconducting NbTi cables from the 3K stage down to the cold stage to avoid signal losses. At the cold stage, a DC block is used to interrupt the galvanic connection to the sample before the signal is fed to the sample. Total attenuation between the MUX and the sample including cable loss is ~ 38 dB.

	DAC	ADC
Model	AD9129	EV10AQ190
Manufacturer	Analog Devices	E2V
Resolution	14 bits	10 bits
Sample rate	2 GS/s	2 GS/s
Effective number of bits	-	7.9 bits
SNR (max sine wave)	-	49 dB
Noise spectral density (n=1)	-165 dBc/Hz	-142 dBc/Hz
Noise spectral density (n=1000)	-121 dBc/Hz	-98 dBc/Hz

Table 3.1: DAC and ADC specifications. (After [80])

The output signal is amplified with a low-noise high-electron-mobility transistor (HEMT) amplifier mounted on the 3K stage with a noise temperature of 5 – 6 K and an amplification of ~ 35 dB (Y214G-1012 *Observatorio de Yebes*). Attenuators and DC-blocks are used analogous to the input path to thermalize the cables. At 300K, the signal is fed back to the MUX electronics.

In the SPACEKIDS input, the signal is amplified by a combination of a tunable attenuator followed by an amplifier, with an additional optional amplifier which can be switched in front of the attenuator if the input signal is too weak. This combination is referred to as a tunable amplifier in Fig. 3.10. Following amplification, an IQ mixer with the LO reference signal is used to downconvert back to a complex IQ signal in the IF band. The I and Q signals are amplified and filtered before they are passed into the DAC board. Here, the signal is digitalized and an FPGA-implemented Fast-Fourier Transform (FFT) is used to generate the final data frames which are sent to the PC. Frames contain the complex transmission data as function of frequency and can be generated with 2^{19} bins at 159 Hz or 2^{16} bins at 1272 Hz.

Figure 3.11 shows the system noise per readout tone as a function of the total number of tones n_{tones} . The noise due to the MUX electronics is dominated by the ADC (see table 3.1) and scales with the number of tones as [80]

$$S_{MUX} = -142 \text{ dBc/Hz} + 10 \log(n_{tones}) + 14 \text{ dB} \quad (3.5)$$

assuming a crest factor of 14 dB. The noise contribution of the LNA is given by

$$S_{LNA} = \frac{k_B T}{P_{tone}} \quad (3.6)$$

where $T \approx 6$ K is the LNA noise temperature and P_{tone} is the tone power at the LNA. In the context of this thesis the system noise is dominated by the LNA, as measurements were carried out with a small number of tones $n_{tones} < 50$ and high power $P_{tone} \approx 80 - 60$ decibel. It should be noted, that the noise spectra given here is with respect to the complex plane. In order to obtain the KID noise, the PSD is divided by $(1 - S_{21,min})/2$ (compare 2.108).

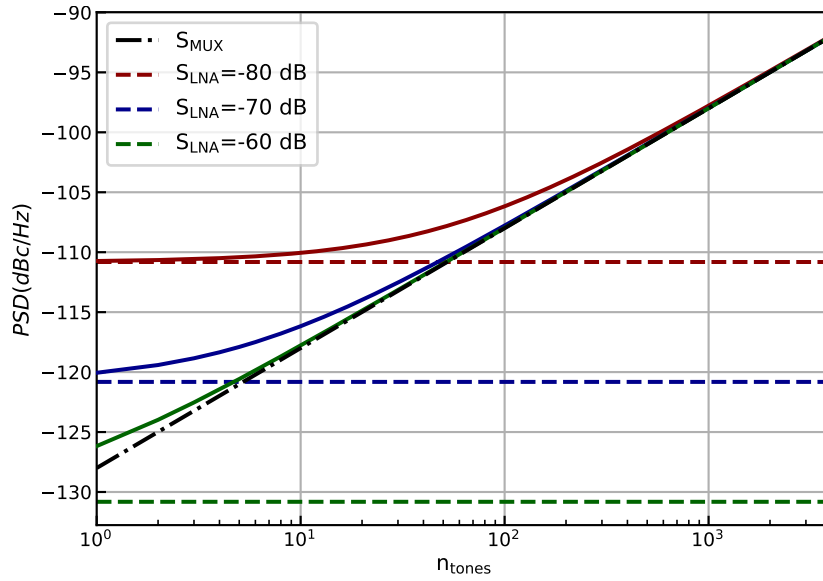


Figure 3.11: System noise as function of number of readout tone n_{tones} . The dashed-dotted black line shows the contribution of the MUX, S_{MUX} . The dashed colored lines show the contribution of the LNA, S_{LNA} , for different tone powers. The solid colored lines show the total system noise, with colors corresponding to those of the dashed lines.

Chapter 4

Large Angle Optical Access in a sub-Kelvin Cryostat

4.1 Introduction

Microwave Kinetic Inductance Detectors (MKIDs) [81] become an increasingly attractive option for large scale imaging instruments [19]. An interesting alternative to lumped element MKIDs [82] are lens-antenna coupled MKIDs [83], which couple radiation using a coherent beam formed by the lens-antenna system. The advantage is that they are sensitive to radiation over a limited angular throughput given by the lens-antenna design. Thereby they reject large angle radiation, which allows the use of a higher temperature optics and Lyot-stop. This results in cryogenically simple camera designs [84].

Imaging arrays of antenna coupled MKIDs have fast beams to reduce the chip area for a given field of view: Fast optics result in a spatially small airy pattern, smaller pixels and smaller arrays. A fast beam is characterized by a small beam waist radius and a large far field opening angle. The beam width of these antennas at the -10 dB taper is typically in the order of $\pm 20^\circ$, which makes measurements of the antennas full beam pattern, including side lobes, challenging to implement. However, it is critical to measure the beam shape to fully understand the detector performance [75]. In this paper we present a cryostat that is designed to enable large angular throughput beam pattern measurements for antenna coupled MKIDs. It fulfills the following requirements:

- Sub-millimeter(sub-mm) wave access from the laboratory through a window with a large opening angle to the detector.
- No reimaging optics in order to measure the unperturbed beam pattern.
- Optical access to the detector over a spectral passband of up to 1 THz.
- Fast cooldown speed of the cryostat and easy assembly process motivated by the fast turnaround speed (1-2 days) necessary for an efficient iterative antenna development.
- The cold stage temperature of less than 270 mK for operation of the detectors.

4.2 System Overview

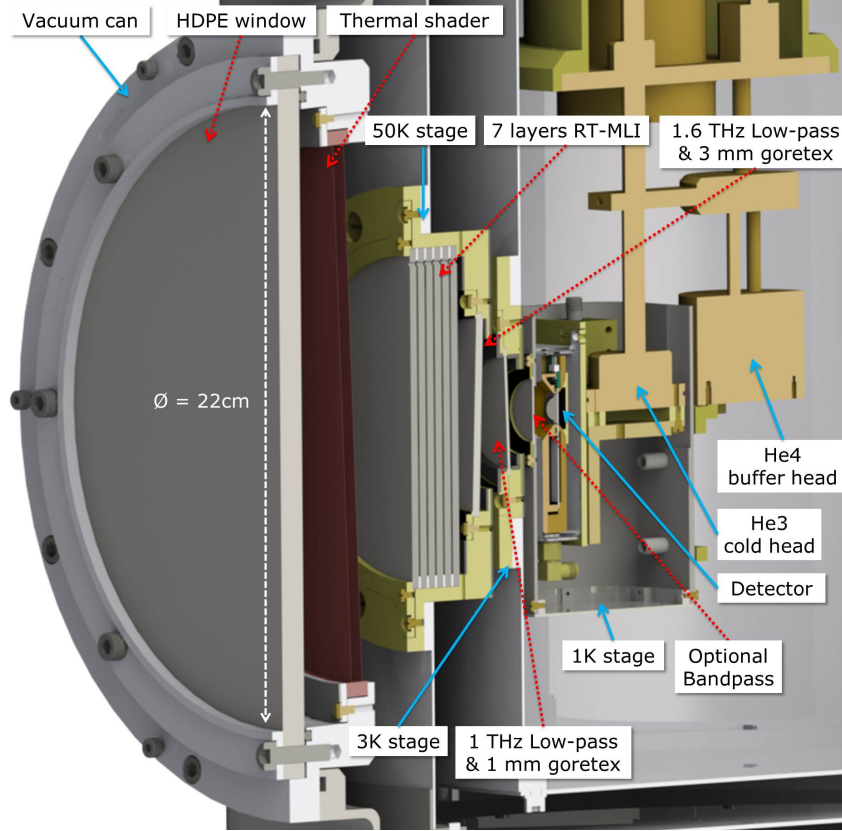


Figure 4.1: Cross section of the cryostat's optical access, showing all windows including the filters. A 1 cm thick polyethylene window in the vacuum can is air-tight but transparent in the sub-mm regime. In addition, a single thermal shader is mounted directly behind the vacuum window. The apertures in the 50K and 3K radiation shields are made of gold-plated copper and serve as mounting point for the filterstack: 7 layers of RT-MLI on the outer side of the 50K window, as well as reflective metal-mesh filters on both the 50K and 3K window. The latter are oriented at angles with respect to each other and the detector to avoid standing waves. Both the 1K radiation shield and the detector assembly are located in tight proximity to the 3K window, with the 1K shield mounted on the ^4He buffer head and the detector assembly directly on the ^3He cold head. The 1K shield is aluminum and serves as an optional mounting point for additional filter. A cryophy magnetic shield is integrated in the detector assembly. (Color figure online.)

A cross section of the optical access for the cryostat is shown in Fig. 4.2. The cryogenic system consists of standard commercially available components. A pulse-tube cooled cryostat (BlueFors Cryogenics) provides 0.9 W cooling power at 4.2 K, where a sorption cooler (*CRC-7B-002*, Chase Research Cryogenics) is mounted that can reach temperatures down to 240 mK. The sorption cooler is a two-stage, single shot system consisting of a ^3He cold head as the mounting point for experiments and a ^4He buffer head.

The windows are in a cone-like configuration, providing a half opening angle of $\theta = 37.8^\circ$

to the center of a detector chip mounted on the cold stage of the sorption cooler. The design of the geometry of these apertures is critical to the cooler performance and will be discussed in detail in the next section. Access to the cold stage is possible by removing only the vacuum can and heat shields, which allows for fast and efficient operation of the system.

The detector assembly mounted on the cold stage can hold different chip dimensions although only an area of (10x10) mm² is optically accessibly. Connection to room temperature electronics to read-out the MKIDs is provided by means of a single pair of semi-rigid coax cables. From room temperature to the 3K stage, 2.19 mm diameter CuNi coax cables are used, while 0.86 mm diameter and 15 mm long NbTi cables (COAX CO., LTD.) provide a lossless connection from 3K to the detector on the cold stage. The thermal load on the cold stage due to the coax cables is only 16 nW, which is negligible compared to radiative loading from the optical access. The readout signal is amplified at the 3K stage using a commercial low noise amplifier [85].

Stage	T [K]	P_{cool}	$P_{l,r,calc}$	$P_{l,c,calc}$	$P_{l,meas}$
50K (PT)	39.5	31.5 W @ 45 K	17 W	-	-
3K (PT)	2.85	0.9 W @ 4.2 K	217 μ W	-	-
1K (⁴ He)	0.81	250 μ W @ 0.85 K	9.3 μ W	0.6 μ W	<50 μ W
sub-K (³ He)	0.265	1 μ W @ 240 mK	4.4 μ W	16 nW	6.0 μ W

Table 4.1: Operating temperatures T and cooling power P_{cool} for all stages of the cryostat in addition to the calculated radiative ($P_{l,r,calc}$) and conductive ($P_{l,c,calc}$) thermal loads as well as the measured thermal load ($P_{l,meas}$) from the optical access. The conductive load is dominated by wiring as the high vacuum in the cryostat ($P \approx 10^{-7}..10^{-10}$ mbar) suppresses gas conduction. Pulse-tube stages are denoted with 'PT' while ⁴He and ³He are the sorption coolers buffer and cold head respectively.

We design an infrared passband from 0 to 950 GHz by a combination of commercial metal mesh filters (QMC Instruments Ltd.), gore tex sheets and a RT-MLI infrared blocking assembly [86]. The combination of the optimized geometry and filter stack allows us to reach a loading on the cold stage of 6 μ W, while the total power entering the cryostat window is 17 W. The spectral filtering thus reduces the input power by 40 dB and the geometric baffling by another 30 dB.

The performance of the cryostat exceeds the requirements for operation (see Table 4.2), reaching a base temperature of 265 mK on the ³He cold head for over 32 hours. A full cooldown from room temperature to base temperature takes about 14 hours. In the next section we will discuss the filter design and geometrical design in detail.

4.3 Detailed System Design

4.3.1 Spectral Filtering

The spectral window accessible for measurement in the cryostat is in first order a low-pass with cut off at $f_c \approx 950$ GHz in order to include the atmospheric windows accessible

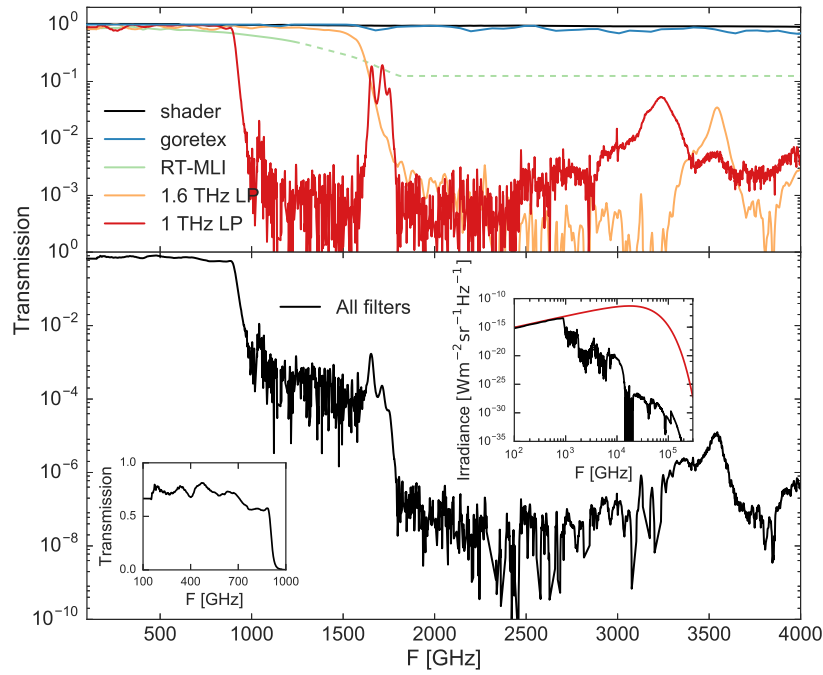


Figure 4.2: The transmission curves of the individual filters are shown in the *top*. At high frequencies, marked by the dotted line, the transmission curve shown for RT-MLI needs to be treated as absorbing material in radiative balance. The *bottom* graph shows the total coherent transmission of the filter stack, which provides rejection better than 10^6 at frequencies above 2 THz. Two inserts show the transmission in the accessible spectral window on a linear scale (*left*) and the reduction of the spectral flux due to the filterstack for a 300 K blackbody (*right*), where the reduction at high frequencies is dominated by the goretex sheets. (Color figure online.)

from high altitude sites such as the Atacama desert [?]. The filter stack in this cryostat consists of four types of filters. A strong focus in the design is to avoid unnecessary filter heating, which has been shown to be a major issue for large filters [87]. The rejection better than 10^6 at high frequencies is necessary to fully suppress the contribution of this regime's blackbody spectrum to the total thermal radiation compared to the power in the band of interest.

The first filter mounted in the cryostat is a thermal shader (QMC Instruments Ltd.) mounted on 300K vacuum can, but which is in radiative balance. It is transparent in-band and reflects power in the near-infrared.

The second filter is the RT-MLI (Radio-Transparent Multi-Layer-Insulation) [86] located at the outward facing side of the 50K window. RT-MLI is a stack of $N = 7$ thin layers of styrofoam, which is transparent up to 1 THz and behaves as a diffusive absorber at higher frequencies. The individual layers of styrofoam have a uniform temperature profile and are in radiative balance, leading to thermal radiation q through the stack that is inversely proportional to the number of layers N plus one:

$$q \propto \frac{1}{N + 1} \quad (4.1)$$

Importantly, the RT-MLI reduces the broad-band infrared loading without relying on conductive cooling of the filters. For our design (see Fig. 4.3.1), the radiative balance of the RT-MLI stack is approximated by setting the minimum transmission at high frequencies, where the scattering nature of styrofoam dominates, to $1/8$ as predicted by Eq. (1).

The third type of filters consists of a 1 mm and a 2.8 mm thin goretex sheet which are absorptive at infrared and particularly optical frequencies. They further complement the RT-MLI by blocking optical and reducing infrared radiation from the laboratory environment.

The final type of filters are commercial low-pass metal mesh filters [87] with sharp cut-off frequencies given by the design of the metal mesh. For this cryostat, a 1.6 THz low-pass filter is located on the 50K stage and a 1 THz low-pass filter is located on the 3K stage.

At the 1K stage of the system is an aperture in which we can place band-pass filters. They reduce the load on the cold stage significantly and are intended for specific detector measurements. They are not needed for cryostat operation and not further considered here.

In the implemented design we use the thermal shader, RT-MLI and goretex to reduce the thermal loading on the lowest temperature stages. This reduces possible filter heating on the metal mesh filters at 50K and 3K. Additionally, the small diameter of the metal mesh filters allows some conductive cooling via the mounting structure, further reducing the problem [87]. The stepped shape of the 50K window is a direct result of this consideration, reducing the diameter $d_{50K} = 72$ mm of the goretex and low-pass filter by a factor of 0.6 compared to the RT-MLI located on the same stage.

4.3.2 Geometric Throughput

The far-infrared access to the cold stage of the system is designed by minimizing the loading of the cold stage and 1K stage while maintaining a large opening angle. Importantly, we found during testing that the ^4He stage of our sorption cooler is limiting the hold time. Hence our goal to minimize the loading power on both stages of the sorption cooler. A python program was developed to quickly simulate the thermal power on all stages for various geometries using a first order approximation of the geometric throughput integral, which underestimates the true value of the integral.

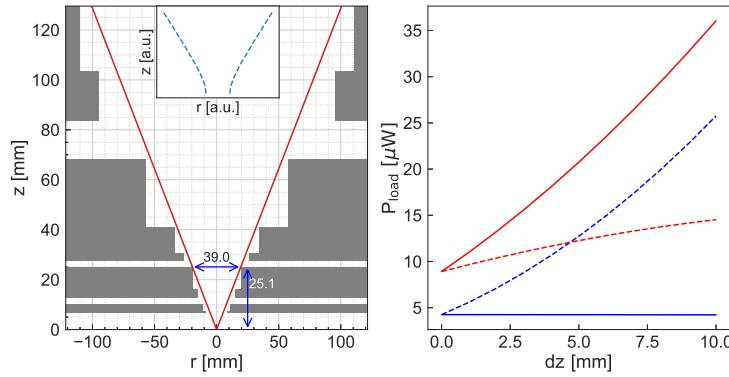


Figure 4.3: On the *Left*, the geometry of the final cryostat design is shown as it is implemented in the geometric throughput simulation. The (0,0) position corresponds to the antenna on the cold stage and the shields (1K, 3K, 50K and vacuum can) are shown in *grey*. The maximum opening angle is shown in *red* and the dimensions for the limiting aperture at the 3K stage are shown in *blue*. The inset qualitatively shows the shape of a gaussian beam. The graph on the *Right* shows two cases for the thermal load on the two stages of the sorption cooler (^4He in *red* and ^3He in *blue*) as a function of distance dz ($dz = 0$ mm indicating the actual position in the cryostat) while keeping a constant opening angle. The *dashed* lines show the increase in power if only the detector assembly is moved inwards and *solid* lines show the case if both the 1K stage and detector assembly are moved inward while maintaining equidistance with each other. (Color figure online.)

For the simulations, the vacuum window is assumed as a perfect blackbody of $T = 300$ K, while all radiation shields are perfect absorbers and the filters only transmissive using the transmission curves shown in Fig. 4.3.1. The effects from filter heating on the total thermal load of the sorption cooler stages are assumed to be negligible due to the design of the filter stack. Additionally, reflections are neglected, as all surfaces around the windows are coated with IR absorber, consisting of black Stycast 2850FT with 1 mm SiC grains [88].

We design the apertures in the vacuum shield, 50K shield and 3K shield to accommodate the previously described filter stack and allow for the vertical assembly of the cryostat. The limiting aperture determining the opening angle is located on the outer edge of the 3K stage, which exploits the large cooling power of the pulse tube (see Table 4.2). We

position the detector assembly and 1K stage as close as possible to the 3K stage, as this results in the lowest possible loading on these two stages (see Fig. 4.3.2). This also leads to small aperture diameters at the higher temperature stages (for a fixed opening angle), which enables the use of smaller metal mesh filters, reducing the effects of filter heating. Additionally, it limits the size of the required vacuum window. The windows are designed in step shapes with a large outer aperture and a small inner aperture (see Fig. 4.3.2) to reduce loading on the colder stages while avoiding grazing incident radiation, as SiC in Stycast has a strongly reduced absorption efficiency at high incident angles [88].

To determine thermal loading of the cold stage from the measured temperature, a load calibration $P(T_{stage})$ was created using a resistive heater mounted on the stage under dark conditions. Temperature measurements were then performed with an absorber mounted at the detector position with open windows. Simulation results are in good agreement with the hereby obtained measurements, predicting a thermal load on the cold stage of $P_{l,r,calc} = 4.4 \mu\text{W}$ compared to the measured $P_{l,meas} = 6.0 \mu\text{W}$.

4.4 Conclusion

We have designed a cryostat for beam pattern measurements in the sub-mm at large angles up to $\theta = 37.8^\circ$. A first-order thermal radiation model was developed and used to design the apertures and their positions on the cryostat thermal stages. The model predicts a load on the cold stage of $4.4 \mu\text{W}$, quite close to the measured value of $6 \mu\text{W}$ and well within the expected accuracy of the model. A filterstack combining various filter types is designed to improve rejection of out-of-band radiation and reduce filter heating. Operation of the cryostat shows excellent performance, reaching a base temperature of 265 mK in 14 h and hold time longer than 32 hours.

Chapter 5

An Ultra Wideband Leaky Lens Antenna for Broadband Spectroscopic Imaging Applications

5.1 Introduction

The emergence of on-chip spectrometers for far-infrared and sub-millimeter astronomy, such as DESHIMA [33], SuperSpec [34] and Micro-Spec [35], emphasises the need for efficient broadband radiation coupling in the frequency range of 100 – 1000 GHz. These spectrometers offer the ability of measuring medium resolution spectra ($F/\Delta F \sim 500$) with an instantaneous relative bandwidth of up to 1:3, complementing high-resolution but bandwidth limited heterodyne instruments. Future versions of these instruments will move towards multi-pixel focal plane arrays, creating sub-mm imaging spectrometers. These large format focal plane arrays (FPA) are ideally based on broad-band antenna systems with a single beam per feed, allowing a tight sampling of the focal plane. These FPA are typically coupled to reflector systems with large Focal distance to Diameter ratio (F/D) >3 . Such antennas can also be used as an alternative for CMB missions using multi-color pixels, such as PolarBear which is currently using a sineous antenna [89, 90].

We demonstrate the leaky lens antenna as an ideal candidate for these applications. This antenna, first demonstrated by Neto et al. [91, 92] at frequencies up to 70 GHz, is characterised by a 1:3 bandwidth, frequency independent, linearly polarized beams and a high, frequency independent aperture efficiency [93]. The first experimental demonstration at 1.55 THz was presented in 2017 by Bueno et al. [94]. These experiments demonstrated super-THz radiation detection with excellent detector sensitivity, but with a limited aperture efficiency $\eta_{ap} = 0.24$, evaluated only at a single frequency. The low aperture efficiency was due to a combination of i) radiation loss in the antenna-detector ground plane, ii) a slight misalignment between the feed and the lens and iii) a mismatch, due to fabrication tolerances, between transmission line and feed. In this paper we demonstrate the fabrication and experimental validation of a leaky lens antenna coupled MKID (Microwave

Kinetic Inductance Detector [81]), which does not suffer from these constraints, over a broad frequency band of 300-900 GHz. We measure the absolute coupling efficiency and far field patterns at 3 frequencies: 350, 650 and 850 GHz using narrow band-pass quasi-optical filters. From these we obtain an aperture efficiency $\eta_{ap} \approx 0.4$ using a Si lens without anti-reflection coating, which is in good agreement with the predicted performance.

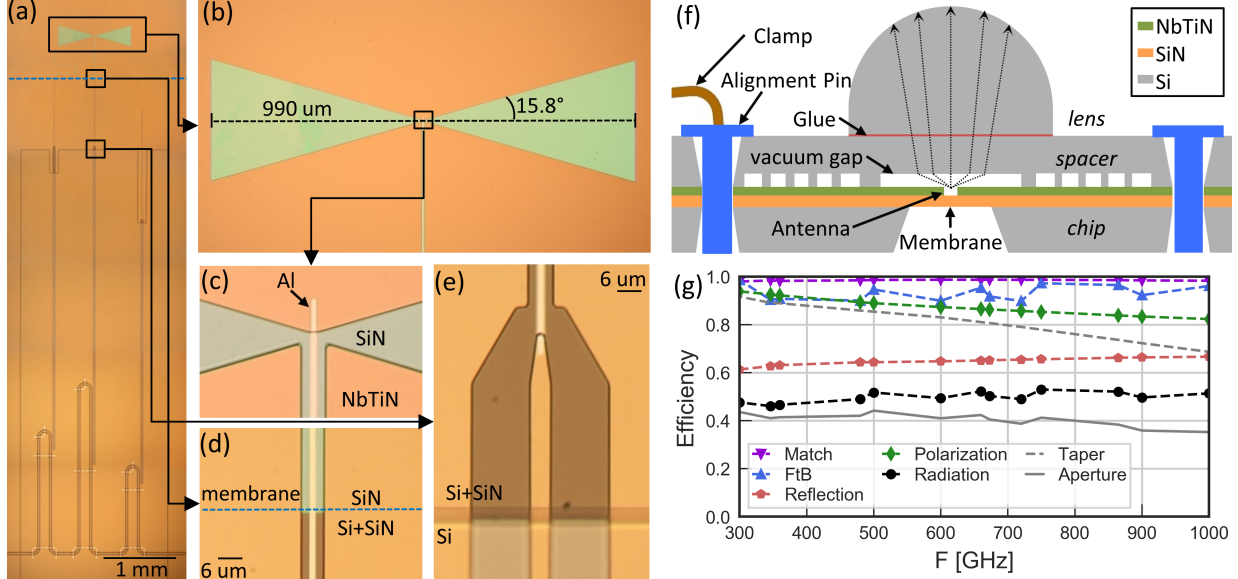


Figure 5.1: (a) Image of the chip center with the tapered antenna slot in the top and the MKID running along the center, coupled to the readout line at the bottom. Additional blind MKIDs are located on the left and right. (b) The leaky wave slot of the antenna on the SiN membrane. (c) Coupling structure to the narrow section of the MKID. The Al center line is shorted via a galvanic connection to the NbTiN ground plane. (d) Narrow MKID section at the membrane edge, marked by the dashed blue line. The 1 μm thick SiN membrane is transparent and therefore appears slightly blue in the back and front illuminated picture. Below the dashed line, the MKID continues on the SiN layer with Si substrate below. (e) The transition between narrow and wide section of the MKID. (f) A schematic of the full 3D assembly including the chip, spacer chip and lens. The total stack height is 4.325 mm. The radiation launched in the vacuum gap is refracted at the Si/vacuum interface. (g) The simulated radiation efficiency and its component efficiencies, with $\eta_{rad} = \eta_{mismatch}\eta_{FTB}\eta_{pol}\eta_{reflection}$.

5.2 Device and Antenna Design

The leaky lens antenna [91] is a lens feed consisting of a leaky wave slot on a thin membrane that is kept at an electrically small distance from the dielectric lens, in order to obtain a directive radiation pattern inside the dielectric which illuminates efficiently the top part of the lens. The leaky wave slot antenna is optimized via simulations in CST with an infinite dielectric medium [95], following the same approach as in [93]. The resulting tapered slot combines a high aperture efficiency which is almost constant over a 1:3 bandwidth and is coupled to a single planar feed. The optimization of the slot to create a frequency independent aperture efficiency results in a tapered slot with a length of 990 μm, slot tapering

angle of 15.8° and a vacuum-gap between antenna and silicon lens of $h = 13.8 \mu\text{m}$. The tapering angle is a compromise between polarization purity and antenna beam width, while the slot length is determined by the lowest frequency. The lens is optimized using a custom Physical Optics (PO) code to create diffraction limited beams with maximized directivity. We use the custom PO code, because the lens size (62λ inside silicon) is too large to allow for full-wave analysis in CST Microwave Studio. This also prevented us from treating multiple reflections inside the lens. This yields a truncated, hyper-hemispherical lens shape with radius of curvature $R = 2.95 \text{ mm}$, extension length $L = 1.0 \text{ mm}$ and truncation angle $\theta = 53.1^\circ$ without anti-reflection coating. The diameter of the truncated lens is 5.5 mm . We achieve a simulated radiation efficiency η_{rad} between 0.45 and 0.55 across the whole frequency band as shown in Fig. 5.1g. The dominant effect is the reflection efficiency due to the lack of anti-reflection coating at the Si-lens surface. Secondly, the polarization efficiency, representing the fraction of the total emitted radiation which is in the co-polarized state, ranges from 94% at low frequencies to 82% at high frequencies due to the relatively large thickness of the vacuum gap which constitutes an inherent tradeoff between polarization purity and directivity. All other contributions to the radiation efficiency, i.e. the feed match (η_{match}) and front-to-back ratio (η_{FTB}), are high. The simulated taper efficiency η_{tap} and aperture efficiency $\eta_{\text{ap}} = \eta_{\text{rad}} \cdot \eta_{\text{tap}}$ are also given in Fig. 5.1 g. We find that $\eta_{\text{ap}} \approx 0.4$ over the whole frequency band. This is slightly worse than corrugated feedhorns, but here we achieve a much larger bandwidth, and comparable to Sinuous antenna's. The development of a broad band anti-reflection coating could increase the aperture efficiency to values approaching the theoretical maximum of 0.8 [96]. Methods with two layers of anti-reflection coating have been demonstrated previously [97, 98] and should allow for a performance of ~ 0.6 over one octave.

We couple the leaky wave slot to a narrow coplanar waveguide (CPW) feed with a NbTiN ground and an Al central line (Fig. 5.1 a-e)). This narrow CPW line is also the last section of an antenna coupled Microwave Kinetic Inductance detector (MKID), which is a $\lambda/4$ CPW resonator with a length of several mm and a resonant frequency of 4.5 GHz. For details on this specific MKID design we refer to Ref. [36]. Radiation coupled to the antenna (panel b) will propagate into the NbTiN-Aluminium CPW line (panel c), where it will be absorbed only in aluminium central line. This is because the frequency of the radiation (300-900 GHz) exceeds the gap frequency of Al ($F_{\Delta, \text{Al}} \approx 93 \text{ GHz}$ for $T_c \approx 1.28 \text{ K}$) but does not exceed the gap frequency of the NbTiN ground plane ($F_{\Delta} \approx 1.1 \text{ THz}$). The NbTiN thereby provides a lossless ground plane for the antenna as well as for the NbTiN-Aluminium CPW line, eliminating ground plane loss as in Ref. [94]. The radiation absorbed in the aluminium changes the complex surface impedance which results in a slight shift in resonant frequency of the MKID. This shift is detected by a sending a single frequency readout signal at the unperturbed resonant frequency of the MKID through the readout line visible in the bottom of Fig. 5.1a. The frequency shift causes a change in transmitted phase in the readout signal that is measured using a homodyne measurement scheme [81].

The narrow CPW section has a line width $w = 2 \mu\text{m}$ and slot width $2.4 \mu\text{m}$, a thickness of 50 nm and a length of 1.5 mm . It is fabricated on top of $1 \mu\text{m}$ SiN. Underneath part of this line, the Si is removed to create a free standing membrane, needed for a correct

operation of the leaky lens antenna (see Fig.5.1f)). Due to its small width, this section has low radiation loss and a high kinetic inductance fraction, relevant for efficient detection of incoming THz radiation. The remaining resonator therefore consists of a wide CPW of $w = 6\text{ }\mu\text{m}$ and $s = 16\text{ }\mu\text{m}$ made of NbTiN on bare Si-substrate, with a transition between the sections and step from SiN to Si as shown in Fig. 5.1e). The wide section of the MKID then ends in a coupling structure that couples the resonator weakly to the CPW readout line. We choose a very low coupling quality factor of $Q_c = 5000$, because the power absorbed in the device during the beam pattern measurements is $\sim 1\text{ nW}$, resulting in a very low internal Q factor of the MKID. Additionally, two meshed layers of low-Tc (0.65 K) β -phase Ta are located on the front and backside of the chip, to reduce stray radiation inside the chip [99]. Two blind MKIDs are located close to the antenna-coupled MKID (see Fig. 5.1a)) as reference detectors.

5.3 Fabrication

We process the chip from a 375 μm thick 4-inch Si wafer coated on both sides with a 1 μm thick, low tensile stress ($\sim 250\text{ MPa}$) SiN layer, deposited using low pressure chemical vapor deposition (LPCVD) (see Fig 5.1f)). The fabrication is similar to the method presented by Bueno *et al.* [94] with steps as follows: i) We etch the SiN on the chip device side with reactive ion etching (RIE) using 35% SF_6 and 65% O_2 to create a sloped edge for the MKID wide section (Fig. 5.1c)). ii) We etch the SiN on the wafer backside, to create a hard mask for later Si removal. iii) We deposit a 350 nm thick, low tensile stress NbTiN layer on the device side using reactive sputtering of a NbTi target in a Nitrogen-Argon atmosphere, with the sloped edge of the SiN providing good step coverage for the NbTiN [78]. We pattern the NbTiN layer defining the antenna slot, the MKID resonator wide section and narrow section ground plane as well as the microwave readout line. We then etch the NbTiN using the recipe of step (i). iv) We sputter a 40 nm thick β -phase Ta layer on the device side of the wafer, which is then patterned and etched to form an absorbing mesh [99]. v) We spin coat 1 μm polyimide LTC9505 on the wafer, which is patterned and cured into dielectric supports for superconducting bridges along the readout line. vi) We sputter a 50 nm thick Al layer on the device side, which is then patterned and wet etched with a commercially available Al etchant (TechniEtch Al80 Al, *Microchemicals GmbH*) to define the central line of the narrow MKID section as well as the bridges along the readout line. vii) The Si wafer is etched in a KOH bath, with the device side protected with a commercial protection tool, to create the membrane opening. viii) After the KOH etch, we deposit 40 nm β -phase Ta on the wafer backside analogous to step (iv).

To create the 3D structure of the lens-antenna shown in 5.1g), we also need a spacer chip and Si-lens. The spacer chip is fabricated on a separate 350 μm thick 4-inch Si wafer with SiN on both sides, which is patterned. The wafer is subsequently etched twice in a KOH bath: Once on the lens facing side to create 4 square holes for the alignment pins, which will ensure the alignment between the lens and the antenna, and once on the antenna facing side to create the 14 μm deep features of the vacuum gap. The Si-lens was made by

a commercial partner (Tydex) according to the specifications of our design.

5.3.1 Assembly

We assemble the device chip, spacer chip and lens in a 2-step procedure: First, the chip and spacer chip are aligned and clamped together using Aluminum alignment pins. The lens is then aligned using a microscope based, home-made tool and glued on top of the spacer wafer using Loctite 406 cyanoacrylate glue, where we use markers on the spacerwafer from the KOH etch for alignment. This glue is chosen for its extremely low viscosity, resulting in a glue gap $< 1 \mu\text{m}$.

5.4 Measurements and Results

5.4.1 Beam Patterns

Measurements of the lens-antenna beam pattern were carried out in the setup shown in Fig. 5.2a), where the chip carrying the detector coupled lens-antenna is located on the cold stage of a cryogen free cryocooler equipped with a $^3\text{He}/^4\text{He}$ sorption fridge with direct optical access to a source located on an optical table at room temperature (see chapter 4). The cryostat reaches a base temperature of $T \sim 265 \text{ mK}$ with a holdtime of ~ 32 hours. The opening angle of $\theta = \pm 20 \text{ deg}$ is limited by the rotatable polarizer mounted on the outside of the cryostat's vacuum window.

The source assembly consists of three main parts: First, a glowbar (Scitec Hawkeye IR-19) operated at $T = 1420 \text{ K}$ is used as a multimoded blackbody source, located at one focal point of an elliptical mirror with a small aperture located at the second focus to create a uniform source pattern. We independently validated the source uniformity using a commercial bolometer and rotation stage. Secondly, an eight-bladed chopper, coated with radiation absorber [88] (Stycast2850FT loaded with 1mm diameter SiC grains), is positioned between the two foci. This allows a temperature modulation between the hot source and chopper blade at room temperature. Finally, the glowbar/chopper combination is mounted on an XY-scanner, allowing the measurement of 2D beam patterns of the antenna in the plane of the scanner. Additionally, the cryostat facing side of the source assembly has multiple blackened plates mounted to it, reducing unwanted reflections.

We perform 3 measurements, each with a different band pass filter on the 1K stage of the cooler. The band pass characteristics are shown in Fig 5.2c). The measured beam patterns represent an integrated beam pattern over the bandwidth of the band pass filter. However, due to the narrow bandwidth, the deviation between integrated beam pattern and that at the center frequency are $< 1 \text{ dB}$ based on simulations.

We extract the MKID response as a function of the source position using time-domain Fourier analysis, extracting the peak at the chopper frequency of $f = 254 \text{ Hz}$ for all scanner positions in a step-and-integrate scan mode. The resulting beam patterns are shown in Fig. 5.3 and compared to simulations carried out at the band pass center frequency. The

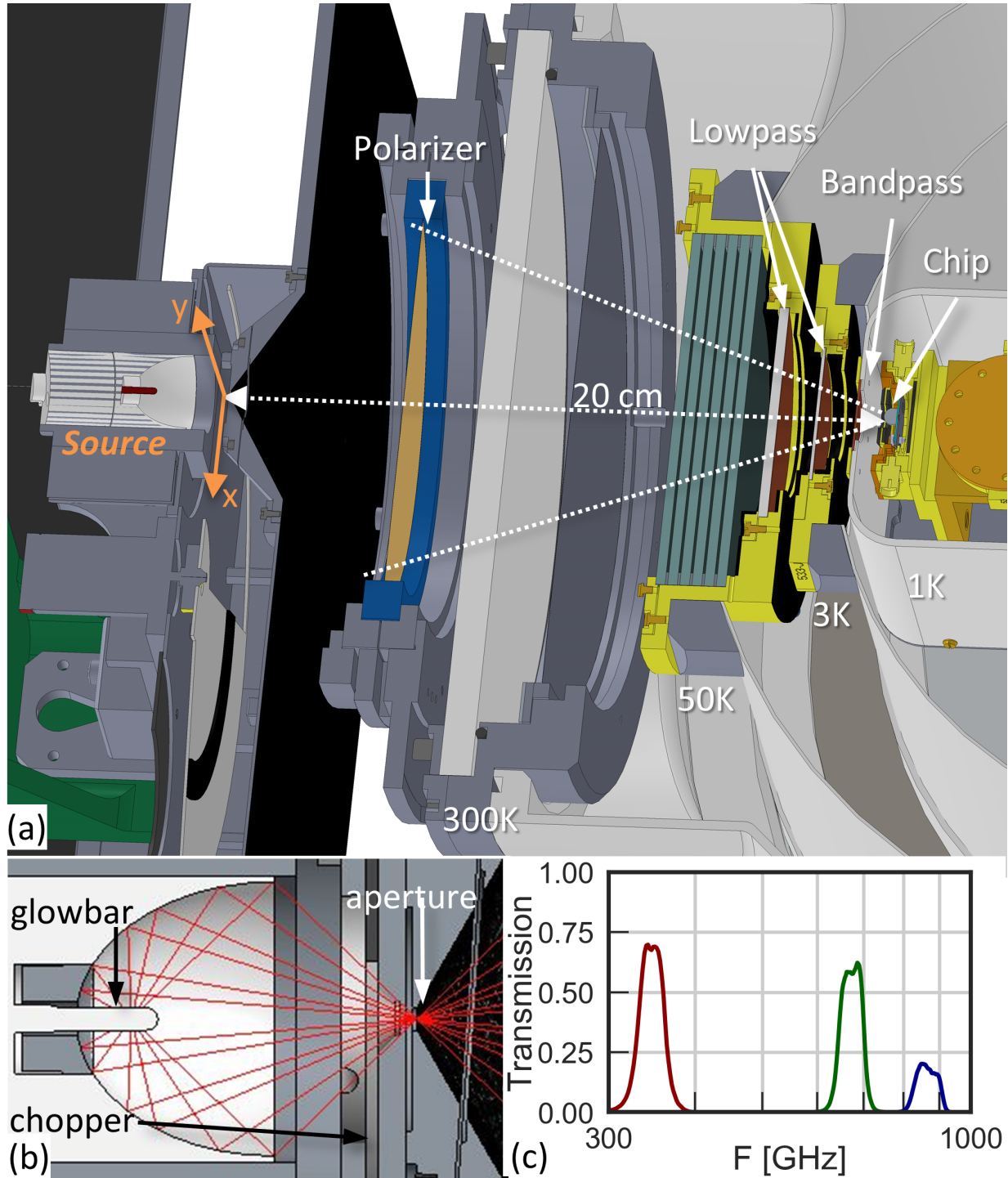


Figure 5.2: (a) The CAD-model of the cryostat optics and the hot-source in the configuration used for beampattern measurements. (b) A close-up of the source assembly. (c) Filter transmission as function of frequency for the 3 individual filters used in the experiment.

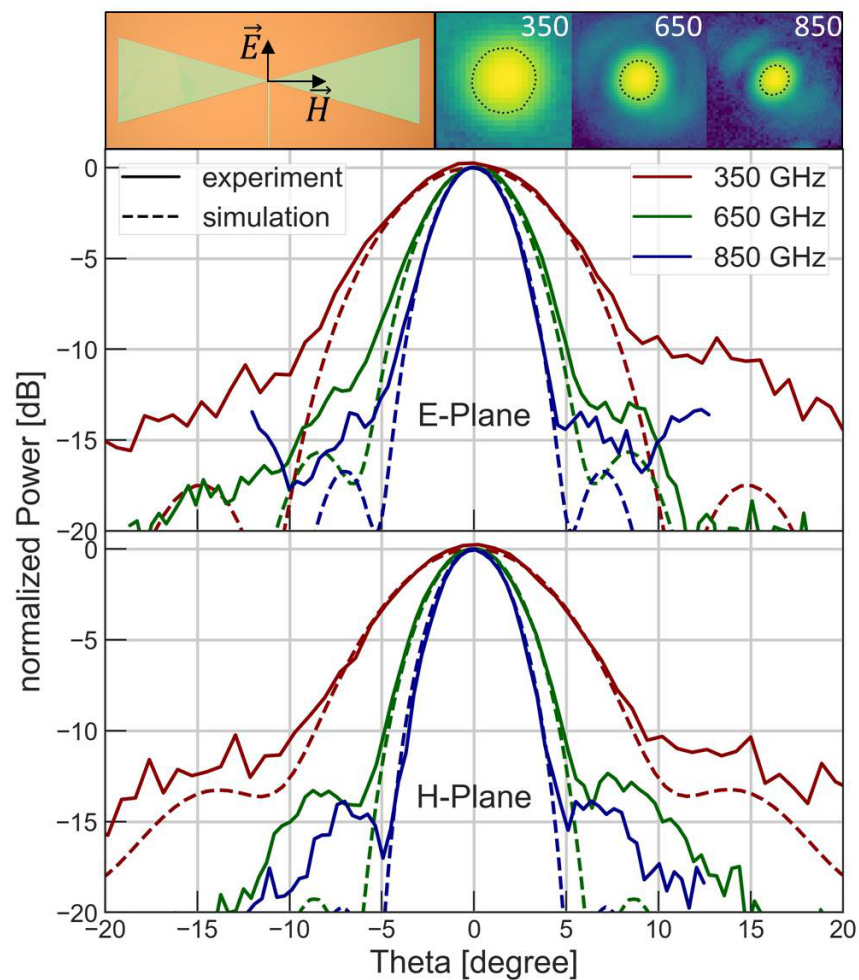


Figure 5.3: The normalized beam patterns in E- and H-plane for all measured frequencies. Insets show $20^\circ \times 20^\circ$ maps of the measured 2D beam patterns (*left to right*: 350, 650, 850 GHz) with a color scale from -20 dB (*dark*) to 0 dB (*light*) and a -3 dB contour line. Additionally, the orientation of the antenna slot compared to the measurement planes is shown in the top-left.

beam patterns, as simulated using the in-house PO tool, do not take into account multiple reflections that occur inside the lens surface because of the absence of an anti-reflection coating. Multiple reflections can result in a decrease in directivity and an increase in sidelobe-level which is difficult to predict and can change significantly with frequency.

All three frequency bands show excellent agreement between experiment and simulation for the main lobe down to the -10 dB level. The beams are diffraction limited as predicted by simulation, with a full width at half maximum (FWHM) of 3.7° at 850 GHz and 8.3° at 350 GHz due to the small lens diameter. The leaky-lens antenna is designed for future multi-pixel spectroscopic instruments with closely packed Focal Plane Arrays. Inherent to such designs is that the leaky-lenses are diffraction limited with maximized directivity, as mentioned in Section II. A diffraction limited beam can be described with an Airy pattern with a maximum theoretical Gaussicity of 82%. The Gaussicity of the beams is about 72% for all three frequencies and are close to the theoretical maximum.

While the beam width is frequency dependent, the bandwidth of it is not significant over the

The measured side lobe levels are around 2 to 5 dB higher than simulated, which we tentatively attribute to multiple reflections inside the lens increasing the effective detected power at large incident angles. An additional possible contribution might be the detection of residual stray-light via surface waves in the chip [99].

We measure the optical efficiency in a separate cryostat which provides a highly controlled environment and is described in detail in Ref. [100]. For this experiment the chip is mounted in a light-tight box on the cryostats cold stage, an adiabatic dilution refrigerator (ADR), operated at a stable 120 mK. An opening in the light-tight box provides a field-of-view through multiple optical filters to a thermal calibration source with a temperature range of 2.7 K - 40 K. The optical filterstacks correspond to the bands of the beam pattern measurements (see Fig. 5.4). However, their out-of-band rejection is much larger, which is needed to sufficiently reject low frequency radiation from the black body source operating at low temperatures.

The angular throughput to the source is limited by an aperture plate to an angle of $\pm 10^\circ$. This is large enough to couple almost to the whole beam at 350 GHz, but avoids straylight from large angles.

5.4.2 Optical Efficiency

We determine the optical coupling efficiency $\eta_{opt}(\nu_0)$ of the MKID coupled lens-antenna at a frequency ν_0 experimentally by measuring the noise-equivalent power NEP_{exp} at a source temperature T_s :

$$\eta_{opt}(\nu_0) = \frac{\int 2P_{s,\nu} h\nu d\nu + \int \frac{4\Delta P_{s,\nu}}{\eta_{pb}} d\nu}{NEP_{exp}^2 - \int 2P_{s,\nu} h\nu F_\nu O_\nu d\nu} \quad (5.1)$$

with the superconductor bandgap Δ , the pair-breaking efficiency $\eta_{pb} \sim 0.4$ for our film [77], the filter transmission F_ν , occupation number O_ν and the single-moded source power after

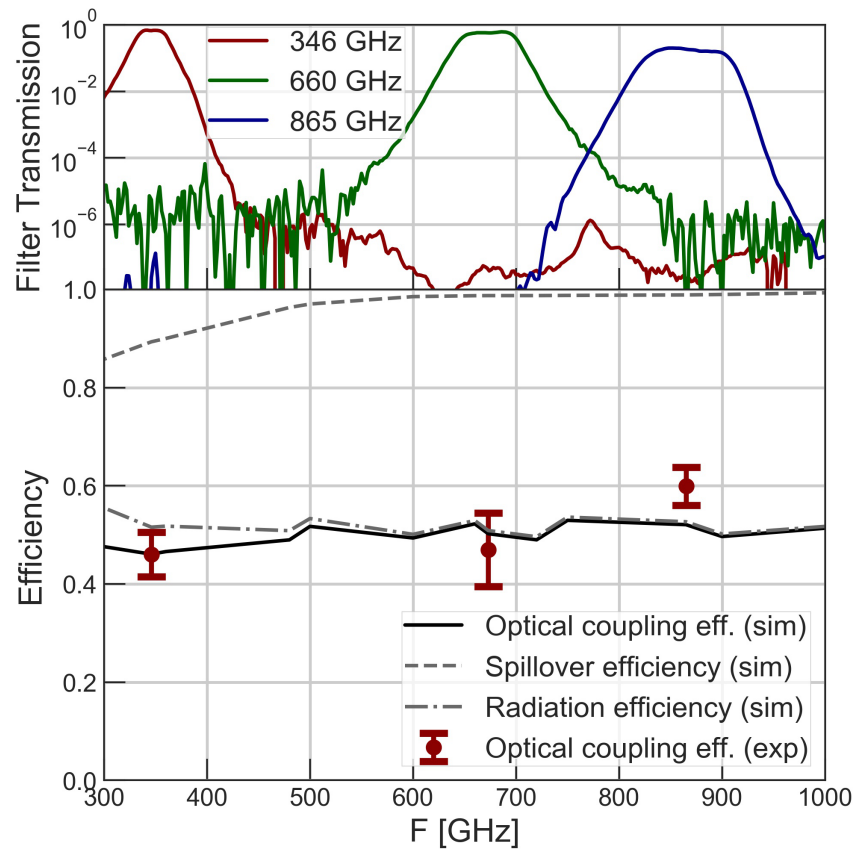


Figure 5.4: (a) The transmission curves for the three optical filterstacks; (b) The measured optical coupling efficiency, together with the simulated values of the optical coupling efficiency and its contributions, the radiation efficiency and spillover efficiency between the lens-antenna and the calibration source.

filter transmission $P_{s,v}$. A detailed description and derivation of this equation and its components can be found in Ferrari *et al.* [75].

This method is valid for narrow frequency bands and photon-noise limited MKIDs, and allows us to obtain precise absolute measurements of the optical efficiency at multiple frequencies across the whole band of the lens-antenna. For our Al based hybrid MKIDs, photon noise limited performance is proven experimentally, if the noise spectrum is white with a roll-off consistent with the quasiparticle lifetime. This is true for the detector presented at absorbed power levels $P > 10$ fW. While it is in principle possible to measure the response over the whole band using a Fourier-transform spectrometer (FTS) [94], this only provides a relative power measurement and not an absolute validation of the optical coupling efficiency of the detector .

The optical coupling efficiency measurements are carried out at multiple T_s , corresponding to a power range between 10 fW and 1 pW, which are averaged to obtain the values shown in Fig. 5.4 in comparison with simulation. For a detailed description of the experimental procedure we refer to Ref. [36]. As shown in bottom panel of Fig. 5.4 we find excellent agreement between the measured and simulated optical coupling efficiency $\eta_{opt} = \eta_{rad} \cdot \eta_{spillover}$ for all frequency bands. Here $\eta_{spillover}$ describes the spillover between the lens-antenna beam and the source, which is close to unity except for the lowest frequency. Hence this results demonstrates that the measured η_{rad} is in good agreement with our model calculation. Together with the good agreement of the patterns which validate the model calculation of η_{tap} , we can conclude that the aperture efficiency $\eta_{ap} = \eta_{rad} \cdot \eta_{tap}$ is well described by our model, and given by $\eta_{ap} \approx 0.4$ over the whole frequency band (see Fig.5.1). Only at 850 GHz we see a slightly higher coupling, possibly due to a small stray light contribution: The beam width is much smaller than the source aperture at this frequency.

5.5 Conclusion

In conclusion, we have measured beam patterns and optical efficiency of a leaky lens antenna over a 1:3 bandwidth around 350 GHz, 650 GHz and 850 GHz. We infer an aperture efficiency of the lens-antenna $\eta_{ap} = 0.4$ over the whole frequency band, based on measurements of the absolute coupling efficiency between the detector and a thermal calibration source together with a good agreement between measured and simulated beam patterns. The aperture efficiency is limited primarily by the antenna radiation efficiency, which is low due to the absence of an anti-reflection coating. The agreement between simulation and experiment show the validity of the design process, allowing for the design of optimised lens-antennas for on-chip spectrometer or CMB applications. The development of a broadband anti-reflection coating would allow for a significant increase in optical efficiency by up to 30%. Given the wide angular extent of the primary field in the dielectric an anti-reflection coating based upon meta-materials is extremely difficult to machine due to the steepness of the lens. An interesting alternative would be the use of stacks of foam as proposed by Ref. [101] or the use of thermal spray coatings [89], which allow for a more

practical approach towards a conformal coating. Changing the lens geometry and feed position could allow for frequency stable patterns [102], with lower directivity, which would allow for a more efficient broad-band coupling to a reflector system.

Chapter 6

Suppression of radiation loss in high kinetic inductance superconducting co-planar waveguides

6.1 Introduction

Superconducting transmission lines, such as co-planar waveguides (CPWs) or microstrips, are increasingly prevalent for cryogenic high-frequency applications upwards of 100 GHz, such as on-chip spectrometers [33, 103, 34], phased array antennas [104] and kinetic inductance parametric amplifiers [105]. These applications require ultra low-loss transmission lines with a loss tangent of $\tan \delta \lesssim 10^{-3}$ and lengths upwards of 100λ , either as an integral part of the circuit in kinetic inductance parametric amplifiers or phased array antennas, or as a connecting element in on-chip spectrometers. Microstrip losses in this frequency range down to $\tan \delta = 2 \times 10^{-3}$ have been measured previously [58]. Here, we focus on losses in CPW. CPW lines have an advantage over microstrip lines in that they do not require a deposited dielectric, which is a source of loss, decoherence and noise. However, CPWs are open structures and can radiate power, which is a source of loss and increases cross coupling to neighboring lines. The dominant radiation loss mechanism is the so-called leaky mode, which is present if the phase velocity in the line exceeds the phase velocity in the substrate. For microwave applications, this can be controlled by reducing the line width, but this becomes increasingly impractical at mm- and sub-mm wavelengths. In superconducting lines, the phase velocity is reduced due to kinetic inductance, which in principle allows to create a line with a phase velocity below the substrate phase velocity, thereby eliminating the leaky mode radiation and creating ultra low-loss transmission lines at frequencies exceeding hundreds of GHz. Dielectric losses in microstrips at frequencies up to 100 GHz have been measured previously [58]. In this paper, we demonstrate lab-on-chip loss measurements of superconducting NbTiN CPW Fabry-Pérot resonators around 350 GHz. We show that the radiation loss can be reduced and even virtually eliminated by reducing the phase velocity, which is accomplished by narrowing the CPW line to a total

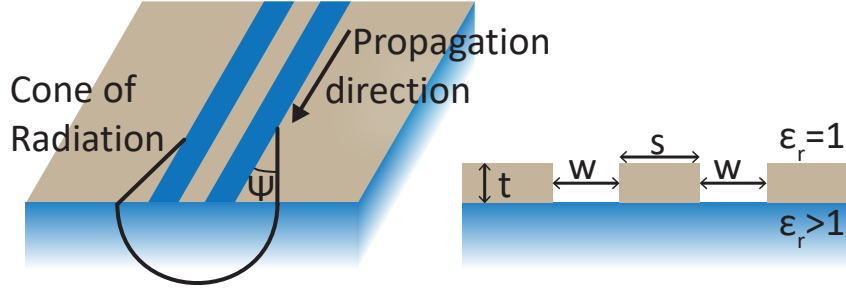


Figure 6.1: a) CPW geometry. b) Cone of radiation emitted along the propagation direction of the CPW mode, with radiation angle Ψ .

width of $\lesssim 6 \mu\text{m}$.

6.2 Radiation Loss Theory

The effective dielectric constant of a transmission line using a perfect electric conductor (PEC) is given by

$$\epsilon_{eff} = c^2 LC \quad (6.1)$$

where c is the speed of light and L and C are the transmission line inductance and capacitance per unit length respectively. In a CPW as shown in Fig. 6.1, this can be approximated by

$$\epsilon_{eff} \approx \frac{\epsilon_r + 1}{2} \quad (6.2)$$

with the dielectric constant of the substrate ϵ_r . The phase velocity $v_{ph} = \frac{c}{\sqrt{\epsilon_{eff}}}$ in the guided CPW mode is therefore faster than in the substrate. This creates a shockwave in the substrate, leading to a radiation cone characterized by the radiation angle Ψ (see Fig. 6.1). The frequency dependent loss factor α at high frequencies due to this shockwave has been derived by Frankel et al. [67] from the electric and magnetic field distributions in the dielectric materials due to the current distribution in a PEC as

$$\alpha_{rad} = \left(\frac{\pi}{2}\right)^5 2 \left(\frac{(1 - \cos^2(\Psi))^2}{\cos(\Psi)} \right) \frac{(s + 2w)^2 \epsilon_r^{3/2}}{c^3 K(\sqrt{1 - k^2}) K(k)} f^3 \quad (6.3)$$

where s and w are the CPW line and slot width, $k = s/(s + 2w)$ and $K(k)$ is the complete elliptical integral of the first kind. It can be seen in Eqn.6.3, that the magnitude of radiation loss is strongly dependent on Ψ which is given by the discrepancy of the dielectric constants

$$\cos(\Psi) = \frac{\sqrt{\epsilon_{eff}(f)}}{\sqrt{\epsilon_r}}. \quad (6.4)$$

For a PEC CPW, this ratio is only dependent on the substrate and independent of the conductor properties. However, in a superconducting CPW, the kinetic inductance per

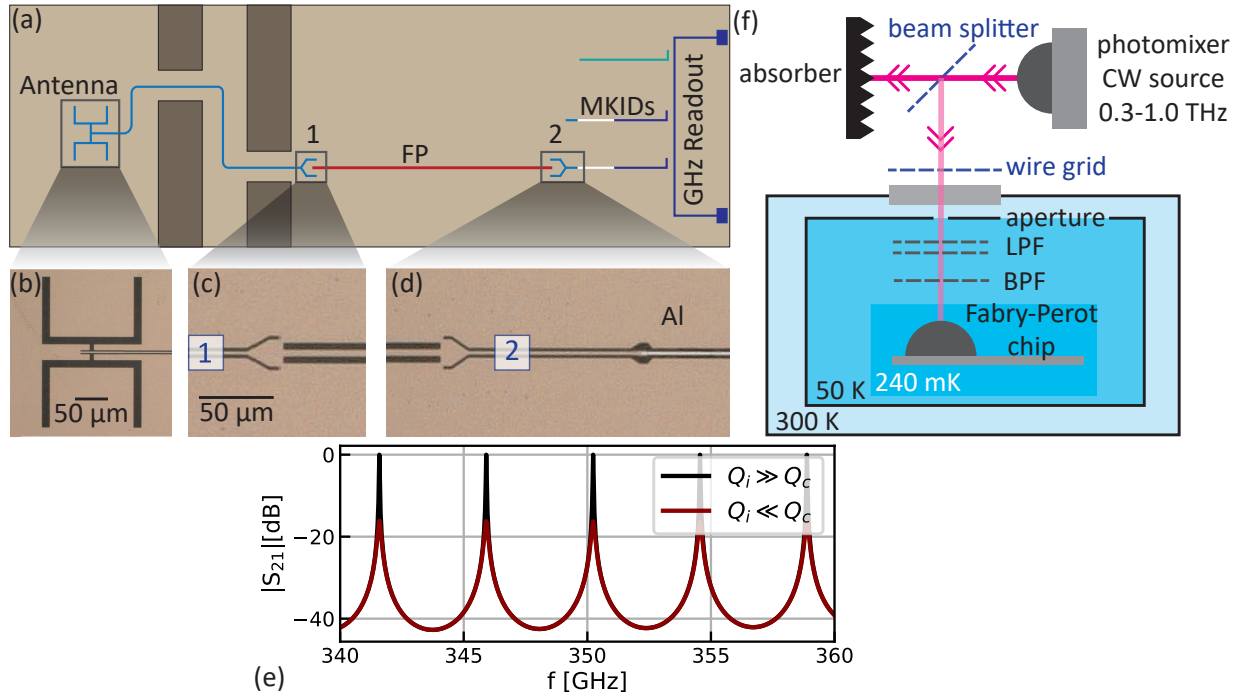


Figure 6.2: a) Chip schematic. b) Picture of antenna. c) Picture of first coupler. d) Picture of second coupler, including the transition to the Aluminum section of the MKID. e) Simulated Fabry-Pérot transmission. f) Experimental setup schematic. The filterstack consists of Low-pass filters (LPF) and a bandpass filter (BPF). The aperture plane is at the 50K window and a polarizing wire grid is located outside the cryostat.

unit length L_k due to the inertia of Cooper pairs needs to be taken into account, changing Eqn. 6.1 to

$$\epsilon_{eff} = c^2(L_g + L_k)C \quad (6.5)$$

where the transmission line inductance is the sum of its kinetic inductance and geometric inductance L_g .

Conceptually, using a CPW with high L_k leads to a suppression of the radiation loss, as the radiative angle Ψ is reduced. If L_k is sufficiently large to obtain $\epsilon_{eff} \geq \epsilon_r$, the radiative shockwave does not form as the phase velocity of the CPW line is slower than in the substrate, resulting in theoretically zero radiation loss. The kinetic inductance L_k increases with the film normal state sheet resistance, a reduced film thickness (in the regime of thin films compared to the penetration depth) and with reducing linewidth. A CPW of a 100 nm NbTiN film of in total 6 μm wide will fulfill the condition that $\epsilon_{eff} > \epsilon_r$ (see chapter 2.2.4). Another method is to use a CPW fabricated on a vanishingly thin dielectric membrane, which can be approximated as a free standing CPW and therefore does not radiate.

Measuring the radiation loss of a superconducting CPW at sub-mm wavelengths requires a highly sensitive device, capable of measuring a loss tangent $\tan \delta < 10^{-3}$. For this purpose we design a chip with a Fabry-Pérot resonator at its core, as shown in the

schematic of 6.2a). A similar device as been used by Göppl et al. [106] at microwave frequencies.

6.3 Device

6.3.1 Fabry-Pérot Concept

The Fabry-Pérot (FP) resonator is a single CPW line terminated by two identical couplers on either end, with the resonance condition

$$F_n = n \frac{c}{2L_{FP}\sqrt{\epsilon_{eff}}} \quad (6.6)$$

where ϵ_{eff} is the effective dielectric constant of the CPW, L_{FP} is the resonator length and n is the mode number. Transmission through the resonator can be described as a series of Lorentzian peaks, where each peak has a loaded Quality factor Q_L given by the resonance frequency and FWHM (full width at half maximum)

$$Q_L = \frac{F_n}{\text{FWHM}_n}. \quad (6.7)$$

The loaded Q-factor is a measure of the power loss per cycle which can be separated in its two primary components:

$$\frac{1}{Q_L} = \frac{1}{Q_c} + \frac{1}{Q_i} \quad (6.8)$$

First, Q_c is the power leakage through the two couplers

$$Q_c(n) = \frac{n\pi}{|S_{2'1'}|^2} \quad (6.9)$$

where $|S_{2'1'}|^2$ is the transmission through a single coupler with ports 1' and 2' (see Figs. 2.13 and 2.15). Second, the internal losses described by Q_i which is defined as

$$Q_i = \frac{\beta}{2\alpha} \quad (6.10)$$

with the propagation constant $\beta = 2\pi/\lambda$ and the loss factor α , where $[\alpha] = \text{Np/m}$. The loss inside the resonator is given by the combination of ohmic loss ($Q_{i,ohm}$), dielectric loss ($Q_{i,diel}$) and radiation loss of the CPW ($Q_{i,rad}$), as well as radiation loss at the coupler ($Q_{i,coup}$):

$$\frac{1}{Q_i} = \frac{1}{Q_{i,ohm}} + \frac{1}{Q_{i,diel}} + \frac{1}{Q_{i,rad}} + \frac{1}{Q_{i,coup}} \quad (6.11)$$

Since Q_L is the measured variable, a precise measurement of Q_i requires exact knowledge of Q_c , which is experimentally difficult due to fabrication constraints. Therefore, measurements in the internal loss dominated regime of $Q_c > Q_i$ are preferred, since then

$Q_L \approx Q_i$ (see Eqn.6.8). However Q_c cannot be increased arbitrarily, as this will reduce the Lorentzian peak height according to

$$|S_{21}|_{max} = \frac{Q_L}{Q_c}, \quad (6.12)$$

as shown in Fig 6.2e). Additionally, we use in the experiments a source with limited frequency resolution, limiting the design range of Q_c as well. Taking these considerations into account, all chips discussed in this paper are designed in Sonnet [68] to have $Q_c^{design} = 2.7 \times 10^4$ at 350 GHz (see chapter 2.4.1). The center frequency of 350 GHz is chosen based on the available experimental setup.

6.3.2 Chip Design

In order to measure the CPW radiation loss dependency on ϵ_{eff} in eqs.(6.3) and (6.4), four chips are designed with varying linewidths w and slotwidths s of the Fabry-Pérot lines as given in Table 6.1. All chips are fabricated on a single 350 μ m thick Sapphire wafer, ensuring common film properties across the chips. The 100 nm NbTiN film is deposited directly on the Sapphire using reactive sputtering of a NbTi target in a Nitrogen-Argon atmosphere [78]. Details on the fabrication can be found in Endo et al. [107], which follows the same route as this paper.

The measured line geometry is determined via SEM (Scanning Electron Microscope) inspection and deviates slightly due to overetch in the fabrication process. Using the surface inductance of $L_s = 1.03$ pH at 350 GHz calculated from the measured film parameters ($T_c = 14.7$ K, $\rho_N = 102$ $\mu\Omega$ cm), and the known parameters of the C-plane Sapphire substrate ($\epsilon_r^C = 11.5$; $\epsilon_r^{AB} = 9.3$), we obtain the measured values of ϵ_{eff} at 350 GHz given in Table 6.1. NbTiN parameters are measured on a test sample close to the FP resonators to eliminate effects of spatial variations in the NbTiN properties [78]. The resonator length is $L_{FP} = 10$ mm, corresponding to mode numbers in the range of 60-90 for the four chips.

A first estimate of the radiation loss, naively using Eqn.6.5 in Eqn.6.3 to account for the kinetic inductance, ranges from $Q_i = 5.6 \times 10^3$ for the 5 μ m line to $Q_i = 5.4 \times 10^6$ for the 3 μ m line; for the 2 μ m line, the equation diverges.

Using Mattis-Bardeen theory [52], we can estimate the ohmic losses to be multiple orders of magnitude lower than the stated loss, which means that radiation loss dominates for $w = s > 2 \mu$ m. It has been shown previously, that highly disordered superconductors,

	$w_d = s_d$ [μ m]	s_{meas} [μ m]	w_{meas} [μ m]	ϵ_{eff}
Chip I	2	1.95	2.15	13.1
Chip II	3	2.95	3.15	10.9
Chip III	4	3.95	4.15	9.5
Chip IV	5	4.95	5.15	9.0

Table 6.1: Designed and measured slot width w and line width s and resulting ϵ_{eff} for each chips Fabry-Pérot resonator.

such as NbTiN, start to deviate from Mattis-Bardeen theory [108] for high frequencies ($f > 0.3\Delta$) and high normal-state resistivity ($\rho_N > 100 \mu\Omega \text{ cm}$). However, both the frequency range of this experiment and the NbTiN film resistivity are at the lower limit and only a minimal deviation is expected.

In order to drive the FP resonator, one coupler (port 1) is connected via a CPW with $w = s = 2 \mu\text{m}$ to a double-slot antenna, centered at 350 GHz. The other coupler (port 2) is directly attached to the shorted end of a Microwave Kinetic Inductance Detector (MKID), which is a $\lambda/4$ resonator with $F_{res} \approx 6.5$ GHz based on the hybrid CPW design introduced by Janssen et al. [36]. In the MKID, a 1.5 mm long, narrow hybrid CPW with a NbTiN ground plane and an Al ($\Delta_{Al} \approx 90 \text{ GHz}$ $T_c = 1.28 \text{ K}$) center line follows directly after a NbTiN coupler section as shown in Fig. 6.2d). Incoming THz radiation is absorbed in the low bandgap Al line, thereby creating quasiparticles which changes the kinetic inductance of the film. This causes a frequency shift of the MKID resonator which is read out with the SPACEKIDs microwave readout [80].

Additional MKIDs, which are not coupled to the Fabry-Pérot and hereafter referred to as blind MKIDs, are placed on the chip as reference detectors. A microwave resonator with the same CPW geometry as the FP resonator is also added (green line in Fig. 6.2a)). Sampling the full FP transmission requires a measurement with a dynamic range of ≈ 50 dB (see Fig. 6.2e)). In order to reduce stray light reaching the MKIDs, the copper holder in which the chip is placed contains a labyrinth structure as indicated in Fig. 6.2a), separating the chips exposed antenna section from the dark Fabry-Pérot section. Additionally, a low-Tc backside layer of beta-Ta is deposited on the chip backside and acts as a stray light absorber [99].

6.4 Experimental Setup

In the experiment we mount an 8 mm Si lens on the chip backside, centered on the antenna, and place both in the Cu sample holder. This is placed on the cold stage of a He-3/He-4 sorption cooler [109], as shown in Fig. 6.2f), operating at $T \approx 250$ mK. A commercial photomixer continuous wave (CW) source [110] is positioned at room temperature and coupled into the cryostat via a beamsplitter to reduce the incoming power and avoid saturation of the MKIDs. The source emits a linear polarized, single frequency signal which is tunable in the range of 0.1...1.2 THz with a minimum step size of ~ 10 MHz and an absolute frequency accuracy of < 2 GHz. A band pass filter stack centered at $F_c = 346$ GHz and > 20 dB out of band suppression is located in the cryostat with a polarizing wire grid mounted on the vacuum window.

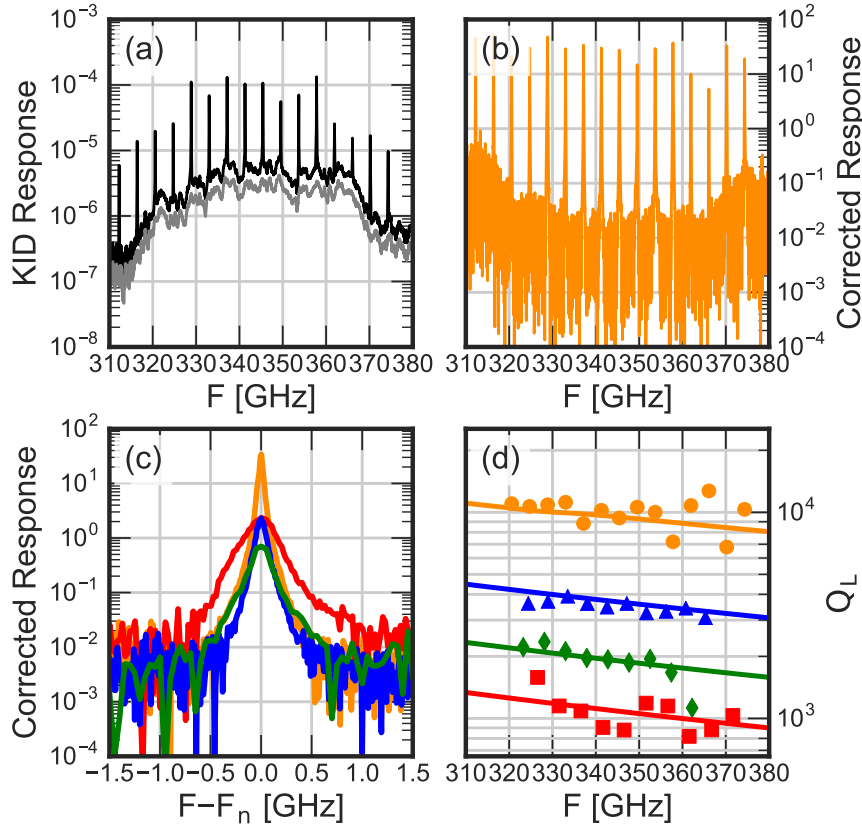


Figure 6.3: (a) Measured spectrum for chip I of the Fabry-Pérot coupled MKID (*black*) and the blind MKID (*grey*). (b) Corrected spectrum of the FP coupled MKID of chip I. (c) Example peaks of the corrected spectra of each chip (I: *orange*; II: *blue*; III: *green*; IV: *red*) (d) Measured Q_L for all chips and as symbols and simulated $Q_{L,sim}$ as lines, using the previous defined color scheme.

6.5 Measurements and Results

6.5.1 Fabry-Pérot Spectra

The FP transmission of the four chips is measured by sweeping the CW source from 310 GHz to 380 GHz in 10 MHz steps with an integration time of 1 s and detecting the resulting MKID response. An electrical on/off modulation of the CW source at $f_{mod} = 11.97$ Hz is employed to avoid $1/f$ noise. As the CW output power and beam shape are not well known, the absolute coupling strength to the MKID is not measured and the given responses are relative to the noise floor. However, the detector linearity in the measurement range was confirmed by measuring at various CW powers and retrieving identical results for the FP peak shapes.

The resulting response S_D of the FP-coupled MKID, shown in Fig. 6.3a) exemplary for chip I, clearly shows the expected regular spaced peaks of the FP resonator combined with a strongly frequency dependent baseline. The blind MKIDs spectrum S_B shows the same

baseline but with a frequency independent offset O compared to S_D . This shared baseline of the two spectra indicates a common power source for both the FP-coupled MKID and blind MKID, which is only present during the frequency sweep of the CW source. We therefore attribute it to CW power directly coupling to the MKIDs. Its frequency dependence is given by inherent fluctuations of the CW source combined with the bandpass filter transmission, both of which are also present in the Fabry-Pérot transmission, while the constant offset is due to the difference in MKID responsivity. We retrieve the corrected FP transmission S_{FP} shown in Fig. 6.3b) using

$$S_{FP} = S_D/S_B - O \quad (6.13)$$

where O is determined in the regions between FP peaks where S_D is dominated by the direct coupling.

A comparison between the FP peaks of the 4 chips (see Fig. 6.3c)) shows sharper and higher peaks for narrower CPWs. This already indicates lower losses for the narrow CPWs, as the experiments were designed for the Q_L -limited regime ($Q_L \approx Q_i$). The peak height difference for chip IV is due to the use of a different aperture, which only affects the direct CW coupling and not the resonance Q factor.

6.5.2 Internal Loss

In order to obtain Q_L the individual peaks are fitted with a Lorentzian function

$$L_n(F) = I \frac{Q_{L,n}^2}{Q_{L,n}^2 + 4 \left(\frac{F - F_n}{F_n} \right)^2} + O_L \quad (6.14)$$

with peak height I and offset O_L , and the fit results plugged into Eqn.6.7. The fitted Q_L is shown in Fig. 6.3d) as dots and compared to simulations shown by lines.

The simulations are carried out in Sonnet (see chapter 2.4) and are based on the measured CPW geometry and NbTiN properties as discussed previously. An excellent agreement with the measured data is found by including the coupling strength S_{21} , and radiation loss of the CPW in these simulations. The observed frequency dependence of Q_L is due to both the changing coupling strength and line loss $\alpha \propto f^3$, while the oscillation in measured Q_L can be explained qualitatively by a standing wave before the first FP coupler with a resonance length $L_{sw} > L_{FP}$.

In order to extract the internal loss from the measured Q_L , the Q_c must be known. While it is in principle possible to measure Q_c directly using the analysis in Fig. 6.2e), this requires a dynamic range > 50 dB or an absolute calibration of the S_{21} at the resonance peaks, both of which are not possible in our experimental system. Therefore, we use the Sonnet simulations of the coupler to obtain Q_c .

We then average over all peaks in the frequency range to retrieve Q_i^{exp} at 350 GHz, shown in Fig. 6.4, which is in excellent agreement with the Sonnet simulations of the CPW radiation loss. It is significantly higher than the analytical solution Q_i^{Fa} for the case of a PEC using Eqn.6.3, with the difference increasing for narrower lines up to a factor

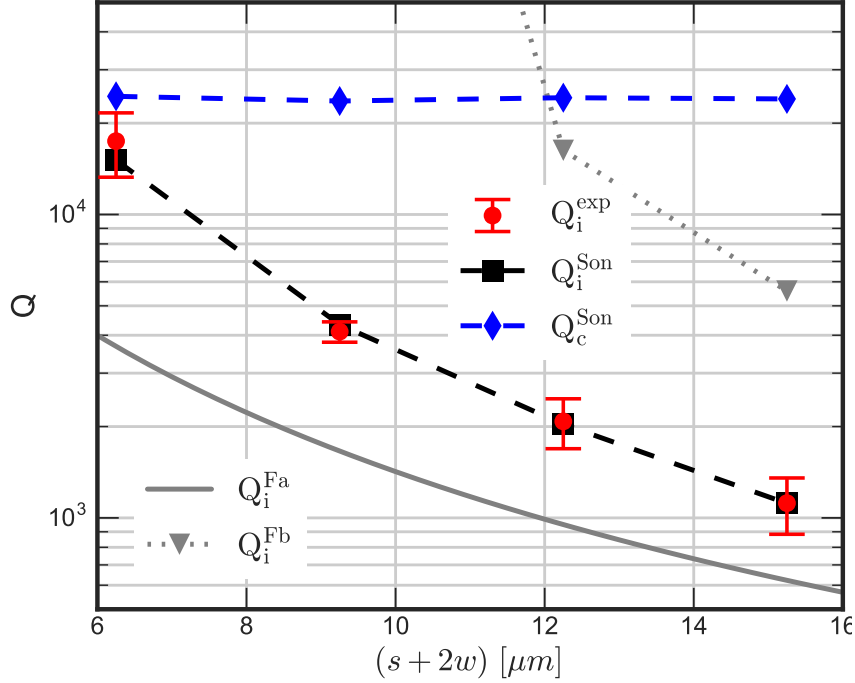


Figure 6.4: Measured Q_i^{exp} compared with sonnet simulations for internal loss Q_i^{Son} and coupling strength Q_c^{chip} , as well as analytical solutions for a PEC CPW Q_i^{Fa} and superconducting CPW Q_i^{Fb} .

of 4. However, it is also significantly lower than the naive approach of substituting the superconducting ϵ_{eff} of Eqn. 6.5 into Eqn.6.3 resulting in Q_i^{Fb} . All four CPW geometries are within the validity range for Eqn.6.3, but as the derivation of Eqn.6.3 is based on a planar PEC geometry, and does not take a superconductor into account, it is not surprising that both of these approaches fail. For Q_i^{Fa} the phase velocity change due to the kinetic inductance is completely neglected, while the naive inclusion of L_k in ϵ_{eff} for Q_i^{Fb} , while correct for phase velocity considerations, does not take into account the actual field distribution in the dielectric. The Q_i of the NbTiN microwave resonator located on each of the chips is measured to be $\approx 2 \times 10^6$, which is consistent with previous experiments [111] and indicates no issues with film quality.

In addition to the quantitative disagreement between the experiment and the analytic solution, we find a non-zero loss for chip I where we expect no radiation loss according to the shockwave model. As $\epsilon_{\text{eff}} > \epsilon_r$ is a fundamental argument against radiation loss due to a shockwave, a different mechanism must be considered. Radiation loss due to the strong fields at the open ended couplers were found to have a negligible contribution in sonnet simulations with $Q \approx 10^5$ (see chapter 2.4.2). Dielectric losses due to the crystalline sapphire substrate are expected to be negligible and can be excluded due to the high Q_i of the microwave resonator. Ohmic losses due to disorder effects in the NbTiN film are expected to be much smaller than observed and are not compatible with the measured width dependence. Additionally, none of these losses are included in the simulation for

Q_i^{son} , where we find a quantitative agreement with the measurements. Due to this excellent agreement, we speculate that we are limited by a different loss mechanism, most likely due to the fundamentally unconfined nature of the CPW mode.

6.6 Conclusion

In conclusion, we have designed, fabricated and measured superconducting on-chip CPW Fabry-Pérot resonators with high kinetic inductance NbTiN ($L_s = 1.03/\text{pH}$) and multiple line dimensions at frequencies from 320 to 380 GHz. We find a line width dependence for the internal loss Q_i , with values of $(1.1 \pm 0.2) \times 10^3$ for a total line width of $15.25 \mu\text{m}$ to $(1.7 \pm 0.4) \times 10^4$ for $6.25 \mu\text{m}$, corresponding to $\alpha = 0.007 \text{ dB/mm}$ and $\alpha = 0.09 \text{ dB/mm}$ respectively. The measured loss is in quantitative agreement with simulations of the radiation loss using Sonnet. However, the analytical solution by Frankel et al. [67] is not valid in the regime of high-kinetic inductance superconductors, underestimating the CPW loss when $\epsilon_{eff} \approx \epsilon_r$.

Furthermore, we show that the on-chip Fabry-Pérot resonator provides a sensitive and highly flexible method for high- Q_i transmission line loss measurements at sub-mm wavelengths. Extensions to other transmission line types, such as microstrips, can be easily achieved by modifying the resonator line and couplers, while the antenna can be exchanged to fit the required frequency range. Further optimization in the quasi-optical path and chip design are viable paths to improve the dynamic range and reduce effects from standing waves. For measurements of narrower lines where even lower losses are expected, a THz source with higher frequency resolution, such as multipliers, is required.

Chapter 7

Losses in superconducting microstrips at sub-mm wavelengths

7.1 Introduction

Low-loss transmission lines are a fundamental requirement for integrated superconducting devices operating at both microwave and sub-mm wavelengths. At microwave frequencies, the primary driver for low-loss transmission lines is the development of qubits and microwave kinetic inductance detectors (MKIDs) based on high quality factor resonators [17, 28], as well as parametric amplifiers based on very long transmission lines $> 100\lambda$ [105]. Additionally, high-impedance transmission lines can be used to further integrate microwave electronics onto the device chip [112, 113]. These devices are predominantly realized using coplanar waveguide (CPW) technology, achieving losses corresponding to $Q_i > 10^6$ [111]. However, the planar nature of CPWs leads to large and complicated designs which can be difficult to scale. Multi-layer structures such as microstrips [114] and parallel-plate capacitors [115] are preferable in order to create smaller devices and easily obtain high-impedance transmission lines, but these structures suffer from increased losses in the additional dielectric layer.

At sub-mm wave frequencies, astronomical applications rely increasingly on integrated devices, such as multi-color/multi-polarization pixels [116], phased array antennas [104] and on-chip filterbanks [33, 34, 103]. These usually use microstrips, as common mode excitation and radiation loss become serious issues at higher frequencies [64] (see chapter 6). However, these devices are usually based on Nb/SiO₂ technology, which has a 690 GHz cutoff due to the critical temperature of Nb and relatively high losses due to the SiO₂.

The losses of microstrips at these frequencies and sub-Kelvin temperatures are generally attributed to the existence and excitation of two-level tunneling systems (TLS) in the bulk of the amorphous dielectric. While the macroscopic behaviour of TLS is relatively well understood, their microscopic origin is still for the most part unclear. Due to the lack of a microscopic understanding, development and investigation of low-loss dielectrics relies heavily on iterative cycles of deposition and measurement. These loss measurements are

usually only carried out at microwave frequencies, under the assumption that material properties are comparable at sub-mm frequencies based on TLS theory [117]. As a result, limited data is available at $f > 100$ GHz and $T < 1$ K, where both signal generation and detection become increasingly challenging.

Measurements comparing microwave and sub-mm wave loss were performed by Chang et al. [118] and Gao et al. [58] on Nb/SiO₂/Nb microstrips at 220 GHz and 110 GHz respectively, and by Endo et al. [119] on NbTiN/SiN/NbTiN microstrips at 650 GHz. These experiments combined quasi-optical techniques with different on-chip test devices exploiting either path length differences (Chang et al.) or resonant structures (Gao et al. and Endo et al.). However, these approaches suffer from large intrinsic uncertainties and are not sufficiently precise to study materials with a lower loss tangent. In the case of resonant structures, this can be mitigated by using long resonators at higher mode numbers, where coupler effects are suppressed.

In this paper, we present loss measurements of superconducting NbTiN/a-Si¹/NbTiN microstrips at microwave and sub-mm wavelengths and at sub-Kelvin temperatures. We show TLS-like behaviour at microwaves, but find a significant increase in loss at sub-mm wavelengths which is inconsistent with the TLS standard model.

7.2 Device Design

We have designed a chip which combines shunted microwave resonators (μ WR) and in-line sub-mm wave Fabry-Pérot resonators (FPR). The μ WR are coupled to a co-planar waveguide (CPW) transmission line (henceforth called readout line) which runs over the entire chip, terminating in bond pads connecting the chip to a sample holder via Al bond wires. The loss as a function of photon number can be obtained by measuring the readout line transmission around the resonance frequency of the shunted resonator and retrieving the loaded quality factor Q_L and minimum transmission $S_{21,min}$ of the lorentzian dip. The internal loss factor Q_i and coupling strength Q_c then follow from the dip depth $S_{21,min} = Q_L/Q_i$ and the loaded quality factor, which can be expressed as

$$Q_L(n) = \frac{nQ_{c,1}Q_i}{nQ_{c,1} + Q_i} \quad (7.1)$$

where n is the mode number of the resonance peak and $Q_{c,1}$ is the coupling strength at $n = 1$, with $Q_c = nQ_{c,1}$ (see chapter 2.3).

For the sub-mm wave case, we excite the FPRs using a quasi-optical scheme, coupling radiation from a coherent source via an antenna and CPW line to the on-chip FPR. The relative power transmitted is measured as a function of source frequency using a microwave kinetic inductance detector (MKID) coupled to the far end of the FPR and read out using the same readout line as the μ WRs. This approach was previously used to measure CPW FPRs (see chapter 6).

¹amorphous silicon

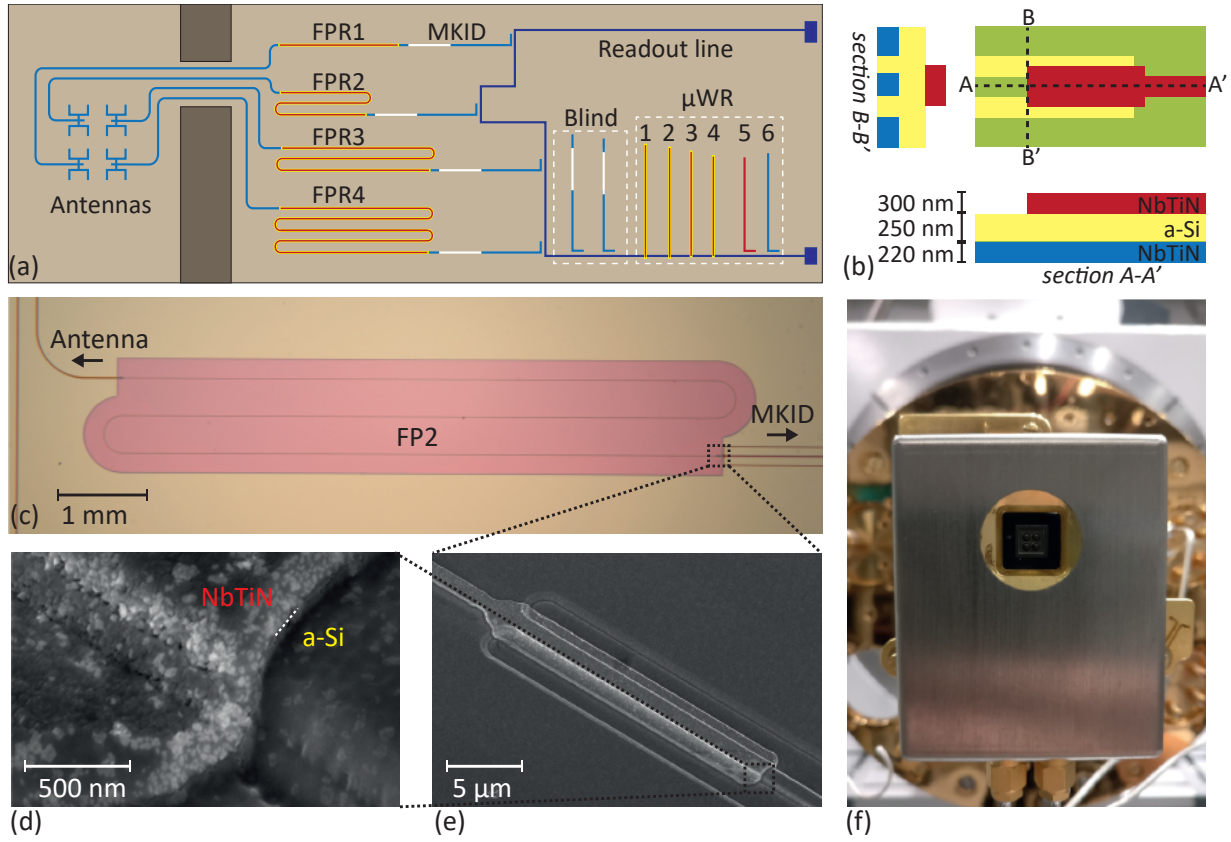


Figure 7.1: a) Chip schematic. NbTiN CPW structures are given in *blue*, the Al/NbTiN CPW of the hybrid MKIDs is given in *white* and microstrip lines are given in *red*. One of the CPW microwave resonators ($\mu\text{WR}5$) is also shown in *red* to highlight the use of the upper NbTiN layer for the CPW center line. b) FPR coupler schematic with two cross sections. c) Optical microscope image of FP2. d) Angled scanning electron microscope (SEM) image of the FPR coupler. e) High-resolution SEM image of the microstrip open end. Overetch into the a-Si layer is visible, with the dotted white line indicating the border between NbTiN and a-Si. f) Picture of the device mounted in the cryostat.

The design of the chip is given in Fig. 7.1a). Six μWR s with resonance frequencies around 6 GHz are coupled to the readout line. Of these, four are half-wave microstrip resonators using NbTiN/a-Si/NbTiN microstrips with a dielectric thickness of $h = 250$ nm and line width $w = 2$ μm , and two are quarter-wave CPW resonators with a linewidth of 6 μm and slot width of 16 μm . The CPW resonators are deposited directly on the Si substrate, with $\mu\text{WR}6$ fully implemented in the lower NbTiN layer, while the center line of $\mu\text{WR}5$ is implemented using the upper NbTiN layer.

We implement four FPRs on the chip, where each FPR is connected to its own separate feeding network via two identical couplers, using the design shown in Fig. 7.1b). All four resonators are made with identical line and coupler geometry, but have different lengths l_{FP} (FPR1: 5 mm; FPR2: 10 mm; FPR3: 20 mm; FPR4: 50 mm). This design was chosen to obtain resonators which, for the same frequency, have different mode numbers but identical Q_i and $Q_{c,1}$.

We use a CPW with 2 μm line and gap width between the antenna and the FPR, since we know its loss to be negligible at sub-mm wave frequencies (see chapter 6). The MKIDs are quarter-wave resonators of a standard Al/NbTiN hybrid CPW design [36], where incoming power is absorbed in a short Al central line, leading to changes in the MKIDs microwave properties which are measured via the microwave readout line.

7.3 Fabrication

We start the fabrication process with a 375 μm thick 4-inch Si wafer (dielectric constant $\epsilon_r = 11.44$ [120]) coated on both sides with a 1 μm thick, low tensile stress (~ 250 MPa) SiN layer ($\epsilon_r = 7$), deposited using low pressure chemical vapor deposition (LPCVD). The SiN on the device side is etched away almost everywhere, except for small patches below the MKID Al center lines [75]. For the FPR and μWR fabrication, we now start by depositing a 220 nm thick NbTiN layer ($T_c = 15.1$ K, $\rho_n = 138 \mu\Omega\text{cm}$) on the device side using reactive sputtering of a NbTi target in a nitrogen-argon atmosphere [78]. This layer is patterned and etched to contain the microstrip ground plane and all CPW elements of the chip. A 250 nm thick a-Si layer $\epsilon_r \approx 10$, deposited using plasma enhanced chemical vapor deposition (PECVD), serves as dielectric layer of the microstrip [121]. We then define the microstrip lines in a second NbTiN layer of 300 nm ($T_c = 15.0$ K, $\rho_n = 104 \mu\Omega\text{cm}$), using the same process as the first NbTiN layer. With the FPR and μWR finalized, we finish fabrication of the MKIDs and microwave readout line using a 1 μm thick layer of polyimide LTC9505 and a 50 nm thick layer of Al ($T_c = 1.25$ K) (see chapter 3.1). Finally, a 40 nm thick layer of β -phase Ta ($T_c = 0.7$ K) is deposited on the backside and patterned into an absorbing mesh for stray light control [99].

As NbTiN and a-Si require the same dry etch agents, an overetch in the order of 40 nm is present for the lower layers, as highlighted in Fig. 7.1e). The thickness of the lower NbTiN layer was increased accordingly to maintain designed antenna and MKID properties.

7.4 Experimental Setup

7.4.1 Microwave Measurement

The μWR s are characterized in a dark cryogenic setup, which is optimized for low-background MKID experiments as discussed in [36, 79], and using a standard homodyne technique enabled by a commercial vector network analyzer (VNA). In order to achieve acceptable noise levels at the low microwave powers required to reach the single-photon regime, a -36 dB attenuation on the input, and an amplifier with 36 dB gain on the output were added to the microwave readout chain at room temperature.

7.4.2 Submillimeter Measurement

For measurements of the FPR transmission, a 2×2 lens-array is mounted on the chip back-side and aligned to the double-slot antennas. Each lens has a hyper-hemispherical shape with 2 mm diameter, creating a diffraction limited beam [102]. The chip is then placed in a Cu sample holder, which is surrounded by a tight-fitting mu-metal magnetic shield (see Fig. 7.1f)). This assembly is mounted on the cold stage of a dilution refrigerator operated at 120 mK. A TERABEAM 1550 (*TOPTICA Photonics AG*) photomixer continuous wave (CW) source at room temperature emits a tunable signal in the range of 0.1...1 THz with a step size of 10 MHz and a bandpass filterstack inside the cryostat that defines a frequency band centered at $f = 346$ GHz. The source signal is attenuated with a beam splitter to keep the MKIDs in a linear operating regime. Frequency multiplexing readout electronics are used to enable simultaneous measurements of all FPRs [80]. Details on the setup can be found in chapter 3.2.

7.5 Measurements and Results

7.6 Microwave Measurement

We measure transmission dips of the μ WRs at 50 mK as a function of readout power in the range of $P_{read} = -65 \dots -157$ dBm, as shown exemplary in Fig. 7.2a) for μ WR1. The internal quality factor Q_i of the resonator is then determined at each power from a Lorentzian fit [122]. We measure $S_{21}(f)$ from 4.7 GHz to 6.7 GHz in 4001 points at $T = 60$ mK, excluding any points falling on a resonance feature, to create a 0 dB transmission reference. Figure 7.2b) shows the resulting Q_i as a function of the average photon number in the resonator per $\lambda/2$, given by

$$\langle n_{ph} \rangle = \frac{P_{int}}{hf^2} \quad (7.2)$$

where P_{int} is the internal power, given for the μ WRs by $P_{int} = mQ^2P_{read}/\pi Q_c$ with $m = 2$ or $m = 1$ for quarter-wave and half-wave resonators respectively. All μ WRs show a characteristic behaviour for TLS loss and can be fitted using [123]

$$\frac{1}{Q_i} = \frac{\tanh(\hbar\omega/2k_bT)}{Q_{i,0}(1 + (\langle n_{ph} \rangle / n_s))^{\beta/2}} + \frac{1}{Q_r} \quad (7.3)$$

where Q_i has a minimum value $Q_{i,0}$ at photon numbers below the saturation value n_s , increases with a slope given by β until other loss source dominate at high photon numbers, saturating at Q_r .

As the CPW resonators do not contain a-Si, their TLS losses are dominated by the metal-substrate and substrate-air interfaces, with crystalline Si as substrate [124]. Both $Q_{i,0}$ and Q_r values (μ WR5: $Q_{i,0} \approx 2.0 \times 10^5$, $Q_r \approx 9.5 \times 10^6$. μ WR6: $Q_{i,0} \approx 1.2 \times 10^5$,

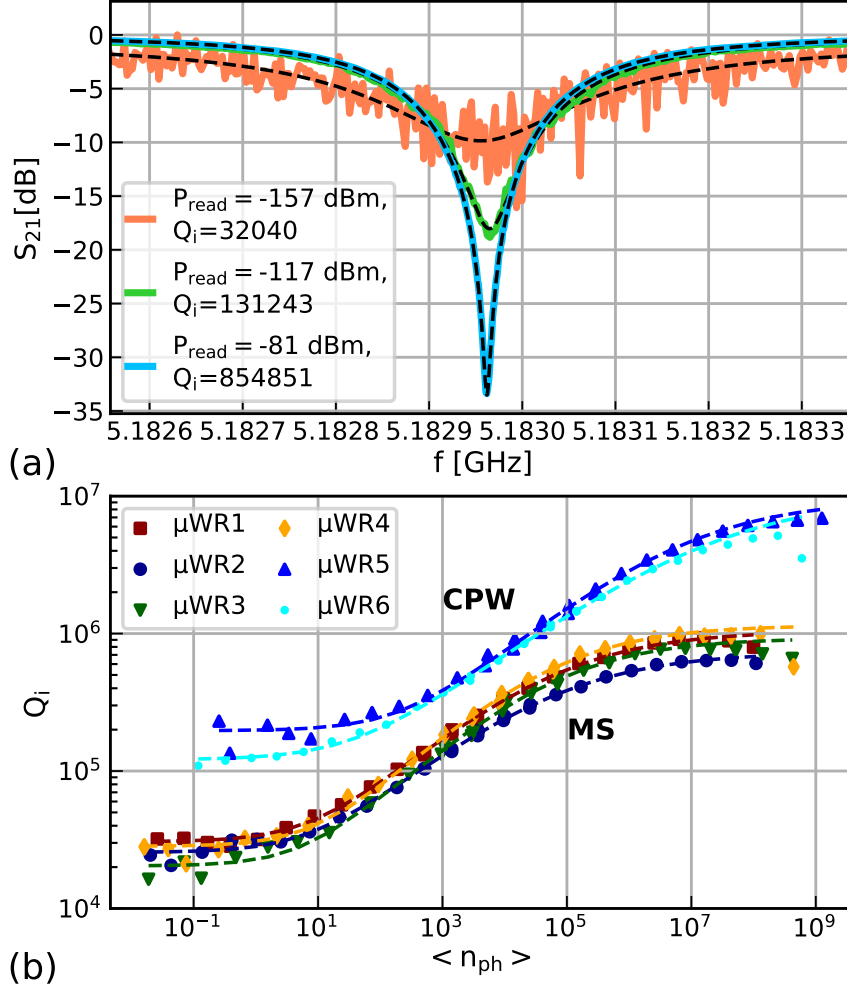


Figure 7.2: a) Transmission for μ WR1 at three different readout powers, with the respective Lorentzian fits shown by the black dotted lines. b) Measured internal quality factor Q_i as function of $\langle n_{\text{ph}} \rangle$ for all μ WRs shown as symbols, with fits of Eq. 7.3 shown by dotted lines with corresponding colors.

$Q_r \approx 9.9 \times 10^6$) are comparable with the state of the art for CPW resonators made of sputtered NbTiN [111], indicating an excellent film and interface quality for both the upper and lower NbTiN layers (sampled by μ WR5 and μ WR6 respectively) with no significant degradation due to the fabrication process. We find values of β between 0.7 and 0.8 for all resonators, which is consistent with literature [123].

Losses in amorphous microstrips are generally dominated by TLS in the bulk dielectric layer [125]. We assume that losses in the metal-substrate interface can be neglected here, due to the surface layer quality shown by the CPW resonators. Consequently, the internal loss factor of the a-Si film, can be obtained as $Q_{i,\text{aSi}}(6 \text{ GHz}) = 27 \pm 4 \times 10^3$ from an average over all microstrip resonators and using

$$Q_{i,\text{aSi}} = FF \times Q_i \quad (7.4)$$

with the filling factor $FF = 0.96$ taking the a-Si layer overetch into account (see Fig. 7.1e). This value corresponds to a loss tangent $\tan \delta = Q_i^{-1} = 3.7 \pm 0.5 \times 10^{-5}$, which is expected for a-Si films [59]. We calculate the filling factor FF by simulating a short microstrip line in CST and varying the loss tangent of the dielectric. The relation between simulated line loss and the set loss tangent is then given by FF .

7.6.1 Submillimeter Measurements

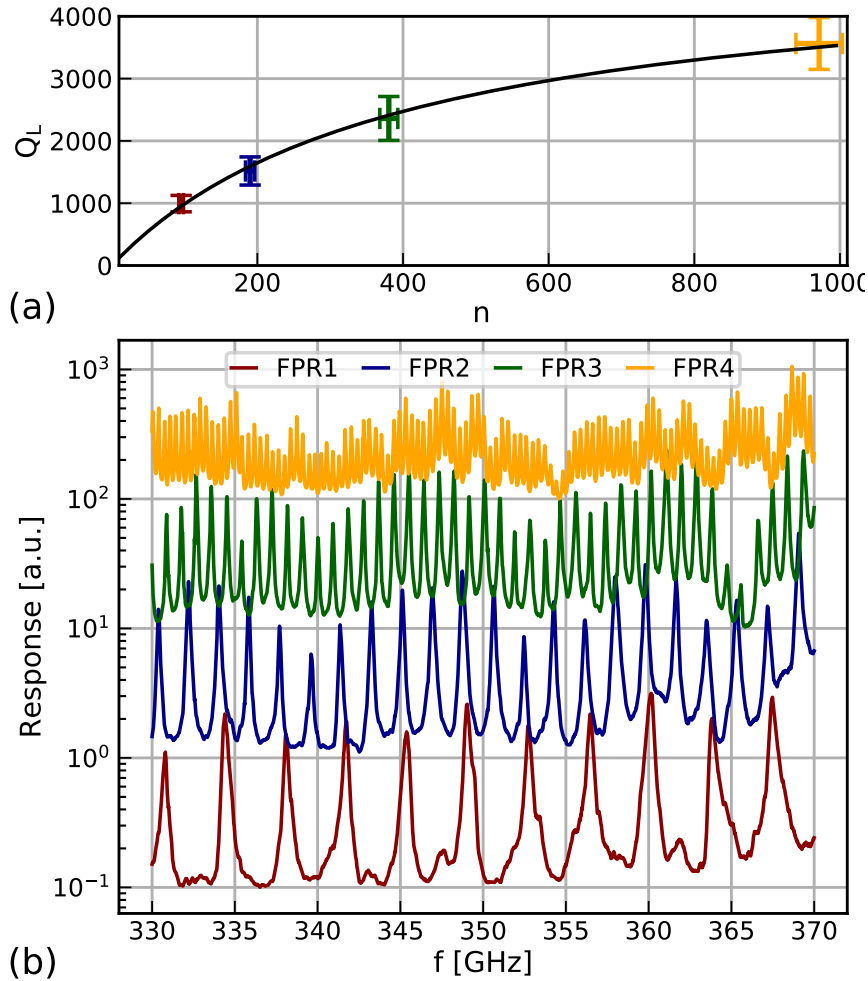


Figure 7.3: (a) Averaged loaded quality factor Q_L as a function of average mode number in the four FPRs. The fit using Eq. 7.1 is shown by the black line. (b) Figure supporting figure a): Measured spectra of the FPRs, offset along the y-axis for better comparison. Line colors correspond to the markers in figure a).

We measure the transmission through the four FPRs as a function of source frequency and apply a correction for directly coupled stray light, using the response of the blind MKID as introduced in chapter 6. Figure 7.3b) shows the resulting spectra containing

clear transmission peaks with an average frequency spacing dF corresponding to the different resonator lengths. Variations in peak height, as well as secondary peaks visible in FPR1, can be explained qualitatively by standing waves before the FPR modifying the transmission through the first coupler with a wavelength corresponding roughly to the electrical distance between antenna and FPR coupler. For each resonance peak, we obtain Q_L from a Lorentzian fit and the mode number from the resonance frequency F_n using $n = F_n/dF$. The standing waves before the FPR also introduce an oscillation in the measured Q_L , due to a modified Q_c .

In this setup, we do not have an absolute reference for unity transmission and can therefore not use the height of the FPR peaks to obtain Q_i and Q_c independently. However, as we are measuring different resonators, each designed with different mode numbers n at the same frequency, we can fit $Q_L(n)$ using Eq. 7.1 to retrieve $Q_{c,1}$ and Q_i . For this purpose, we take the mean value of Q_L for each resonator, as plotted in Fig. 7.3a), while assuming that Q_L is linear with frequency and that the standing wave oscillations are sampled well enough to be averaged out. The resulting mean value then corresponds to the value at the center frequency of the measurement band, 350 GHz, while the error bars are a measure of both the statistical scatter and the linear slope over the averaged frequency range. A fit to Eq. 7.1 then results in $Q_{c,1} = 12.4 \pm 0.7$ and $Q_i = 4.9 \pm 0.3 \times 10^3$.

Following Eq. 7.4, we then obtain the internal loss factor of a-Si at 350 GHz as $Q_{i,asi}(350 \text{ GHz}) = 4.7 \pm 0.3 \times 10^3$, corresponding to a loss tangent of $\tan \delta(350 \text{ GHz}) = 2.1 \pm 0.1 \times 10^{-4}$ which represents a significantly higher loss compared to the microwave regime, where $\tan \delta(6 \text{ GHz}) = 3.7 \pm 0.5 \times 10^{-5}$. Furthermore, we estimate the maximum incident power at the FPR to be less than 5 pW, placing the FPR in the single-photon regime with $n_{ph} < 8$. The increased loss at sub-mm wave frequencies is in disagreement with the TLS standard model, where a constant loss is predicted in the single-photon regime when $\hbar\omega \gg k_B T$, which is the case for both measurements.

A possible explanation of this discrepancy, could be a modified TLS model with a frequency dependent density of states $N(f)$. Such a model has been recently used to describe dephasing and noise due to TLS, combining interacting TLS with the power-law of $N(f) \propto (f^\mu)$ with $\mu \approx 0.3$ obtained from noise measurements [126]. We find that a value of $\mu \approx 0.4$ would resolve the discrepancy in our measurement. Note, that the power dependence of $\beta < 1$ we find at microwave frequencies is also often identified with interacting TLS. Alternatively, it is possible that we observe the low-frequency tail of resonant phonon absorption peaks at far-infrared wavelengths. Room temperature measurements of SiO_x and SiN in the far-infrared regime indicate that such a low-frequency tail could have the relevant magnitude [127, 128]. Losses in the NbTiN film due to disorder effects should also be considered. However, we consider this highly unlikely to be the dominant effect, since measurements on a NbTiN CPW line with a similar film yield a $Q_i \approx 17 \times 10^3$ limited fully by radiation losses (see chapter 6). We also find no indication in DC- or microwave-measurements that the NbTiN film quality of either the top- or bottom layer is degraded. The two CPW datasets in Fig. 7.2 represent a CPW line from each NbTiN layer. Further experiments in the 100 – 1000GHz frequency range, in combination with microwave measurements, are needed to clarify this issue.

7.7 Conclusions

In conclusion, we measured the losses of high-Q resonators made of NbTiN/a-Si/NbTiN microstrips in the single-photon regime at 6 GHz and 350 GHz. Particularly, we demonstrate an effective method to independently measure Q_i and Q_c at sub-mm wave frequencies without an absolute power calibration, using multiple Fabry-Pérot resonators on a single chip. This method can be easily extended up to the bandgap frequency of NbTiN around 1 THz. We measure a very low loss tangent for the a-Si film at microwave frequencies, with a power dependence that is consistent with TLS theory. At sub-mm wave frequencies, we find an unexpected increase in the loss tangent, which requires further investigation to identify the root cause.

Chapter 8

Conclusion

This thesis describes the research work carried out over a period of five years (From January 2016 to May 2021) at Delft University of Technology and the Netherlands Institute for Space Research (SRON). Its focus lies on the experimental characterization of the building blocks required for the next generation of superconducting integrated circuits at sub-millimeter wavelengths. In this chapter, we first summarize the most significant results of this research and then provide an outlook on the implications for future research.

8.1 Wideband Leaky-Lens Antenna

In chapter 5 I describe the demonstration of a superconducting leaky-lens antenna for operation in the 300 – 900 GHz frequency band.

The lens-antenna design represents an iteration on previous prototypes, combining a tapered leaky wave slot fabricated in a superconducting NbTiN film on a SiN membrane with a hyper-hemispherical Si lens. We perform measurements of the lens-antenna's far field pattern and optical efficiency at three frequency bands, centered at 346 GHz, 660 GHz and 865 GHz, covering the antennas full 1 : 3 bandwidth. These experiments are carried out with a dedicated chip where the antenna feed is directly coupled to a microwave kinetic inductance detector (MKID).

In order to enable these measurements, a cryogenic system was designed with large angular access ($\theta = 37.8^\circ$) over a 0.1 – 1 THz frequency band. This system, described in chapter 4, uses a commercial pulsetube cooler combined with a $^4\text{He}/^3\text{He}$ sorption cooler cold stage on which the device chip is mounted. Careful design of the optical access limits the thermal load on the cold stage to $\sim 6 \mu\text{W}$, which enables a base temperature of 265 mK with a hold time around 32 h.

The measured far field patterns are in good agreement with simulations down to -10 dB, showing a frequency dependent beam width as expected with a full width half maximum of 3.7° at 850 GHz and 8.3° at 350 GHz. We find an aperture efficiency of around $\eta_{ap} \approx 0.4$ over the whole antenna bandwidth, which represents the highest measured for a leaky-lens antenna at sub-millimeter wavelengths to date. This result is primarily limited by the

antenna radiation efficiency due to the absence of anti-reflection coating. The agreement between simulation and experiment show the validity of the design process, allowing the design of optimized lens-antennas for on-chip spectrometers or CMB applications.

Implementing a wideband anti-reflection(AR) coating could allow for a significant increase in optical efficiency up to 30 %. A possible solution for this would be the implementation of a multi-layer coating on the lens surface using a combination of different Stycast mixtures [129]. Such an AR-coating is currently in development, and preliminary results in a laboratory setting with a single Stycast layer are promising.

This work on the leaky-lens antenna shows the feasibility of broadband radiation detection within the entire relevant frequency window for far-infrared astronomy from the ground. The upper end of the measured 1 : 3 frequency band corresponds to the highest accessible frequency band for ground-based observations (~ 950 GHz) and is close to the limit of the NbTiN superconducting bandgap (~ 1.1 THz). Scaling to frequencies below 350 GHz is easily possible, and has already been achieved for a design at 240 – 720 GHz that is optimized for the optical system of the ASTE telescope in Chile [130].

8.2 On-chip Fabry-Pérot Resonator

In chapters 6 and 7 I discuss two implementations of the on-chip fabry-pérot resonator (FPR) as a flexible and sensitive tool to measure very low losses of superconducting transmission lines at sub-millimeter wavelengths and sub-Kelvin temperatures. The on-chip FPR consists of a long transmission line section terminated by two couplers on either end. On one end, it is coupled to a transmission line coming from a lens-antenna which can be illuminated with a tunable single frequency THz source, while the other end is coupled to an MKID acting as power detector. Losses in the FPRs are then obtained by measuring the resonance peaks in the transmission spectrum and extracting the internal quality factor Q_i from the loaded quality factor Q_L . This extraction of Q_i usually requires either an absolute power calibration or careful simulations to distinguish between Q_i and the coupling quality factor Q_c . However, both simulations and absolute power calibration at sub-millimeter wavelengths are difficult and error prone.

We introduce a new approach, where we implement four FPRs, identical in all aspects except for the resonator length, with independent feeding networks on a single chip. This allows us to extract Q_i and Q_c independently from a single measurement, eliminating the need of an absolute power calibration. This is possible due to the different mode-number dependencies of $Q_c \propto n$ and $Q_i \propto \text{const}$, which can be distinguished during analysis by combining the resonance peak data of all four on-chip FPRs.

This design is easily adaptable to different transmission line geometries, as all FPRs on a chip share the same coupler design, which can be changed independently of the feeding network, antenna and MKIDs. Therefore, only a single coupler design is required for a new chip to integrate the transmission line with an existing chip design. Additionally, only a simple change of the antenna design is required to access a different frequency range.

8.3 Transmission Line Losses

We applied the on-chip FPR concept to loss measurements of two different transmission line types, co-planar waveguides (CPW) and microstrips, described in chapters 6 and 7 respectively. These structures represent the most commonly used types in superconducting integrated circuits at sub-millimeter wavelengths. Losses for both transmission lines are measured in a narrow frequency band centered at 350 GHz.

Losses in CPWs are measured using the old approach, with a single FPR per chip and relying on simulations to account for the coupling quality factor. We design, fabricate and measure four chips, each containing a CPW-FPR of a different total line width ranging from $w_{tot} = 6.25 \mu\text{m}$ to $w_{tot} = 15.25 \mu\text{m}$. The CPWs are fabricated on top of a Sapphire substrate in a 100 nm thin NbTiN film with a surface inductance of $L_s = 1.03 \text{ pH}$.

We show that the high kinetic inductance of the superconducting CPW can suppress its radiation loss, measuring a significant loss reduction compared to the case of a perfect electric conductor, with a width dependence for the FPRs Q_i ranging from $(1.1 \pm 0.2) \times 10^3$ for $w_{tot} = 15.25 \mu\text{m}$ to $(1.7 \pm 0.4) \times 10^4$ for $w_{tot} = 6.25 \mu\text{m}$. These experimental results are in excellent agreement with simulations of the CPW radiation loss. This indicates the current analytical solutions to be incomplete, as these predict a complete elimination of radiation loss for the narrowest measured CPW. This is due to the guided mode being slower than the phase velocity in the sapphire substrate thereby preventing a radiation cone to form. We consider losses in the substrate layer, the superconducting film and at the coupler to be significantly lower than the measured value. The exact loss mechanism is unknown at this moment and would require theoretical and experimental follow-up investigations to determine. Simulations have shown, that losses continue to decrease with CPW width and that ultra narrow CPW lines ($w_{tot} \leq 3 \mu\text{m}$) based on thin NbTiN films should allow for $Q > 50,000$.

The measured loss of the narrowest CPW line is sufficiently small for it to be used in the feeding network of on-chip filterbanks like DESHIMA [33], where internal quality factors in the order of $Q_i > 10^4$ are usually required to avoid a significant reduction of the total system efficiency. For the filters themselves, no significant losses are introduced when the internal quality factor is much larger than the desired resolution $Q_i > 10R$. The measurement would therefore imply that the CPW can be used in a DESHIMA-like filterbank with $R \sim 500$, requiring $Q_i > 5,000$. However, the implementation in a filterbank introduces major issues which are not present in the measured FPR, as the parallel coupling of the filters to the line leads to imbalances in the CPW manifesting as highly radiative common mode excitations. This leads to significant losses in the CPW filters, making them not viable for use in an astronomical instrument.

A microstrip line, in contrast to a CPW, does not radiate strongly and supports only a single guided mode. Its performance is however expected to be limited by losses in the amorphous dielectric layer. Losses in a NbTiN/a-Si/NbTiN microstrip are measured using the new approach, with a single chip containing four FPR of varying length. We obtain an internal quality factor of the transmission line of $Q_i = 4.9 \pm 0.3 \times 10^3$, which we attribute primarily to two-level system (TLS) loss in the bulk dielectric characterized by

a slightly reduced quality factor $Q_{i,aSi}(350 \text{ GHz}) = 4.7 \pm 0.3 \times 10^3$ due to the fill factor of the dielectric. This corresponds to a loss tangent of a-Si $\tan \delta(350 \text{ GHz}) = 2.1 \pm 0.1 \times 10^{-4}$ in the single-photon regime.

The microstrip loss measurements are accompanied by experiments at microwave frequencies, using microwave resonators located on the same chip. These experiments show expected TLS-like behaviour in their power dependence, but we find a significantly lower single-photon loss tangent of $\tan \delta(6 \text{ GHz}) = 3.7 \pm 0.5 \times 10^{-5}$ which is in disagreement with the standard TLS model, where a frequency independent loss is predicted for this regime.

We consider two hypotheses to be the most likely explanations for this discrepancy. First, a modification of the TLS model with a frequency dependent density of states $N(E)$. Using the power-law suggested by Faoro et al. [126] comes close to a quantitative match. Second, it is possible that we observe the low-frequency tail of resonant phonon absorption peaks at far-infrared wavelengths. Room temperature measurements of SiO_x and SiN in the far-infrared regime indicate that such a low-frequency tail could have the relevant magnitude [127, 128]. Further experiments, discussed in 8.4.2 are required to distinguish these hypothesis.

The measured losses of a-Si at 350 GHz are low enough for this material to be used in the filterbank of a DESHIMA-like device with a resolution of $R \sim 500$, requiring $Q_i > 5,000$.

8.4 Future Outlook

8.4.1 Advanced Astronomical Instrumentation

Both the demonstration of low losses in the NbTiN/a-Si/NbTiN microstrip and the prototype for a high efficiency ultra wideband leaky-lens antenna are crucial building blocks which enable advanced superconducting integrated circuits (SICs), such as the next generation DESHIMA 2.0 on-chip filterbank.

Figure 8.1 shows pictures of a first prototype chip for DESHIMA 2.0 which has a 1 : 2 bandwidth at 220 – 440GHz, enabled by the leaky-lens antenna in this thesis. The filterbank, as shown in Figs. 8.1b-c), contains 357 bandpass filters made from NbTiN/a-Si/NbTiN microstrips. The microstrip design is based on the results of chapter 7, which showed sufficiently low dielectric losses for use in the filterbank, with $Q_{i,ms} = 4.9 \pm 0.3 \times 10^3$. For the terahertz feedline connecting antenna and filterbank, a low-loss narrow NbTiN CPW is used, transitioning into a microstrip near the filterbank. The CPW for this line is a direct implementation of the narrowest line presented in chapter 6, which has negligible losses with $Q_{i,cpw} = (1.7 \pm 0.4) \times 10^4$. The microwave kinetic inductance detectors (MKIDs) are based on the standard hybrid Al-NbTiN CPW design with a short microstrip section to facilitate coupling to the bandpass filter. This SIC design is strongly based on the loss data obtained in this thesis and builds on the strengths of the various transmission line types, where the complex design of the filterbank is enabled by the NbTiN/a-Si/NbTiN microstrips, while comparatively simple sections like the feedline are implemented with lower loss CPWs. The filters are made with microstrips and not planar technology, as

planar filters have been shown to radiate strongly due to their resonant structure and the presence of highly radiative common mode excitations [107, 37]. Microstrips do not suffer from these issues and are therefore the only viable option for the filters, despite the slightly larger measured losses of the FPR experiments.

DESHIMA 2.0 will represent a major breakthrough for sub-millimeter wave astronomy, as it allows measurements over a large frequency bandwidth using only a small readout bandwidth.

The next step beyond DESHIMA 2.0 will be instruments with multiple spatial pixels to take the final step to a terahertz integral field unit. Such an instrument can be envisioned by simply combining multiple pixels of DESHIMA 2.0, as shown in 8.2, where multiple filterbanks with a lens-antenna each are located on a single wafer-sized chip. Furthermore, on-chip fourier-transform spectrometers (FTS) with high spectral resolution of $R \sim 50,000$ could be realized based on the demonstrated on-chip FPR technology, by using extremely narrow CPW lines. Frequency tuning of the FTS can be achieved by applying a small DC current and exploiting the current dependence of a superconductors kinetic inductance.

8.4.2 Physics at Sub-millimeter Wavelengths

The flexibility of the on-chip Fabry-Pérot resonator system enables the exploration of various physical properties at sub-Kelvin temperatures and sub-millimeter wavelengths up to the bandgap of NbTiN at 1.1 THz.

Understanding the dominant loss mechanism for dielectric loss in this regime is important for pushing on-chip spectrometers to higher frequencies. Dedicated loss measurements up to 1.1 THz with microstrip lines are the best available method to study these losses in the full 0.1 – 1 THz band. This can be achieved with on-chip FPRs by simply exchanging the narrowband double-slot antenna with a wideband antenna such as the leaky-lens antenna of this thesis. The frequency dependence can then be obtained by splitting a single wideband measurement into multiple frequency bins which are analyzed separately analogous to chapter 7. Measuring the power dependence of losses at sub-millimeter wavelengths can also offer insights into the underlying physics, but the measurable power range is currently limited by MKID saturation. Saturation of the MKIDs can be solved to an extent by switching from Al to a different power-absorbing material within the hybrid MKID design, such as α -Ta, thereby increasing its power handling in exchange for worse sensitivity. The reduced sensitivity should not be an issue, as it is not a limiting factor in the current experiments. However, properly sampling the power dependence of two-level system limited losses requires covering multiple orders of magnitude in input power, which might prove difficult to achieve in practice.

Besides the dielectric properties, the on-chip FPR can also be used to probe the properties of the NbTiN films at frequencies up to the superconducting bandgap. This could provide insights into loss mechanisms close to the gap frequency, which are not well understood. Such an experiment would have to be based on very narrow CPW lines $w_{tot} \leq 3 \mu\text{m}$, in order to limit effects from radiation loss and avoid dielectric losses. The maximum accessible Q_i is currently limited to $Q_i \approx 20,000$ by the frequency resolution of the photomixer

terahertz source. This can however be improved by using a different source with better frequency resolution, such as a multipliers.

8.5 Impact of the Research

The work described in this thesis has led to a number of journal and conference publications. Moreover, a M.Sc. level thesis work was supervised with related topics to the work listed in this thesis.

The results presented in this thesis have enabled the design and fabrication of the next generation DESHIMA on-chip spectrometer, which will be fielded at the ASTE telescope in early 2022 [131]. This work will therefore enable new astronomical observations and insights.

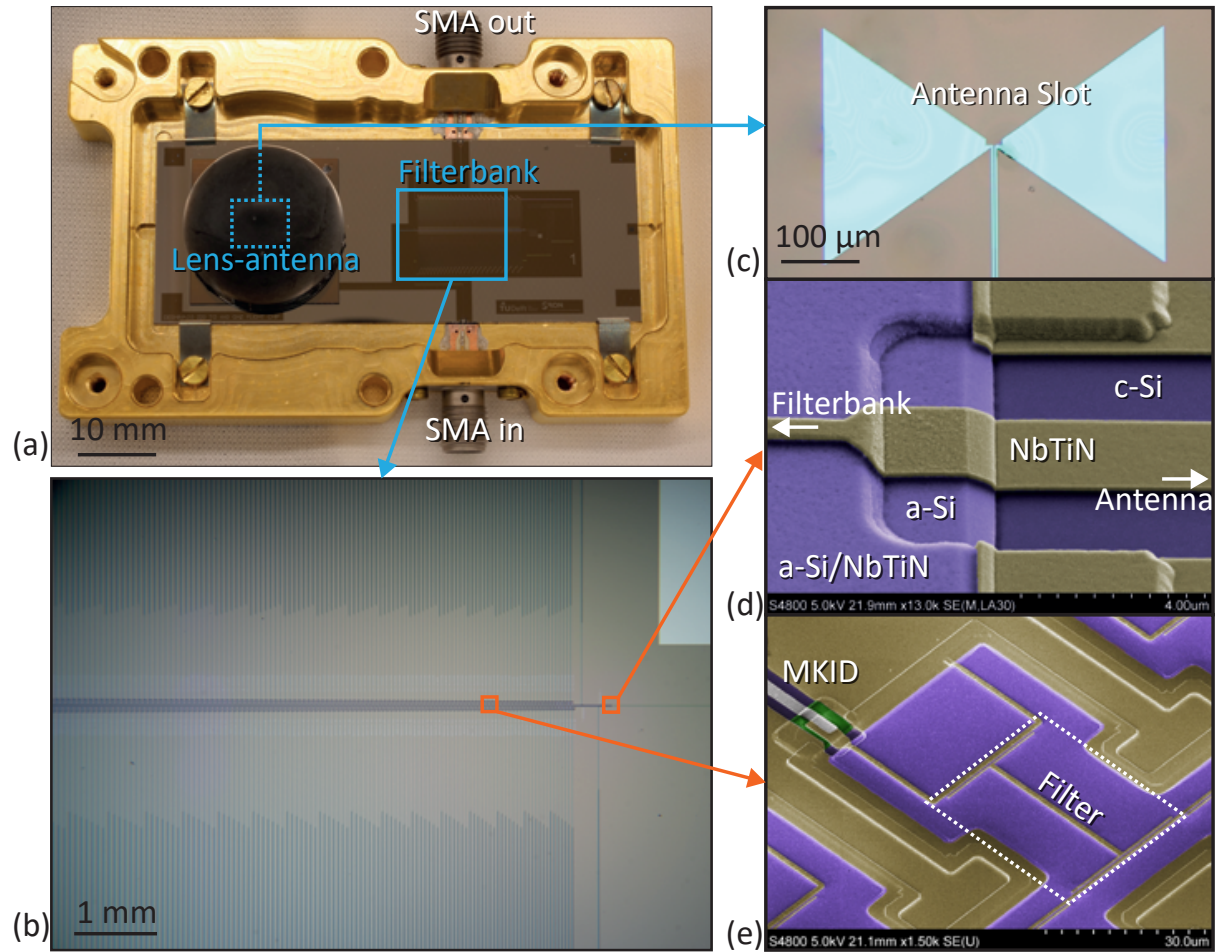


Figure 8.1: (a) Picture of a DESHIMA 2.0 including the silicon lens, mounted in a copper holder. (b) Close-up picture of the microstrip filterbank. The feed line from the antenna runs horizontally through the image and individual hybrid MKIDs are visible as vertical lines. (c) Backside illuminated picture of the Leaky-lens antenna on SiN membrane (before mounting of the lens). (d) False-color Scanning electron microscope (SEM) image of the CPW-microstrip transition before the filterbank. (e) False-color SEM image of a single filter in the filterbank.

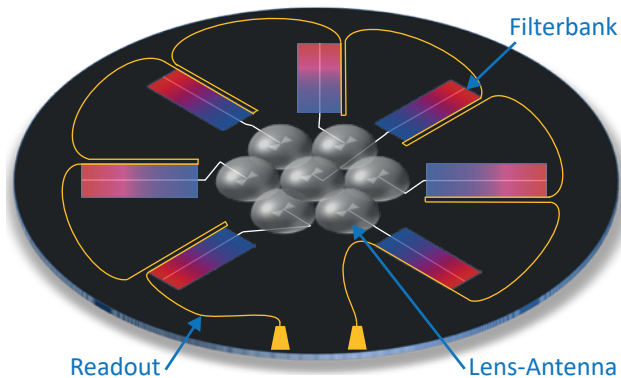


Figure 8.2: Concept design of a terahertz imaging spectrometer with 7 spatial pixels on a wafer-sized chip.

Appendix A

Process Flow Details

A.1 LT122: Leaky-Lens Antenna

1. The fabrication process starts with a 375 μm thick 4-inch Si wafer (dielectric constant $\epsilon_r = 11.44$ at cryogenic temperatures [120]) coated on both sides with a 1 μm thick, low tensile stress (~ 250 MPa) SiN layer ($\epsilon_r = 7$), deposited using low pressure chemical vapor deposition (LPCVD).
2. The SiN on the device side is etched with reactive ion etching (RIE) using 35 % SF_6 and 65 % O_2 to create a sloped edge.
 - Cleaning (organic contaminants): Piranha ($\text{H}_2\text{SO}_4:\text{H}_2\text{O}_2$ mixed 3:1) at 85 °C for 10 min.
 - SiN layer roughening.
 - RIE: 5 mTorr pressure, 50 W power, 345 V bias, 25 sccm O_2 -flow, 13.5 sccm SF_6 -flow, 10 s etch time .
 - Descum: 5 mTorr pressure, 50 W power, 260 V bias, 25 sccm O_2 -flow, 90 s etch time.
 - Patterning.
 - Resist coating: Resist type *AZ 6632* at 1800 rpm rotation speed for 30 s.
 - Soft bake on hotplate at 110 °C for 150 s.
 - Exposure: 435 mJ/cm² dose over 21.7 s.
 - Development: Developer type *AZ 351B*, 5:1 ratio water/developer, 60 s development time.
 - Hard bake at 120 °C for 60 s.
 - RIE.
 - SiN etch: 5 mTorr pressure, 50 W power, 345 V bias, 25 sccm O_2 -flow, 13.5 sccm SF_6 -flow, 27 min etch time .

- Descum: 100 mTorr pressure, 50 W power, 260 V bias, 25 sccm O₂-flow, 90 s etch time.
 - Resist removal: Spin wafer at 4002 rpm for 30 s and spray acetone.
 - Cleaning: Acetone bath for 2 min.
3. A 350 nm thick, virtually stress free NbTiN layer is deposited on the device side using reactive sputtering of a NbTi target in a Nitrogen-Argon atmosphere. The process was carried out in a Nordiko 2000 machine in the cleanroom of Kavli Nanolab at the TU Delft [78]. The film has a critical temperature $T_c = 14.9$ K and a resistivity of $\rho_n = 130 \mu\Omega \text{ cm}$.
- Cleaning (organic contaminants): Piranha at 85 °C for 10 min.
 - Cleaning (surface oxide): 10 % diluted HF at room temperature for 10 s.
 - Sputter deposition.
 - Presputter: 100 sccm Ar-flow, 7.5 sccm N₂-flow, 440 W power, 7.8 mTorr pressure, 326 ± 5 V for 240 s.
 - Sputter: 100 sccm Ar-flow, 7.5 sccm N₂-flow, 440 W power, 7.8 mTorr pressure, 343 ± 2 V for 245 s.
4. The NbTiN layer is patterned to form the antenna slot, MKID sections and the microwave readout line. It is then etched using the recipe of step 2.
- Patterning.
 - Resist coating: Resist type *AZ 6632* at 4000 rpm rotation speed for 30 s.
 - Soft bake on hotplate at 110 °C for 120 s.
 - Exposure: 203 mJ/cm² dose over 11.5 s.
 - Development: Developer type *AZ 351B*, 5:1 ratio water/developer, 60 s development time.
 - RIE.
 - NbTiN etch: 5 mTorr pressure, 50 W power, 345 V bias, 25 sccm O₂-flow, 13.5 sccm SF₆-flow, 14 min etch time .
 - Descum: 100 mTorr pressure, 50 W power, 260 V bias, 25 sccm O₂-flow, 90 s etch time
 - Resist removal: Spin wafer at 4002 rpm for 30 s and spray acetone.
 - Cleaning: Acetone bath for 2 min.
5. A 40 nm thick layer of β -phase Ta ($T_c \approx 0.6$ K) is deposited on the device side.
- Sputter deposition: 5 mTorr pressure, 876 W power, 56 s deposition time
6. The Ta layer is patterned and etched to form an absorbing mesh.

- Patterning.
 - Resist coating: Resist type *AZ 6612* at 4000 rpm rotation speed for 30 s.
 - Soft bake on hotplate at 110 °C for 60 s.
 - Exposure: 113 mJ/cm² dose over 6 s.
 - Development: Developer type *AZ 351B*, 5:1 ratio water/developer, 60 s development time.
 - RIE.
 - Ta etch: 10 mTorr pressure, 60 W power, 315 V bias, 30 sccm Ar-flow, 13.5 sccm SF₆-flow, 2 min etch time.
 - Descum: 100 mTorr pressure, 50 W power, 260 V bias, 25 sccm CHF₃-flow, 30 s
 - O₂ Etch: 100 mTorr pressure, 50 W power, 260 V bias, 25 sccm O₂-flow, 30 s
 - Resist removal: Spin wafer at 4002 rpm for 30 s and spray acetone.
7. A 1 μm thick layer of polyimide LTC9505 is spin coated on the wafer.
- Coating: Polyimide *LTC9505* at 5500 rpm rotation speed for 45 s.
 - Soft bake on hotplate at 100 °C for 180 s.
8. The polyimide layer is patterned and cured into dielectric supports for the bridges along the microwave readout line.
- Exposure: 210 mJ/cm² dose over 10.5 s.
 - Development: 3 Baths
 - Bath 1: Developer type *HTRD2* for 70 s
 - Bath 2: Mixture 1:1 (*HTRD2:RER600*) for 70 s
 - Bath 3: Developer type *RER600* for 30 s
 - Cleaning in oxygen plasma: 100 mTorr pressure, 50 W power, 260 V bias, 25 sccm O₂-flow, 30 s etch time
 - Cure in oven at 250 °C for 3 h.
9. A 50 nm thick layer of Al ($T_c = 1.25$ K) is deposited.
- Cleaning in oxygen plasma: 100 mTorr pressure, 50 W power, 260 V bias, 25 sccm O₂-flow, 30 s etch time
 - Cleaning (surface oxides): 1 % diluted HF at room temperature for 60 s.
 - Al sputter deposition: 5 mTorr pressure, 876 W power, ≈ 100 s deposition time.

10. The Al layer is patterned to form the hybrid MKID center line and bridges along the microwave readout line. The layer is wet etched using TechniEtch Al80 Al etchant (*Microchemicals GmbH*).
 - Dehydration bake at 110 °C for 120 s.
 - Resist coating: Resist type *AZ 1518* at 4000 rpm rotation speed for 30 s.
 - Soft bake on hotplate at 110 °C for 90 s.
 - Exposure: 100 mJ/cm² dose over 5 s.
 - Development: Developer type *AZ Developer*, 1:1 ratio water/developer, 40 s development time.
 - Hard bake at 125 °C for 75 s.
 - Cleaning in oxygen plasma: 100 mTorr pressure, 50 W power, 260 V bias, 25 sccm O₂-flow, 30 s etch time
 - Etching with TechniEtch Al80 for 90 s.
 - Resist removal: Spin wafer at 4002 rpm for 30 s and spray acetone.
11. The backside SiN is patterned and etched to create a hard mask for the Si removal in the next step.
 - Patterning.
 - Resist coating: Resist type *AZ 6632* at 4000 rpm rotation speed for 30 s.
 - Soft bake on hotplate at 110 °C for 120 s.
 - Exposure: 225 mJ/cm² dose over 15 s.
 - Development: Developer type *AZ 351B*, 5:1 ratio water/developer, 60 s development time.
 - RIE.
 - SiN etch: 5 mTorr pressure, 50 W power, 345 V bias, 25 sccm O₂-flow, 13.5 sccm SF₆-flow, 27 min etch time .
 - Descum: 100 mTorr pressure, 50 W power, 260 V bias, 100 sccm O₂-flow,, 15 sccm CHF₃-flow, 30 s etch time
 - O₂ Etch: 100 mTorr pressure, 50 W power, 260 V bias, 100 sccm O₂-flow, 30 s
 - Resist removal: Spin wafer at 4002 rpm for 30 s and spray acetone.
 - Cleaning: Acetone bath for 2 min.
12. The Si wafer is etched in a KOH bath to create the membrane opening from the backside. The device side is protected with a commercial protection tool.
 - Protective resist coating: Resist type *AZ 6632* at 4000 rpm rotation speed for 30 s.

- KOH etching (using KOH protection tool): KOH solution of 25 %, chemical mix of 1000 g KOH and 3 L water, at 75 °C.
 - Rinse in UP water.
 - Cleaning (RCA2/SC2): RCA2/SC2 (HCL:H₂O₂:water mixed 1:1:5) at 70 °C for 10 min.
13. A 40 nm thick layer of β -phase Ta is deposited on the backside analogous to step 5.
- Sputter deposition: 5 mTorr pressure, 876 W power, 56 s deposition time
14. The Ta layer on the backside is patterned and etched analogous to step 6.
- Patterning.
 - Resist coating: Resist type *AZ 6612* at 4000 rpm rotation speed for 30 s.
 - Soft bake on hotplate at 110 °C for 60 s.
 - Exposure: 113 mJ/cm² dose over 6 s.
 - Development: Developer type *AZ 351B*, 5:1 ratio water/developer, 60 s development time.
 - RIE.
 - Ta etch: 10 mTorr pressure, 60 W power, 315 V bias, 30 sccm Ar-flow, 13.5 sccm SF₆-flow, 2 min etch time.
 - Descum: 100 mTorr pressure, 50 W power, 260 V bias, 25 sccm CHF₃-flow, 30 s
 - O₂ Etch: 100 mTorr pressure, 50 W power, 260 V bias, 25 sccm O₂-flow, 30 s
 - Resist removal: Spin wafer at 4002 rpm for 30 s and spray acetone.

A.2 LT121: Co-Planar Waveguide Fabry-Perot

1. The fabrication process starts with a 350 μm C-plane Sapphire wafer ($\epsilon_r^C = 11.5$, $\epsilon_r^{AB} = 9.3$).
2. A 100 nm thick NbTiN layer ($T_c = 14.7$ K, $\rho_n = 102 \mu\Omega \text{ cm}$) is deposited on the device side using reactive sputtering of a NbTi target in a Nitrogen-Argon atmosphere. The process was carried out in a Evatec LLS801 machine in the cleanroom of SRON in Utrecht using the static deposition method as detailed by Thoen et al. [78].
 - Cleaning (organic contaminants): H₃PO₄ (pure) at 110 °C for 30 min.
 - Sputter deposition.
 - Presputter: 100 sccm Ar-flow, 7.5 sccm N₂-flow, 440 W power, 7.8 mTorr pressure, 326 ± 5 V for 240 s.

- Sputter: 100 sccm Ar-flow, 7.5 sccm N₂-flow, 440 W power, 7.8 mTorr pressure, 343 ± 2 V for 245 s.
3. The NbTiN layer is patterned to form the antenna slot, the Fabry-Perot resonator line, MKID sections and the microwave readout line. It is then etched with reactive ion etching (RIE) using 35 % SF₆ and 65 % O₂ to create a sloped edge.
 - Patterning.
 - Resist coating: Resist type *AZ 6632* at 4000 rpm rotation speed for 30 s.
 - Soft bake on hotplate at 110 °C for 120 s.
 - Exposure: 203 mJ/cm² dose over 11.5 s.
 - Development: Developer type *AZ 351B*, 5:1 ratio water/developer, 60 s development time.
 - RIE.
 - NbTiN etch: 5 mTorr pressure, 50 W power, 345 V bias, 25 sccm O₂-flow, 13.5 sccm SF₆-flow, 14 min etch time .
 - Descum: 100 mTorr pressure, 50 W power, 260 V bias, 25 sccm O₂-flow, 90 s etch time
 - Resist removal: Spin wafer at 4002 rpm for 30 s and spray acetone.
 - Cleaning: Acetone bath for 2 min.
 4. A 1 µm thick layer of polyimide LTC9505 is spin coated on the wafer.
 - Coating: Polyimide *LTC9505* at 5500 rpm rotation speed for 45 s.
 - Soft bake on hotplate at 100 °C for 180 s.
 5. The polyimide layer is patterned and cured into dielectric supports for the bridges along the microwave readout line.
 - Exposure: 210 mJ/cm² dose over 10.5 s.
 - Development: 3 Baths
 - Bath 1: Developer type *HTRD2* for 70 s
 - Bath 2: Mixture 1:1 (*HTRD2:RER600*) for 70 s
 - Bath 3: Developer type *RER600* for 30 s
 - Cleaning in oxygen plasma: 100 mTorr pressure, 50 W power, 260 V bias, 25 sccm O₂-flow, 30 s etch time
 - Cure in oven at 250 °C for 3 h.
 6. A 40 nm thick layer of Al ($T_c = 1.28$ K) is deposited.
 - Cleaning in oxygen plasma: 100 mTorr pressure, 50 W power, 260 V bias, 25 sccm O₂-flow, 30 s etch time

- Cleaning (surface oxides): 1 % diluted HF at room temperature for 60 s.
 - Al sputter deposition: 5 mTorr pressure, 876 W power, 108 s deposition time.
7. The Al layer is patterned to form the hybrid MKID center line and bridges along the microwave readout line. The layer is wet etched using TechniEtch Al80 Al etchant (*Microchemicals GmbH*).
- Dehydration bake at 110 °C for 120 s.
 - Resist coating: Resist type *AZ 1518* at 4000 rpm rotation speed for 30 s.
 - Soft bake on hotplate at 110 °C for 90 s.
 - Exposure: 100 mJ/cm² dose over 5 s.
 - Development: Developer type *AZ Developer*, 1:1 ratio water/developer, 40 s development time.
 - Hard bake at 125 °C for 75 s.
 - Cleaning in oxygen plasma: 100 mTorr pressure, 50 W power, 260 V bias, 25 sccm O₂-flow, 30 s etch time
 - Etching with TechniEtch Al80 for 90 s.
 - Resist removal: Spin wafer at 4002 rpm for 30 s and spray acetone.
8. A 40 nm thick layer of β -phase Ta ($T_c \approx 0.6$ K) is deposited on the backside.
- Cleaning in oxygen plasma: 100 mTorr pressure, 50 W power, 260 V bias, 25 sccm O₂-flow, 4 min etch time
 - Sputter deposition: 5 mTorr pressure, 876 W power, 56 s deposition time.
9. The Ta layer on the backside is patterned and etched to create an absorbing mesh.
- Patterning.
 - Resist coating: Resist type *AZ 6612* at 4000 rpm rotation speed for 30 s.
 - Soft bake on hotplate at 110 °C for 60 s.
 - Exposure: 113 mJ/cm² dose over 6 s.
 - Development: Developer type *AZ 351B*, 5:1 ratio water/developer, 60 s development time.
 - RIE.
 - Ta etch: 10 mTorr pressure, 60 W power, 315 V bias, 30 sccm Ar-flow, 13.5 sccm SF₆-flow, 2 min etch time.
 - Descum: 100 mTorr pressure, 50 W power, 260 V bias, 25 sccm CHF₃-flow, 30 s
 - O₂ Etch: 100 mTorr pressure, 50 W power, 260 V bias, 25 sccm O₂-flow, 30 s
 - Resist removal: Spin wafer at 4002 rpm for 30 s and spray acetone.

A.3 LT189: Microstrip Fabry-Perot

1. The fabrication process starts with a 350 μm thick 4-inch Si wafer (dielectric constant $\epsilon_r = 11.44$ at cryogenic temperatures [120]) coated on both sides with a 0.3 μm thick, low tensile stress (~ 250 MPa) SiN layer ($\epsilon_r = 7$), deposited using low pressure chemical vapor deposition (LPCVD).
2. The SiN on the device side is etched with reactive ion etching (RIE) using 35 % SF_6 and 65 % O_2 to create a sloped edge.
 - Cleaning (organic contaminants): Piranha ($\text{H}_2\text{SO}_4:\text{H}_2\text{O}_2$ mixed 3:1) at 85 °C for 5 min.
 - SiN layer roughening.
 - RIE: 5 mTorr pressure, 50 W power, 345 V bias, 25 sccm O_2 -flow, 13.5 sccm SF_6 -flow, 10 s etch time .
 - Descum: 5 mTorr pressure, 50 W power, 260 V bias, 25 sccm O_2 -flow, 90 s etch time.
 - Patterning.
 - Resist coating: Resist type *ECI 3027* at 4000 rpm rotation speed for 30 s.
 - Soft bake on hotplate at 110 °C for 120 s.
 - Exposure: 200 mJ/cm^2 dose over 10 s.
 - Development: Developer type *AZ 351B*, 5:1 ratio water/developer, 60 s development time.
 - Hard bake at 120 °C for 60 s.
 - RIE.
 - SiN etch: 5 mTorr pressure, 50 W power, 345 V bias, 25 sccm O_2 -flow, 13.5 sccm SF_6 -flow, 10 min etch time .
 - Descum: 100 mTorr pressure, 50 W power, 260 V bias, 25 sccm O_2 -flow, 90 s etch time.
 - Resist removal: Spin wafer at 4002 rpm for 30 s and spray acetone.
 - Cleaning: Acetone bath for 2 min.
3. A 220 nm thick NbTiN layer ($T_c = 14.7$ K, $\rho_n = 102 \mu\Omega \text{ cm}$) is deposited on the device side using reactive sputtering of a NbTi target in a Nitrogen-Argon atmosphere. The process was carried out in a Evatec LLS801 machine in the cleanroom of SRON in Utrecht using the static deposition method as detailed by Thoen et al. [78].
 - Cleaning (organic contaminants): Piranha at 85 °C for 10 min.
 - Cleaning (surface oxide): 10 % diluted HF at room temperature for 10 s.
 - Sputter deposition.

- Presputter: 100 sccm Ar-flow, 7.5 sccm N₂-flow, 440 W power, 7.8 mTorr pressure, 326 ± 5 V for 240 s.
 - Sputter: 100 sccm Ar-flow, 7.5 sccm N₂-flow, 440 W power, 7.8 mTorr pressure, 343 ± 2 V for 245 s.
4. The NbTiN layer is patterned to form the antenna slot, the Fabry-Perot resonator line, MKID sections and the microwave readout line. It is then etched using the same recipe as step 2.
- Patterning.
 - Resist coating: Resist type *AZ 6632* at 4000 rpm rotation speed for 30 s.
 - Soft bake on hotplate at 110 °C for 120 s.
 - Exposure: 203 mJ/cm² dose over 11.5 s.
 - Development: Developer type *AZ 351B*, 5:1 ratio water/developer, 60 s development time.
 - RIE.
 - NbTiN etch: 5 mTorr pressure, 50 W power, 345 V bias, 25 sccm O₂-flow, 13.5 sccm SF₆-flow, 9 min etch time .
 - Descum: 100 mTorr pressure, 50 W power, 260 V bias, 25 sccm O₂-flow, 90 s etch time
 - Resist removal: Spin wafer at 4002 rpm for 30 s and spray acetone.
 - Cleaning: Acetone bath for 2 min.
 - Cleaning (AZ100 remover): AZ100 remover at 80 °C for 5 min
 - Cleaning (Surface oxide removal and hydrogen passivation): 10 % diluted HF at room temperature for 30 s.
5. A 250 nm thick a-Si layer $\epsilon_r \approx 10$. is deposited using plasma enhanced chemical vapor deposition (PECVD). This process was carried out in the cleanroom of the KAVLI institute at the TU Delft.
- Cleaning (Surface oxide removal and hydrogen passivation): 10 % diluted HF at room temperature for 10 s.
 - PECVD deposition: 250 nm over 7 min and 9 s at 250 °C.
6. The a-Si layer is patterned and etched, defining the dielectric layer of the microstrip using the same recipe as step 2. As the process is not selective against NbTiN, the lower NbTiN will experience overetch in places where a-Si is removed. This is accounted for in the chosen NbTiN layer thickness during the design process.
- Resist coating: Resist type *ECI3027* at 4000 rpm rotation speed for 30 s.
 - Soft bake on hotplate at 110 °C for 120 s.

- Exposure: 160 mJ/cm² dose over 10 s.
 - Development: Developer type *AZ 351B*, 5:1 ratio water/developer, 60 s development time.
 - RIE.
 - a-Si etch: 5 mTorr pressure, 50 W power, 345 V bias, 25 sccm O₂-flow, 13.5 sccm SF₆-flow, 8 min etch time .
 - Descum: 100 mTorr pressure, 50 W power, 260 V bias, 25 sccm O₂-flow, 90 s etch time
 - Resist removal: Spin wafer at 4002 rpm for 30 s and spray acetone.
 - Cleaning: Acetone bath for 2 min.
7. A second NbTiN layer of 100 nm is deposited using the same process as step 3.
- Cleaning (AZ100 remover): AZ100 remover at 85 °C for 5 min.
 - Cleaning (surface oxide): 10 % diluted HF at room temperature for 10 s.
 - Sputter deposition.
 - Presputter: 100 sccm Ar-flow, 7.5 sccm N₂-flow, 440 W power, 7.8 mTorr pressure, 326 ± 5V for 240 s.
 - Sputter: 100 sccm Ar-flow, 7.5 sccm N₂-flow, 440 W power, 7.8 mTorr pressure, 343 ± 2V for 245 s.
8. The NbTiN layer is patterned and etched to form the microstrip line using the same process as step 2. Overetch will occur analogous to step 6, which is also accounted for during the design process.
- Patterning.
 - Resist coating: Resist type *AZ 6632* at 4000 rpm rotation speed for 30 s.
 - Soft bake on hotplate at 110 °C for 120 s.
 - Exposure: 140 mJ/cm² dose over 7 s.
 - Development: Developer type *AZ 351B*, 5:1 ratio water/developer, 60 s development time.
 - RIE.
 - NbTiN etch: 5 mTorr pressure, 50 W power, 345 V bias, 25 sccm O₂-flow, 13.5 sccm SF₆-flow, 7 min etch time .
 - Descum: 100 mTorr pressure, 50 W power, 260 V bias, 25 sccm O₂-flow, 90 s etch time
 - Resist removal: Spin wafer at 4002 rpm for 30 s and spray acetone.
 - Cleaning: Acetone bath for 2 min.

9. A 1 μm thick layer of polyimide LTC9505 is spin coated on the wafer.
 - Coating: Polyimide *LTC9505* at 5500 rpm rotation speed for 45 s.
 - Soft bake on hotplate at 100 °C for 180 s.
10. The polyimide layer is patterned and cured into dielectric supports for the bridges along the microwave readout line.
 - Exposure: 210 mJ/cm² dose over 10.5 s.
 - Development: 3 Baths
 - Bath 1: Developer type *HTRD2* for 70 s
 - Bath 2: Mixture 1:1 (*HTRD2:RER600*) for 70 s
 - Bath 3: Developer type *RER600* for 30 s
 - Cleaning in oxygen plasma: 100 mTorr pressure, 50 W power, 260 V bias, 25 sccm O₂-flow, 30 s etch time
 - Cure in oven at 250 °C for 3 h.
11. A 50 nm thick layer of Al ($T_c = 1.28$ K) is deposited.
 - Cleaning in oxygen plasma: 100 mTorr pressure, 50 W power, 260 V bias, 25 sccm O₂-flow, 30 s etch time
 - Cleaning (surface oxides): 1 % diluted HF at room temperature for 60 s.
 - Al sputter deposition: 5 mTorr pressure, 876 W power, 108 s deposition time.
12. The Al layer is patterned to form the hybrid MKID center line and bridges along the microwave readout line. The layer is wet etched using TechniEtch Al80 Al etchant (*Microchemicals GmbH*).
 - Dehydration bake at 110 °C for 120 s.
 - Resist coating: Resist type *AZ 1518* at 4000 rpm rotation speed for 30 s.
 - Soft bake on hotplate at 110 °C for 90 s.
 - Exposure: 100 mJ/cm² dose over 5 s.
 - Development: Developer type *AZ Developer*, 1:1 ratio water/developer, 40 s development time.
 - Hard bake at 125 °C for 75 s.
 - Cleaning in oxygen plasma: 100 mTorr pressure, 50 W power, 260 V bias, 25 sccm O₂-flow, 30 s etch time
 - Etching with TechniEtch Al80 for 90 s.
 - Resist removal: Spin wafer at 4002 rpm for 30 s and spray acetone.

13. A 40 nm thick layer of β -phase Ta ($T_c \approx 0.6$ K) is deposited on the backside.
 - Cleaning in oxygen plasma: 100 mTorr pressure, 50 W power, 260 V bias, 25 sccm O₂-flow, 4 min etch time
 - Sputter deposition: 5 mTorr pressure, 876 W power, 56 s deposition time.
14. The Ta layer on the backside is patterned and etched to create an absorbing mesh
 - Patterning.
 - Resist coating: Resist type *AZ 6612* at 4000 rpm rotation speed for 30 s.
 - Soft bake on hotplate at 110 °C for 60 s.
 - Exposure: 113 mJ/cm² dose over 6 s.
 - Development: Developer type *AZ 351B*, 5:1 ratio water/developer, 60 s development time.
 - RIE.
 - Ta etch: 10 mTorr pressure, 60 W power, 315 V bias, 30 sccm Ar-flow, 13.5 sccm SF₆-flow, 2 min etch time.
 - Descum: 100 mTorr pressure, 50 W power, 260 V bias, 25 sccm CHF₃-flow, 30 s
 - O₂ Etch: 100 mTorr pressure, 50 W power, 260 V bias, 25 sccm O₂-flow, 30 s
 - Resist removal: Spin wafer at 4002 rpm for 30 s and spray acetone.

References

- [1] ALMA Partnership, C. L. Brogan, L. M. Pérez, T. R. Hunter, W. R. F. Dent, A. S. Hales, R. E. Hills, S. Corder, E. B. Fomalont, C. Vlahakis, Y. Asaki, D. Barkats, A. Hirota, J. A. Hodge, C. M. V. Impellizzeri, R. Kneissl, E. Liuzzo, R. Lucas, N. Marcelino, S. Matsushita, K. Nakanishi, N. Phillips, A. M. S. Richards, I. Toledo, R. Aladro, D. Broguiere, J. R. Cortes, P. C. Cortes, D. Espada, F. Galarza, D. Garcia-Appadoo, L. Guzman-Ramirez, E. M. Humphreys, T. Jung, S. Kamenon, R. A. Laing, S. Leon, G. Marconi, A. Mignano, B. Nikolic, L. A. Nyman, M. Radiszcz, A. Remijan, J. A. Rodón, T. Sawada, S. Takahashi, R. P. J. Tilanus, B. Vila Vilaro, L. C. Watson, T. Wiklind, E. Akiyama, E. Chapillon, I. de Gregorio-Monsalvo, J. Di Francesco, F. Gueth, A. Kawamura, C. F. Lee, Q. Nguyen Luong, J. Mangum, V. Pietu, P. Sanhueza, K. Saigo, S. Takakuwa, C. Ubach, T. van Kempen, A. Wootten, A. Castro-Carrizo, H. Francke, J. Gallardo, J. Garcia, S. Gonzalez, T. Hill, T. Kaminski, Y. Kurono, H. Y. Liu, C. Lopez, F. Morales, K. Plarre, G. Schieven, L. Testi, L. Videla, E. Villard, P. Andreani, J. E. Hibbard, and K. Tatematsu, “The 2014 ALMA Long Baseline Campaign: First Results from High Angular Resolution Observations toward the HL Tau Region,” *Astrophys. J. Lett.*, vol. 808, no. 1, pp. L3, July 2015.
- [2] Aigen Li and B. T. Draine, “Infrared Emission from Interstellar Dust. II. The Diffuse Interstellar Medium,” *Astrophys. J.*, vol. 554, no. 2, pp. 778–802, June 2001.
- [3] C. J. Lonsdale, D. Farrah, and H. E. Smith, “Ultraluminous Infrared Galaxies,” *Astrophysics Update* 2, p. 285, 2006.
- [4] Planck Collaboration, Aghanim, N., Akrami, Y., Arroja, F., Ashdown, M., Aumont, J., Baccigalupi, C., Ballardini, M., Banday, A. J., Barreiro, R. B., Bartolo, N., Basak, S., Battye, R., Benabed, K., Bernard, J.-P., Bersanelli, M., Bielewicz, P., Bock, J. J., Bond, J. R., Borrill, J., Bouchet, F. R., Boulanger, F., Bucher, M., Burigana, C., Butler, R. C., Calabrese, E., Cardoso, J.-F., Carron, J., Casaponsa, B., Challinor, A., Chiang, H. C., Colombo, L. P. L., Combet, C., Contreras, D., Crill, B. P., Cuttaia, F., de Bernardis, P., de Zotti, G., Delabrouille, J., Delouis, J.-M., Désert, F.-X., Di Valentino, E., Dickinson, C., Diego, J. M., Donzelli, S., Doré, O., Douspis, M., Ducout, A., Dupac, X., Efstathiou, G., Elsner, F., Enßlin, T. A., Eriksen, H. K., Falgarone, E., Fantaye, Y., Fergusson, J., Fernandez-Cobos, R., Finelli, F., Forastieri,

- F., Frailis, M., Franceschi, E., Frolov, A., Galeotta, S., Galli, S., Ganga, K., Génova-Santos, R. T., Gerbino, M., Ghosh, T., González-Nuevo, J., Górski, K. M., Gratton, S., Gruppuso, A., Gudmundsson, J. E., Hamann, J., Handley, W., Hansen, F. K., Helou, G., Herranz, D., Hildebrandt, S. R., Hivon, E., Huang, Z., Jaffe, A. H., Jones, W. C., Karakci, A., Keihänen, E., Keskitalo, R., Kiiveri, K., Kim, J., Kisner, T. S., Knox, L., Krachmalnicoff, N., Kunz, M., Kurki-Suonio, H., Lagache, G., Lamarre, J.-M., Langer, M., Lasenby, A., Lattanzi, M., Lawrence, C. R., Le Jeune, M., Leahy, J. P., Lesgourgues, J., Levrier, F., Lewis, A., Liguori, M., Lilje, P. B., Lilley, M., Lindholm, V., López-Caniego, M., Lubin, P. M., Ma, Y.-Z., Macías-Pérez, J. F., Maggio, G., Maino, D., Mandolesi, N., Mangilli, A., Marcos-Caballero, A., Maris, M., Martin, P. G., Martinelli, M., Martínez-González, E., Matarrese, S., Mauri, N., McEwen, J. D., Meerburg, P. D., Meinhold, P. R., Melchiorri, A., Mennella, A., Migliaccio, M., Millea, M., Mitra, S., Miville-Deschênes, M.-A., Molinari, D., Moneti, A., Montier, L., Morgante, G., Moss, A., Mottet, S., Münchmeyer, M., Natoli, P., Nørgaard-Nielsen, H. U., Oxborrow, C. A., Pagano, L., Paoletti, D., Partridge, B., Patanchon, G., Pearson, T. J., Peel, M., Peiris, H. V., Perrotta, F., Pettorino, V., Piacentini, F., Polastri, L., Polenta, G., Puget, J.-L., Rachen, J. P., Reinecke, M., Remazeilles, M., Renault, C., Renzi, A., Rocha, G., Rosset, C., Roudier, G., Rubiño-Martín, J. A., Ruiz-Granados, B., Salvati, L., Sandri, M., Savelainen, M., Scott, D., Shellard, E. P. S., Shiraishi, M., Sirignano, C., Sirri, G., Spencer, L. D., Sunyaev, R., Suur-Uski, A.-S., Tauber, J. A., Tavagnacco, D., Tenti, M., Terenzi, L., Toffolatti, L., Tomasi, M., Trombetti, T., Valiviita, J., Van Tent, B., Vibert, L., Vielva, P., Villa, F., Vittorio, N., Wandelt, B. D., Wehus, I. K., White, M., White, S. D. M., Zacchei, A., and Zonca, A., “Planck 2018 results - i. overview and the cosmological legacy of planck,” *A&A*, vol. 641, pp. A1, 2020.
- [5] Daniel Baumann, Mark G. Jackson, Peter Adshead, Alexandre Amblard, Amjad Ashoorioon, Nicola Bartolo, Rachel Bean, Maria Beltrán, Francesco de Bernardis, Simeon Bird, Xingang Chen, Daniel J. H. Chung, Loris Colombo, Asantha Cooray, Paolo Creminelli, Scott Dodelson, Joanna Dunkley, Cora Dvorkin, Richard Easther, Fabio Finelli, Raphael Flauger, Mark P. Hertzberg, Katherine Jones-Smith, Shamit Kachru, Kenji Kadota, Justin Khoury, William H. Kinney, Eiichiro Komatsu, Lawrence M. Krauss, Julien Lesgourgues, Andrew Liddle, Michele Liguori, Eugene Lim, Andrei Linde, Sabino Matarrese, Harsh Mathur, Liam McAllister, Alessandro Melchiorri, Alberto Nicolis, Luca Pagano, Hiranya V. Peiris, Marco Peloso, Levon Pogosian, Elena Pierpaoli, Antonio Riotto, Uroš Seljak, Leonardo Senatore, Sarah Shandera, Eva Silverstein, Tristan Smith, Pascal Vaudrevange, Licia Verde, Ben Wandelt, David Wands, Scott Watson, Mark Wyman, Amit Yadav, Wessel Valkenburg, and Matias Zaldarriaga, “Probing Inflation with CMB Polarization,” in *CMB Polarization Workshop: Theory and Foregrounds: CMBPol Mission Concept Study*, Scott Dodelson, Daniel Baumann, Asantha Cooray, Joanna Dunkley, Aurelien Fraisse, Mark G. Jackson, Alan Kogut, Lawrence Krauss, Matias Zaldarriaga, and Kendrick Smith, Eds., June 2009, vol. 1141 of *American Institute of Physics*

- Conference Series*, pp. 10–120.
- [6] L. Page, G. Hinshaw, E. Komatsu, M. R.olta, D. N. Spergel, C. L. Bennett, C. Barnes, R. Bean, O. Doré, J. Dunkley, M. Halpern, R. S. Hill, N. Jarosik, A. Kogut, M. Limon, S. S. Meyer, N. Odegard, H. V. Peiris, G. S. Tucker, L. Verde, J. L. Weiland, E. Wollack, and E. L. Wright, “Three-Year Wilkinson Microwave Anisotropy Probe (WMAP) Observations: Polarization Analysis,” *ApJS*, vol. 170, no. 2, pp. 335–376, June 2007.
 - [7] Planck Collaboration, “Planck 2015 results - xv. gravitational lensing,” *A&A*, vol. 594, pp. A15, 2016.
 - [8] R. A. Sunyaev and Ya. B. Zeldovich, “The Observations of Relic Radiation as a Test of the Nature of X-Ray Radiation from the Clusters of Galaxies,” *Comments on Astrophysics and Space Physics*, vol. 4, pp. 173, Nov. 1972.
 - [9] Tony Mroczkowski, Daisuke Nagai, Kaustuv Basu, Jens Chluba, Jack Sayers, Rémi Adam, Eugene Churazov, Abigail Crites, Luca Di Mascolo, Dominique Eckert, Juan Macias-Perez, Frédéric Mayet, Laurence Perotto, Etienne Pointecouteau, Charles Romero, Florian Ruppen, Evan Scannapieco, and John ZuHone, “Astrophysics with the Spatially and Spectrally Resolved Sunyaev-Zeldovich Effects. A Millimetre/Submillimetre Probe of the Warm and Hot Universe,” *Space Sci Rev*, vol. 215, no. 1, pp. 17, Feb. 2019.
 - [10] Caitlin M. Casey, Desika Narayanan, and Asantha Cooray, “Dusty star-forming galaxies at high redshift,” *Physics reports*, vol. 541, no. 2, pp. 45–161, Aug. 2014.
 - [11] H. Dole, G. Lagache, J. L. Puget, K. I. Caputi, N. Fernández-Conde, E. Le Floc’h, C. Papovich, P. G. Pérez-González, G. H. Rieke, and M. Blaylock, “The cosmic infrared background resolved by Spitzer. Contributions of mid-infrared galaxies to the far-infrared background,” *A&A*, vol. 451, no. 2, pp. 417–429, May 2006.
 - [12] Planck Collaboration, “Planck 2013 results. XXIX. The Planck catalogue of Sunyaev-Zeldovich sources,” *A&A*, vol. 571, pp. A29, Nov. 2014.
 - [13] B. D. Jackson, G. de Lange, T. Zijlstra, M. Kroug, T. M. Klapwijk, and J. A. Stern, “Niobium titanium nitride-based superconductor-insulator-superconductor mixers for low-noise terahertz receivers,” *Journal of Applied Physics*, vol. 97, no. 11, pp. 113904–113904–8, June 2005.
 - [14] Paul F. Goldsmith, “Sub-Millimeter Heterodyne Focal-Plane Arrays for High-Resolution Astronomical Spectroscopy,” *URSI Radio Science Bulletin*, vol. 362, pp. 53–73, Sept. 2017.
 - [15] Christopher Groppi, Christopher Walker, Craig Kulesa, Dathon Golish, Jenna Kloosterman, Sander Weinreb, Glenn Jones, Joseph Bardin, Hamdi Mani, Tom

- Kuiper, Jacob Kooi, Art Lichtenberger, Thomas Cecil, Patrick Puetz, Gopal Narayanan, and Abigail Hedden, “Test and integration results from SuperCam: a 64-pixel array receiver for the 350 GHz atmospheric window,” in *Millimeter, Submillimeter, and Far-Infrared Detectors and Instrumentation for Astronomy V*, Wayne S. Holland and Jonas Zmuidzinas, Eds., July 2010, vol. 7741 of *Society of Photo-Optical Instrumentation Engineers (SPIE) Conference Series*, p. 77410X.
- [16] K. D. Irwin, “An application of electrothermal feedback for high resolution cryogenic particle detection,” *Applied Physics Letters*, vol. 66, no. 15, pp. 1998–2000, Apr. 1995.
- [17] Peter K. Day, Henry G. LeDuc, Benjamin A. Mazin, Anastasios Vayonakis, and Jonas Zmuidzinas, “A broadband superconducting detector suitable for use in large arrays,” *Nature*, vol. 425, no. 6960, pp. 817–821, Oct. 2003.
- [18] Duncan Farrah, Kimberly Ennico Smith, David Ardila, Charles M. Bradford, Michael Dipirro, Carl Ferkinhoff, Jason Glenn, Paul Goldsmith, David Leisawitz, Thomas Nikola, Naseem Rangwala, Stephen A. Rinehart, Johannes Staguhn, Michael Zemcov, Jonas Zmuidzinas, James Bartlett, Sean Carey, William J. Fischer, Julia Kamenetzky, Jeyhan Kartaltepe, Mark Lacy, Dariusz C. Lis, Lisa Locke, Enrique Lopez-Rodriguez, Meredith MacGregor, Elisabeth Mills, Samuel H. Moseley, Eric J. Murphy, Alan Rhodes, Matt Richter, Dimitra Rigopoulou, David Sanders, Ravi Sankrit, Giorgio Savini, John-David Smith, and Sabrina Stierwalt, “Review: far-infrared instrumentation and technological development for the next decade,” *Journal of Astronomical Telescopes, Instruments, and Systems*, vol. 5, pp. 020901, Apr. 2019.
- [19] A. Catalano, R. Adam, P. Ade, P. André, H. Aussel, A. Beelen, A. Benoît, A. Bideaud, N. Billot, O. Bourrion, M. Calvo, G. Coiffard, B. Comis, F. X. Désert, S. Doyle, J. Goupy, C. F. Kramer, G. Lagache, S. Leclercq, J. F. Lestrade, J. F. Macías-Pérez, A. Maury, P. Mauskopf, F. Mayet, A. Monfardini, F. Pajot, E. Pascale, L. Perotto, G. Pisano, N. Ponthieu, V. Revéret, A. Ritacco, L. Rodriguez, C. Romero, H. Roussel, F. Ruppín, K. Schuster, A. Sievers, J. Soler, S. Triqueneaux, C. Tucker, and R. Zylka, “The NIKA2 commissioning campaign: performance and first results,” *arXiv e-prints*, p. arXiv:1605.08628, May 2016.
- [20] W. S. Holland, D. Bintley, E. L. Chapin, A. Chrysostomou, G. R. Davis, J. T. Dempsey, W. D. Duncan, M. Fich, P. Friberg, M. Halpern, K. D. Irwin, T. Jenness, B. D. Kelly, M. J. MacIntosh, E. I. Robson, D. Scott, P. A. R. Ade, E. Atad-Ettinger, D. S. Berry, S. C. Craig, X. Gao, A. G. Gibb, G. C. Hilton, M. I. Hollister, J. B. Kycia, D. W. Lunney, H. McGregor, D. Montgomery, W. Parkes, R. P. J. Tilanus, J. N. Ullom, C. A. Walther, A. J. Walton, A. L. Woodcraft, M. Amiri, D. Atkinson, B. Burger, T. Chuter, I. M. Coulson, W. B. Dorcise, C. Dunare, F. Economou, M. D. Niemack, H. A. L. Parsons, C. D. Reintsema, B. Sibthorpe, I. Smail, R. Sudiwala, and H. S. Thomas, “SCUBA-2: the 10 000 pixel bolometer camera on the James Clerk Maxwell Telescope,” *MNRAS*, vol. 430, no. 4, pp. 2513–2533, Apr. 2013.

- [21] “Integral Field Units, ESO,” <https://www.eso.org/public/teles-instr/technology/ifu/>, Accessed: 2021-05-15.
- [22] L. Earle, P. Ade, J. Aguirre, R. Aikin, J. Battle, J. Bock, C. M. Bradford, M. Dragan, L. Duband, J. Glenn, G. Griffin, V. Hristov, P. Maloney, H. Matsuhara, B. Naylor, H. Nguyen, M. Yun, and J. Zmuidzinas, “Z-Spec: a broadband direct-detection millimeter-wave spectrometer – instrument status and first results,” in *Society of Photo-Optical Instrumentation Engineers (SPIE) Conference Series*, Jonas Zmuidzinas, Wayne S. Holland, Stafford Withington, and William D. Duncan, Eds., June 2006, vol. 6275 of *Society of Photo-Optical Instrumentation Engineers (SPIE) Conference Series*, p. 627510.
- [23] Carl Ferkinhoff, Thomas Nikola, Stephen C. Parshley, Gordon J. Stacey, Kent D. Irwin, Hsiao-Mei Cho, and Mark Halpern, “ZEUS-2: a second generation submillimeter grating spectrometer for exploring distant galaxies,” in *Millimeter, Submillimeter, and Far-Infrared Detectors and Instrumentation for Astronomy V*, Wayne S. Holland and Jonas Zmuidzinas, Eds., July 2010, vol. 7741 of *Society of Photo-Optical Instrumentation Engineers (SPIE) Conference Series*, p. 77410Y.
- [24] A. Fasano, M. Aguiar, A. Benoit, A. Bideaud, O. Bourrion, M. Calvo, A. Catalano, A. P. de Taoro, G. Garde, A. Gomez, M. F. Gomez-Renasco, J. Goupy, C. Hoarau, R. Hoyland, J. F. Macías-Pérez, J. Marpaud, A. Monfardini, G. Pisano, N. Ponthieu, J. A. Rubiño-Martín, D. Tourres, C. Tucker, A. Beelen, G. Bres, M. De Petris, P. de Bernardis, G. Lagache, L. Lamagna, G. Luzzi, M. Marton, S. Masi, R. Rebolo, and S. Roudier, “The KISS Experiment,” *Journal of Low Temperature Physics*, vol. 199, no. 1-2, pp. 529–536, Apr. 2020.
- [25] The CONCERTO Collaboration, Ade, P., Aravena, M., Barria, E., Beelen, A., Benoit, A., Béthermin, M., Bounmy, J., Bourrion, O., Bres, G., De Breuck, C., Calvo, M., Cao, Y., Catalano, A., Désert, F.-X., Durán, C.A., Fasano, A., Fenouillet, T., Garcia, J., Garde, G., Goupy, J., Groppi, C., Hoarau, C., Lagache, G., Lambert, J.-C., Leggeri, J.-P., Levy-Bertrand, F., Macías-Pérez, J., Mani, H., Marpaud, J., Mauskopf, P., Monfardini, A., Pisano, G., Ponthieu, N., Prieur, L., Roni, S., Roudier, S., Tourres, D., and Tucker, C., “A wide field-of-view low-resolution spectrometer at apex: Instrument design and scientific forecast,” *A&A*, vol. 642, pp. A60, 2020.
- [26] Griffin, M. J., Abergel, A., Abreu, A., Ade, P. A. R., André, P., Augeres, J.-L., Babbedge, T., Bae, Y., Baillie, T., Baluteau, J.-P., Barlow, M. J., Bendo, G., Benielli, D., Bock, J. J., Bonhomme, P., Brisbin, D., Brockley-Blatt, C., Caldwell, M., Cara, C., Castro-Rodriguez, N., Cerulli, R., Chanial, P., Chen, S., Clark, E., Clements, D. L., Clerc, L., Coker, J., Communal, D., Conversi, L., Cox, P., Crumb, D., Cunningham, C., Daly, F., Davis, G. R., De Antoni, P., Delderfield, J., Devin, N., Di Giorgio, A., Didschuns, I., Dohlen, K., Donati, M., Dowell, A., Dowell, C. D., Duband, L., Dumaye, L., Emery, R. J., Ferlet, M., Ferrand, D., Fontignie, J., Fox,

- M., Franceschini, A., Frerking, M., Fulton, T., Garcia, J., Gastaud, R., Gear, W. K., Glenn, J., Goizel, A., Griffin, D. K., Grundy, T., Guest, S., Guillemet, L., Hargrave, P. C., Harwit, M., Hastings, P., Hatziminaoglou, E., Herman, M., Hinde, B., Hristov, V., Huang, M., Imhof, P., Isaak, K. J., Israelsson, U., Ivison, R. J., Jennings, D., Kiernan, B., King, K. J., Lange, A. E., Latter, W., Laurent, G., Laurent, P., Leeks, S. J., Lellouch, E., Levenson, L., Li, B., Li, J., Lilienthal, J., Lim, T., Liu, S. J., Lu, N., Madden, S., Mainetti, G., Marliani, P., McKay, D., Mercier, K., Molinari, S., Morris, H., Moseley, H., Mulder, J., Mur, M., Naylor, D. A., Nguyen, H., O'Halloran, B., Oliver, S., Olofsson, G., Olofsson, H.-G., Orfei, R., Page, M. J., Pain, I., Panuzzo, P., Papageorgiou, A., Parks, G., Parr-Burman, P., Pearce, A., Pearson, C., Pérez-Fournon, I., Pinsard, F., Pisano, G., Podosek, J., Pohlen, M., Polehampton, E. T., Pouliquen, D., Rigopoulou, D., Rizzo, D., Roseboom, I. G., Roussel, H., Rowan-Robinson, M., Rownd, B., Saraceno, P., Sauvage, M., Savage, R., Savini, G., Sawyer, E., Scharmberg, C., Schmitt, D., Schneider, N., Schulz, B., Schwartz, A., Shafer, R., Shupe, D. L., Sibthorpe, B., Sidher, S., Smith, A., Smith, A. J., Smith, D., Spencer, L., Stobie, B., Sudiwala, R., Sukhatme, K., Surace, C., Stevens, J. A., Swinyard, B. M., Trichas, M., Tourette, T., Triou, H., Tseng, S., Tucker, C., Turner, A., Vaccari, M., Valtchanov, I., Vigroux, L., Virique, E., Voellmer, G., Walker, H., Ward, R., Waskett, T., Weilert, M., Wesson, R., White, G. J., Whitehouse, N., Wilson, C. D., Winter, B., Woodcraft, A. L., Wright, G. S., Xu, C. K., Zavagno, A., Zemcov, M., Zhang, L., and Zonca, E., "The herschel-spire instrument and its in-flight performance*," *A&A*, vol. 518, pp. L3, 2010.
- [27] A. J. Anderson, P. A. R. Ade, Z. Ahmed, J. E. Austermann, J. S. Avva, P. S. Barry, R. Basu Thakur, A. N. Bender, B. A. Benson, L. E. Bleem, K. Byrum, J. E. Carlstrom, F. W. Carter, T. Cecil, C. L. Chang, H. M. Cho, J. F. Cliche, T. M. Crawford, A. Cukierman, E. V. Denison, T. de Haan, J. Ding, M. A. Dobbs, D. Dutcher, W. Everett, A. Foster, R. N. Gannon, A. Gilbert, J. C. Groh, N. W. Halverson, A. H. Harke-Hosemann, N. L. Harrington, J. W. Henning, G. C. Hilton, G. P. Holder, W. L. Holzapfel, N. Huang, K. D. Irwin, O. B. Jeong, M. Jonas, T. Khaire, L. Knox, A. M. Kofman, M. Korman, D. Kubik, S. Kuhlmann, N. Kuklev, C. L. Kuo, A. T. Lee, E. M. Leitch, A. E. Lowitz, S. S. Meyer, D. Michalik, J. Montgomery, A. Nadolski, T. Natoli, H. Nguyen, G. I. Noble, V. Novosad, S. Padin, Z. Pan, J. Pearson, C. M. Posada, A. Rahlin, C. L. Reichardt, J. E. Ruhl, L. J. Saunders, J. T. Sayre, I. Shirley, E. Shirokoff, G. Smecher, J. A. Sobrin, A. A. Stark, K. T. Story, A. Suzuki, Q. Y. Tang, K. L. Thompson, C. Tucker, L. R. Vale, K. Vanderlinde, J. D. Vieira, G. Wang, N. Whitehorn, V. Yefremenko, K. W. Yoon, and M. R. Young, "SPT-3G: A Multichroic Receiver for the South Pole Telescope," *Journal of Low Temperature Physics*, vol. 193, no. 5-6, pp. 1057–1065, Dec. 2018.
- [28] Frank Arute, Kunal Arya, Ryan Babbush, Dave Bacon, Joseph C. Bardin, Rami Barends, Rupak Biswas, Sergio Boixo, Fernando G. S. L. Brandao, David A. Buell, Brian Burkett, Yu Chen, Zijun Chen, Ben Chiaro, Roberto Collins, William Court-

- ney, Andrew Dunsworth, Edward Farhi, Brooks Foxen, Austin Fowler, Craig Gidney, Marissa Giustina, Rob Graff, Keith Guerín, Steve Habegger, Matthew P. Harrigan, Michael J. Hartmann, Alan Ho, Markus Hoffmann, Trent Huang, Travis S. Humble, Sergei V. Isakov, Evan Jeffrey, Zhang Jiang, Dvir Kafri, Kostyantyn Kechedzhi, Julian Kelly, Paul V. Klimov, Sergey Knysh, Alexander Korotkov, Fedor Kostritsa, David Landhuis, Mike Lindmark, Erik Lucero, Dmitry Lyakh, Salvatore Mandrà, Jarrod R. McClean, Matthew McEwen, Anthony Megrant, Xiao Mi, Kristel Michielsen, Masoud Mohseni, Josh Mutus, Ofer Naaman, Matthew Neeley, Charles Neill, Murphy Yuezhen Niu, Eric Ostby, Andre Petukhov, John C. Platt, Chris Quintana, Eleanor G. Rieffel, Pedram Roushan, Nicholas C. Rubin, Daniel Sank, Kevin J. Satzinger, Vadim Smelyanskiy, Kevin J. Sung, Matthew D. Trevithick, Amit Vainsencher, Benjamin Villalonga, Theodore White, Z. Jamie Yao, Ping Yeh, Adam Zalcman, Hartmut Neven, and John M. Martinis, “Quantum supremacy using a programmable superconducting processor,” *Nature*, vol. 574, no. 7779, pp. 505–510, 2019.
- [29] L. R. D’Addario, “An SIS mixer for 90–120 GHz with gain and wide bandwidth,” *International Journal of Infrared and Millimeter Waves*, vol. 5, no. 11, pp. 1419–1442, Nov. 1984.
- [30] Jonas Zmuidzinas, Henry G. Leduc, Jeffrey A. Stern, and Scott R. Cypher, “Two-junction tuning circuits for submillimeter SIS mixers,” *IEEE Transactions on Microwave Theory Techniques*, vol. 42, no. 4, pp. 698–706, Apr. 1994.
- [31] V. P. Koshelets and S. V. Shitov, “TOPICAL REVIEW: Integrated superconducting receivers,” *Superconductor Science Technology*, vol. 13, no. 5, pp. R53–R69, May 2000.
- [32] Y. Inoue, P. Ade, Y. Akiba, C. Aleman, K. Arnold, C. Baccigalupi, B. Barch, D. Barron, A. Bender, D. Boettger, J. Borrill, S. Chapman, Y. Chinone, A. Cukierman, T. de Haan, M. A. Dobbs, A. Ducout, R. Dünner, T. Elleflot, J. Errard, G. Fabbian, S. Feeney, C. Feng, G. Fuller, A. J. Gilbert, N. Goeckner-Wald, J. Groh, G. Hall, N. Halverson, T. Hamada, M. Hasegawa, K. Hattori, M. Hazumi, C. Hill, W. L. Holzapfel, Y. Hori, L. Howe, F. Irie, G. Jaehnig, A. Jaffe, O. Jeong, N. Katayama, J. P. Kaufman, K. Kazemzadeh, B. G. Keating, Z. Kermish, R. Keskitalo, T. S. Kisner, A. Kusaka, M. Le Jeune, A. T. Lee, D. Leon, E. V. Linder, L. Lowry, F. Matsuda, T. Matsumura, N. Miller, K. Mizukami, J. Montgomery, M. Navaroli, H. Nishino, H. Paar, J. Peloton, D. Poletti, G. Puglisi, C. R. Raum, G. M. Rebeiz, C. L. Reichardt, P. L. Richards, C. Ross, K. M. Rotermond, Y. Segawa, B. D. Sherwin, I. Shirley, P. Siritanasak, N. Stebor, R. Stompor, J. Suzuki, A. Suzuki, O. Tajima, S. Takada, S. Takatori, G. P. Teply, A. Tikhomirov, T. Tomaru, N. Whitehorn, A. Zahn, and O. Zahn, “POLARBEAR-2: an instrument for CMB polarization measurements,” in *Millimeter, Submillimeter, and Far-Infrared Detectors and Instrumentation for Astronomy VIII*, Wayne S. Holland and Jonas Zmuidzinas, Eds.,

- July 2016, vol. 9914 of *Society of Photo-Optical Instrumentation Engineers (SPIE) Conference Series*, p. 99141I.
- [33] Akira Endo, Kenichi Karatsu, Yoichi Tamura, Tai Oshima, Akio Taniguchi, Tatsuya Takekoshi, Shin'ichiro Asayama, Tom J. L. C. Bakx, Sjoerd Bosma, Juan Bueno, Kah Wuy Chin, Yasunori Fujii, Kazuyuki Fujita, Robert Huiting, Soh Ikarashi, Tsuyoshi Ishida, Shun Ishii, Ryohei Kawabe, Teun M. Klapwijk, Kotaro Kohno, Akira Kouchi, Nuria Llombart, Jun Maekawa, Vignesh Murugesan, Shunichi Nakatsubo, Masato Naruse, Kazushige Ohtawara, Alejandro Pascual Laguna, Junya Suzuki, Koyo Suzuki, David J. Thoen, Takashi Tsukagoshi, Tetsutaro Ueda, Pieter J. de Visser, Paul P. van der Werf, Stephen J. C. Yates, Yuki Yoshimura, Ozan Yurduseven, and Jochem J. A. Baselmans, "First light demonstration of the integrated superconducting spectrometer," *Nature Astronomy*, vol. 3, pp. 989–996, Aug 2019.
 - [34] E. Shirokoff, P. S. Barry, C. M. Bradford, G. Chattopadhyay, P. Day, S. Doyle, S. Hailey-Dunsheath, M. I. Hollister, A. Kovács, C. McKenney, H. G. Leduc, N. Llombart, D. P. Marrone, P. Mauskopf, R. O'Brient, S. Padin, T. Reck, L. J. Swenson, and J. Zmuidzinas, "MKID development for SuperSpec: an on-chip, mm-wave, filter-bank spectrometer," in *Millimeter, Submillimeter, and Far-Infrared Detectors and Instrumentation for Astronomy VI*, Wayne S. Holland, Ed. International Society for Optics and Photonics, 2012, vol. 8452, pp. 209 – 219, SPIE.
 - [35] Giuseppe Cataldo, Wen-Ting Hsieh, Wei-Chung Huang, S. Harvey Moseley, Thomas R. Stevenson, and Edward J. Wollack, "Micro-spec: an ultracompact, high-sensitivity spectrometer for far-infrared and submillimeter astronomy," *Appl. Opt.*, vol. 53, no. 6, pp. 1094–1102, Feb 2014.
 - [36] R. M. J. Janssen, J. J. A. Baselmans, A. Endo, L. Ferrari, S. J. C. Yates, A. M. Baryshev, and T. M. Klapwijk, "High optical efficiency and photon noise limited sensitivity of microwave kinetic inductance detectors using phase readout," *Applied Physics Letters*, vol. 103, no. 20, pp. 203503, 2013.
 - [37] Alejandro Pascualallaguna, Kenichi Karatsu, David Thoen, Vignesh Murugesan, Bruno Buijtendorp, Akira Endo, and Jochem Baselmans, "Terahertz band-pass filters for wideband superconducting on-chip filter-bank spectrometers," *IEEE Transactions on Terahertz Science and Technology*, 2021.
 - [38] J.R. Hook and H.E. Hall, *Solid State Physics*, Manchester Physics Series. Wiley, 2013.
 - [39] Leon N Cooper, "Bound electron pairs in a degenerate fermi gas," *Physical Review*, vol. 104, no. 4, pp. 1189, 1956.
 - [40] C. A. Reynolds, B. Serin, W. H. Wright, and L. B. Nesbitt, "Superconductivity of isotopes of mercury," *Phys. Rev.*, vol. 78, pp. 487–487, May 1950.

- [41] Emanuel Maxwell, “Isotope effect in the superconductivity of mercury,” *Phys. Rev.*, vol. 78, pp. 477–477, May 1950.
- [42] J. Bardeen, L. N. Cooper, and J. R. Schrieffer, “Theory of superconductivity,” *Phys. Rev.*, vol. 108, pp. 1175–1204, Dec 1957.
- [43] A.L. Fetter and J.D. Walecka, *Quantum Theory of Many-particle Systems*, Dover Books on Physics. Dover Publications, 2003.
- [44] SB Kaplan, CC Chi, DN Langenberg, Jhy-Jiun Chang, S Jafarey, and DJ Scalapino, “Quasiparticle and phonon lifetimes in superconductors,” *Physical Review B*, vol. 14, no. 11, pp. 4854, 1976.
- [45] F. London, H. London, and Frederick Alexander Lindemann, “The electromagnetic equations of the supraconductor,” *Proceedings of the Royal Society of London. Series A - Mathematical and Physical Sciences*, vol. 149, no. 866, pp. 71–88, 1935.
- [46] TE Faber and Alfred Brian Pippard, “The penetration depth and high-frequency resistance of superconducting aluminium,” *Proceedings of the Royal Society of London. Series A. Mathematical and Physical Sciences*, vol. 231, no. 1186, pp. 336–353, 1955.
- [47] Alfred Brian Pippard and William Lawrence Bragg, “An experimental and theoretical study of the relation between magnetic field and current in a superconductor,” *Proceedings of the Royal Society of London. Series A. Mathematical and Physical Sciences*, vol. 216, no. 1127, pp. 547–568, 1953.
- [48] J. Pearl, “Current distribution in superconducting films carrying quantized fluxoids,” *Applied Physics Letters*, vol. 5, no. 4, pp. 65–66, 1964.
- [49] Taeyoon Hong, Kyujin Choi, Kyung Ik Sim, Taewoo Ha, Byung Cheol Park, Hirotake Yamamori, and Jae Hoon Kim, “Terahertz electrodynamics and superconducting energy gap of nb_{1-x}tin,” *Journal of Applied Physics*, vol. 114, no. 24, pp. 243905, 2013.
- [50] JA Stern, B Bumble, HG LeDuc, JW Kooi, and J Zmuidzinas, “Fabrication and dc-characterization of nb_{1-x}tin based sis mixers for use between 600 and 1200 ghz,” in *Proc. 9th Int. Symp. Space THz Technol.* Pasadena, CA, 1998, pp. 305–313.
- [51] Jonas Zmuidzinas, “Superconducting microresonators: Physics and applications,” *Annual Review of Condensed Matter Physics*, vol. 3, no. 1, pp. 169–214, 2012.
- [52] D. C. Mattis and J. Bardeen, “Theory of the anomalous skin effect in normal and superconducting metals,” *Phys. Rev.*, vol. 111, pp. 412–417, Jul 1958.
- [53] J. Gao, J. Zmuidzinas, A. Vayonakis, P. Day, B. Mazin, and H. Leduc, “Equivalence of the Effects on the Complex Conductivity of Superconductor due to Temperature Change and External Pair Breaking,” *Journal of Low Temperature Physics*, vol. 151, no. 1-2, pp. 557–563, Apr. 2008.

- [54] R. L. Kautz, “Picosecond pulses on superconducting striplines,” *Journal of Applied Physics*, vol. 49, no. 1, pp. 308–314, Jan 1978.
- [55] David M Pozar, *Microwave engineering; 4th ed.*, Wiley, Hoboken, NJ, 2011.
- [56] Rami Barends, “Photon-detecting superconducting resonators,” 2009.
- [57] G. Yassin and S. Withington, “Electromagnetic models for superconducting millimetre-wave and sub-millimetre-wave microstrip transmission lines,” *Journal of Physics D Applied Physics*, vol. 28, no. 9, pp. 1983–1991, Sept. 1995.
- [58] J.R. Gao, Anastasios Vayonakis, Omid Noroozian, Jonas Zmuidzinas, Peter Day, and Henry Leduc, “Measurement of loss in superconducting microstrip at millimeter-wave frequencies,” vol. 1185, 12 2009.
- [59] Aaron D. O’Connell, M. Ansmann, R. C. Bialczak, M. Hofheinz, N. Katz, Erik Lucero, C. McKenney, M. Neeley, H. Wang, E. M. Weig, A. N. Cleland, and J. M. Martinis, “Microwave dielectric loss at single photon energies and millikelvin temperatures,” *Applied Physics Letters*, vol. 92, no. 11, pp. 112903, Mar. 2008.
- [60] Christian Enss and Siegfried Hunklinger, *Low-Temperature Physics*, 2005.
- [61] Jürgen Lisenfeld, Alexander Bilmes, Shlomi Matityahu, Sebastian Zanker, Michael Marthaler, Moshe Schechter, Gerd Schön, Alexander Shnirman, Georg Weiss, and Alexey V. Ustinov, “Decoherence spectroscopy with individual two-level tunneling defects,” *Scientific Reports*, vol. 6, no. 1, pp. 23786, Mar. 2016.
- [62] H. Wang, M. Hofheinz, J. Wenner, M. Ansmann, R. C. Bialczak, M. Lenander, Erik Lucero, M. Neeley, A. D. O’Connell, D. Sank, M. Weides, A. N. Cleland, and John M. Martinis, “Improving the coherence time of superconducting coplanar resonators,” *Applied Physics Letters*, vol. 95, no. 23, pp. 233508, 2009.
- [63] B Chiaro, A Megrant, A Dunsworth, Z Chen, R Barends, B Campbell, Y Chen, A Fowler, I C Hoi, E Jeffrey, J Kelly, J Mutus, C Neill, P J J O’Malley, C Quintana, P Roushan, D Sank, A Vainsencher, J Wenner, T C White, and John M Martinis, “Dielectric surface loss in superconducting resonators with flux-trapping holes,” *Superconductor Science and Technology*, vol. 29, no. 10, pp. 104006, aug 2016.
- [64] M. Spirito, G. Gentile, and A. Akhnoukh, “Multimode analysis of transmission lines and substrates for (sub)mm-wave calibration,” in *82nd ARFTG Microwave Measurement Conference*, 2013, pp. 1–6.
- [65] Pieter J. de Visser, *Quasiparticle dynamics in aluminium superconducting microwave resonators*, Ph.D. thesis, Delft University of Technology, 2014.
- [66] R. E. Collin, *Foundations for Microwave Engineering*, McGraw-Hill series in electrical engineering. McGraw-Hill, 1992.

- [67] M. Y. Frankel, S. Gupta, J. A. Valdmanis, and G. A. Mourou, "Terahertz attenuation and dispersion characteristics of coplanar transmission lines," *IEEE Transactions on Microwave Theory and Techniques*, vol. 39, no. 6, pp. 910–916, June 1991.
- [68] EM User's Manual, "Sonnet software," *Inc., Liverpool, NY*, 2008.
- [69] Akira Endo, Alejandro Pascual Laguna, Sebastian Hähnle, Kenichi Karatsu, David J. Thoen, Vignesh Murugesan, and Jochem J. A. Baselmans, "Simulating the radiation loss of superconducting submillimeter wave filters and transmission lines using Sonnet EM," in *Society of Photo-Optical Instrumentation Engineers (SPIE) Conference Series*, Dec. 2020, vol. 11453 of *Society of Photo-Optical Instrumentation Engineers (SPIE) Conference Series*, p. 114532T.
- [70] A. Pascual Laguna, ," private communication.
- [71] Benjamin A. Mazin, *Microwave Kinetic Inductance Detectors*, Ph.D. thesis, California Institute of Technology, 2004.
- [72] P. J. de Visser, J. J. A. Baselmans, P. Diener, S. J. C. Yates, A. Endo, and T. M. Klapwijk, "Number fluctuations of sparse quasiparticles in a superconductor," *Phys. Rev. Lett.*, vol. 106, pp. 167004, Apr 2011.
- [73] Jiansong Gao, Jonas Zmuidzinis, Benjamin A Mazin, Henry G LeDuc, and Peter K Day, "Noise properties of superconducting coplanar waveguide microwave resonators," *Applied Physics Letters*, vol. 90, no. 10, pp. 102507, 2007.
- [74] Jiansong Gao, Miguel Daal, John M Martinis, Anastasios Vayonakis, Jonas Zmuidzinis, Bernard Sadoulet, Benjamin A Mazin, Peter K Day, and Henry G Leduc, "A semiempirical model for two-level system noise in superconducting microresonators," *Applied Physics Letters*, vol. 92, no. 21, pp. 212504, 2008.
- [75] L. Ferrari, O. Yurduseven, N. Llombart, S. J. C. Yates, J. Bueno, V. Murugesan, D. J. Thoen, A. Endo, A. M. Baryshev, and J. J. A. Baselmans, "Antenna coupled mkid performance verification at 850 ghz for large format astrophysics arrays," *IEEE Transactions on Terahertz Science and Technology*, vol. 8, no. 1, pp. 127–139, 2018.
- [76] T.L. Wilson, K. Rohlf, and Hüttemeister S., *Tools of Radio Astronomy*, Springer-Verlag, 2013.
- [77] T. Guruswamy, D. J. Goldie, and S. Withington, "Quasiparticle generation efficiency in superconducting thin films," *Superconductor Science Technology*, vol. 27, no. 5, pp. 055012, May 2014.
- [78] D. J. Thoen, B. G. C. Bos, E. A. F. Haalebos, T. M. Klapwijk, J. J. A. Baselmans, and A. Endo, "Superconducting nbtin thin films with highly uniform properties over a \varnothing 100 mm wafer," *IEEE Transactions on Applied Superconductivity*, vol. 27, no. 4, pp. 1–5, June 2017.

- [79] P. J. de Visser, J. J. A. Baselmans, J. Bueno, N. Llombart, and T. M. Klapwijk, “Fluctuations in the electron system of a superconductor exposed to a photon flux,” *Nature Communications*, vol. 5, pp. 3130, Feb. 2014.
- [80] J. van Rantwijk, M. Grim, D. van Loon, S. Yates, A. Baryshev, and J. Baselmans, “Multiplexed readout for 1000-pixel arrays of microwave kinetic inductance detectors,” *IEEE Transactions on Microwave Theory and Techniques*, vol. 64, no. 6, pp. 1876–1883, June 2016.
- [81] Peter K. Day, Henry G. LeDuc, Benjamin A. Mazin, Anastasios Vayonakis, and Jonas Zmuidzinas, “A broadband superconducting detector suitable for use in large arrays,” *Nature*, vol. 425, pp. 817, Oct 2003.
- [82] S. Doyle, P. Mauskopf, J. Naylon, A. Porch, and C. Duncombe, “Lumped Element Kinetic Inductance Detectors,” *Journal of Low Temperature Physics*, vol. 151, no. 1-2, pp. 530–536, Apr. 2008.
- [83] J. J. A. Baselmans, J. Bueno, S. J. C. Yates, O. Yurduseven, N. Llombart, K. Karatsu, A. M. Baryshev, L. Ferrari, A. Endo, D. J. Thoen, P. J. de Visser, R. M. J. Janssen, V. Murugesan, E. F. C. Driessen, G. Coiffard, J. Martin-Pintado, P. Hargrave, and M. Griffin, “A kilo-pixel imaging system for future space based far-infrared observatories using microwave kinetic inductance detectors,” *aap*, vol. 601, pp. A89, May 2017.
- [84] S. Heyminck, B. Klein, R. Güsten, C. Kasemann, A. Baryshev, J. Baselmans, S. Yates, and T. M. Klapwijk, “Development of a MKID Camera for APEX,” in *Twenty-First International Symposium on Space Terahertz Technology*, Mar. 2010, p. 262.
- [85] Isaac López-Fernández, Carmen Diez, Juan Daniel Gallego, and Alberto Barcia, “Wide Band Cryogenic IF Amplifiers for ALMA and Herschel Receivers,” in *Fourteenth International Symposium on Space Terahertz Technology*, Chris Walker and John Payne, Eds., Apr. 2003, pp. 502–504.
- [86] J. Choi, H. Ishitsuka, S. Mima, S. Oguri, K. Takahashi, and O. Tajima, “Radio-transparent multi-layer insulation for radiowave receivers,” *Review of Scientific Instruments*, vol. 84, no. 11, pp. 114502–114502–6, Nov. 2013.
- [87] Carole E. Tucker and Peter A. R. Ade, “Thermal filtering for large aperture cryogenic detector arrays,” in *Society of Photo-Optical Instrumentation Engineers (SPIE) Conference Series*, Jonas Zmuidzinas, Wayne S. Holland, Stafford Withington, and William D. Duncan, Eds., June 2006, vol. 6275 of *Society of Photo-Optical Instrumentation Engineers (SPIE) Conference Series*, p. 62750T.

- [88] T. O. Klaassen, M. C. Diez, C. Smorenburg, K. J. Wildeman, J. H. Blok, and G. Jakob, "Optical Characterization of Absorbing Coatings for Sub-millimeter Radiation," in *Twelfth International Symposium on Space Terahertz Technology*, Imram Mehdi, Ed., Dec. 2001, p. 400.
- [89] Y. Inoue et al., "POLARBEAR-2: an instrument for CMB polarization measurements," *Proc. SPIE Int. Soc. Opt. Eng.*, vol. 9914, pp. 99141I, 2016.
- [90] Roger O'Brient, Peter Ade, Kam Arnold, Jennifer Edwards, Greg Engargiola, William L. Holzapfel, Adrian T. Lee, Michael J. Myers, Erin Quealy, Gabriel Rebeiz, Paul Richards, and Aritoki Suzuki, "A dual-polarized broadband planar antenna and channelizing filter bank for millimeter wavelengths," *Applied Physics Letters*, vol. 102, no. 6, pp. 063506, 2013.
- [91] A. Neto, "Uwb, non dispersive radiation from the planarly fed leaky lens antenna 2014; part 1: Theory and design," *IEEE Transactions on Antennas and Propagation*, vol. 58, no. 7, pp. 2238–2247, July 2010.
- [92] A. Neto, S. Monni, and F. Nennie, "Uwb, non dispersive radiation from the planarly fed leaky lens antenna 2014; part ii: Demonstrators and measurements," *IEEE Transactions on Antennas and Propagation*, vol. 58, no. 7, pp. 2248–2258, July 2010.
- [93] O. Yurduseven, N. Llombart Juan, and A. Neto, "A dual-polarized leaky lens antenna for wideband focal plane arrays," *IEEE Transactions on Antennas and Propagation*, vol. 64, no. 8, pp. 3330–3337, Aug 2016.
- [94] J. Bueno, O. Yurduseven, S. J. C. Yates, N. Llombart, V. Murugesan, D. J. Thoen, A. M. Baryshev, A. Neto, and J. J. A. Baselmans, "Full characterisation of a background limited antenna coupled kid over an octave of bandwidth for thz radiation," *Applied Physics Letters*, vol. 110, no. 23, pp. 233503, 2017.
- [95] N. Llombart and A. Neto, "Thz time-domain sensing: The antenna dispersion problem and a possible solution," *IEEE Transactions on Terahertz Science and Technology*, vol. 2, no. 4, pp. 416–423, July 2012.
- [96] Paul F Goldsmith, *Quasioptical Systems: Gaussian Beam Quasioptical Propagation and Applications*, Wiley, Hoboken, NJ, 1998.
- [97] A. Nadolski, A. M. Kofman, J. D. Vieira, P. A. R. Ade, Z. Ahmed, A. J. Anderson, J. S. Avva, R. Basu Thakur, A. N. Bender, B. A. Benson, J. E. Carlstrom, F. W. Carter, T. W. Cecil, C. L. Chang, J. F. Cliche, A. Cukierman, T. de Haan, J. Ding, M. A. Dobbs, D. Dutcher, W. Everett, A. Foster, J. Fu, J. Gallichio, A. Gilbert, J. C. Groh, S. T. Guns, R. Guyser, N. W. Halverson, A. H. Harke-Hosemann, N. L. Harrington, J. W. Henning, W. L. Holzapfel, N. Huang, K. D. Irwin, O. B. Jeong, M. Jonas, A. Jones, T. S. Khaire, M. Korman, D. L. Kubik, S. Kuhlmann, C. L. Kuo, A. T. Lee, A. E. Lowitz, S. S. Meyer, D. Michalik, J. Montgomery, T. Natoli,

- H. Nguyen, G. I. Noble, V. Novosad, S. Padin, Z. Pan, J. Pearson, C. M. Posada, W. Quan, A. Rahlin, J. E. Ruhl, J. T. Sayre, E. Shirokoff, G. Smecher, J. A. Sobrin, A. A. Stark, K. T. Story, A. Suzuki, K. L. Thompson, C. Tucker, K. Vanderlinde, G. Wang, N. Whitehorn, V. Yefremenko, K. W. Yoon, and M. R. Young, "Broadband anti-reflective coatings for cosmic microwave background experiments," in *Millimeter, Submillimeter, and Far-Infrared Detectors and Instrumentation for Astronomy IX*, Jonas Zmuidzinas and Jian-Rong Gao, Eds., July 2018, vol. 10708 of *Society of Photo-Optical Instrumentation Engineers (SPIE) Conference Series*, p. 1070843.
- [98] P. Siritanasak, C. Aleman, K. Arnold, A. Cukierman, M. Hazumi, K. Kazemzadeh, B. Keating, T. Matsumura, A. T. Lee, C. Lee, E. Quealy, D. Rosen, N. Stebor, and A. Suzuki, "The Broadband Anti-reflection Coated Extended Hemispherical Silicon Lenses for Polarbear-2 Experiment," *Journal of Low Temperature Physics*, vol. 184, no. 3-4, pp. 553–558, Aug. 2016.
- [99] S. J. C. Yates, A. M. Baryshev, O. Yurduseven, J. Bueno, K. K. Davis, L. Ferrari, W. Jellema, N. Llombart, V. Murugesan, D. J. Thoen, and J. J. A. Baselmans, "Surface wave control for large arrays of microwave kinetic inductance detectors," *IEEE Transactions on Terahertz Science and Technology*, vol. 7, no. 6, pp. 789–799, Nov 2017.
- [100] Jochem Baselmans, Stephen Yates, Pascale Diener, and Pieter de Visser, "Ultra low background cryogenic test facility for far-infrared radiation detectors," *Journal of Low Temperature Physics*, vol. 167, no. 3, pp. 360–366, May 2012.
- [101] A. Nadolski, A. M. Kofman, J. D. Vieira, P. A. R. Ade, Z. Ahmed, A. J. Anderson, J. S. Avva, R. Basu Thakur, A. N. Bender, B. A. Benson, J. E. Carlstrom, F. W. Carter, T. W. Cecil, C. L. Chang, J. F. Cliche, A. Cukierman, T. de Haan, J. Ding, M. A. Dobbs, D. Dutcher, W. Everett, A. Foster, J. Fu, J. Gallichio, A. Gilbert, J. C. Groh, S. T. Guns, R. Guyser, N. W. Halverson, A. H. Harke-Hosemann, N. L. Harrington, J. W. Henning, W. L. Holzapfel, N. Huang, K. D. Irwin, O. B. Jeong, M. Jonas, A. Jones, T. S. Khair, M. Korman, D. L. Kubik, S. Kuhlmann, C. L. Kuo, A. T. Lee, A. E. Lowitz, S. S. Meyer, D. Michalik, J. Montgomery, T. Natoli, H. Nguyen, G. I. Noble, V. Novosad, S. Padin, Z. Pan, J. Pearson, C. M. Posada, W. Quan, A. Rahlin, J. E. Ruhl, J. T. Sayre, E. Shirokoff, G. Smecher, J. A. Sobrin, A. A. Stark, K. T. Story, A. Suzuki, K. L. Thompson, C. Tucker, K. Vanderlinde, G. Wang, N. Whitehorn, V. Yefremenko, K. W. Yoon, and M. R. Young, "Broadband anti-reflective coatings for cosmic microwave background experiments," in *Millimeter, Submillimeter, and Far-Infrared Detectors and Instrumentation for Astronomy IX*, Jul 2018, vol. 10708 of *Society of Photo-Optical Instrumentation Engineers (SPIE) Conference Series*, p. 1070843.
- [102] D. F. Filipovic, S. S. Gearhart, and G. M. Rebeiz, "Double-slot antennas on extended hemispherical and elliptical silicon dielectric lenses," *IEEE Transactions on Microwave Theory and Techniques*, vol. 41, no. 10, pp. 1738–1749, Oct 1993.

- [103] G. Cataldo, E. M. Barrentine, B. T. Bulcha, N. Ehsan, L. A. Hess, O. Noroozian, T. R. Stevenson, K. U-Yen, E. J. Wollack, and S. H. Moseley, “Second-generation design of micro-spec: A medium-resolution, submillimeter-wavelength spectrometer-on-a-chip,” *Journal of Low Temperature Physics*, vol. 193, no. 5, pp. 923–930, Dec 2018.
- [104] P. A. R. Ade, R. W. Aikin, M. Amiri, D. Barkats, S. J. Benton, C. A. Bischoff, J. J. Bock, J. A. Bonetti, J. A. Brevik, I. Buder, E. Bullock, G. Chattopadhyay, G. Davis, P. K. Day, C. D. Dowell, L. Duband, J. P. Filippini, S. Fliescher, S. R. Golwala, M. Halpern, M. Hasselfield, S. R. Hildebrandt, G. C. Hilton, V. Hristov, H. Hui, K. D. Irwin, W. C. Jones, K. S. Karkare, J. P. Kaufman, B. G. Keating, S. Kefeli, S. A. Kernasovskiy, J. M. Kovac, C. L. Kuo, H. G. LeDuc, E. M. Leitch, N. Llombart, M. Lueker, P. Mason, K. Megerian, L. Moncelsi, C. B. Netterfield, H. T. Nguyen, R. O’Brien, R. W. Ogburn IV, A. Orlando, C. Pryke, A. S. Rahlin, C. D. Reintsema, S. Richter, M. C. Runyan, R. Schwarz, C. D. Sheehy, Z. K. Staniszewski, R. V. Sudiwala, G. P. Teply, J. E. Tolan, A. Trangsud, R. S. Tucker, A. D. Turner, A. G. Viereg, A. Weber, D. V. Wiebe, P. Wilson, C. L. Wong, K. W. Yoon, and J. Zmuidzinas and, “ANTENNA-COUPLED TES BOLOMETERS USED IN BICEP2, keck array, AND SPIDER,” *The Astrophysical Journal*, vol. 812, no. 2, pp. 176, oct 2015.
- [105] Byeong Ho Eom, Peter K. Day, Henry G. LeDuc, and Jonas Zmuidzinas, “A wideband, low-noise superconducting amplifier with high dynamic range,” *Nature Physics*, vol. 8, no. 8, pp. 623–627, Aug. 2012.
- [106] M. Göppl, A. Fragner, M. Baur, R. Bianchetti, S. Filipp, J. M. Fink, P. J. Leek, G. Puebla, L. Steffen, and A. Wallraff, “Coplanar waveguide resonators for circuit quantum electrodynamics,” *Journal of Applied Physics*, vol. 104, no. 11, pp. 113904, 2008.
- [107] Akira Endo, Kenichi Karatsu, Alejandro Pascual Laguna, Behnam Mirzaei, Robert Huiting, David Thoen, Vignesh Murugesan, Stephen J. C. Yates, Juan Bueno, Nuri V. Marrewijk, Sjoerd Bosma, Ozan Yurduseven, Nuria Llombart, Junya Suzuki, Masato Naruse, Pieter J. de Visser, Paul P. van der Werf, Teunis M. Klapwijk, and Jochem J. A. Baselmans, “Wideband on-chip terahertz spectrometer based on a superconducting filterbank,” *Journal of Astronomical Telescopes, Instruments, and Systems*, vol. 5, no. 3, pp. 1 – 12, 2019.
- [108] E. F. C. Driessen, P. C. J. J. Coumou, R. R. Tromp, P. J. de Visser, and T. M. Klapwijk, “Strongly disordered tin and nbtin s -wave superconductors probed by microwave electrodynamics,” *Phys. Rev. Lett.*, vol. 109, pp. 107003, Sep 2012.
- [109] S. Hähnle, J. Bueno, R. Huiting, S. J. C. Yates, and J. J. A. Baselmans, “Large angle optical access in a sub-kelvin cryostat,” *Journal of Low Temperature Physics*, May 2018.

- [110] ,” TERABEAM 1550 (TOPTICA Photonics AG, Lochhamer Schlag 19, 82166 Gräfelfing, Germany).
- [111] R. Barends, N. Vercruyssen, A. Endo, P. J. de Visser, T. Zijlstra, T. M. Klapwijk, P. Diener, S. J. C. Yates, and J. J. A. Baselmans, “Minimal resonator loss for circuit quantum electrodynamics,” *Applied Physics Letters*, vol. 97, no. 2, pp. 023508, July 2010.
- [112] A. Wagner, L. Ranzani, G. Ribeill, and T. A. Ohki, “Demonstration of a superconducting nanowire microwave switch,” *Applied Physics Letters*, vol. 115, no. 17, pp. 172602, 2019.
- [113] Marco Colangelo, Di Zhu, Daniel F. Santavicca, Brenden A. Butters, Joshua C. Bienfang, and Karl K. Berggren, “Compact and Tunable Forward Coupler Based on High-Impedance Superconducting Nanowires,” *Physical Review Applied*, vol. 15, no. 2, pp. 024064, Feb. 2021.
- [114] Benjamin A. Mazin, Daniel Sank, Sean McHugh, Erik A. Lucero, Andrew Merrill, Jiansong Gao, David Pappas, David Moore, and Jonas Zmuidzinas, “Thin film dielectric microstrip kinetic inductance detectors,” *Applied Physics Letters*, vol. 96, no. 10, pp. 102504, Mar. 2010.
- [115] Samir Beldi, Faouzi Boussaha, Jie Hu, Alessandro Monfardini, Alessandro Traini, Florence Levy-Bertrand, Christine Chaumont, Manuel Gonzales, Josiane Firminy, Florent Reix, Michael Rosticher, Shan Mignot, Michel Piat, and Piercarlo Bonifacio, “High q-factor near infrared and visible al₂o₃-based parallel-plate capacitor kinetic inductance detectors,” *Opt. Express*, vol. 27, no. 9, pp. 13319–13328, Apr 2019.
- [116] M. J. Myers, K. Arnold, P. Ade, G. Engargiola, W. Holzapfel, A. T. Lee, X. Meng, R. O’Brien, P. L. Richards, H. Spieler, and H. T. Tran, “Antenna-Coupled Bolometer Arrays for Measurement of the Cosmic Microwave Background Polarization,” *Journal of Low Temperature Physics*, vol. 151, no. 1-2, pp. 464–470, Apr. 2008.
- [117] W. A. Phillips, “REVIEW ARTICLE: Two-level states in glasses,” *Reports on Progress in Physics*, vol. 50, no. 12, pp. 1657–1708, Dec. 1987.
- [118] C. L. Chang, P. A.R. Ade, Z. Ahmed, S. W. Allen, K. Arnold, J. E. Austermann, A. N. Bender, L. E. Bleem, B. A. Benson, J. E. Carlstrom, H. M. Cho, S. T. Ciocys, J. F. Cliche, T. M. Crawford, A. Cukierman, J. Ding, T. De Haan, M. A. Dobbs, D. Dutcher, W. Everett, A. Gilbert, N. W. Halverson, D. Hanson, N. L. Harrington, K. Hattori, J. W. Henning, G. C. Hilton, G. P. Holder, W. L. Holzapfel, J. Hubmayr, K. D. Irwin, R. Keisler, L. Knox, D. Kubik, C. L. Kuo, A. T. Lee, E. M. Leitch, D. Li, M. McDonald, S. S. Meyer, J. Montgomery, M. Myers, T. Natoli, H. Nguyen, V. Novosad, S. Padin, Z. Pan, J. Pearson, C. Posada Arbelaez, C. L. Reichardt, J. E. Ruhl, B. R. Saliwanchik, G. Simard, G. Smecher, J. T. Sayre, E. Shirokoff, A. A.

- Stark, K. Story, A. Suzuki, K. L. Thompson, C. Tucker, K. Vanderlinde, J. D. Vieira, A. Vikhlinin, G. Wang, V. Yefremenko, and K. W. Yoon, “Low loss superconducting microstrip development at argonne national lab,” *IEEE Transactions on Applied Superconductivity*, vol. 25, no. 3, pp. 0–4, 2015.
- [119] a. Endo, C. Sfiligoj, S. J C Yates, J. J a Baselmans, D. J. Thoen, S. M H Javadzadeh, P. P. Van Der Werf, a. M. Baryshev, and T. M. Klapwijk, “On-chip filter bank spectroscopy at 600-700 GHz using NbTiN superconducting resonators,” *Applied Physics Letters*, vol. 103, no. 3, pp. 1–5, 2013.
- [120] James W. Lamb, “Miscellaneous data on materials for millimetre and submillimetre optics,” *International Journal of Infrared and Millimeter Waves*, vol. 17, no. 12, pp. 1997–2034, Dec. 1996.
- [121] Bruno T. Buijtendorp, Juan Bueno, David J. Thoen, Vignesh Murugesan, Paolo M. Sberna, Jochem J. A. Baselmans, Sten Vollebregt, and Akira Endo, “Characterization of low-loss hydrogenated amorphous silicon films for superconducting resonators,” *arXiv e-prints*, p. arXiv:2012.07692, Dec. 2020.
- [122] M. S. Khalil, M. J. A. Stoutimore, F. C. Wellstood, and K. D. Osborn, “An analysis method for asymmetric resonator transmission applied to superconducting devices,” *Journal of Applied Physics*, vol. 111, no. 5, pp. 054510, 2012.
- [123] M. Molina-Ruiz, Y. J. Rosen, H. C. Jacks, M. R. Abernathy, T. H. Metcalf, X. Liu, J. L Dubois, and F. Hellman, “Origin of mechanical and dielectric losses from two-level systems in amorphous silicon,” 2020.
- [124] J. Wenner, R. Barends, R. C. Bialczak, Yu Chen, J. Kelly, Erik Lucero, Matteo Mariantoni, A. Megrant, P. J. J. O’Malley, D. Sank, A. Vainsencher, H. Wang, T. C. White, Y. Yin, J. Zhao, A. N. Cleland, and John M. Martinis, “Surface loss simulations of superconducting coplanar waveguide resonators,” *Applied Physics Letters*, vol. 99, no. 11, pp. 113513, Sept. 2011.
- [125] Werner Karl-Gustav Daalman, “Noise and loss in superconducting resonators,” 2014.
- [126] Lara Faoro and Lev B. Ioffe, “Interacting tunneling model for two-level systems in amorphous materials and its predictions for their dephasing and noise in superconducting microresonators,” *Physical Review B*, vol. 91, no. 1, pp. 014201, Jan. 2015.
- [127] Giuseppe Cataldo, Edward J. Wollack, Ari D. Brown, and Kevin H. Miller, “Infrared dielectric properties of low-stress silicon oxide,” *Optics Letters*, vol. 41, no. 7, pp. 1364, Apr. 2016.
- [128] Giuseppe Cataldo, James A. Beall, Hsiao-Mei Cho, Brendan McAndrew, Michael D. Niemack, and Edward J. Wollack, “Infrared dielectric properties of low-stress silicon nitride,” *Optics Letters*, vol. 37, no. 20, pp. 4200, Oct. 2012.

- [129] Tom Nitta, Shigeyuki Sekiguchi, Yutaro Sekimoto, Kenji Mitsui, Norio Okada, Kenichi Karatsu, Masato Naruse, Masakazu Sekine, Hiroshi Matsuo, Takashi Noguchi, Masumichi Seta, and Naomasa Nakai, “Anti-reflection Coating for Cryogenic Silicon and Alumina Lenses in Millimeter-Wave Bands,” *Journal of Low Temperature Physics*, vol. 176, no. 5-6, pp. 677–683, Sept. 2014.
- [130] S.O. Dabironezare, G. Carluccio, A. Pascual Laguna, S. Hähnle, J.J. Baselmans, and N. Llombart, “Quasi-optical system for the aste telescope with 1:3 bandwidth at sub-mm wave,” in *2019 44th International Conference on Infrared, Millimeter, and Terahertz Waves (IRMMW-THz)*, 2019, pp. 1–2.
- [131] A. Taniguchi, K. Karatsu, Y. Tamura, T. Takekoshi, T.J.L.C. Bakx, T. Oshima, J. Bueno, B. Buijtendorp, Y. Fujii, K. Fujita, R. Huiting, T. Ishida, S. Ishii, R. Kawabe, K. Kohno, A. Kouchi, N. Llombart, J. Maekawa, V. Murugesan, S. Nakatsubo, A. Pascual Laguna, D.J. Thoen, P.P. van der Werf, S.J.C. Yates, S.O. Dabironezare, S. Hähnle, J.J.A. Baselmans, M. Gouwerok, M. Rybak, K. Matsuda, S. Brackenhoff, A. Doing, H. Akamatsu, T. Kitayama, and Endo A., “Development of an integrated superconducting spectrometer for science-grade astronomical observations,” in *19th International Workshop on Low Temperature Detectors (LTD19)*, 2021, 19th International Workshop on Low Temperature Detectors (LTD19).

Summary

Superconducting Integrated Circuits at Sub-millimeter Wavelengths

Superconducting integrated circuits (SICs) represent a natural step forward for devices operating at frequencies from microwave up to sub-millimeter wavelengths. They offer massive miniaturization via compact design based on low-loss superconducting transmission lines. At sub-millimeter wavelengths, the development of SICs is driven by astronomical instruments where it could allow the realization of an imaging spectrometer, combining simultaneous imaging and spectroscopy capabilities into a single instrument analogous to integral field units in the infrared and optical regimes. Such an imaging spectrometer can be achieved with SICs by integrating the required elements, such as spectral filters and polarizers, with the detectors onto a single chip. Without this integration, the dispersive system for even a single spatial pixel at these wavelengths would be prohibitively large and could not be realistically scaled up to allow imaging.

Astronomical signals are exceedingly weak, typically requiring many nights of exposure to get a good signal to noise ratio. It is therefore imperative that the instrument has minimal losses before its detectors. As a consequence, the losses of each element in the SIC needs to be minimized, which requires careful characterization of the individual elements, including antenna, filters, detectors and connecting transmission lines. The primary focus of this thesis lies on the experimental characterization of the wideband antenna and the low-loss superconducting transmission lines.

All experiments in this thesis are based on a lab-on-chip approach where an SIC element of interest, such as the antenna or transmission line, is placed into a dedicated chip design to characterize its performance in isolation of any other elements. The chip design, fabrication and laboratory setup for each experiment are given in chapter 3.

In chapter 4 we design and validate the cryogenic system used in the remainder of the thesis. For an experiment at sub-millimeter wavelengths, sources are often operated at room temperatures while the test device is placed in a cryostat at sub-kelvin temperatures. This requires windows in the cryostat, which allow radiation to reach the device without overheating it. We have designed such an optical access with a very wide opening angle of $\theta = 37.8^\circ$ over a $0.1 - 1$ THz frequency band. The system uses a commercial pulsetube cooler combined with a $^4\text{He}/^3\text{He}$ sorption cooler cold stage, with a base temperature of 265 mK and a hold time around 32 h. The combination of wide opening angle, large frequency band and long hold time enables a wide range of experiments, such as beam pattern measurements and spectral measurements.

In chapter 5 we demonstrate efficient radiation coupling at sub-millimeter wavelengths over an unprecedented large bandwidth from 300 – 900 GHz. The lens-antenna consists of a tapered leaky-wave slot etched in a superconducting NbTiN film on a SiN membrane, a hyper-hemispherical Si lens and a Si spacer wafer to create a 13.8 μm thin air gap between the antenna slot and the Si lens. The slot is directly coupled to a NbTiN/Al hybrid microwave kinetic inductance detector (MKID), which is connected to a microwave readout scheme. NbTiN is used for this device as it exhibits a high superconducting bandgap frequency of 1.1 THz, eliminating resistive losses over the full antenna bandwidth. We measure the lens-antenna's far field pattern and optical efficiency at three narrow frequency bands, covering the antennas full 1:3 bandwidth. The experimental results for both beam pattern and optical efficiency are in good agreement with simulations. We find an aperture efficiency of around $\eta_{apt} \approx 0.4$ over the full antenna bandwidth, which represents the highest measured value for a leaky-lens antenna at sub-millimeter wavelengths to date. This result is limited by the absence of anti-reflection (AR) coating in this experiment and implementing a wideband AR coating can increase the efficiency by up to 30 %.

Transmission lines are the fundamental building block of any SIC, with co-planar waveguides (CPWs) and microstrip lines as the most commonly used types. While resistive losses are not a concern due to the use of a superconducting film, both CPW and microstrips have other intrinsic loss mechanisms, with radiation loss and dielectric loss as the dominant loss mechanisms for CPW and microstrip respectively. Accurate measurements of very low losses in superconducting transmission lines at sub-millimeter wavelengths are highly difficult to achieve, as the electronics used at microwave frequencies can not simply be scaled. As a consequence, our current understanding of the relevant loss mechanisms in this regime is insufficient, with limited or non-existent data. We show in this thesis that on-chip Fabry-Perot resonators (FPRs) are a simple, flexible and accurate method to measure these very low losses at sub-millimeter wavelengths and sub-Kelvin temperatures.

In chapter 6, we show that NbTiN based superconducting CPW transmission lines are limited by radiation losses at 350 GHz, and that these losses can be suppressed by using a superconductor with high kinetic inductance. We design multiple chips, each containing a single FPR with a different CPW line width which is coupled to an antenna on one side and to an MKID on the other. We carry out a frequency sweep with a tunable continuous-wave photomixer source coupled to the antenna and read out the MKID response to obtain the FPRs transmission spectrum. The spectrum then consists of multiple resonance peaks with a peak shape that depends on the CPW transmission line losses and the coupling strength of the FPR to the MKID and antenna. By correcting for the coupling strength using simulations we obtain the losses of the CPW line, which are in excellent agreement with radiation loss simulations and represent a significant suppression of radiation loss compared to a CPW with no kinetic inductance.

In chapter 7, we measure the losses of a NbTiN/a-Si/NbTiN microstrip at 350 GHz. Microstrip transmission lines do not suffer from radiation loss and offer more compact and less complex circuit designs, which makes them more attractive than CPW in many applications. Here, we also demonstrate that combining multiple FPRs of different lengths on a single chip can be used to obtain the transmission line loss without the need for simulations

of the resonators coupling strength. We carry out a frequency sweep analogous to that of the CPW loss measurement of chapter 6 and obtain the transmission spectrum for all FPRs simultaneously. Combining the analysis of the four spectra then directly provides the microstrip loss. In addition, we measure the power dependent loss of microwave resonators which are included on the same chip to obtain comparative microwave data around 6 GHz. Here, we observe a power dependence consistent with two-level system (TLS) theory, but the measured loss is significantly lower than that at 350 GHz. This difference is not expected in the TLS standard model and could point to different loss mechanisms in this frequency regime. Additionally, the losses are about six times higher than those of the narrowest CPW in chapter 6, but still sufficiently low for use in next generation on-chip spectrometers.

With the demonstration of the wideband antenna, low-loss CPW and microstrip lines, this work has created the building blocks needed for future imaging spectrometers. The first prototype, still with a single pixel, is DESHIMA-2, which uses all three structures developed in this work.

Summary

Supergeleidende geïntegreerde circuits voor sub-millimeter golflengtes

Supergeleidende geïntegreerde circuits (SIC's) zijn een natuurlijke stap voorwaarts voor chips die werken op de golflengtes van microgolven tot op zogenaamde sub-millimeter straling. SIC's maken een enorme miniaturisatie mogelijk door middel van compacte designs gebaseerd op supergeleidende transmissie-lijnen. Voor sub-mm straling, met een golflengte iets onder de 1 mm, wordt de ontwikkeling bepaald door de mogelijkheid om nieuwe astronomische instrumenten te maken: Spectroscopische camera's, die het mogelijk maken om afbeeldingen te maken waarbij voor elk pixel een gedetailleerd spectrum van de gemeten straling beschikbaar is, analoog aan zogenaamde IFU's, 'integral field units', die al bestaan voor optische en nabij infraroodstraling. Zo'n spectroscopische camera kan gemaakt worden met SIC's door al de elementen, zoals spectrale- en polarisatiefilters samen met detectoren te integreren op een enkele chip. Zonder deze integratie zou een spectrometer voor een enkel pixel al heel groot worden zodat een combinatie van veel pixels onmogelijk zou zijn.

Astronomische signalen zijn extreem zwak, er zijn typisch vele nachten nodig om voor een astronomische observatie een goede signaal-ruisverhouding te krijgen. Daarom is het van extreem belang dat er geen signaal verloren gaat in de instrumentatie voordat het gemeten wordt. Om die reden moeten de verliezen in al de elementen van de SIC's worden geminimaliseerd, waarvoor een zorgvuldige karakterisatie van al de individuele elementen van de SIC' nodig is: Dit zijn bijvoorbeeld de antennes, filters, signaallijnen en de detectoren. De focus van dit proefschrift is de experimentele karakterisatie van de breedbandige antenne, en de supergeleidende transmissielijnen voor toekomstige SIC's voor de astronomie.

Alle experimenten in dit proefschrift zijn gebaseerd op een 'lab-op-chip' aanpak, waarbij de enkele elementen, zoals antenne of transmissielijn, worden geplaatst op een chip die speciaal ontwikkeld is om het specifieke element te testen. Het ontwerp van deze chips, de fabricage en de meetopstelling worden besproken in hoofdstuk 3.

In hoofdstuk 4 ontwerpen en testen we het koelsysteem dat gebruikt wordt in de rest van het proefschrift. Voor een experiment op sub-millimeter golflengtes gebruiken we stralingsbronnen die werken op kamertemperatuur, terwijl de chip in een cryostaat is geplaatst op temperaturen onder de 1 K ($0\text{ K} = -273\text{ °C}$). Hiervoor zijn vensters in de cryostaat nodig die het mogelijk maken voor de sub-mm straling om de chip te bereiken, zonder dat deze wordt oververhit door de thermische straling van de rest van het experiment op kamertemperatuur. Wij hebben een systeem ontwikkeld van vensters die dit mogelijk maakt met een

grote openingshoek van $\theta = 37.8^\circ$ die straling doorlaat over een 0.1 – 1 THz bandbreedte. Dit systeem maakt gebruik van een commerciële koeler met een minimumtemperatuur van 265 mK die 32 uur lang vastgehouden wordt, waarna de $^4\text{He}/^3\text{He}$ koeler een uur lang opnieuw afgekoeld moet worden. De combinatie van een grote openingshoek, grote bandbreedte en het vasthouden van een temperatuur van 265 mK gedurende 32 uur maakt een groot aantal experimenten mogelijk, zoals bundel patroon metingen en spectrale metingen.

In hoofdstuk 5 demonstreren we efficiënte stralingskoppeling met een antenne over een ongeëvenaarde bandbreedte van 300 – 900 GHz. Het lens-antenne systeem wat we hiervoor gebruiken is gebaseerd op een ‘lekkende golfantenne’ (leaky wave antenna) die gefabriceerd is van een supergeleidende NbTiN (niobium titaan nitride) film op een SiN (silicium nitride) membraan, gecombineerd met een Si lens en een Si afstandhouder die een $13.8\mu\text{m}$ ruimte creëert tussen de lens en de antenne. De antenne maakt onderdeel uit van een NbTiN/Aluminium MKID (microgolf Kinetische Inductie Detector). NbTiN wordt in deze chip gebruikt omdat het een grote supergeleidende overgangsfrequentie heeft van 1.1 THz. Voor lagere frequenties heeft dit materiaal geen elektrische verliezen, wat de antenne dus efficiënter maakt. In het experiment hebben we de optische koppeling en bundelpatroon gemeten in een smalle band rond 3 centrale frequenties die de hele 1:3 bandbreedte van de antenne overspanen. De experimentele resultaten zijn in goede overeenstemming met de simulaties en we vinden een ‘aperture efficiëntie’ $\eta_{apt} \approx 0.4$ over de hele bandbreedte. Dit is de hoogste waarde voor een dergelijke antenne die tot nu toe gemeten is. De beperkende factor is de afwezigheid van een anti-reflectie laag, die een verbetering zou kunnen geven van 30 %.

Transmissielijnen zijn de fundamentele bouwsteen in elk SIC, waarbij CPW lijnen (Coplanar waveguides) en microstrip-lijnen de meest gebruikte soorten zijn. Ohmse verliezen spelen geen rol bij supergeleiders, maar ander mechanismes zijn wel belangrijk, zoals stralingsverliezen en diëlectrische verliezen voor respectief CPW lijnen en microstriplijnen. Nauwkeurige metingen van de zeer kleine verliezen in supergeleidende transmissielijnen op sub-mm golflengtes zijn extreem moeilijk, omdat er geen geschikte elektronica voor is om dit te doen. Hierdoor is ons begrip van de mechanismes die zorgen voor verliezen in dit regime onvoldoende, en is er bijna geen experimentele data. In dit proefschrift laten we zien dat Fabry-Perot resonatoren (FPR) gemaakt van supergeleidende transmissielijnen een simpele, exacte methode zijn om deze verliezen te meten.

In hoofdstuk 6 laten we zien dat NbTiN CPW lijnen op 350 GHz gelimiteerd worden door stralingsverliezen en dat deze verliezen heel klein gemaakt kunnen worden door het gebruiken van een supergeleider met een hoge kinetische inductie. We ontwerpen verschillende chips, elk met een FPR met een CPW lijn met andere dimensies, gekoppeld aan een antenne aan de ene kant en een MKID detector aan de andere kant. We meten de response van de detector als functie van de frequentie van een input signaal dat gegenereerd wordt door een fotomixer. Op deze manier verkrijgen we de transmissie van de FPR als functie van de aangeboden signaalfrequentie. Dit frequentie-spectrum bestaat uit verschillende resonatiepieken wiens vorm afhangt van de verliezen in de CPW lijn en de koppelstructuren van de FPR. Door de corrigeren voor de koppelstructuren verkrijgen we de verliezen in de CPW lijn. Deze zijn in zeer goede overeenstemming met simulaties die ervan uit-

gaan dat alleen stralingsverliezen een rol spelen. Uit deze simulaties blijkt ook dat de stralingsverliezen in een CPW zonder kinetische inductie veel groter zijn.

In hoofdstuk 7 meten we de verliezen in een NbTiN/a-Si (amorf Silicium)/NbTiN microstrip transmissielijn op 350 GHz. Microstriplijnen zijn een 3D structuur die geen last hebben van stralingsverliezen en maken compactere structuren mogelijk. Om die reden zijn ze voor veel applicaties aantrekkelijker dan CPW lijnen. In dit hoofdstuk laten we zien dat we met een chip met 4 FPR's van verschillende lengte direct de verliezen in de lijn kunnen meten zonder dat we een simulatie nodig hebben van de koppelstructuren, wat nog wel nodig was in hoofdstuk 6. In het experiment meten we respons van de 4 lijnen tegelijkertijd als functie van de frequentie van het photomixer-signaal net als in hoofdstuk 6 en verkrijgen op die manier de frequentie-response. De analyse van de 4 metingen samen geeft direct het verlies in de microstriplijn. We meten ook de verliezen in microstrip resonatoren met een resonantiefrequentie van ongeveer 6 GHz, die gefabriceerd zijn op dezelfde chip. In de 6 GHz resonatoren zien we een afhankelijkheid van de verliezen met het aangeboden signaalvermogen, wat consistent is met de 2 level (TLS) theorie. Echter, die verliezen op 6 GHz zijn veel lager dan op 350 GHz, wat de TLS theorie niet voorspelt. Ook zijn de verliezen ongeveer 6 maal hoger dan voor de smalste CPW lijnen van hoofdstuk 6, maar nog steeds goed genoeg voor een toepassing in de volgende generatie on-chip spectrometers.

Met de demonstratie van een breedbandige antenne, CPW lijnen en microstriplijnen met erg lage verliezen op 350 GHz heeft dit proefschrift de bouwstenen gecreëerd voor toekomstige beeldvormende spectrometers. Het eerste prototype, met nog steeds 1 pixel, is DESHIMA-2 en gebruikt al de 3 structuren ontwikkeld in dit proefschrift.

List of Publications

Journal Papers

- J1.** S. Hähnle, J. Bueno, R. Huiting, S. J. C. Yates and J. J. A. Baselmans, "Large Angle Optical Access in a Sub-Kelvin Cryostat," *Journal of Low Temperature Physics* , vol. 193, pp. 833-840, May 2018.
- J2.** S. Hähnle, O. Yurduseven, S. van Berkel, N. Llombart, J. Bueno, S. J. C. Yates, V. Murugesan, D. J. Thoen, A. Neto and J. J. A. Baselmans, "An Ultra-Wideband Leaky Lens Antenna for Broadband Spectroscopic Imaging Applications," *IEEE Transactions on Antennas and Propagation* , vol. 68, no. 7, pp. 5675 - 5679, Feb. 2020.
- J3.** S. Hähnle, N. v. Marrewijk, A. Endo, K. Karatsu, D. J. Thoen, V. Murugesan and J. J. A. Baselmans, "Suppression of radiation loss in high kinetic inductance superconducting co-planar waveguides," *Applied Physics Letters* , vol. 116, no. 18, pp. 182601, May 2020.
- J4.** S. Hähnle, K. Kouwenhoven, B. Buijtenorp, A. Endo, K. Karatsu, D. J. Thoen, V. Murugesan and J. J. A. Baselmans, "Superconducting microstrip losses at microwave and sub-millimeter wavelengths," *Physical Review Applied* , vol. 16, no. 1, pp. 014019, July 2021

Conference Papers

- C1.** S. O. Dabironezare, G. Carluccio, A. Pascual Laguna, S. Hähnle, J. J. Baselmans, N. Llombart, "Quasi-Optical System for the ASTE Telescope with 1:3 Bandwidth at Sub-mm Wave", *The 13th European Conference on Antennas and Propagation (EuCAP 2019)*, Krakow, Poland, April 2019
- C2.** A. Endo, A. P. Laguna, S. Hähnle, K. Karatsu, D. J. Thoen, V. Murugesan and J. J. Baselmans, "Simulating the radiation loss of superconducting submillimeter wave filters and transmission lines using Sonnet EM," *SPIE Astronomical Telescopes + Instrumentation*, Yokohama, Japan, June 2020

Thesis Co-Supervised

- T1.** K. Kouwenhoven, "Dielectric Loss Measurements at Sub-K Temperatures and Terahertz Frequencies," M.Sc. thesis, Delft University of Technology, Delft, The Netherlands, Aug. 2019.

Curriculum Vitae

Sebastian Hähnle

12 July 1989	Born in Munich, Germany
2009 – 2012	BSc Physics Heidelberg University, Heidelberg, Germany
2012 – 2015	MSc Physics Thesis title: <i>Thermodynamic Properties of Holmium in Gold</i> Heidelberg University, Heidelberg, Germany
2016 – 2021	PhD Candidate Dissertation title: <i>Superconducting Integrated Circuits at Sub-millimeter Wavelengths</i> Delft University of Technology, Delft, The Netherlands

Acknowledgements

This work would not have been possible without the supervision, support and guidance of many people. While my name is on the cover of this thesis, the pages within couldn't exist without them. First of all, I want to thank my promotors, Prof. Jochem Baselmans and Dr. Akira Endo.

Jochem, I literally can not thank you enough for the support you have given me over these past years. It was a privilege to learn from you and you really were an excellent guide through the mountainous terrain of this PhD.

Akira, your passion and attention to the smallest details has been an inspiration. Thank you for the many long and fruitful discussions.

Furthermore, I want to thank the committee members, Prof. Driessen, Prof. LLombart, Prof. Sarro, Dr. Doyle and Dr. de Visser for taking their time to read and evaluate this thesis.

I want to thank everyone who helped realize the experiments in Delft, Utrecht and Groningen. Experimental work is rarely possible alone and this thesis was no exception. Juan "Obi-Juan Kenobi" Bueno, for the supervision inside and outside the lab. You helped me find the calm and patience to deal with all the inevitable setbacks experimental research brings with it. David and Vignesh, for their cleanroom wizardry which made all of these experiments possible. Thank you for all the chips you have made over these years and the readiness to always answer my questions regarding fabrication. Kenichi, for the support in the Cryolab and the Deshimac. Stephen Yates, for the introduction to the intricacies of beam pattern measurements and the support you gave me in Groningen. Pieter, for your expertise on superconductivity and MKIDs. Ozan, for the design and simulations of the leaky lens antenna. Robert Huiting, for the many mechanical designs from cryostat optics to the hotsource assembly and everyone in the mechanical workshop at SRON Utrecht for bringing those designs to life.

I am very grateful to my colleagues at the Terahertz Sensing group in Delft: all the staff members, Post-Docs, PhDs students, Master and Bachelor students. You created a friendly, open and collaborative atmosphere which I enjoyed and hope to find again. I especially thank Prof. Andrea Neto for your insights in the field of electromagnetics, as well as the many insightful academic and non-academic discussions and Prof. Nuria Llombart for the patient explanations of antenna theory. Special thanks also goes to the amazing secretary team of the Terahertz Sensing group, especially Everdine, and the HR department of SRON. You made the most stressful situations uncomplicated and easier to

manage.

A particular thanks also goes to Shahab, Alejandro, Sven, Christina and Nuri, who took large parts of the PhD journey alongside me. Thank you all for a great time, the strange conversations in and outside the office and simply being brilliant people. Last but not least Kevin, whom I had the pleasure to supervise during his master thesis - it was almost too easy at times.

Finally, I want to thank my family for always being there when I need you.

